Title
Cosmology and galaxy evolution from large-scale structure

Author
Krolewski, Alexander Grant

Publication Date
2020

Peer reviewed|Thesis/dissertation

Cosmology and galaxy evolution from large-scale structure

By

Alexander Grant Krolewski

A dissertation submitted in partial satisfaction of the

requirements for the degree of

Doctor of Philosophy

in

Astrophysics

in the

Graduate Division

of the

University of California, Berkeley

Committee in charge:

Professor Martin White, Chair
Professor Uros Seljak
Professor Bill Holzapfel
Professor Dan Weisz
Dr. Simone Ferraro

Summer 2020

Cosmology and galaxy evolution from large-scale structure

Abstract

Cosmology and galaxy evolution from large-scale structure

by

Alexander Grant Krolewski

Doctor of Philosophy in Astrophysics

University of California, Berkeley

Professor Martin White, Chair

In this thesis, I use data from large scale structure surveys to explore both galaxy evolution and cosmology. My thesis covers four distinct areas: galaxy spin alignments with large-scale structure filaments (Chapters 2 and 3); voids in the Lyman-α forest (Chapter 4); quasar evolution and the thermal Sunyaev-Zel'dovich effect (Chapter 5); and cross-correlations between unWISE infrared galaxies and the cosmic microwave background (Chapters 6 and 7).

Hierarchical structure formation imprints a characteristic alignment between large-scale filaments and dark matter halos: low-mass halos accrete perpendicular to the filaments and thus acquire spin along the filament, whereas high-mass halos grow by mergers and thus acquire spin perpendicular to the filament. These spin alignments lead to correlations between galaxy shapes and large-scale structure, a major systematic for weak lensing surveys. I study the prospects for detecting this signal at $z \sim 2.5$ using filaments measured in the Lyman-α forest, and also present an upper limit on galaxy spin-filament alignments at $z \sim 0.1$ with the MaNGA survey of galaxy kinematics.

Voids are a powerful probe of dark energy, modified gravity, and neutrino mass. I present the highest-redshift detection of voids ($z \sim 2.5$) and first detection of voids in the Lyman-α forest. I show that these voids are $> 5\sigma$ underdense in coeval spectroscopic galaxies, and characterize their stacked profile and distribution of sizes.

The thermal Sunyaev-Zel'dovich effect is a powerful probe of hot halo gas. I study the physical origin of the tSZ-quasar cross-correlation. On large scales, it probes the bias of the hot halo gas, and future tSZ-quasar cross-correlation studies will constrain the amplitude of the tSZ signal across all halos at $0 < z < 2$. On small scales, the tSZ signal scales as $M^{5/3}$, and is thus sensitive to the distribution of quasar host halos. tSZ cross-correlations from the DESI survey should place interesting constraints on quasar models that otherwise match quasar clustering and luminosity function data. Moreover, because DESI is fainter than previous quasar samples, the tSZ signal should be dominated by contributions from the host halo virialization rather than from energy injection by AGN feedback, which scales with the quasars' luminosity.

Chapters 6 and 7 explore the cosmological constraining power of infrared galaxies from the unWISE catalog in tandem with cosmic microwave background observations. In Chapter 7, I measure the cross-correlation between unWISE infrared galaxies at $z < 2$ and Planck CMB lensing. With signal-to-noise of 80, this is the highest-significance detection of CMB lensing cross-correlations thus far, offering the potential for percent-level constraints on the amplitude of matter clustering. In Chapter 7, I describe the measurement and systematics tests; the most significant systematic is the uncertain redshift distribution of the unWISE galaxies, which I measure using cross-correlations with SDSS spectroscopic galaxies and quasars. In Chapter 7 I measure the cross-correlation between unWISE galaxies and CMB temperature on large scales from the integrated Sachs-Wolfe effect. This is a 3 to 4σ detection of dark energy and holds promise for constraining modified gravity models throughout the dark energy dominated epoch.

To my parents and grandparents

Contents

List of Figures

List of Tables

Acknowledgments

In crafting these acknowledgments, I have come to realize how fortunate I've been to learn astrophysics at Berkeley. The research environment here has been truly excellent, in the department as a whole and particularly in the BCCP and LBL cosmology groups. Berkeley is one of the best places in the world to train as a cosmologist, and I've been truly privileged to learn from a large number of very smart people.

I would like to start by thanking my advisors and mentors. To my advisor, Martin White, for teaching me about all areas of cosmology, from theory to simulations to statistical inference. Martin, your support and guidance have been invaluable, and I hope to emulate both your breadth of knowledge and your scientific skepticism. To my mentor, Simone Ferraro, for leading me into our work with the unWISE catalog, and teaching me so much about the CMB. I have been the very fortunate beneficiary of Simone's wisdom about CMB lensing and cross-correlations, and it has been thrilling to work on such interesting and impactful science together. Simone's presence as a friend has been just as important, particularly throughout the pandemic—without our regular science chats and hikes, the past few months would have been much harder to bear.

I'd also like to thank my previous advisors and mentors, Shirley Ho, Peter Nugent, Khee-Gan Lee, and Zarija Lukic. I had a lot of fun working on our projects together, and learned an enormous amount about galaxy alignments, simulations and large-scale structure from Shirley; and the Lyman-α forest, observations, and hydrodynamic simulations from K.G., Zarija, and Peter. I especially appreciate the supportive and collaborative atmosphere that Shirley fostered in her group, which was greatly helpful to me as a somewhat overwhelmed young graduate student. Together, these early projects facilitated my growth and development as a cosmologist, and I'm glad to be able to include them in this thesis.

I would also like to thank my committee members, Martin White, Uros Seljak, Dan Weisz, Bill Holzapfel and Simone Ferraro, for their advice.

I'd like to thank Zack Slepian for being a mentor, great roommate and steadfast friend. Thanks Zack for all those late nights at the Milvia Street dinner table, when we were allegedly doing astrophysics but we both know it was really a front for hanging out, talking through problems both scientific and personal, and listening to transcendent Bach, Beethoven, Brahms, and others. The research notebook system has been a godsend organizationally and scientifically, and I'm continually amazed and impressed by your affinity for integrals and analytic solutions. It's been great to work on science with someone who's

also a good friend.

I would be remiss not thank my many coauthors on the papers constituting the bulk of this thesis. To Eddie Schlafly, for making the unWISE catalog a reality and for being one of the most careful and thorough scientists I've met. I thank Marcelo Alvarez for introducing me to CMB secondary anisotropies, imparting much computational knowledge, and bringing the tSZ expertise to our quasar-tSZ cross-correlation cross-correlation work. I'm grateful to Yu Feng for providing the CrowCanyon simulations that we used to validate methods and pipelines for CMB lensing cross-correlations, and teaching me how to use them even after leaving the field!

Pok-Fung (Sunny) Chan was a great summer student assisting me on the MaNGA filament alignment project, and I learned a lot from teaching him about astrophysics and cosmology. Yen-chi Chen's statistics knowledge and filament catalog also played an essential role in the MaNGA alignment project. Though we never overlapped, Casey Stark's work was an excellent example to me in my early days as the Lyman-α grad student, and his Dachshund Wiener filter code (what a name!) was very enabling for my CLAMATO work. After I moved to CMB cross-correlations, I'm glad that Ben Horowitz picked up the mantle as Lyman-α grad student, and am honored that he included me to help advise his undergraduate research group and to participate in the TARDIS reconstruction paper (another great name). It's also been great collaborating with Miguel Zumalacarregui and Janina Renk on the unWISE integrated Sachs-Wolfe project; I've really enjoyed learning about modifications to General Relativity from them as they've led this work interpreting the measured signal.

I'd also like to thank my collaborators on work that hasn't yet appeared in a paper, mostly within the DESI collaboration. Michael Wilson provided an excellent "baptism by fire" in the DESI collaboration, and our work on DESI survey strategy and at the Barcelona meeting was both exhausting and exhilirating. Pat McDonald and his Fisher forecasting code were also supremely helpful with this study. I look forward to continue collaborating with them and many other DESI members over the next five years.

I'd also like to thank my fellow cosmology students, Ben Horowitz, Chirag Modi, Ellie Kitanidis, Siyu He, Stephen Chen, and James Parkes. Thank you Ellie and James for many useful conversations as we figured out CMB lensing and unWISE together. Siyu, James, Elena Giusarma and Elena Massara were excellent office mates, sharing the cold corner office in Building 50. Thanks also to my cohort of astro grad students, Saundra Albers, Max Genecov, Deepthi Gorthi, Nick Kern, Michael Medford, and Wren Suess, and your help and support in the trying early days of the PhD. I'm especially grateful to Michael Medford for being an excellent friend, office mate, sounding board, and NERSC oracle in our days on the 2nd and 5th floors of Campbell. Finally, department administrators Dexter Stewart and Amber Banayat have played a crucial role in keeping everything running smoothly and helping me sort out many administrative problems along the way.

My journey as an astronomer and physicist really began at Harvard, and without the support of many people there I would surely be doing something less interesting these days. Josh Speagle's incredible enthusiasm and knowledge was crucial in sending me down this path, as was Dave Charbonneau's inspirational introductory astronomy class (also with

assistance and encouragement from teaching assistant and now Berkeley professor Courtney Dressing). Most important was my time working for Daniel Eisenstein, who remains a major scientific influence; I was incredibly lucky to receive his guidance as an undergraduate.

Finally, I am grateful to my (non-astronomy) friends and family. I could not have completed my higher-education journey without my parents' unwavering support and love. Mom and Dad, you have taught me so much and have been excellent role models throughout my life. I must also thank Michael Schroeder, Damon Bollens, and Jesse Zhang for being incredible friends throughout my PhD, both in person (Damon and Jesse) and remotely (Michael).

This dissertation was typeset using the ucastrothesis LaTeX template.

Chapter 1

Introduction

1.1 Cosmology overview

Cosmology is one of the newest subfields of physics. When my advisor was born, very little of today's knowledge about the universe was in place. When I was born, the broadest outlines of the field were established but key parts of the model were missing and parameters were uncertain to within a factor of two. Now the standard ΛCDM model of cosmology is very well-established, matches data to very high significance, and has few percent errors on cosmological parameters (Planck Collaboration et al. 2018a, Fig. 1.1). This vast increase in knowledge is a major triumph in our understanding of the physics of the universe, but is far from complete.

The ΛCDM model (Peebles 1984; Vittorio & Silk 1985; Efstathiou et al. 1990; Ostriker & Steinhardt 1995; Krauss & Turner 1995; Liddle et al. 1996) works very well but is a purely phenomenological model, with many important questions about the underlying physics unanswered. It posits that the universe is composed of normal matter from the standard model of particle physics (photons, neutrinos, and everything else, a.k.a. "baryons" to a cosmologist); dark matter that interacts primarily gravitationally, and only extremely weakly via other forces (Peebles 1982); and dark energy, whose negative pressure drives an accelerating expansion of the universe. The dynamics of the universe are governed by General Relativity and thus determined by the energy density of each component. The initial conditions are set by quantum fluctuations of the inflaton field (Starobinsky 1980; Guth 1981), which classically freeze to a nonzero value when the wavelength of the fluctuation becomes longer than the Hubble scale. This seeds the universe with the right order-of-magnitude density fluctuations (Mukhanov & Chibisov 1981; Mukhanov et al. 1992).

After inflation, the universe is radiation-dominated. As it cools and expands, relativistic protons, neutrons and electrons annihilate; due to a very small initial imbalance between particles and anti-particles, some residual particles remain. The conditions for the primordial imbalance, baryogenesis, were enumerated by Sakharov (Sakharov 1991). The mechanism for baryogenesis is unclear, with leptogenesis (Fukugita & Yanagida 1986) and the Affleck-Dine mechanism (Affleck & Dine 1985) among the top contenders. As the universe continues

to cool, the interaction rates for certain processes will drop below the Hubble rate, leading to thermal freezeout of neutrinos and possibly the dark matter, if it is composed of a weakly interacting massive particle (WIMP) (Steigman & Turner 1985).

The next major transition is when the universe cools enough to permit the formation of atoms. Since photons interact with free electrons far more readily than hydrogen atoms, this leads to a massive increase in the optical depth of the universe, and nearly all of the photons in the universe free-stream across the universe from the "surface of last scattering." This relic emission is called the Cosmic Microwave Background, first detected by Penzias & Wilson (1965) and Dicke et al. (1965). It is a nearly perfect blackbody (Fixsen 2009) and its anisotropies are a rich source of information about the early universe (Peebles 1968; Peebles & Yu 1970; Peebles 1982). Since the anisotropies are small, $\delta\rho/\rho \sim 10^{-5}$, they can be efficiently computed using linear perturbation theory (Ma & Bertschinger 1995) and in practice are computed using standard "Boltzmann codes" (Seljak & Zaldarriaga 1996; Lewis et al. 2000; Blas et al. 2011). The CMB anisotropies have provided powerful constraints on cosmological parameters. They have established the cold dark matter model (Efstathiou et al. 1992), determined that the universe is spatially flat (Knox & Page 2000; Pierpaoli et al. 2000) and strongly constrained multiple cosmological parameters (Spergel et al. 2003; Bennett et al. 2003; Planck Collaboration et al. 2018a). Fig 1.1 shows the most recent CMB anisotropy measurements from the Planck survey.

During radiation domination, structure growth via gravitational collapse is inhibited by radiation pressure. When the universe becomes matter dominated, however, the pressure drops and structure can begin to grow. In the linear regime, the growth is scale-independent and most compactly described in Fourier space, because Fourier modes of the density field with different wavevector k grow independently in the linear regime. Therefore, cosmologists often work in Fourier space using the power spectrum of the density field $P(k)$:

$$\delta(k) = \int d^3x\, \delta(x) e^{ikx} \tag{1.1}$$

$$\langle \delta(k)\delta(k')\rangle = (2\pi)^3 P(k)\delta^3(k-k') \tag{1.2}$$

where the first equation relates the matter overdensity $\delta \equiv (\rho - \bar{\rho})/\bar{\rho}$ to its Fourier transform. Note also that comparison to theory requires a two-point function, $P(k)$ or its Fourier transform the correlation function $\xi(r) \equiv \langle \delta(x)\delta(x+r)\rangle$, because the initial phase of the density field is random and realization-dependent, but its correlations are sensitive to the underlying physics. In the linear regime ($\delta << 1$), the density field δ is a Gaussian random field with Fourier modes growing independently

$$P_{\rm linear}(k,z) = D^2(z) P_{\rm linear}(k) \tag{1.3}$$

where $D(z)$ is the linear growth factor, which is very well-approximated by (Linder & Cahn 2007)

$$D(z) = \Omega_m(z)^{\gamma=0.55} \tag{1.4}$$

As δ becomes large, structure formation couples different Fourier modes of the density field.

Eventually overdensities collapse into bound objects called dark matter halos (Gunn & Gott 1972; Navarro et al. 1997). The large-scale distribution of halos provides striking qualitative evidence for cold dark matter instead of hot (relativistic) or warm (mildly relativistic) dark matter (Blumenthal et al. 1984; Davis et al. 1985).

After CMB photons decouple from the baryon-photon plasma, the universe is almost entirely neutral. However, the first stars and galaxies emit enough photons to reionize the universe (Pritchard & Loeb 2012) and by $z \sim 6$, quasar absorption spectra show the remaining neutral fraction must be $< 10^{-4}$ (Gunn & Peterson 1965; Fan et al. 2006). Quasar absorption spectra probe the neutral fraction by measuring the "forest" of redshifted Lyman-α absorption lines in quasar spectra from structure at different redshifts along the line of sight to the quasar. At $z \sim 3$, fluctuations in Lyα absorption trace fluctuations in the density field, as confirmed by hydrodynamic simulations of the intergalactic medium (Cen & Ostriker 1992; Katz et al. 1992; Katz et al. 1996; Miralda-Escudé et al. 1996; Weinberg et al. 2003; McQuinn 2015). As a result, the Lyα forest is a powerful probe of small-scale structure at $z \sim 2$ (where the 1216 Å Lyα line is redshifted into the optical) and can place strong constraints on the amplitude of the matter power spectrum and the neutrino mass (Seljak et al. 2005; McDonald et al. 2006).

Within a bound overdensity, the behavior of dark matter is relatively simple: it forms a diffuse halo, generally triaxial in shape, with a standard density profile (Navarro et al. 1997) and universal mass function (Tinker et al. 2008, 2010). Galaxy formation within the halo is much more complex. Baryons can cool efficiently and thus collapse to a much smaller radius than the dark matter. Like halos, galaxies are biased tracers of the dark matter inhabiting density peaks (Bardeen et al. 1986). This has led to physical models for galaxy clustering such as the halo model (Seljak 2000), the halo occupation distribution model (Zheng et al. 2005), and subhalo abundance matching (Vale & Ostriker 2004; Shankar et al. 2006; Conroy et al. 2006). These models are widely used in cosmology with the intention of marginalizing over the uncertain galaxy properties.

A more detailed understanding of galaxies, including the effect of feedback from supermassive black holes and supernovae, requires hydrodynamic simulations. Hydrodynamic simulations are severely limited by resolution and box size compared to gravity-only (N-body) simulations, but recently have begun to match a number of significant galaxy observational properties, including the bimodality of galaxy properties and the presence of disks (Vogelsberger et al. 2014).

At $z < 1$, a new component begins to dominate over dark matter: dark energy, which drives an accelerating expansion of the universe. The accelerated expansion of the universe was first discovered in observations of type Ia supernovae as standard candles (Riess et al. 1998; Perlmutter et al. 1999) and cemented by standard ruler observations of baryon acoustic oscillations in galaxy clustering (Alam et al. 2017). The physical origin of dark energy remains mysterious (Weinberg et al. 2013; Mortonson et al. 2013; Tanabashi et al. 2018). While quantum field theory predicts a zero-point energy associated with the vacuum, this is 60 orders of magnitude higher than the observed dark energy (Martin 2012). Prominent alternatives include modifications to general relativity (Baker et al. 2013), typically with

Parameter	Value
$\Omega_b h^2$	0.022447
$\Omega_{\rm cdm} h^2$	0.11923
$100\theta_{\rm MC}$	1.041010
τ	0.0568
$\ln(10^{10} A_s)$	3.0480
n_s	0.96824
H_0	67.70
Ω_m	0.3106
Ω_Λ	0.6894
σ_8	0.8110

Table 1.1: Constraints on spatially flat ΛCDM models from Planck plus BAO data. Top parameters are the standard 6 parameters; τ is the optical depth to the CMB, A_s the amplitude of initial fluctuations, n_s is the power-law slope of the initial power spectrum; $\theta_{\rm MC}$ is the angular size of the sound horizon. Bottom 4 parameters are derived from the top 6.

screening on small scales to ensure agreement with local tests in the Solar System (Jain & Khoury 2010). Examples of these models include Horndeski theories (Horndeski 1974) and massive gravity (Hinterbichler 2012). Another potential solution to the problem is anthropic: if the cosmological constant is allowed to vary in space (or among vacua in the string landscape), we must live in a world where the cosmological constant is compatible with the existence of intelligent observers, requiring a very small value for the cosmological constant (Weinberg 1989; Martel et al. 1998).

The temperature and polarization anisotropies of the cosmic microwave background are the best source of information constraining ΛCDM, due to the rich assortment of features in the CMB power spectra (see Table 1.1 for best-fit parameters). Standard rulers and standard candles are another key source of cosmological information, particularly for late-time parameters such as dark energy. These are objects of known or very well-calibrated transverse distance or luminosity, which are compared to their angular size and observed flux, respectively. This yields line-of-sight distances, in turn constraining cosmology from the distance-redshift relation.

As primary CMB experiments reach the cosmic variance noise floor[1], other sources of cosmological information will be required. One promising source considered in this thesis is the matter power spectrum, $P(k)$ (Fig. 1.2), which is most sensitive to σ_8, Ω_m and Ω_b (though it can be used to constrain other parameters; Ivanov et al. 2019; Colas et al. 2019; D'Amico et al. 2020; Ivanov et al. 2020; Philcox et al. 2020). σ_8, the amplitude of linear matter power spectrum, scales the observed nonlinear power spectrum. Ω_b (in tandem with Ω_m) affects the BAO wiggles. Finally, Ω_m sets the turnover in the matter power spectrum.

[1]Planck is cosmic variance limited for temperature but not polarization, i.e. the main source of noise is the fact that we only have one sky, not the instrumental noise.

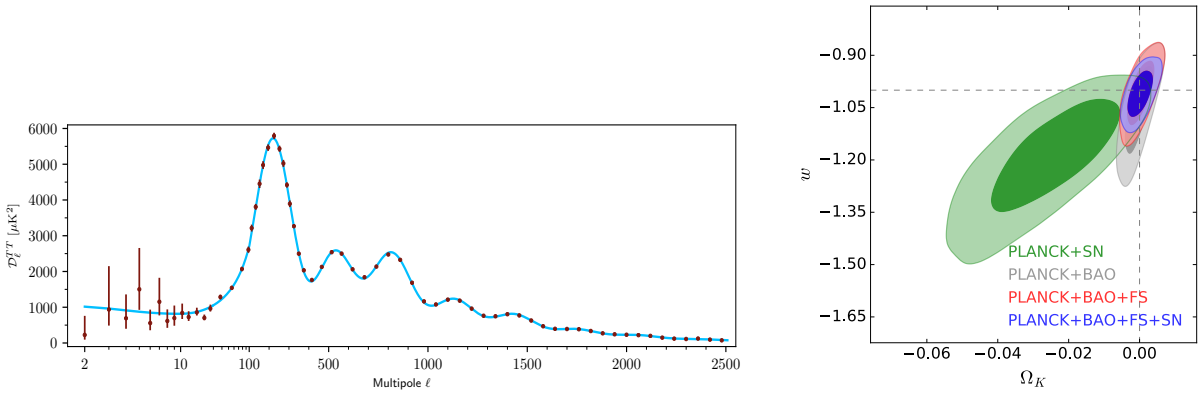

Figure 1.1: *Left:* Angular power spectrum of cosmic microwave background temperature anisotropies, $D_\ell^{TT} \equiv \ell(\ell+1)C_\ell^{TT}/2\pi$, from the Planck final release (Planck Collaboration et al. 2018a). $C_\ell^{TT}/2\pi$ is the spherical harmonic transform of the temperature field, $C_\ell^{TT} \equiv \langle|a_{\ell m}^{TT}|^2\rangle$. Blue curve is ΛCDM model, which fits the data extremely well on all scales. While deficits at $\ell = 2$ and $\ell = 20$ are seemingly significant by eye, they do not constitute strong evidence for models other than ΛCDM (Planck Collaboration et al. 2014f, 2016c). *Right:* Constraints on dark energy from the low-redshift universe in tandem with Planck, from type 1a supernovae (green), distance information from baryon acoustic oscillations (gray) and from the full shape of the galaxy power spectrum (red). The x axis is the curvature parameter (a flat universe has $\Omega_k = 0$) and the y-axis is the equation of state of dark energy, $w \equiv P/\rho$, equal to -1 for a cosmological constant.

The turnover is determined by the epoch when modes re-enter the cosmological horizon (they exited the horizon when inflation shrunk the cosmological horizon to be smaller than all modes of interest). Small modes re-enter the horizon first, during radiation domination when their growth was suppressed by radiation pressure. Meanwhile large modes remained larger than the cosmological horizon and thus causally disconnected, allowing them to grow. Once they came back within the horizon during matter domination, they continued to grow. This leads to a characteristic turnover in the power spectrum between large modes whose growth continued unabated and small modes whose growth was suppressed during radiation domination.

In this thesis, I present work in three broad areas drawn from the above: galaxy and quasar evolution; the small-scale Lyα forest and voids; and amplitude and growth of structure measurements from CMB lensing cross-correlations. I describe each of these areas in more detail below.

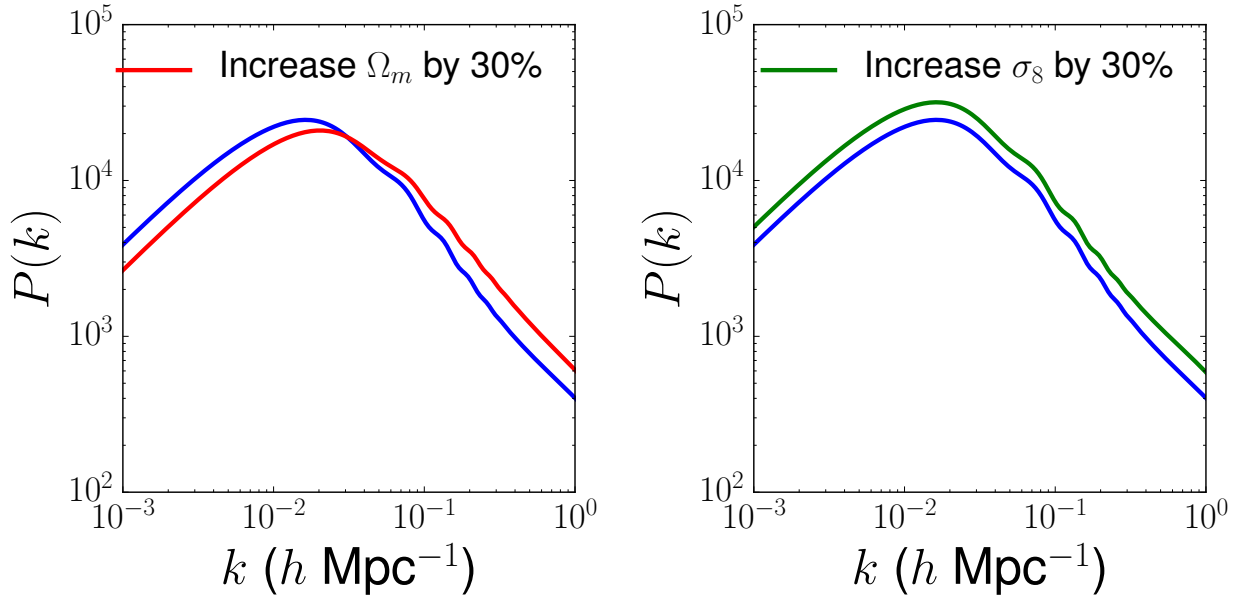

Figure 1.2: *Left:* Changing Ω_m shifts the peak of the matter power spectrum, while (*right*) changing σ_8 varies its amplitude.

1.2 Galaxy evolution in a cosmological framework

1.2.1 Galaxy alignments

Galaxy formation is tied to the properties of the host dark matter halo, with some scatter. One fundamental observable for the galaxy-halo connection is the stellar mass-halo mass relation (Moster et al. 2010; Behroozi et al. 2013, 2018). This relation is nonlinear, with a peak at halo mass 10^{12} $M_\odot$, where star formation is most efficient. At higher masses, star formation is less efficient due to AGN feedback, whereas at lower masses star formation is less efficient due to stellar and supernovae feedback. At all masses, the stellar to halo mass fraction is significantly less than the baryonic to total mass fraction; that is, most baryons do not end up in stars, but rather remain in gas. The star formation history of the universe also shows a distinct peak at $z \sim 2$ and declines thereafter (Madau & Dickinson 2014).

Galaxy alignments with halos and large-scale structure are another intriguing aspect of the connection between galaxies and dark matter. Halos acquire their angular momentum from tidal torquing by surrounding large-scale structure (Peebles 1969; Doroshkevich 1970; White 1984), which aligns the angular momentum with the traceless part of the tidal tensor. Under the Zel'dovich approximation (Zel'dovich 1970) and at the center of mass of a protohalo, its angular momentum L at time t is given by:

$$L_i(t) = a^2(t)\dot{D}(t)\epsilon_{ijk}D_{jl}I_{lk} \tag{1.5}$$

where a is the scale factor of the universe, $a = 1/(1+z)$, relating the size of the universe

at redshift z to the size of the universe today; $D(z)$ is the linear growth factor defined by Eq. 1.3 above; ϵ_{ijk} is the antisymmetric tensor (i.e. Eq. 1.5 is a cross product); I is the inertia tensor of the protohalo in Lagrangian space (i.e. following the cosmological fluid as it moves in time); and D is the deformation tensor, i.e. the second derivative of the gravitational potential at its minimum:

$$D_{jl} = -\frac{\partial^2 \Phi}{\partial q_j \partial q_l}\bigg|_{q=0} \tag{1.6}$$

Only the traceless part of the deformation and inertia tensors contribute to the cross product; thus we often refer to the traceless tidal tensor T instead

$$T_{ij} = D_{ij} - D_{ii}\delta_{ij}/3 \tag{1.7}$$

Nonlinear evolution leads to deviations from Eq. 1.5, weakening the relationship and causing the angular momentum and traceless tidal tensors to decouple (Porciani et al. 2002).

Halo alignments can also be described relative to filaments and sheets of the dark matter field rather than the tidal tensor. In a dark matter field given by gravitational potential ϕ, the equation of motion is

$$\ddot{\vec{x}} = -\vec{\nabla}\phi \tag{1.8}$$

and thus can be linearized using the traceless tidal tensor

$$\ddot{x}_i = -T_{ij}(x_{\rm eq})(x_j - x_{\rm eq,j}) \tag{1.9}$$

where $x_{\rm eq}$ is the minimum of the potential at which T_{ij} is evaluated. Therefore, in the Zel'dovich picture of structure formation (Zel'dovich 1970; Hahn et al. 2007b), the dynamics are determined by the eigenvalues of T_{ij} (Figure 2.1). If T_{ij} has no positive eigenvalues, all orbits are unstable and particles are moving away from $x_{\rm eq}$; this corresponds to a void environment. In constrast, in a cluster (or knot) environment, all eigenvalues of T_{ij} are positive and particles are collapsing toward $x_{\rm eq}$. The intermediate cases are sheets (one positive and two negative eigenvalues) and filaments (two positive and one negative eigenvalues).

Studies of halo alignments using full N-body simulations generally describe the alignments using filaments and sheets rather than the tidal tensor. They find qualitatively different behavior for low mass ($M < 10^{12} M_\odot$) and high mass halos. Low mass halos acquire spin parallel to the filament, as matter collapses and rotates in the plane perpendicular to the filament; this is the same alignment as predicted by tidal torque theory. In contrast, high mass halos acquire spins perpendicular to the filament direction as mergers convert motion along the filament into spin (Bailin & Steinmetz 2005; Aragón-Calvo et al. 2007; Hahn et al. 2007a; Codis et al. 2012; Trowland et al. 2013; Aragon-Calvo & Yang 2014; Dubois et al. 2014; Codis et al. 2015; Ganeshaiah Veena et al. 2018; Wang & Kang 2018; Wang et al. 2018) (Fig. 1.3). This measurement is necessarily dependent on the definition of the filament finder (see discussion in Cautun et al. 2014). The important point here is that the same filament finder is used in both data and theory or simulations; in Chapters 2 and 3 of this thesis, I ensure that is the case.

Moving from halo-filament alignments to galaxy-filament alignments adds an additional layer of complexity. Unlike dark matter, baryons can cool and collapse, creating a rotation-supported disk as they do so (Fall & Efstathiou 1980; Blumenthal et al. 1986; Mo et al. 1998). Indeed, the stability of a rotational disk requires the co-existence of a halo with comparable mass; this provided some of the earliest theoretical evidence for dark matter (Ostriker & Peebles 1973). Baryonic collapse conserves specific angular momentum j (the ratio between angular momentum J and mass M, $j \equiv J/M$). Therefore, the halo spin parameter λ can be related to the ratio between the disk size $R_{\rm disk}$ and the halo size $R_{\rm halo}$

$$\lambda \sim \frac{j}{R_{\rm halo} V} \sim \frac{R_{\rm disk}}{R_{\rm halo}} \tag{1.10}$$

where v is the galaxy rotation velocity, which is observed to be nearly constant across a wide range of scales (Rubin & Ford 1970; Rubin et al. 1980). The resulting disk sizes are roughly consistent with observations (Courteau 1997; Bullock et al. 2001; Burkert 2009). However, other parts of the theory are less consistent with data. The angular momentum of simulated galaxies is often far too small (Steinmetz & Navarro 1999; Navarro & Steinmetz 2000), possibly due to overcooling of the baryons, so additional stellar and supernova feedback are required to increase galaxy angular momentum to match data (Maller & Dekel 2002; Maller et al. 2002). These hydrodynamic processes lead to misalignments between galaxy and dark matter halo spins (van den Bosch et al. 2002; Bett 2012) and motivate spin-filament alignment studies using hydrodynamic instead of gravity-only simulations (Dubois et al. 2014; Codis et al. 2015; Wang et al. 2018) (Fig. 1.3).

The complexity of the physics involved motivates observational studies of galaxy-filament alignments to better understand angular momentum transfer in halos and galaxies. Studies at $z \sim 0$ inferring galaxy spins from their shapes have generally found weak evidence in favor of the transition mass picture described above (Tempel et al. 2013; Tempel & Libeskind 2013; Pahwa et al. 2016). However, these studies are hampered by the weakness of the signal and the small sample size. This previous work motivates my work described in Chapters 2 and 3, which considers different approaches to the problem.

Previous observational work has been focused on $z \sim 0$, where galaxy surveys have sufficient density to measure the cosmic web. However, in Chapter 2 I consider the feasibility of measuring spin-filament alignments at $z \sim 2$, using the Lyα forest (Sec. 1.3) as a sensitive probe of the cosmic web that is much more observationally feasible than observing the cosmic web using galaxy surveys. Galaxies at $z \sim 2$ are quite different from galaxies in the local universe, with higher star formation rates and more rotational support (Conselice 2014); they are also nearer to their formation epoch. As a result, spin-filament alignments may be quite different at $z \sim 2$ than at $z \sim 0$, and comparing alignments across different epochs will be quite valuable for studying galaxy and halo formation.

In Chapter 3, I measure spin-filament alignments at $z \sim 0$ using spins directly measured from the galaxy velocity field by the MaNGA integral field unit survey of spatially-resolved galaxy kinematics. This work complements previous observational work inferring the galaxy's spin axis from its shape.

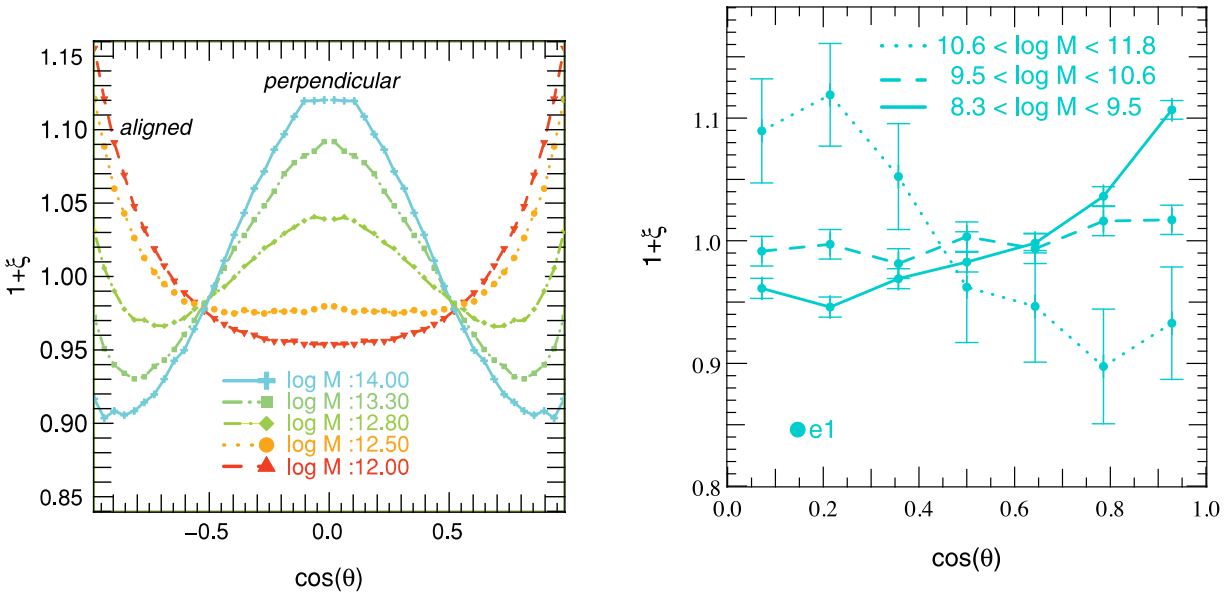

Figure 1.3: *Left:* Alignments between filaments and dark matter halos (Codis et al. 2012), moving from aligned at low halo mass to perpendicular at high halo mass. *Right:* Alignments between filaments (as traced by the first eigenvector of the tidal tensor, $\hat{e_1}$) and galaxy spins in a hydrodynamic simulation (Codis et al. 2015), as a function of stellar mass. This hydrodynamic simulation shows a similar mass-dependent transition as N-body simulations.

Galaxy alignments are important as a weak lensing systematic in addition to their role in galaxy formation. Weak lensing distorts galaxy shapes as photons propagate across the universe, leading to correlations between neighboring galaxy shapes. Therefore, intrinsic alignments between neighboring galaxies or between galaxies and large-scale structure can be a major systematic for cosmic shear (Hirata & Seljak 2004). The intrinsic alignment signal remains poorly measured, particularly for disk galaxies (Hirata et al. 2007; Mandelbaum et al. 2011) and additional constraints from spin-filament alignments can help constrain models for intrinsic alignments.

1.2.2 Quasars and galaxy evolution

Quasars are extremely bright objects ($> 10^{12} L_{\odot}$) at cosmological distances whose radiation comes from accretion around a central supermassive black hole. Shortly after their discovery (Schmidt 1963), it was realized that due to their tremendous distances and luminosities, quasars must originate from gravitational accretion rather than nuclear fusion, as accretion is the only process with efficiencies high enough (up to 6% for a non-rotating black hole) to create such bright objects (Hoyle & Fowler 1963; Salpeter 1964; Zel'dovich & Novikov 1965; Lynden-Bell 1969).

While emitting quasars occur most frequently at high redshift ($z \sim 2$), local observations have found that virtually every spheroidal system (elliptical galaxy or spiral bulge) contains a central supermassive black hole (Kormendy & Richstone 1995). Moreover, the mass of the black hole is tied to the properties of the host galaxy or bulge (Magorrian et al. 1998; Gebhardt et al. 2000; Ferrarese & Merritt 2000; Ferrarese 2002; Marconi & Hunt 2003; McConnell & Ma 2013) (Fig. 1.4). This suggests that accreting black holes play a key role in galaxy evolution, and that most or all galaxies eventually go through a quasar phase; the rarity of quasars is because their lifetime is short compared to a Hubble time. Quasars are generally assumed to be triggered by major mergers (Treister et al. 2010) (Fig. 1.4), although some models trigger quasars by thermal instabilities instead (Ciotti & Ostriker 1997).

The energy liberated by the quasar also has a profound impact on the surrounding gas. The total accretion energy of a 10^9 $M_\odot$ black hole is comparable to the thermal energy in a 4×10^{13} $M_\odot$ dark matter halo, so even relatively weak coupling between the emitted radiation and the surrounding gas should have a large impact. AGN feedback is generally grouped into two broad categories: winds (non-relativistic, broad-angle outflows driven by an optical quasar) and jets (narrow-angle, relativistic outflows launched by a radio-loud quasar; often also referred to as "radio mode") (Alexander & Hickox 2012). Feedback is favored to explain the black hole-spheroid co-evolution. Analytic models of momentum-driven outflows can reproduce the observed scaling relations (King et al. 2011), as can simulation-based approaches directly injecting 5-15% of the total energy radiated by the quasar into the surrounding gas (Booth & Schaye 2010). Moreover, it is thought that AGN feedback in $M > 10^{13} M_\odot$ halos prevents cooling to suppress star formation, creating the decrease in star-formation efficiency at high mass (Behroozi et al. 2018) and yielding agreement with observed stellar mass and luminosity functions of galaxies (Croton et al. 2006).

In Chapter 5, I explore how the thermal Sunyaev-Zel'dovich effect (described below in Section 1.4.2) can be used to test models of quasar halo occupation and constrain quasar feedback. This measurement can help illuminate the efficiency of AGN feedback, and can also provide information on the quasar halo occupation, which is otherwise quite uncertain.

1.3 Small-scale matter distribution from the Lyα forest

The Lyman-α forest arises from redshifted Lyα 1216 Å absorption in the spectra of background quasars (Fig. 1.5). Different wavelengths in the observed quasar spectrum thus correspond to different redshifts rather than different peculiar velocities; this is known as the "fluctuating Gunn-Peterson" approximation (Gunn & Peterson 1965). The optical depth of the Lyα forest $\tau_{\rm GP}$ is

$$\tau_{\rm GP} = \frac{\pi e^2}{m_e c} f_\alpha \lambda_\alpha H^{-1}(z) n_{\rm HI} \tag{1.11}$$

where f_α is the oscillator strength for Lyα, λ_α is the Lyα rest wavelength, and the transmitted flux is related to the optical depth in the usual way, $F = \exp(-\tau_{\rm GP})$ (Weinberg et al. 1997). This formula immediately implies that at $z \sim 2$, the Lyα forest is sensitive to incredibly low

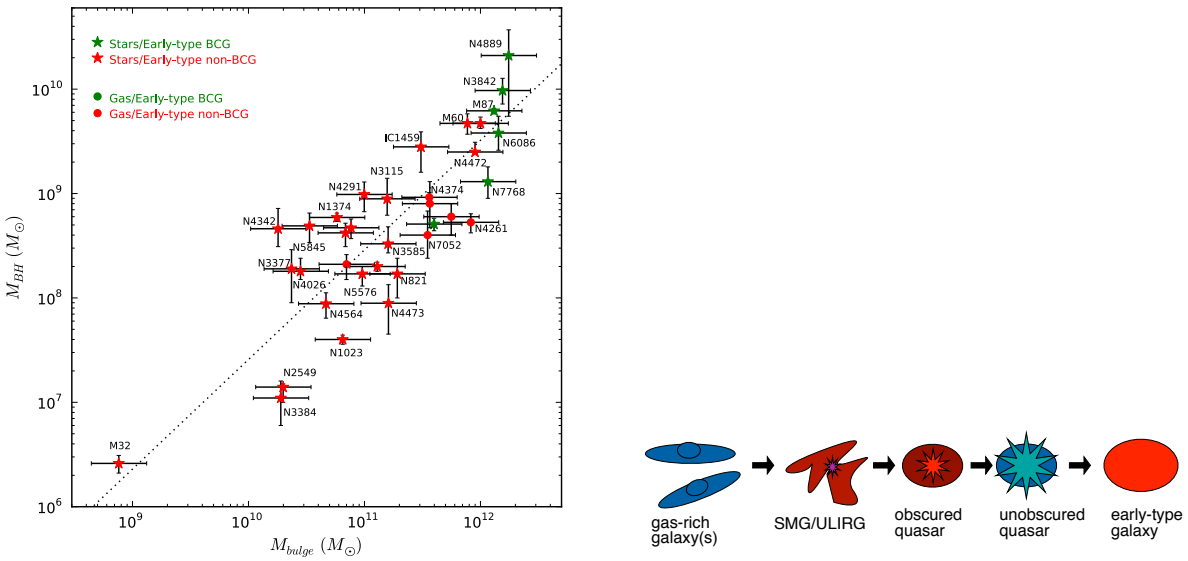

Figure 1.4: *Left:* Correlation between black hole mass and mass of the host bulge (McConnell & Ma 2013). This relationship is generally taken as evidence for coevolution between the galaxy and the central black hole. *Right:* Model for quasar triggering from Sanders et al. (1988).

densities of hydrogen, $n_{\rm HI} \sim 10^{-10}$ cm^{-3} or neutral fraction $x_{\rm HI} \sim 10^{-5}$. (McQuinn 2015). The neutral hydrogen fraction can be further related to the baryon density:

$$x_{\rm HI} = \frac{\alpha_A n_e}{\Gamma} \propto \frac{\rho T^{-0.7}}{\Gamma} \tag{1.12}$$

where α_A is the hydrogen recombination coefficient and Γ is the photoionization rate, set by the background density of ionizing photons, ρ is the baryon density, and the second proportionality brings in the temperature dependence of α_A at $T \sim 10^4$ K, the temperature of the intergalactic medium. Furthermore, simulations have found that the temperature can be very well approximated as a power-law in density (Croft et al. 1997; Hui & Gnedin 1997)

$$T = T_0 \left(\frac{\rho}{\bar{\rho}}\right)^{\gamma} \tag{1.13}$$

The gas density field relevant for the Lyα forest is assumed to be cosmological, i.e. galaxy feedback is assumed not to affect the low-density intergalactic medium (Theuns et al. 2002). The photoionization rate Γ is assumed to be spatially uniform, because the mean free path of the ionizing photons is much longer than the separation between sources. Metal line contamination is small ($< 10\%$ of the Lyα absorption; Schaye et al. 2003) and systems with broad damping wings (grossly violating the fluctuating Gunn-Peterson approximation) are rare and can be removed from the spectra. Finally, on very small scales ($< 100\ h^{-1}$ kpc), gas pressure and thermal broadening smooths out fluctuations in the IGM.

Subject to these caveats and assumptions and as a consequence of Equations 1.12 and 1.13, fluctuations in the Lyα forest directly trace fluctuations in the density field. Moreover, because τ saturates at high densities, the Lyα forest is most sensitive to moderate-overdensity gas, $\rho/\bar{\rho} \sim 1 - 20$, in contrast to galaxy surveys, which measure galaxies where the density contrast is hundreds.

As a result, the Lyα forest has been a powerful probe of inflation, neutrino masses, and the coldness of dark matter (Seljak et al. 2005; McDonald et al. 2006; Seljak et al. 2006; Viel & Haehnelt 2006; Viel et al. 2008a, 2010), mostly using one-dimensional power spectra (i.e. ignoring correlations between neighboring sightlines). Precise measurements of the small-scale pressure and thermal broadening also offer rich information about the astrophysics of the Lyα forest and the temperature history of the IGM (Rorai et al. 2013). More recently, the BOSS survey has measured the three-dimensional power spectrum and correlation function of the Lyα forest (Slosar et al. 2011; de Sainte Agathe et al. 2019). BOSS used 3D clustering on large scales ($\sim$ 100 h^{-1} Mpc) to measure the baryon acoustic oscillation feature as a standard ruler. This yields a measurement of the comoving distance to $z \sim 2$. These studies measure the fluctuations in the transmitted flux

$$\delta_F = \frac{F}{\langle F(z) \rangle} - 1 \tag{1.14}$$

where $F = \exp(-\tau)$ and $\langle F(z) \rangle$ is the mean transmitted flux at each redshift. On large scales, δ_F is a tracer of the matter field δ, albeit with a negative bias since larger values of the flux imply lower densities.

IGM tomography takes the 3D clustering measurement of BOSS one step further and uses Lyman-break galaxies as well as quasars to increase the sightline density by a factor of ~ 20, dramatically increasing the plane-of-sky resolution. This allows us to essentially map the density field of the $z \sim 2$ universe with few Mpc precision. This technique takes advantage of the unique sensitivity of the Lyα forest to near-mean density gas, and the fact that each sightline covers hundreds of Mpc along the line of sight, making this technique dramatically cheaper than galaxy surveys at mapping large-scale structure. In this thesis, I conduct two pilot studies demonstrating the usefulness of IGM tomography. First, in Chapter 2, I show that future IGM tomography studies may constrain alignments between filaments and galaxy spins at $z \sim 2$—a measurement that heretofore required high-density galaxy surveys only found in the local universe. Second, in Chapter 4, I present the first detection of $z \sim 2$ voids in the Lyα forest using the CLAMATO pilot IGM tomography survey. Since the Lyα forest is sensitive to near mean-density gas, it is uniquely powerful for probing voids. Voids are a powerful probe of modified gravity and neutrinos, and large void samples from IGM tomography may enable interesting cosmology constraints at $z \sim 2$.

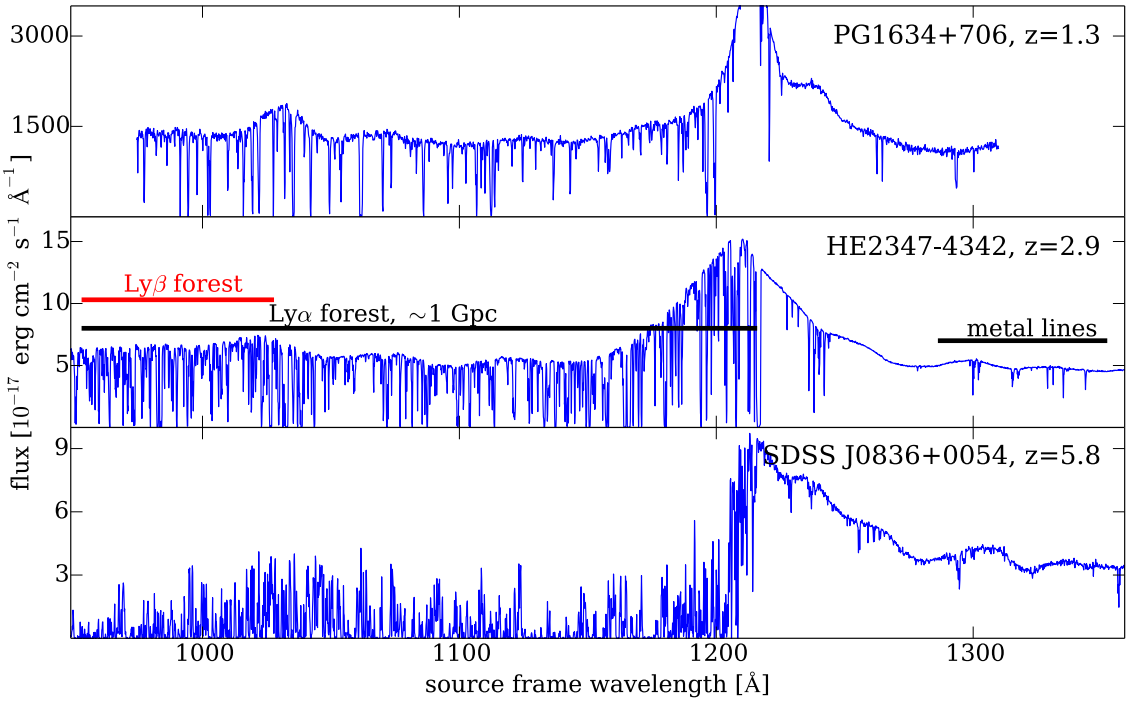

Figure 1.5: *Left:* Lyman-α forest at a variety of redshifts (McQuinn 2015). The x axis is translated to the rest-frame wavelength of the quasar, and thus traces redshift within the Lyα forest.

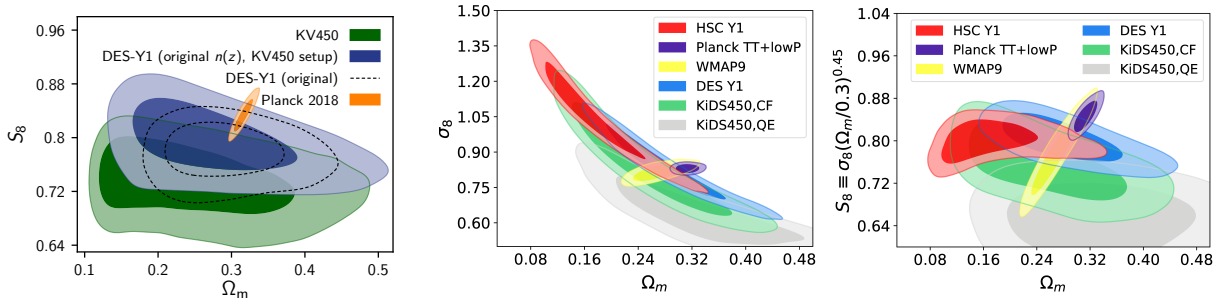

Figure 1.6: *Left:* Tension between Planck and KiDS in the $S_8 \equiv \sqrt{\sigma_8/0.3}$-$\Omega_m$ plane (Hildebrandt et al. 2020). The figure uses S_8 rather than σ_8 because KiDS is most sensitive to a degenerate combination of σ_8 and Ω_m. *Right:* Tension between HSC and Planck in the σ_8-Ω_m and S_8-Ω_m planes (note the slightly different definition of S_8 here) (Hikage et al. 2019).

1.4 Frontiers in cosmology

1.4.1 Motivation: tensions and extensions

While the ΛCDM paradigm presented in Sec. 1.1 is well-supported by most available evidence, it does leave some open questions. First, there are some tensions with certain datasets. Most famously, the Hubble parameter H_0 is different by $\sim 5\sigma$ between the local distance ladder and the value derived from Planck (Riess et al. 2019). This tension is difficult to resolve with changes to the theory, and if ΛCDM is the culprit, the solution must come from changing the expansion rate immediately before matter domination (Knox & Millea 2020). Theories that change the expansion rate in this way are rather contrived and are therefore somewhat disfavored in favor of more mundane explanations (i.e. systematics in the analysis).

There are also a number of tensions between weak lensing surveys and CMB/BAO surveys. Perhaps the most noticeable of these is the σ_8 tension (Hikage et al. 2019; Hildebrandt et al. 2020). The small-scale lensing amplitude has also been found to be 30% lower than expected from galaxy clustering (Leauthaud et al. 2017), and there are also some hints of large-scale departure from CMB lensing cross-correlations (Pullen et al. 2016). However, these tensions are much less significant than the Hubble tension, and also come with significant confounders which may explain them: uncertainty in the details of very small-scale clustering may explain the finding of Leauthaud et al. (2017), and the σ_8 tension could be caused by uncertainties in the source redshift distribution (Hildebrandt et al. 2020).

Future cosmology measurements offer tremendous promise in constraining dark energy and the neutrino mass. Despite their very nearly zero mass, neutrinos have played an outsize role in cosmology, and their mass can be constrained by measuring their signature suppression of the power spectrum on large scales (Hu et al. 1998). Dark energy remains a major focus for future projects. One particularly exciting possibility is constraining modifications to general relativity that separately modify the potentials responsible for gravitational lensing

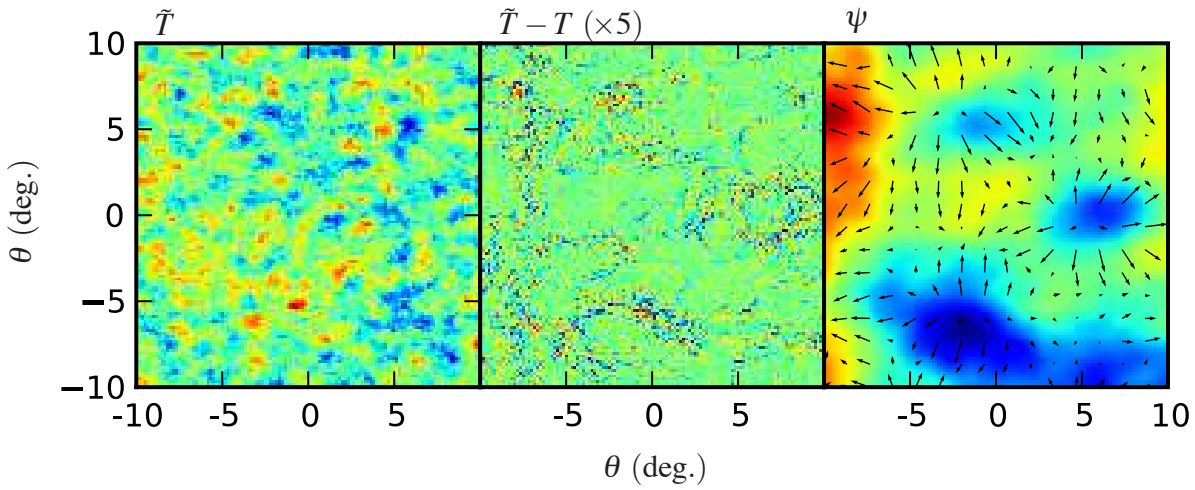

Figure 1.7: Schematic of CMB lensing reconstruction from Hanson et al. (2010). Left panel shows the observed, lensed CMB, $\tilde{T}$; center panel shows the difference between lensed and unlensed CMB (the effect of lensing), and right panel shows the reconstructed lensing potential ψ from the quadratic estimator.

and dynamics. More generally, constraints on modified gravity models can disfavor these models as explanations for the accelerating expansion of the universe.

1.4.2 CMB secondary anisotropies

While the temperature anisotropies of the primary CMB are now measured to the cosmic variance limit (indicating that we cannot measures these modes any better), the CMB will remain a powerful probe into the future through secondary anisotropies. These are anisotropies in the CMB arising from distortions as photons propagate through the entire universe, rather than arising from the primary CMB at the surface of last scattering. These photons are lensed by intervening matter and scattered by hot electrons. Scattering by thermal electrons in hot halo gas is called the thermal Sunyaev-Zel'dovich (tSZ) effect (Sunyaev & Zeldovich 1970) and distorts the CMB spectrum. I explore the tSZ effect from electrons in quasar host halos in Chapter 5.

CMB lensing is a powerful probe of all matter along the line of sight to the CMB. Lensing distorts the primary CMB, coupling previously independent Fourier modes to create a small but very distinct imprint on the CMB (Fig. 1.7). By taking advantage of this characteristic distortion, we can write down a quadratic estimator for the CMB lensing potential from CMB temperature and polarization maps (Hu & Okamoto 2002). In going from the emitted CMB temperature field T to the observed lensed field $\tilde{T}$, lensing remaps photon positions from $\vec{x}$ to $\vec{x} + \vec{\alpha}$

$$\tilde{T}(\vec{x}) = T(\vec{x} + \vec{\alpha}(\vec{x})) = T(\vec{x}) + \vec{\nabla}\psi \cdot \vec{\nabla}T + ... \tag{1.15}$$

where the second equality is a Taylor expansion and we have rewritten the expression in terms of the lensing potential, as defined by $\vec{\alpha} \equiv \vec{\nabla}\psi$. The multiplication in real space becomes a convolution in Fourier space, so the lensed temperature becomes

$$\tilde{T}(\vec{\ell}) = T(\vec{\ell}) - \int \frac{d^2\vec{L}}{2\pi} \vec{L} \cdot (\vec{\ell} - \vec{L})\, \psi(\vec{L})\, T(\vec{\ell} - \vec{L}) \tag{1.16}$$

Since the unlensed CMB power spectrum is diagonal, multiplying by $\tilde{T}(\vec{\ell} - \vec{L})$ yields a delta function, analogous to the "Fourier trick"

$$\langle \tilde{T}(\vec{\ell})\, \tilde{T}(\vec{\ell} - \vec{L}) \rangle = \delta(\vec{L}) C_\ell^{TT} + \frac{1}{2\pi} \left[(\vec{L} - \vec{\ell}) \cdot \vec{L}\, C^{TT}_{|\vec{\ell} - \vec{L}|} + \vec{\ell} \cdot \vec{L}\, C_\ell^{TT} \right] \psi(\vec{L}) \tag{1.17}$$

Thus for $\vec{L} \neq 0$, $\psi(\vec{L})$ can be estimated by summing over all $\vec{\ell}$ with the appropriate weights $g(\vec{\ell}, \vec{L})$:

$$\psi_{\rm QE}(\vec{L}) = N(\vec{L}) \int \tilde{T}(\vec{\ell})\, \tilde{T}(\vec{L} - \vec{\ell})\, g(\vec{\ell}, \vec{L}) \tag{1.18}$$

where $N(\vec{L})$ is the normalization, and the weights $g(\vec{\ell}, \vec{L})$ are chosen to minimize the variance of the estimator (Zaldarriaga & Seljak 1999; Hu 2001; Hu & Okamoto 2002). The power spectrum of $\psi_{\rm QE}(\vec{L})$ then contains the true power spectrum of $\psi_(\vec{L})$, a mean-field term $\langle\psi\rangle$ from noise inhomogeneity and sky cuts; the lensing reconstruction noise $N^{(0)}(\vec{L})$, primarily from the disconnected (Gaussian) 4-point function of the primary CMB; a contribution by point sources to the connected 4-point function; and a contribution $N^{(1)}(\vec{L})$ from wavevectors other than $\vec{L}$ that contribute to $\psi_{\rm QE}(\vec{L})$ (Kesden et al. 2003; Planck Collaboration et al. 2014c, 2016b, 2018f).

The CMB lensing auto power spectrum is detected at 40σ in Planck (Planck Collaboration et al. 2018f) and has allowed powerful constraints on σ_8 and Ω_m (Das et al. 2011; Sherwin et al. 2017; Planck Collaboration et al. 2018f; Bianchini et al. 2020). Future CMB lensing measurements will place strong constraints on the neutrino mass (Allison et al. 2015a). However, CMB lensing is a two-dimensional measurement, so it can only probe the integrated mass distribution along the line of sight and is not sensitive to the growth of structure throughout cosmic time. By cross-correlating CMB lensing with a galaxy sample, CMB lensing tomography can increase the signal-to-noise ratio, isolate redshifts of interest, and break important degeneracies between the expansion history and growth of perturbations (Hu 1999, 2002). I present a measurement of cross-correlations between Planck CMB lensing and infrared galaxies at $0 < z < 2$ from the unWISE catalog in Chapter 6. This is the highest signal-to-noise detection of CMB lensing cross-correlations to date, and the first CMB lensing cross-correlation to exceed the detection significance of the Planck CMB lensing auto spectrum.

The integrated Sachs-Wolfe effect is a distortion in the CMB temperature power spectrum due to gravitational redshifting of CMB photons along the line of sight (Sachs & Wolfe 1967; Rees & Sciama 1968). Photons redshift and blueshift as they pass through gravitational

potentials. In matter domination, the potentials are constant in time and there is no signal, but in dark energy domination, they decay, leading to a net gravitational blue-shift of the photons:

$$\left(\frac{\Delta T}{T}\right)_{\rm ISW} = -\frac{2}{c^3}\int_0^{\chi_\star} d\chi \dot{\Phi} \tag{1.19}$$

where $\chi_\star$ is the comoving distance to the CMB and $\dot{\Phi}$ is the derivative of the gravitational potential. The integrated Sachs-Wolfe effect is not detectable in the CMB temperature auto-spectrum, but has been detected in cross-correlation with galaxy samples (Giannantonio et al. 2012; Ferraro et al. 2015; Planck Collaboration et al. 2016d). This is an interesting signal because it is a direct probe of the decay of the potentials and thus dark energy. It thus provides a direct measurement of dark energy (Nolta et al. 2004; Giannantonio et al. 2006; Ho et al. 2008) and a direct constraint on various dark energy and modified gravity models (Crittenden & Turok 1996; Kamionkowski 1996; Hu 2002; Zhao et al. 2010; Renk et al. 2017). As an all-sky survey containing galaxies throughout the entire epoch of dark energy domination to $z \sim 2$, unWISE is well-suited for an ISW measurement. In Chapter 7, I present a measurement of the ISW effect through the cross-correlation between unWISE galaxies and the Planck CMB power spectrum at low ℓ.

Chapter 2

Measuring alignments between galaxies and the cosmic web at $z \sim 2-3$ using IGM tomography

Abstract

Many galaxy formation models predict alignments between galaxy spin and the cosmic web (i.e. directions of filaments and sheets), leading to intrinsic alignment between galaxies that creates a systematic error in weak lensing measurements. These effects are often predicted to be stronger at high-redshifts ($z \gtrsim 1$) that are inaccessible to massive galaxy surveys on foreseeable instrumentation, but IGM tomography of the Lyα forest from closely-spaced quasars and galaxies is starting to measure the $z \sim 2-3$ cosmic web with requisite fidelity. Using mock surveys from hydrodynamical simulations, we examine the utility of this technique, in conjunction with coeval galaxy samples, to measure alignment between galaxies and the cosmic web at $z \sim 2.5$. We show that IGM tomography surveys with $\lesssim 5$ h^{-1} Mpc sightline spacing can accurately recover the eigenvectors of the tidal tensor, which we use to define the directions of the cosmic web. For galaxy spins and shapes, we use a model parametrized by the alignment strength, $\Delta\langle\cos\theta\rangle$, with respect to the tidal tensor eigenvectors from the underlying density field, and also consider observational effects such as errors in the galaxy position angle, inclination, and redshift. Measurements using the upcoming $\sim 1\,\mathrm{deg}^2$ CLAMATO tomographic survey and 600 coeval zCOSMOS-Deep galaxies should place 3σ limits on extreme alignment models with $\Delta\langle\cos\theta\rangle \sim 0.1$, but much larger surveys encompassing $> 10,000$ galaxies, such as Subaru PFS, will be required to constrain models with $\Delta\langle\cos\theta\rangle \sim 0.03$. These measurements will constrain models of galaxy-cosmic web alignment and test tidal torque theory at $z \sim 2$, improving our understanding of the physics of intrinsic alignments.

2.1 Introduction

Gravitational collapse of the Gaussian random-phase initial conditions produced by inflation creates a network of dense nodes connected by filaments and sheets and separated by voids, the "cosmic web" (Zeldovich et al. 1982; Klypin & Shandarin 1983; Einasto et al. 1984; Davis et al. 1985; Geller & Huchra 1989; Bond et al. 1996). As a result of nonlinear structure formation, the cosmic web is distinctly non-Gaussian. In the Zel'dovich approximation, collapse occurs sequentially along the principal axes of the deformation tensor, as matter flows out of voids onto sheets, collapses into filaments and finally streams into high-density nodes (Zel'dovich 1970). The accretion of matter determines the shapes and angular momenta of galaxies and their host dark matter halos, naturally suggesting a connection between the cosmic web and galaxy shapes and spins.

In the linear regime, the evolution of the angular momentum of a protohalo is described by tidal torque theory (TTT, Peebles 1969; Doroshkevich 1970; White 1984). TTT predicts that the protohalo's angular momentum will be aligned with the intermediate eigenvector of the tidal tensor. However, nonlinear evolution can significantly weaken this alignment (Porciani et al. 2002), driving alignments with other preferred directions (e.g. the direction of filaments, along which matter is accreting; Codis et al. 2012).

Alignments between the cosmic web and halo shapes and spins have been extensively studied in N-body simulations (Kiessling et al. 2015; see Tables 1 and 2 in Forero-Romero et al. (2014) for a recent compilation of results). Many workers suggest that halo spins transition from parallel to filaments at low halo mass to perpendicular to filaments at high mass (Bailin & Steinmetz 2005, Aragón-Calvo et al. 2007, Hahn et al. 2007a, Codis et al. 2012, Trowland et al. 2013, Aragon-Calvo & Yang 2014). In addition, Dubois et al. (2014) and Codis et al. (2015), using the cosmological hydrodynamical simulation HorizonAGN, argue that galaxy spin alignments exhibit a similar transition mass. However, these results are dependent on the measurement algorithm, simulation, and environmental classification (Kiessling et al. 2015), and it is unclear if spin-filament alignments are the dominant spin-cosmic web alignment. For instance, Libeskind et al. (2013) find a similar transition from aligned to anti-aligned in voids and sheets as well as filaments, although with a different transition mass in each web type, and Forero-Romero et al. (2014) find no alignment at low mass and argue that sheet alignments are as significant as filament alignments at high mass. In direct contradiction to the picture described above, the cosmological zoom simulations of Hahn et al. (2010) suggest that massive disk galaxies have spins parallel to their host filaments while low-mass disk galaxies have spins aligned along the intermediate axis of the tidal tensor.

In contrast, halo shape-cosmic web alignments are both stronger and more robust to measure than spin-cosmic web alignments (Kiessling et al. 2015), although they have been less extensively studied. The major axis of the halo inertia tensor is preferentially aligned along filaments, in the plane of sheets (Altay et al. 2006, Hahn et al. 2007a, Aragón-Calvo et al. 2007, Zhang et al. 2009, Libeskind et al. 2013, Forero-Romero et al. 2014) and parallel to the surface of voids (i.e. the plane of sheets; Patiri et al. 2006, Brunino et al. 2007, Cuesta

et al. 2008). Shape-cosmic web alignments monotonically increase from weak to strong as a function of mass, with no transition mass (Hahn et al. 2007a, Aragón-Calvo et al. 2007, Zhang et al. 2009, Libeskind et al. 2013, Forero-Romero et al. 2014). Using the MassiveBlack-II cosmological hydrodynamical simulation, Chen et al. (2015) report similar results for alignments between galaxy shapes and filaments. Galaxy shape-cosmic web alignments are closely related to ellipticity-tidal shear correlations (Codis et al. 2015), the "GI" term of intrinsic alignments that is a potential major systematic for upcoming missions such as LSST, WFIRST and EUCLID that aim to measure the dark energy equation of state using weak lensing tomography (Hirata & Seljak 2004, Bridle & King 2007, Kirk et al. 2012).

Observational studies of galaxy-cosmic web alignment require large numbers of galaxy redshifts to trace the cosmic web in 3D, and are therefore primarily feasible only at low redshift. Observations of alignments between spiral galaxy spin and void surfaces/sheets have produced conflicting results ranging from parallel to random to perpendicular alignment (Trujillo et al. 2006, Slosar & White 2009, Varela et al. 2012). Locally, Navarro et al. (2004) find that spiral galaxy spins preferentially lie in the supergalactic plane (see also Aryal & Saurer 2004). Early observations reported that spiral galaxy spins are aligned with the intermediate axis of the tidal shear tensor in concordance with TTT predictions (Lee & Pen 2002, Lee & Erdogdu 2007), and are therefore aligned perpendicular to filaments (Jones et al. 2010, Zhang et al. 2015). However, more recently Tempel et al. (2013) and Tempel & Libeskind (2013) have found that spiral galaxy spins are parallel to filaments and lenticular/elliptical galaxy spins are perpendicular to filaments, in concordance with the transition mass picture from simulations. Similarly, Pahwa et al. (2016) find that elliptical galaxy spins lie perpendicular to filaments and normal to sheets, while spiral galaxy spins exhibit much weaker alignments along filaments. In accordance with shape-cosmic web alignments from simulations, Zhang et al. (2013) find that galaxy major axes preferentially align with filaments and along sheets, a relationship that is weak for blue galaxies and highly significant for bright red galaxies.

Similar measurements at higher redshift ($z > 0.5$) are challenging due to the difficulty of measuring the cosmic web from the galaxy distribution, requiring large samples of faint galaxies to achieve sufficient spatial resolution of a few Mpc, although surveys such as VIPERS (Guzzo et al. 2014, Malavasi et al. 2016) are pushing this to $z \sim 0.7$. Even with future 30m-class telescopes, it would be extremely time-consuming to obtain the requisite galaxy samples at $z > 1$ due to the high number densities required. Studies of Lyman-α nebulae have discovered filaments around quasars at $z \sim 2.5$ (Cantalupo et al. 2012, 2014, Cai et al. 2016b), but they probe very small, non-representative volumes around the rarest density peaks, which are unsuitable for statistical studies of galaxy alignments.

At higher redshifts, Lyman-α forest tomography (Pichon et al. 2001, Caucci et al. 2008) offers an alternative method for characterizing the cosmic web at $z \sim 2$, the epoch of peak star formation, by using observations of Lyα forest absorption in closely-spaced quasars and Lyman-break galaxies to reconstruct the IGM absorption field. Using this technique, current instrumentation can probe a spatial resolution of a few Mpc (Lee et al. 2016), similar to the resolution of cosmic web studies at $z < 0.5$ (c.f. the GAMA Survey; Eardley et al. 2015).

By simulating IGM tomographic observations with realistic signal-to-noise, resolution, and sightline separation, we have shown that the reconstructed flux fields visually match the underlying dark matter density (Lee et al. 2014a) and can be used to find high-redshift protoclusters and voids (Stark et al. 2015, Stark et al. 2015). Moreover, sufficiently large surveys (with $\gtrsim 1$ deg of contiguous sky coverage) can recover kinematically-defined cosmic web classifications with a fidelity comparable to low-redshift surveys using the galaxy density field (Lee & White 2016). These results suggest that IGM tomography could allow measurement of galaxy shape-cosmic web alignments at $z \sim 2.5$ in the near future.

In this paper, we will discuss the prospects for measuring galaxy-cosmic web alignments using IGM tomography surveys with mean sightline separations of $\langle d_\perp \rangle = [1.4, 2.5, 4, 6.5]$ h^{-1} Mpc. These reflect both existing and possible future surveys. Firstly, $\langle d_\perp \rangle = 2.5$ h^{-1} Mpc reflects the ongoing COSMOS Lyman-Alpha Mapping And Tomography Observations (CLAMATO) survey[1] (for which the pilot phase is being completed; see Lee et al. 2014b, 2016), which aims to cover ~ 1 deg^2 in the COSMOS field using the LRIS spectrograph on the 10.3-m Keck-I telescope. CLAMATO will cover a redshift range $2.2 < z < 2.5$, mapping $\sim 10^6 h^{-3}$ Mpc^3 comoving volume with a spatial resolution of 2.5 h^{-1} Mpc. By $\sim$ 2020, the Subaru Prime-Focus Spectrograph (PFS) will begin operation (Takada et al. 2014), and an IGM tomographic survey building on the PFS galaxy evolution survey, but obtaining additional sightline spectra and higher S/N, could cover ~ 20 deg^2 with $\langle d_\perp \rangle = 4$ h^{-1} Mpc. On the other hand, an IGM tomography map could be constructed "for free" using the $i < 24$ LBGs targeted for the PFS Galaxy Evolution Survey (Takada et al. 2014) without additional IGM tomography targets, yielding $\langle d_\perp \rangle = 6.5$ h^{-1} Mpc. Finally, the proposed FOBOS instrument on Keck will offer much greater ($\sim 10\times$) multiplexing and field-of-view than LRIS on the same telescope, allowing for deeper integrations and hence denser sightline sampling of $\langle d_\perp \rangle \sim 1.4$ h^{-1} Mpc while surveying ~ 1 deg^2, similar to CLAMATO.

In this paper, we will estimate the quality of cosmic web direction measurements (e.g. direction of filaments, normal vector to sheets, etc.) using mock observations based on the Nyx hydrodynamic IGM simulations. We will discuss the feasibility for measuring galaxy-cosmic web alignments using these surveys in tandem with coeval galaxy samples at $z \sim 2.5$.

2.2 Methods

2.2.1 Nyx simulations and mock observations

We use a cosmological hydrodynamical simulation generated with the N-body plus Eulerian hydrodynamics Nyx code (Almgren et al. 2013). It has a 100 h^{-1} Mpc box size with 4096^3 cells and particles, resulting in a dark matter particle mass of $1.02 \times 10^6 h^{-1} M_\odot$ and spatial resolution of 24 h^{-1} kpc. As discussed in Lukić et al. (2015), this resolution is sufficient to resolve the filtering scale below which the IGM is pressure supported and to reproduce the flux statistics at percent accuracy at redshift $z = 2.4$. The box covers a

[1] http://clamato.lbl.gov/

similar size to the proposed CLAMATO and FOBOS survey volumes. We use a flat ΛCDM cosmology with $\Omega_m = 0.3$, $\Omega_b = 0.047$, $h = 0.685$, $n_s = 0.965$, and $\sigma_8 = 0.8$, consistent with latest Planck measurements (Planck Collaboration et al. 2016a).

In Nyx, the baryons are modeled as an ideal gas on a uniform grid. The baryons have a primordial composition with hydrogen and helium mass abundances of 75% and 25%, respectively. We account for photoionization, recombination, and collisional excitation of all neutral and ionized species of hydrogen and helium, which evolve in ionization equilibrium with the uniform UV background given by Haardt & Madau (2012), with the mean flux normalized to match observational values. The reaction and cooling rates used in the code are given in Lukić et al. (2015). This simulation does not model star-formation and hence has no feedback from stars, galaxies, or AGNs, but these are expected to have a negligible effect on the Lyα forest statistics (Viel et al. 2013). Future Nyx IGM simulations will include galaxy formation physics in order to self-consistently simulate a galaxy population, allowing better interpretation of the relationship between galaxies and the Lyα forest.

We generated 512^2 absorption skewers with a spacing of 0.2 h^{-1} Mpc and sampled from these skewers to create mock data. We computed the Lyα forest flux fluctuation along each skewer

$$\delta_F = F/\langle F \rangle - 1 \tag{2.1}$$

where $F = \exp(-\tau)$ and τ is the Lyα optical depth, computed in redshift space and Doppler broadened using the gas temperature. Hereafter we refer to δ_F as the flux.

We then create mock spectra that reflect the data quality expected from current and upcoming surveys. First, we randomly select absorption skewers with the appropriate mean sightline spacing $\langle d_\perp \rangle$ and rebin them along the line of sight to a resolution of 0.78 h^{-1} Mpc, similar to the line-of-sight spectral resolution from the CLAMATO spectra.

We simulate noise by assuming the S/N per pixel is a unique constant for each skewer. To determine S/N for each skewer, we draw from a power-law S/N distribution $\mathrm{d}n_{\mathrm{los}}/\mathrm{dS/N} \propto \mathrm{S/N}^{-\alpha}$ (Stark et al. 2015; hereafter S15b), where S/N ranges between 1.5 (the minimum S/N in CLAMATO; Lee et al. 2014b, 2016) and infinity. Lee et al. (2014a) found that $\alpha \sim 2.5$ for the LBGs and QSOs that we target; however, as the sightline separation increases, the sources targeted become brighter and we move further along the exponential tail of the luminosity function, so α becomes larger. S15b find $\alpha = 2.9$ (3.6) for $\langle d_\perp \rangle = 2.5$ (4) h^{-1} Mpc, respectively. They did not determine α for $\langle d_\perp \rangle < 2\ h^{-1}$ Mpc or $> 4\ h^{-1}$ Mpc; therefore we use $\alpha = 2.7$ (3.6) for our $\langle d_\perp \rangle = 1.4$ (6.5) h^{-1} Mpc map, identical to the S15b values for $\langle d_\perp \rangle = 2$ (4) h^{-1} Mpc. We confirm the power-law distribution is appropriate by comparing it to the S/N distribution of observed pixels from the CLAMATO pilot observations. Using the simulated S/N distribution, we add noise to each pixel assuming a Gaussian distribution. We also model the effect of continuum-fitting error with an RMS of 10%: $F_{\mathrm{obs}} = F_{\mathrm{sim}}/(1 + \delta_{\mathrm{cont}})$ where δ_{cont} is a random Gaussian deviate, identical for all pixels within a skewer, with mean 0 and standard deviation 0.1. This reflects the continuum-fitting uncertainties expected from data with comparable S/N (Lee et al. 2012).

For the tomographic reconstruction, we use the publicly available Wiener filter recon-

struction code of Stark et al. (2015) [2] to create a 3D map of the flux field. The Wiener filter is ideal for reconstruction as it provides a minimum variance estimate of the 3D field, assuming the field is normally distributed (Caucci et al. 2008, Lee et al. 2014a, Stark et al. 2015). The reconstructed signal is

$$\hat{s} = \mathbf{S}_{\rm md}(\mathbf{S}_{\rm dd} + \mathbf{N})^{-1}\boldsymbol{d} \tag{2.2}$$

where $\boldsymbol{d}$ is the data, $\mathbf{N}$ is the noise covariance, $\mathbf{S}_{\rm md}$ is the map-data covariance, and $\mathbf{S}_{\rm dd}$ is the data-data covariance. We assume that the noise covariance is diagonal, so that $N_{ij} = n_i^2\delta_{ij}$ where n_i is the simulated noise for each pixel. We further assume that $\mathbf{S}_{\rm md} = \mathbf{S}_{\rm dd} = S$:

$$S = \sigma_F^2 \exp\left[-\frac{\Delta x_\perp^2}{2l_\perp^2} - \frac{\Delta x_\parallel^2}{2l_\parallel^2}\right] \tag{2.3}$$

We use $\sigma_F^2 = 0.05$ and isotropic smoothing with $l_\parallel = l_\perp = \langle d_\perp \rangle$. Hereafter we refer to the reconstructed flux as $\delta_F^{\rm rec}$ and the simulated flux as δ_F. The mock Lyα skewers and IGM tomography maps are publicly released on the web[3].

2.2.2 Defining the Cosmic Web

We measure the cosmic web directions using the eigenvectors of the deformation tensor, an approach inspired by the cosmic web classifications of Hahn et al. (2007b). While there are many alternative cosmic web classifiers (see enumeration in Cautun et al. 2014), we prefer the deformation tensor approach for a variety of reasons: it allows direct comparison with Lee & White (2016); it is physically motivated by the Zel'dovich approximation; and it is directly related to the gravitational shear field relevant for weak-lensing intrinsic alignments (Codis et al. 2015).

The deformation tensor is defined as the Hessian of the gravitational potential Φ:

$$D_{ij} = \frac{\partial^2 \Phi}{\partial x_i \partial x_j} \tag{2.4}$$

The Hessian is most efficiently calculated in Fourier space, using the Poisson equation in suitable units where $4\pi G = 1$, $\nabla^2\Phi = k^2\Phi = \delta_k$. Therefore we can directly compute the Fourier transform of D_{ij} from the density:

$$\widetilde{D}_{ij}(k) = \frac{k_i k_j}{k^2}\delta_k \tag{2.5}$$

and inverse-Fourier transform to obtain D_{ij}. To compute D_{ij}, we define δ as the sum of the matter and baryonic overdensity measured in redshift space, binned on a 128^3 grid and smoothed with a Gaussian kernel with standard deviation $R_G = 2\ h^{-1}\,$Mpc (see below for

[2] https://github.com/caseywstark/dachshund
[3] http://tinyurl.com/hg7u4dg

details of smoothing). We then diagonalize the deformation tensor at every point in space to obtain its eigenvectors, $\hat{e}_1$, $\hat{e}_2$, and $\hat{e}_3$, where the eigenvectors correspond to eigenvalues $\lambda_1 < \lambda_2 < \lambda_3$. In the Zel'dovich approximation, collapse proceeds first along $\hat{e}_3$ and last along $\hat{e}_1$.

Note that the traceless tidal shear tensor

$$T_{ij} = \frac{\partial^2 \Phi}{\partial x_i \partial x_j} - \frac{1}{3}\nabla^2 \Phi \delta_{ij} \tag{2.6}$$

which is more relevant than D_{ij} for intrinsic alignment (Codis et al. 2015), shares its eigenvectors with the deformation tensor. As a result, we will use the phrases "eigenvectors of the tidal tensor" and "eigenvectors of the deformation tensor" interchangeably.

We define the cosmic web directions of the IGM tomography map, which reconstructs the Lyα forest flux, as the eigenvectors of the pseudo-deformation tensor (Lee & White 2016), where we simply substitute the Fourier transform of the flux field, δ_F, for δ_k in Equation 2.5. Since δ_F has the opposite sign as δ_k, we order the eigenvalues of the pseudo-deformation tensor from largest to smallest.

We classify each point as a node, filament, sheet or void using the number of eigenvalues greater than a nonzero threshold value $\lambda_{\rm th}$, similar to Lee & White (2016) and Forero-Romero et al. (2009). A nonzero threshold leads to a better agreement with visually prominent sheets and filaments (Forero-Romero et al. 2009) and is physically justified because directions with a small positive λ are contracting so slowly they may not collapse in a Hubble time. Similar to Lee & White (2016), we choose $\lambda_{\rm th,m}$ by matching the volumetric void fraction in the matter density to the $\sim 19\%$ void fraction of Stark et al. (2015). We choose the threshold for the flux, $\lambda_{\rm th,F}$, using the same condition on the void fraction for the $\langle d_\perp \rangle = 1.4$, 2.5, 4, and 6.5 h^{-1} Mpc reconstructions.

The eigenvectors of the deformation tensor are related to the underlying geometry and kinematics of the cosmic web. In the Zel'dovich approximation, matter collapses along an eigenvector if its eigenvalue is positive, and expands along an eigenvector if its eigenvalue is negative (Hahn et al. 2007b). In a filament, there is only one negative eigenvalue, thus $\hat{e}_1$ is the only direction of expansion, making it the long axis of the filament. Similarly, in a sheet, there is only one positive eigenvalue, making $\hat{e}_3$ the normal vector to the sheet. Therefore, we define the directions of the cosmic web using the eigenvectors of the tidal tensor.

Following Lee & White (2016), we smooth the deformation tensor to minimize the effects of reconstruction noise and remove small-scale fluctuations. They found that a Gaussian kernel with $R_G \sim 1.5\langle d_\perp \rangle$ was appropriate for this purpose (see also Caucci et al. 2008). Therefore, we use smoothing kernels with $R_G = [2, 4, 6, 10]$ for $\langle d_\perp \rangle = [1.4,\ 2,\ 4,\ 6.5]$ reconstructions. A larger smoothing scale leads to a more homogeneous map with less variation in $\delta_F^{\rm rec}$, so maps with a larger $\langle d_\perp \rangle$ have a smaller spread in $\delta_F^{\rm rec}$ (Figure 2.2).

We also smooth the underlying matter density which we use for comparison. Since our cosmic web classification scheme is based on the Zel'dovich approximation, it is only valid up to the mildly nonlinear scales where the Zel'dovich approximation fails (Eardley et al. 2015). Therefore, smoothing on scales of a few h^{-1} Mpc is appropriate to eliminate highly

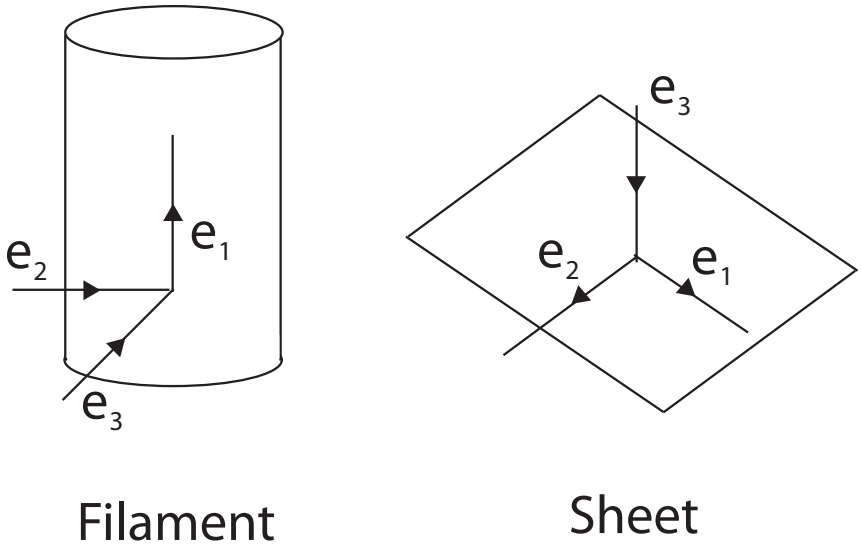

Figure 2.1: Relationship between eigenvectors of the tidal tensor (or equivalently, deformation tensor) and cosmic web directions. Arrows indicate expansion or contraction along a given eigenvector.

non-linear scales. We choose a matter smoothing scale of 2 h^{-1} Mpc, comparable to the smoothing scales used in shape-cosmic web and spin-cosmic web alignment studies from simulations (see compilation in Forero-Romero et al. 2014).

The choice of smoothing scale is ultimately arbitrary; for instance, we could follow Lee & White (2016) and choose a different matter density smoothing scale for each reconstruction, matching the smoothing scales of the flux map and the matter. However, we prefer to use a single "true" matter map to generate galaxy spins (see Section 2.2.4). The results in this paper are qualitatively similar if we instead match the matter smoothing scale to the reconstruction smoothing scale, in that the recovery of the eigenvectors declines from $\langle d_\perp \rangle = 1.4\ h^{-1}$ Mpc to 6.5 h^{-1} Mpc. However, the decline is much less steep if we match smoothing scales; thus, much of the misalignment between the matter field and IGM tomography maps with $\langle d_\perp \rangle > 2\ h^{-1}$ Mpc is due to the mismatch in smoothing scales.

Figure 2.2 compares the matter density field to the reconstructed flux field for $\langle d_\perp \rangle = 1.4$, 2.5, 4, and 6.5 h^{-1} Mpc for an 0.8 h^{-1} Mpc slice through the simulation box. We also show the simulated redshift-space δ_F field, equivalent to a "perfect resolution" IGM tomography survey. We overplot headless vectors corresponding to the projection of $\hat{e}_1$ onto the xy plane; arrowheads are not displayed because the sign of $\hat{e}_1$ is arbitrary. The IGM tomography surveys are smoothed using the smoothing scales defined above, while the matter density and simulated flux field, δ_F, are smoothed with $R_G = 2\ h^{-1}$ Mpc. The simulated flux and $\langle d_\perp \rangle = 1.4\ h^{-1}$ Mpc fields reproduce the matter density well, although with a very different

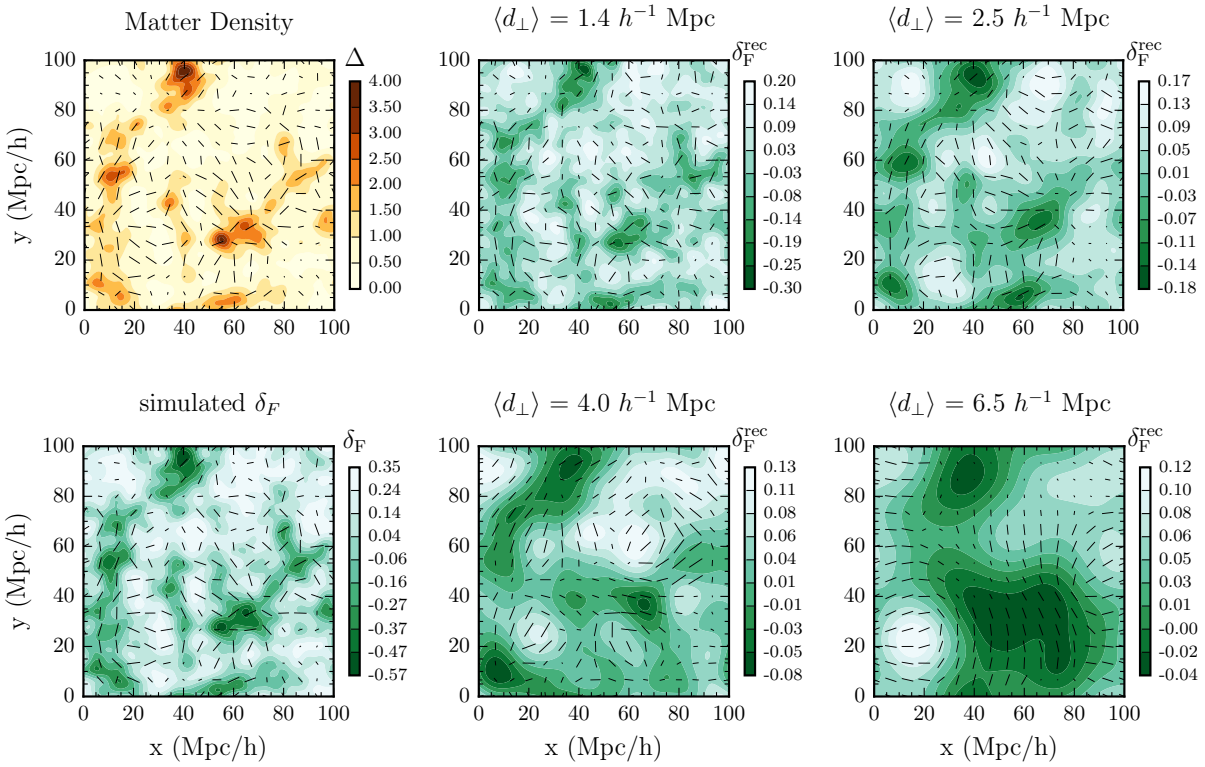

Figure 2.2: Matter density (dark matter plus baryons) and δ_F from the simulations (left) and $\delta_F^{\rm rec}$ from simulated IGM tomography observations with varying $\langle d_\perp \rangle$ (right). All quantities are evaluated in redshift space. The figures show a slice through the full simulation box with width 0.8 h^{-1} Mpc along the line of sight. The overplotted vectors are $\hat{e}_1$ determined from the corresponding field.

dynamical range owing to the nonlinear transformation from δ to δ_F. The simulated flux and $\langle d_\perp \rangle = 1.4\ h^{-1}\,\mathrm{Mpc}$ maps reproduce the small-scale structure in the matter-density $\hat{e}_1$ quite well, while larger $\langle d_\perp \rangle$ yield a smoother distribution of δ_F^{rec} and $\hat{e}_1$ that captures the large-scale features but misses much of the smaller-scale structure.

2.2.3 Galaxy spin observations

Measuring galaxy-cosmic web alignments at $z \sim 2.5$ requires a large galaxy sample with accurate redshifts and structural parameters. The typical half-light radius of a $z \sim 2.4$ galaxy is ~ 0.3" (Giavalisco et al. 1996, Van Der Wel et al. 2014). Space-based or adaptive-optics observations are therefore preferred for measuring structural parameters at $z \sim 2.4$, although the shapes of faint galaxies can be measured well from the ground with deep exposures and ~ 0.5" seeing (Chang et al. 2013). Additionally, LSST plans to measure cosmic shear out to $z \sim 3$ using ground-based observations with 0.7" mean seeing (LSST Science Collaboration et al. 2009).

Galaxy spins can be determined from galaxy images using the galaxy's position angle and axis ratio assuming the galaxy is an oblate spheroid spinning about its short axis (Haynes & Giovanelli 1984). The position angle defines the direction of the projected major axis, while the inclination is calculated from the axis ratio, assuming the galaxy is circular if viewed face-on and the intrinsic thickness is known. As a result, this method is only applicable to spiral or spheroidal galaxies, which can be approximated as oblate spheroids (e.g Lee & Erdogdu 2007, Tempel et al. 2013). For elliptical galaxies with minimal rotation, alignments between the galaxy's major axis and the projected eigenvectors of the tidal tensor are most relevant.

The spin axis is then assumed to be the minor axis of the galaxy ellipsoid. In principle the spin and minor axis may be misaligned, though both observations and simulations find small misaligments (Franx et al. 1991, Codis et al. 2015), $\sim 15^\circ$ at $z \sim 2$ (Wisnioski et al. 2015). High resolution or adaptive-optics IFU observations can measure the kinematic major axes of galaxies at $z \sim 2$ (e.g. Wisnioski et al. 2015), but even large surveys with KMOS or NIRSpec (Giardino et al. 2016) may only accumulate 1000 galaxies over the next several years, far smaller than the sample sizes expected from wide-field imaging surveys.

Galaxies at $z \sim 2$ have a clumpier and more irregular morphology than galaxies at low redshift (Lotz et al. 2006, Elmegreen et al. 2005). This may present an additional challenge for measuring the major axis and ellipticity of the light profile. In addition, the intrinsic thickness is a major source of systematic error in determining the inclination: it varies by morphology (Haynes & Giovanelli 1984) and potentially also with redshift, as galaxies at $z \sim 2$ are thicker than galaxies at low redshift (Law et al. 2012). Furthermore, only the absolute value of the inclination is measurable, so there will always be a degeneracy between spins pointing towards the observer and spins pointing away from the observer, except for face-on or edge-on galaxies. Alignment studies have attempted to mitigate this degeneracy in several ways (Lee & Erdogdu 2007, Varela et al. 2012, Slosar & White 2009, Pahwa et al.

2016, Trujillo et al. 2006) but ultimately the degeneracy will degrade the measured alignment signal.

To understand the impact of these systematics on alignment measurements at $z \sim 2$, we include realistic errors in the galaxies' position angles and inclinations. Since the inclination measurements may be particularly impacted by systematic errors from the unknown intrinsic thickness and anisotropies in the PSF, we consider both 3D and 2D alignment measurements, where the 2D alignment measurements ignore the z-direction of the eigenvectors altogether. To model the spin degeneracy, we randomly select each spin to face either towards or away from the observer.

2.2.4 Galaxy alignment model

We wish to remain agnostic about the mechanisms and strength of the galaxy-cosmic web alignment signal. Hence, we assign galaxy spins to the simulation halos using a stochastic relationship between the eigenvectors of the tidal tensor of the matter density field and galaxy spin. This prescription allows us greater flexibility to adjust the strengths of galaxy alignments compared to adhering to the results of a single simulation. The galaxy formation physics governing the shape-cosmic web relationship are not well understood (e.g. see disagreement between MassiveBlackII and HorizonAGN alignment results at low redshift; Tenneti et al. 2015, Chisari et al. 2016), so flexibility in modeling this relationship is valuable. Moreover, it is not clear which eigenvector the spin is most strongly aligned with, so our model allows us to adjust the alignment strength with any of the three eigenvectors (although for simplicity we do not consider alignments with more than one eigenvector at a time).

Our model takes as input $\langle \cos\theta \rangle$, the mean of the cosine of the angle between the galaxy spins and the local eigenvector of the matter field tidal tensor. We parametrize the PDF of $\mu \equiv \cos\theta$ as

$$P(\mu) = a\mu^2 + c \tag{2.7}$$

where $c = 1 - a/3$ such that $P(\mu)$ is normalized.

To compare to various observational and simulation results, we parameterize $P(\mu)$ using $\langle \cos\theta \rangle$ rather than a:

$$a = 12\langle \cos\theta \rangle - 6 \tag{2.8}$$

Equation 2.7 roughly reproduces $P(\mu)$ as measured from simulations (e.g. Aragón-Calvo et al. 2007, Zhang et al. 2009, Codis et al. 2012, Libeskind et al. 2013, Trowland et al. 2013, Dubois et al. 2014, Aragon-Calvo & Yang 2014, Codis et al. 2015). A representative value of $\langle \cos\theta \rangle$ from simulations is given by Codis et al. (2015), $\langle \cos\theta \rangle = 0.509$, similar to $\langle \cos\theta \rangle$ for $\hat{e}_1$-spin alignments measured at low redshift (Tempel & Libeskind 2013, Zhang et al. 2013, Pahwa et al. 2016) and spin-filament alignments in simulations (Dubois et al. 2014) and observations (Tempel et al. 2013). Moreover, for small deviations from random alignments, Equation 2.7 agrees well with Equation 5 in Lee & Erdogdu (2007), who derive an analytic expression for the misalignment angle between galaxy spin and $\hat{e}_2$ in tidal torque theory.

To assign each galaxy a spin axis, we start by finding the eigenvectors of the tidal tensor of the matter density field at the nearest grid point to the galaxy's redshift-space position. The misalignment angle θ is randomly drawn from Equation 2.7 and the azimuthal angle ϕ from the uniform distribution between 0 and 2π. Since both the eigenvectors and the galaxy spin axis are headless vectors, we randomly generate a direction for the galaxy spin as well. Last, we add a random Gaussian deviate with standard deviation $\sigma_{\rm PA}$ (σ_i) to the position angle (inclination), and randomly choose whether the galaxy spin will be oriented towards or away from the observer.

2.2.5 IGM and galaxy survey parameters

We estimate the significance of a galaxy-cosmic web alignment measurement with fiducial parameters $\langle d_\perp \rangle = 2.5\ h^{-1}\,$Mpc, 10000 coeval galaxies, redshift errors of 100 km s^{-1}, $\sigma_{\rm PA} = 10^\circ$ and $\sigma_i = 10^\circ$. Subsequently, we consider how the significance of the alignment signal varies with different sightline spacings, galaxy sample sizes and redshift and structural parameter errors.

Sightline spacings of 6.5, 4.0, 2.5, and 1.4 $h^{-1}\,$Mpc are considered, as well as the full noiseless δ_F simulation grid (with 0.8 $h^{-1}\,$Mpc voxels) as the limiting case of "perfect" IGM tomography. The 4.0, 2.5, and 1.4 $h^{-1}\,$Mpc spacings correspond to the sightline spacings expected for the PFS, CLAMATO, and FOBOS IGM tomography surveys, respectively, while 6.5 $h^{-1}\,$Mpc is the sightline spacing of an IGM reconstructions using only the baseline PFS galaxy evolution survey (Takada et al. 2014) without incorporating additional targets for tomography.

We use coeval galaxy samples of 600, 3000, 10000 and 30000 galaxies. The density of target galaxies for tomography differs by an order of magnitude between the $\langle d_\perp \rangle = 1.4$ and $4.0\ h^{-1}\,$Mpc cases, so the galaxy samples were chosen to span an order of magnitude as well, allowing us to directly compare the importance of coeval galaxy sample size versus number of sightlines. The fiducial 10000 galaxy sample does not require 10000 galaxies in 1 deg^2 (the angular size of our simulation box at $z \sim 2.4$); rather, the galaxies may be spread over a wider area if the tomographic map also has the same coverage. The cosmic web recovery does not depend on halo mass of the galaxies (Figure 2.5), so we emulate a survey with larger area by simply including lower-mass galaxies in our sample.

The 10000 galaxy sample is similar to the number of $2.15 < z < 2.55$ redshifts that the PFS galaxy evolution survey could obtain. Structural parameters for such a sample could be measured either from the deep HyperSuprimeCam imaging used for PFS targeting or from wide-field space-based imaging from Euclid or WFIRST. More ambitious future surveys could perform IGM tomography with even larger samples of coeval galaxies, such as the proposed "Billion-Object Apparatus" (Dodelson et al. 2016), which could execute a CLAMATO-like survey over 10^5 deg^2 with a few hundred coeval galaxies per square degree. As a conservative choice, we therefore include a 30000 galaxy sample to represent these futuristic surveys. At the other extreme, we also consider a 600 galaxy sample, roughly matching the number of coeval galaxies in the CLAMATO volume, primarily from the zCOSMOS-deep survey

(Scoville et al. 2007, Lilly et al. 2007).

The fiducial redshift errors are 100 km s^{-1}, appropriate for redshifts from nebular emission lines in rest-frame optical spectra (Steidel et al. 2010). We consider redshift errors of 300 km s^{-1}, appropriate for redshifts from UV absorption lines or Lyα emission lines (Steidel et al. 2010, Kriek et al. 2015), and 500 km s^{-1}, appropriate for emission-line redshifts from grism spectra (Kriek et al. 2015, Momcheva et al. 2016a). We also consider the maximal redshift errors allowed by our box size, in which the z position of each galaxy in the box is drawn from a uniform distribution. This produces a distribution with $\sigma_v \sim 2000$ km s^{-1}, somewhat better than typical photometric redshifts ($\sigma_v \gtrsim 9000$ km s^{-1}) or Lyα tomographic redshifts ($\sigma_v \gtrsim 3000$ km s^{-1}; Schmittfull & White 2016).

The fiducial error on the galaxy position angle is 10°, consistent with position angle errors as estimated from both cosmic shear measurements from HST imaging (Leauthaud et al. 2007, Joachimi et al. 2013) and from structural parameter measurements using CANDELS imaging (Van Der Wel et al. 2012)[4] for galaxies with magnitudes, sizes, and Sersic indices typical of $z \sim 2$ galaxies. We also consider position angle errors of 5° and 20° in order to determine the importance of imaging quality. These position angle errors may not be appropriate for ground-based imaging, which generally suffers from increased uncertainty in shape modeling (e.g. Chang et al. 2013). We therefore also consider position angle errors of 40°, which may be more realistic for structural parameters derived from ground-based imaging.

We use a fiducial inclination error of 10°. The error on the inclination can be related to the error on the ellipticity using Taylor series error propagation. Using the ellipticity errors from the CANDELS catalog for $z \sim 2$ galaxies assuming intrinsic thickness 0.25 (Van Der Wel et al. 2012), we find a median $\sigma_i = 6°$. To conservatively account for systematic errors from the intrinsic thickness and possible departures from axisymmetry, the fiducial value of σ_i is 10°. We also consider $\sigma_i = 5°$ and $\sigma_i = 20°$ to determine the impact of inclination error on our measurement.

For each measurement, we simulate galaxy selection by randomly selecting $N_{\rm gal}$ halos with $M_h > 10^{10.5} M_\odot$. While this is does not reflect a realistic selection function, the cosmic web recovery does not depend on mass (Figure 2.5) so we expect similar results for realistic selection functions. This also allows us to mock up larger-area surveys without using a larger simulation box, as we can simply select more galaxies within the same 100 h^{-1} Mpc volume.

To simulate the cosmic web-galaxy spin alignment measurement, we measure $\langle \cos \theta_{rg} \rangle$, the dot product of the reconstructed eigenvector and the galaxy spin, as a function of $\langle \cos \theta_{mg} \rangle$, where θ_{mg} is the angle between the matter field eigenvector and the galaxy spin. We turn this into a significance above random by subtracting 0.5, the mean of $\cos \theta$ for a random distribution, and dividing by the standard deviation of 1000 simulations of the measurement.

[4] These methods differ most importantly in that the weak-lensing analyses are somewhat more careful about accounting for systematic errors from PSF variation than the galaxy shape analyses. Also, the weak-lensing analyses present their results in terms of error on the galaxy polarization or ellipticity, while the galaxy shape analyses directly report the errors on the position angle. Polarization/ellipticity errors can be translated to PA errors using Taylor series error propagation.

Table 2.1: Fidelity of Cosmic Web Classification

$\langle d_\perp \rangle$	Smoothing	Flux Eigenvalue	Fraction by ΔN^+ (%)			Volume overlap (%)			
(h^{-1} Mpc)	(h^{-1} Mpc)	Threshold	-1	0	1	Node	Filament	Sheet	Void
δ_F	2	$\lambda_{\rm th,F} < -0.0175$	8.8	83.9	7.2	67.0	82.9	85.2	84.7
1.4	2	$\lambda_{\rm th,F} < -0.0101$	15.2	69.2	14.7	45.7	66.1	72.8	67.5
2.5	4	$\lambda_{\rm th,F} < -0.0095$	17.9	61.1	18.9	24.0	54.2	67.3	60.2
4.0	6	$\lambda_{\rm th,F} < -0.0090$	22.4	52.5	20.7	16.7	46.8	59.3	48.3

Note. — $\Delta N^+ = N^+_{\rm matter} - N^+_{\rm F}$ where N^+ is the number of eigenvalues with $\lambda > \lambda_{\rm th}$ in a given map. Fraction by ΔN^+ refers to the volume fraction of the map where ΔN^+ has that value. Volume overlap is the fraction of all points classified as a particular web element in the matter field that are also classified as that web element in the flux map. We use $\lambda_{\rm th,m} = 0.043$ and a smoothing scale of 2 h^{-1} Mpc for the matter field.

For 2D measurements, the significance is defined as $\langle \theta_{rg} \rangle - \pi/4$ divided by the standard deviation, since a random vector in 2D follows a uniform distribution in θ. Computing the significance using $\langle \cos\theta_{rg} \rangle$ gives similar results to other reasonable choices, such as the difference between the number of aligned and anti-aligned galaxies.

2.3 Results

2.3.1 Recovery of cosmic web directions

We first compare our cosmic web classification to Lee & White (2016), who use an N-body simulation rather than a hydrodynamic IGM simulation and match the DM and IGM tomography smoothing scales. We confirm their finding that IGM tomography can recover cosmic web classifications with similar fidelity to low-redshift surveys, suggesting this finding is insensitive to the details of the simulation and the choice of smoothing scale.

The fraction of the volume with $\Delta N^+ = 0$ is somewhat lower in our $\langle d_\perp \rangle = 2.5$ h^{-1} Mpc reconstruction than in Lee & White (2016), as they find [15,69,15]% of the volume was classified within [-1,0,+1] eigenvalues. However, we do not match the matter smoothing scale to the IGM tomography smoothing scale and we include continuum errors in our mock absorption skewers, both of which degrade the reconstructions. Compared to Lee & White (2016), we recover sheets, voids, and filaments with slightly lower fidelity, and nodes with significantly lower fidelity.

Figure 2.3 displays the PDF of $\cos\theta$, where θ is the misalignment angle between the matter field tidal tensor eigenvectors and the pseudo-deformation tensor eigenvectors from

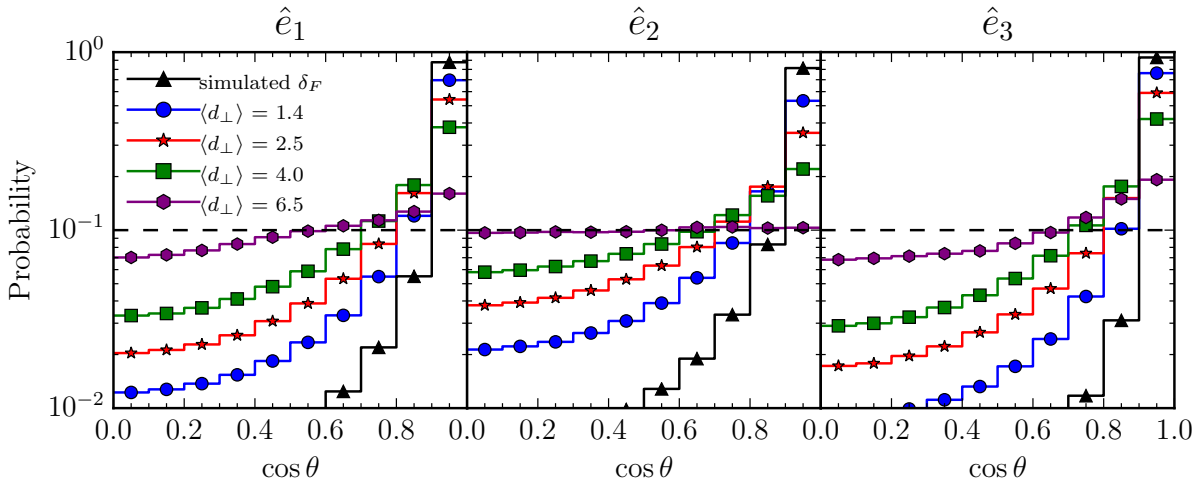

Figure 2.3: PDF of the cosine of the misalignment angle between the cosmic web directions from the matter density field and the cosmic web directions from the simulated IGM tomography observations. We also show the misalignment angle between the matter density cosmic web and the cosmic web computed from the simulated δ_F with 2 h^{-1} Mpc smoothing, which is the ideal case of a perfect reconstruction from Lyα forest data. In all cases the matter density field is smoothed on 2 h^{-1} Mpc scales. The horizontal dashed line is the distribution expected for random alignments.

the reconstructed IGM maps. We also compute the misalignment angle PDF between the matter field tidal tensor eigenvectors and the pseudo-deformation tensor eigenvectors from the simulated δ_F smoothed on 2 h^{-1} Mpc scales, equivalent to an idealized reconstruction with no instrumental noise and infinite sightline density.

The mock surveys with $\langle d_\perp \rangle < 5$ h^{-1} Mpc recover the eigenvectors of the tidal tensor at high significance. The recovery of the eigenvectors degrades quickly for $\langle d_\perp \rangle > 5$ h^{-1} Mpc, due in part to the mismatch between $\langle d_\perp \rangle$ and the 2 h^{-1} Mpc smoothing scale of the matter field. The mean of the cosine of the misalignment angle for [$\hat{e}_1$, $\hat{e}_2$, $\hat{e}_3$] is [0.874, 0.809, 0.901] for $\langle d_\perp \rangle = 1.4$ h^{-1} Mpc, [0.813, 0.716, 0.833] for $\langle d_\perp \rangle = 2.5$ h^{-1} Mpc, [0.736, 0.629, 0.757] for $\langle d_\perp \rangle = 4.0$ h^{-1} Mpc, and [0.573, 0.508, 0.600] for $\langle d_\perp \rangle = 6.5$ h^{-1} Mpc. Errors on these quantities are $< 0.1\%$. The mean of the cosine of the misalignment angle between is [0.945, 0.921, 0.967] using the simulated δ_F field. This is the upper limit of how well Lyα absorption measurements can measure the eigenvectors of the tidal tensor.

We also compute the mean of the misalignment angle at halo positions only. For [$\hat{e}_1$, $\hat{e}_2$, $\hat{e}_3$], we find means of [0.891, 0.837, 0.919] for $\langle d_\perp \rangle = 1.4$ h^{-1} Mpc, [0.815, 0.722, 0.838] for $\langle d_\perp \rangle = 2.5$ h^{-1} Mpc, [0.734, 0.628, 0.761] for $\langle d_\perp \rangle = 4.0$ h^{-1} Mpc, [0.571, 0.516, 0.607] for $\langle d_\perp \rangle = 6.5$ h^{-1} Mpc, and [0.950, 0.929, 0.970] for simulated δ_F. The differences between these values and the means of $\cos\theta$ using the entire grid are quite modest, although statistically significant.

Figure 2.4 shows the quality of cosmic web recovery as a function of cosmic web type as

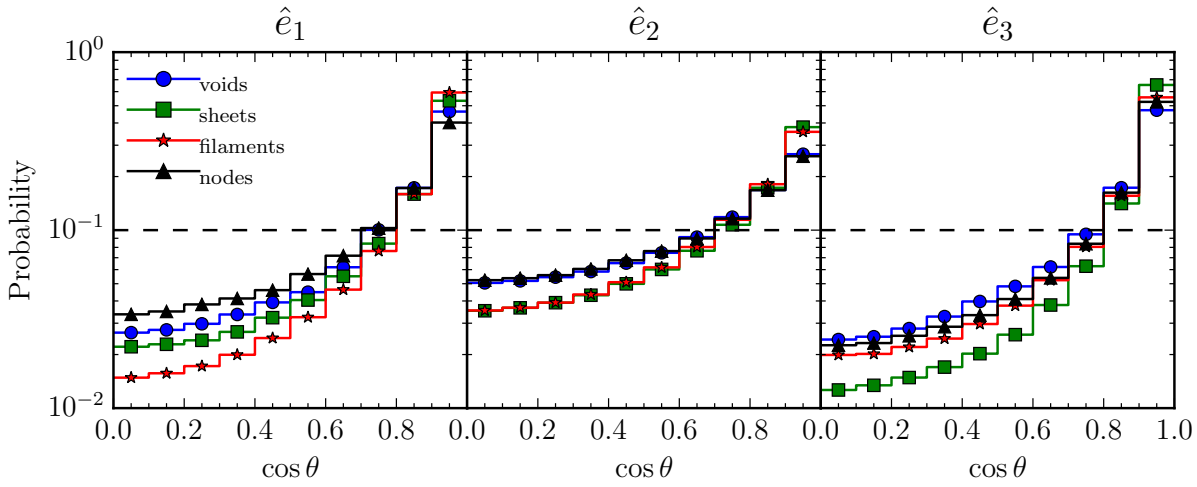

Figure 2.4: PDF of the cosine of the misalignment angle between the cosmic web directions from the matter density field and the cosmic web directions from the simulated IGM tomography observations, using the $\langle d_\perp \rangle = 2.5\ h^{-1}\,\mathrm{Mpc}$ reconstruction and splitting by classification in the matter map. All distributions are significantly different according to Kolmogorov-Smirnov tests.

classified in the matter map, using the $\langle d_\perp \rangle = 2.5\ h^{-1}\,\mathrm{Mpc}$ reconstruction. Mirroring the results in Table 2.1, $\hat{e}_1$, $\hat{e}_2$, and $\hat{e}_3$ are recovered worst in nodes. Despite the relatively high volume overlap for the void recovery, the tidal tensor eigenvectors are recovered slightly worse in voids than in anisotropic structures such as filaments and sheets. All three eigenvalues are similar in voids, possibly causing confusion between perpendicular eigenvalues and leading to the poorer recovery of the cosmic web in voids. The recovery of eigenvectors in sheets and filaments are similar, although $\hat{e}_1$ is recovered better in filaments while $\hat{e}_3$ is recovered better in sheets. This is unsurprising given the connection between the eigenvectors and the geometry of the cosmic web, as $\hat{e}_1$ in filaments and $\hat{e}_3$ in sheets correspond to inherently anisotropic directions that should be easier to recover.

We additionally test the quality of the reconstruction as a function of halo mass. We divide the halo catalog into four bins and measure the angle between the eigenvectors in the matter field and the eigenvectors in the $\langle d_\perp \rangle = 2.5\ h^{-1}\,\mathrm{Mpc}$ reconstruction using the nearest grid point in redshift space. The recovery of the eigenvectors is nearly independent of the halo mass (Figure 2.5). None of the distributions are significantly different at the $p = 0.05$ level (2 sigma) according to Kolmogorov-Smirnov tests, implying that the eigenvectors can be recovered accurately at galaxy positions independent of halo mass.

We provide the first assessment of the accuracy of tidal tensor reconstruction by comparing the tidal tensor eigenvectors from the matter field to the tidal tensor eigenvectors from realistic mock observations. We expect that IGM tomography will be better at recovering the tidal tensor eigenvectors than existing or upcoming galaxy surveys at the same redshift, such as zCOSMOS or PFS; these will provide much coarser cosmic web maps with galaxy

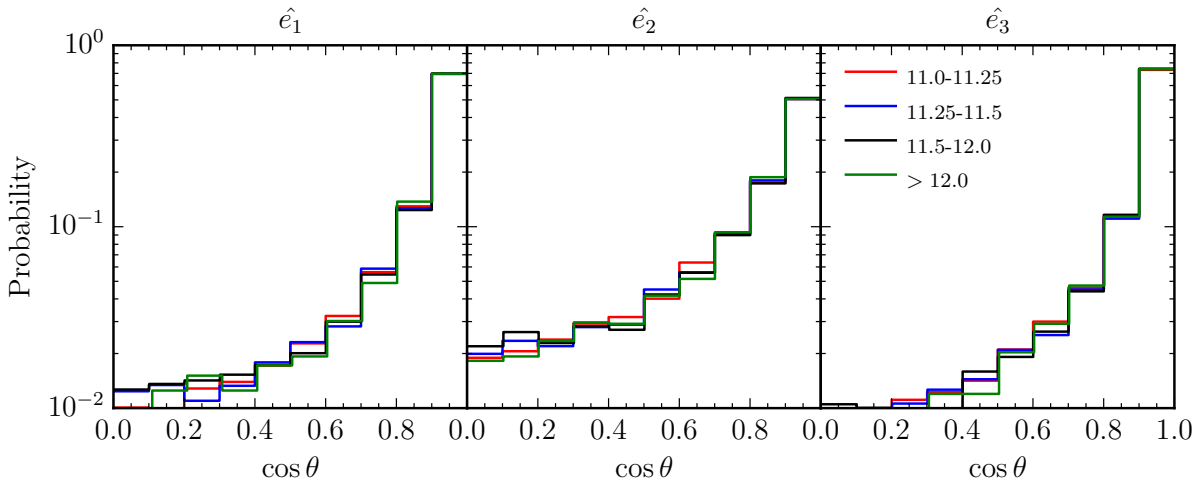

Figure 2.5: PDF of the cosine of the misalignment angle between the cosmic web directions from the matter density field and the cosmic web directions from the simulated IGM tomography observations, using the $\langle d_\perp \rangle = 2.5\ h^{-1}\,\mathrm{Mpc}$ reconstruction. Misalignment angles are computed at the nearest grid point for each dark matter halo. The four groups are labeled by halo mass in units of $\log M_\odot$.

separations of 9 (13) h^{-1} Mpc for PFS (zCOSMOS) (Diener et al. 2013, Takada et al. 2014). For instance, since protocluster identification with zCOSMOS required additional follow-up spectroscopy (Diener et al. 2015), the zCOSMOS redshift survey alone is likely insufficient to measure the cosmic web at $z > 2$. In addition, cosmic web maps from IGM tomography are free from many of the biases that make measuring the cosmic web from spectroscopic $z \sim 2$ galaxy surveys difficult: these surveys have complex selection functions (e.g. Diener et al. 2013), inaccurate and/or biased redshift estimates (e.g., Adelberger et al. 2005, Steidel et al. 2010, Rakic et al. 2012), cannot detect close pairs due to slit collisions (Wilson et al. 2015), and preferentially select star forming galaxies, which may be biased towards particular regions of the cosmic web (Alpaslan et al. 2015). In contrast, IGM tomography sightlines provide an unbiased sampling of the foreground cosmic web, and errors from pixel noise and continuum errors are well-understood, making a subdominant contribution to errors in the reconstruction.

2.3.2 Predictions for galaxy-cosmic web alignment measurements

Several workers have considered the alignment of galaxies and the cosmic web in simulations, but thus far observational studies of the galaxy-cosmic web alignment have been restricted to low redshift ($z \lesssim 0.5$) where sufficiently large galaxy catalogs exist to measure the cosmic web (Lee & Pen 2002, Lee & Erdogdu 2007, Tempel et al. 2013, Tempel & Libeskind 2013, Zhang et al. 2013, 2015, Pahwa et al. 2016; although see Malavasi et al. 2016

for recent results at $\langle z \rangle \sim 0.7$). We now consider the prospects for a galaxy-cosmic web alignment study at $z \sim 2$ using the cosmic web from IGM tomography maps and coeval galaxy samples from space-based or large ground-based telescopes.

First, we estimate the significance of the measured galaxy-eigenvector alignment signal as a function of the true strength of the galaxy-eigenvector alignment. We describe the PDF of the true galaxy-eigenvector misalignment angle using Equation 2.7, and thus parameterize the galaxy-eigenvector alignment strength using the deviation of $\langle \cos\theta \rangle$ from 0.5 (i.e. the deviation from random alignments):

$$\Delta\langle \cos\theta \rangle \equiv \langle \cos\theta \rangle - 0.5 \tag{2.9}$$

Note that the significance of a model with $-\Delta\langle \cos\theta \rangle$ is identical to the significance of a model with $\Delta\langle \cos\theta \rangle$ because the spins and eigendirections are headless vectors invariant under the transformation $\theta \to \pi - \theta$. Therefore, we only plot significances as a function of positive $\Delta\langle \cos\theta \rangle$.

In Figure 2.6, we show the forecasted significance of the alignment signal between galaxies and $\hat{e}_1$, as a function of the sightline spacing, number of galaxies, expected redshift error, and errors on the galaxy position angle and inclination. Our fiducial values for these quantities are $\langle d_\perp \rangle = 2.5\ h^{-1}\,\mathrm{Mpc}$, 10000 coeval galaxies, redshift errors of 100 km s^{-1}, and position angle and inclination errors of 10°. A different random seed is used in each panel, leading to very slight differences between the fiducial case in different panels. The 1-σ error on $\Delta\langle \cos\theta \rangle$ of ~ 0.01 for the fiducial measurement of alignment with $\hat{e}_1$ is somewhat larger than 1-σ errors from alignment measurements using low-redshift galaxies (~ 0.005 for similar galaxy sample sizes in Tempel et al. 2013, Tempel & Libeskind 2013, Pahwa et al. 2016).

Figure 2.6 shows the significance of alignment measurements between galaxy spins and $\hat{e}_1$, $\hat{e}_2$, and $\hat{e}_3$ as a function of the true alignment strength between galaxy spin and $\hat{e}_1$, $\hat{e}_2$ and $\hat{e}_3$. Consistent with Figure 2.3, alignments with $\hat{e}_1$ and $\hat{e}_3$ can be detected at similar levels of significance, while alignments with $\hat{e}_2$ will be detected with somewhat lower significance. We note that $\hat{e}_2$ alignments are detected at similar significance for both 2D and 3D measurements. We attribute this to redshift-space distortions in the map, which cause $\hat{e}_2$ to lie preferentially in the plane of the sky, because the directions of maximal and minimal compression ($\hat{e}_1$ and $\hat{e}_3$) are biased towards the line of sight due to compression and rarefaction from redshift-space distortions. Measuring alignments between real-space matter density eigenvectors and redshift-space δ_F^{rec} eigenvectors yields a similar reduction between 2D and 3D alignment measurements for $\hat{e}_1$, $\hat{e}_2$, and $\hat{e}_3$.

Tidal torque theory predicts that galaxy spin is aligned with $\hat{e}_2$. Using an analytic quadratic alignment model (Lee & Pen 2000), Lee & Erdogdu (2007) derive a PDF for the misalignment angle as a function of c, a correlation parameter ranging from 0 (random alignments) to 1 (perfect spin-shear alignments). In the limit of small $\Delta\langle \cos\theta \rangle$, this PDF can be well approximated by Equation 2.7 via Taylor series expansion. For the fiducial $\hat{e}_2$ alignment measurement we find a 1-σ error on $\Delta\langle \cos\theta \rangle \sim 0.015$, which translates to a 1-σ error on $c \sim 0.08$. Previous measurements at low redshift have achieved lower error

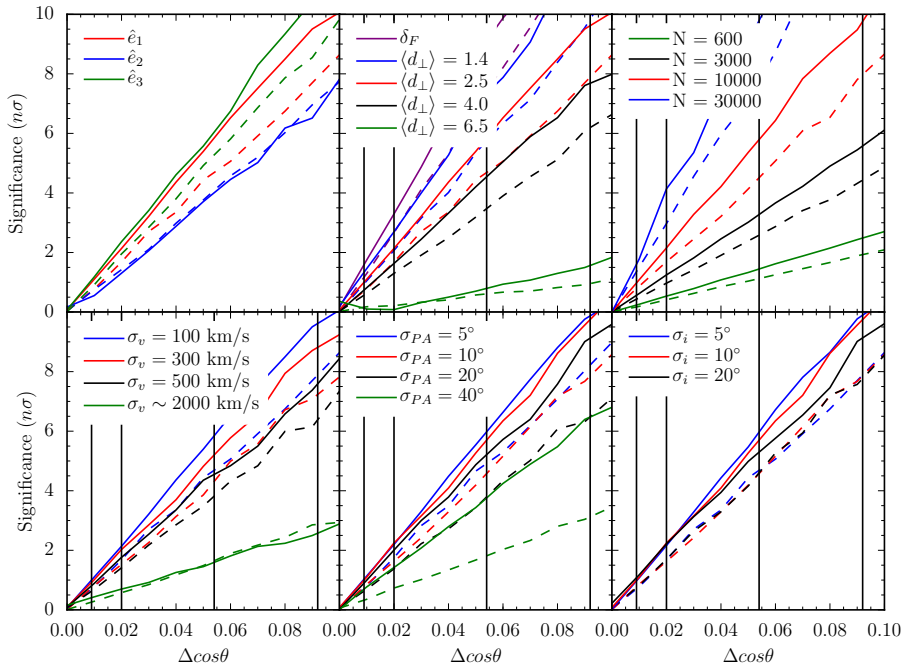

Figure 2.6: Forecasted significance of the measured galaxy spin-cosmic web alignment as a function of the true alignment between galaxy spins and the cosmic web. The y-axis indicates the significance of the measurement in units of σ, while the x-axis indicates the deviation of the true alignment from random. For all panels except the top left, the galaxy spin axis is misaligned from $\hat{e}_1$ by an angle drawn from Equation 2.7 with $\langle \cos\theta \rangle = \Delta \cos\theta + 0.5$. In the top left panel, the galaxy spin axis is misaligned from either $\hat{e}_1$, $\hat{e}_2$, or $\hat{e}_3$. For all panels, the solid lines refer to 3D measurements (alignment between eigenvector and 3D galaxy spin inferred from position angle and ellipticity of the galaxy image) while the dashed lines refer to 2D measurements (alignment between the eigenvector projected in the plane of the sky and the galaxy position angle). Our fiducial survey has $\langle d_\perp \rangle = 2.5$ h^{-1} Mpc, 10000 galaxies, $\sigma_v = 100$ km s^{-1}, $\sigma_{\rm PA} = 10°$, and $\sigma_i = 10°$. In each panel, we vary exactly one of these parameters while keeping the others fixed. *Top left:* Forecasts for alignments between galaxy spin and $\hat{e}_1$, $\hat{e}_2$ and $\hat{e}_3$. *Top center:* Forecasts for alignment between galaxy spin and $\hat{e}_1$ for a variety of IGM tomography surveys with different sightline spacings, including a "perfect" survey where the map is given by δ_F from the simulation. Vertical lines indicate different alignment models from simulations, as defined in Table 2.2. *Top right:* forecasts for alignment between galaxy spin and $\hat{e}_1$ for coeval galaxy samples of different sizes. *Bottom left:* Forecasts for alignment between galaxy spin and $\hat{e}_1$ for different redshift errors. *Bottom center:* Forecasts for alignment between galaxy spin and $\hat{e}_1$ for different errors in the galaxy position angle. *Bottom right:* Forecasts for alignment between galaxy spin and $\hat{e}_1$ for different errors in the inclination. Note that changing the inclination error does not affect the 2D measurement because it does not incorporate any information from the inclination.

Table 2.2: Summary of alignment models

$\Delta\langle\cos\theta\rangle$	Description	Reference
0.009	$z \sim 1.2$ alignments between $\hat{e}_1$ and galaxy spin from Horizon-AGN	Codis et al. (2015)
0.020	$z \sim 2.3$ alignments between filaments and galaxy spins from HorizonAGN	Dubois et al. (2014)
0.054	$z \sim 1.05$ alignment between $\hat{e}_1$ and halo shape (N-body), plus misalignment between halo shape and galaxy shape, alignments extrapolated to $z \sim 2.4$ and $M_h \sim 10^{12} M_\odot$ assuming alignments constant as a function of M_h	Hahn et al. (2007a), Okumura et al. (2009)
0.092	$z \sim 1.05$ alignment between $\hat{e}_1$ and halo shape (N-body), plus misalignment between halo shape and galaxy shape, alignments extrapolated to $z \sim 2.4$ and $M_h \sim 10^{12} M_\odot$ assuming alignments constant as a function of M_h/M_{nl}	Hahn et al. (2007a), Okumura et al. (2009)

Note. — Alignment models considered in Figure 2.6. See text for details. Each alignment model is parameterized using Equation 2.7 with $\langle\cos\theta\rangle = 0.5 + \Delta\cos\theta$.

bars: Lee & Pen (2002) find $c = 0.28 \pm 0.07$ [5], Lee & Erdogdu (2007) find $c = 0.08 \pm 0.01$, and Lee & Pen (2007) find $c = 0.0 \pm 0.05$ for red galaxies and $c = 0.33 \pm 0.07$ for blue galaxies. If $c \sim 0.2 - 0.3$ at $z \sim 2.4$, IGM tomography surveys with $\langle d_\perp \rangle = 2.5\ h^{-1}\,\mathrm{Mpc}$ and 10000 coeval galaxies will measure this alignment at $\sim 3\sigma$. However, nonlinear evolution is expected to decrease the alignment between spin and $\hat{e}_2$ over time (Porciani et al. 2002), leading to a larger value of c at high redshift than low redshift. These results suggest that the combination of galaxy surveys at low redshift and IGM tomography surveys at high redshift may be able to constrain the redshift evolution of the alignment, providing a rigorous test of tidal torque theory.

Figure 2.6 shows the importance of varying different parameters of the IGM and galaxy observations. Varying the sightline spacing from $\langle d_\perp \rangle = 1.4\,h^{-1}\,\mathrm{Mpc}$ to $\langle d_\perp \rangle = 4\,h^{-1}\,\mathrm{Mpc}$ is equivalent to decreasing the number of sightlines by an order of magnitude. Thus, comparison of the top center and top right panels of Figure 2.6 shows that close to the fiducial sightline spacing of $2.5\ h^{-1}\,\mathrm{Mpc}$, increasing the number of coeval galaxies is more important than increasing the number of background Lyα forest sightlines. However, the measured significance of the signal drops dramatically for sightline spacings $\langle d_\perp \rangle > 4\ h^{-1}\,\mathrm{Mpc}$. This suggests that a wide-field survey such as PFS is preferable for measuring galaxy-cosmic web alignments, as it would be best positioned to deliver a large coeval galaxy sample, while the coarser sightline spacing of $4\ h^{-1}\,\mathrm{Mpc}$ only modestly lowers the significance compared to CLAMATO with $\langle d_\perp \rangle = 2.5\ h^{-1}\,\mathrm{Mpc}$. However, the poor performance of the $\langle d_\perp \rangle = 6.5\ h^{-1}\,\mathrm{Mpc}$ survey suggests that PFS will require a supplemental tomography component to achieve the necessary sightline spacing to detect galaxy-cosmic web alignments.

Varying the fiducial position angle and inclination errors by a factor of two makes relatively little difference for measuring the alignment signal. We also test a model with a relatively large PA error of 40°, which may be more representative of the shape errors in a ground-based survey. In this case, much more of the constraining power comes from the inclination. If the survey is also unable to recover the inclinations due to large uncertainties in measuring the axis ratio, the significance of the alignment signal drops dramatically. Therefore, reasonably precise estimates of the position angle ($\sigma_{\mathrm{PA}} \lesssim 30°$) will be necessary to measure alignments between galaxy spin and the cosmic web.

The impact of spectroscopic redshift errors are quite modest, as Figure 2.6 shows little difference between a sample with redshift errors ~ 100 km s^{-1} (e.g. redshifts measured from rest-frame optical nebular emission lines) and a sample with redshift errors ~ 300 km s^{-1} (e.g. redshifts measured from rest-frame UV absorption lines). Even grism redshifts ($\sigma_v \sim 500$ km s^{-1}) lead to only modest degradation of the alignment signal.

At fixed number density, a redshift error of ~ 2000 km s^{-1} from the sample with randomized positions leads to a drastic reduction in the constraining power of the survey. However, photometric samples offer much greater number densities than spectroscopic samples due to the less stringent observational requirements. In Figure 2.7, we show that alignment measurements with the "photometric" sample (randomized galaxy positions) require 10000

[5] Lee & Pen (2002) expresses their result in terms of $a_T = (3/5)c$. See Lee & Pen (2001) for the difference between a_T and c.

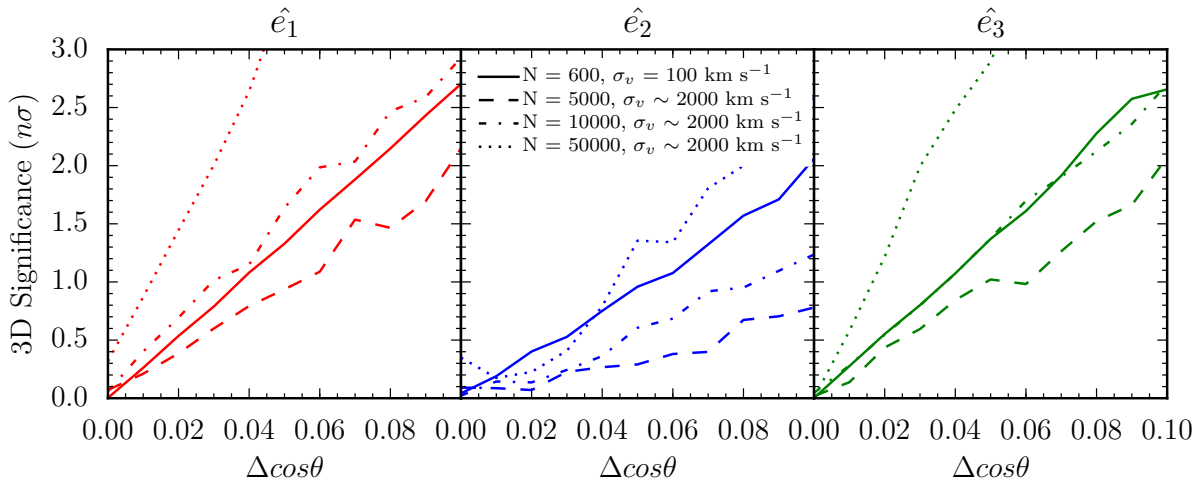

Figure 2.7: Comparison between spin-cosmic web alignment using galaxies with $\sigma_v = 100$ km s^{-1} versus $\sigma_v \sim 2000$ km s^{-1}. The latter redshift errors are substantially smaller than typical redshift errors for photometric surveys, but are the maximum errors permitted by the size of our simulation box. We compare samples of 5000, 10000, and 50000 "photometric" galaxies to a baseline survey with 600 spectroscopic galaxies. We use fiducial survey parameters of $\langle d_\perp \rangle = 2.5\ h^{-1}$ Mpc, $\sigma_{\rm PA} = 10°$ and $\sigma_i = 10°$.

to 50000 galaxies to achieve similar significance to alignment measurements with 600 spectroscopic galaxies ($\sigma_v = 100$ km s^{-1}). By comparison, the CLAMATO volume contains ~ 600 spectroscopic galaxies and ~ 10000 photometric galaxies. The redshift error of the randomized sample is considerably smaller than either the photometric redshift accuracy in COSMOS (~ 9000 km s^{-1}; Laigle et al. 2016) or optimistic forecasts for tomographic redshift accuracy (~ 3000 km s^{-1}; Schmittfull & White 2016), suggesting that spectroscopic galaxy samples are preferable for measuring spin-cosmic web alignments.

We also explore the possibilities for constraining alignment models based on results from simulations. Simulations have measured a broad variety of alignments (e.g. between halo/galaxy spins/shapes and filaments/$\hat{e}_1$) across a wide range of redshifts. In general, simulations have found stronger alignments between halo shapes and the cosmic web than between halo spins and the cosmic web (Hahn et al. 2007a). While the discussion above is framed in terms of galaxy spin alignments, ultimately we are measuring the major axis of the galaxy image, which may be set by either the spin or the shape of the galaxy and ultimately the dark matter halo. Therefore, we consider alignment models from both galaxy spin and halo shape.

We use the simulation results of Hahn et al. (2007a) to create an alignment model based on halo shape. Hahn et al. (2007a) studies the alignment between halo shape and $\hat{e}_1$ at $z = 0$, 0.49, and 1.05. After accounting for the mass dependence by scaling by the mass scale of nonlinear collapse $M_*(z)$ they find no additional redshift dependence.

We extrapolate the results of Hahn et al. (2007a) to $z \sim 2.3$ to create an alignment model. Hahn et al. (2007a) parameterizes the mass dependence of their result using M_h/M_* where M_* is the mass for which a 1-σ fluctuation reaches the threshold for spherical collapse, $\delta_c = 1.686$. At $z \sim 2.3$, the typical halo ($M_h \sim 10^{12} M_\odot$) in the coeval galaxy sample has $M \gtrsim 100 M_*$, leading to an extremely strong alignment signal, median $\cos\theta = 0.78$ ($\langle\cos\theta\rangle = 0.73$ assuming the PDF follows Equation 2.7). More conservatively, it is possible that above $z \sim 1.05$ the alignment signal is constant with M_h rather than M_h/M_*. In this case, the typical halo detected in our galaxy sample has $M \sim 10 M_{*,z=1.05}$, leading to a slightly weaker median $\cos\theta = 0.7$ ($\langle\cos\theta\rangle = 0.64$) between $\hat{e}_1$ and halo shape. To translate from halo shape alignments to galaxy shape alignments, we use the halo-galaxy misalignment model of Okumura et al. (2009), a Gaussian distribution of halo-galaxy misalignment angles with dispersion 35°. We find $\Delta\langle\cos\theta\rangle = 0.092$ (0.054) for the Hahn et al. (2007a) model using M_h/M_* (M_h) to determine alignments.

In contrast to the shape measurements, several workers have measured alignments between galaxy spins and the cosmic web using hydrodynamic simulations of the galaxies. These include Codis et al. (2015), who measure alignments between galaxy spin and $\hat{e}_1$ at $z \sim 1.2$, finding $\Delta\langle\cos\theta\rangle = 0.009$. Similarly, Dubois et al. (2014) measure alignments between galaxy spin and filaments for galaxies between $z \sim 1.2$ and $z \sim 3$ and find $\Delta\langle\cos\theta\rangle = 0.02$. These alignments are similar to alignments inferred from simulations of halo spin-cosmic web alignments (Hahn et al. 2007a, Trowland et al. 2013) with a galaxy-halo spin misalignment following Bett (2012). The spin-web alignment is considerably weaker than the shape-web alignment, consistent with results from dark matter halos (Hahn et al. 2007a) and possibly related to stronger shape-cosmic web alignments for early-type than late-type galaxies observed at low redshift (Tempel & Libeskind 2013, Pahwa et al. 2016) and the considerably stronger intrinsic alignments observed for early-type than late-type galaxies (Joachimi et al. 2013, Mandelbaum et al. 2006).

Figure 2.6 shows that IGM tomography surveys in tandem with wide-field galaxy surveys would be able to detect or rule out alignment models based on halo shape (e.g. from Hahn et al. (2007a) at high significance. Even the combination of the CLAMATO survey and zCOSMOS galaxy survey (with $N_{\rm gal} \sim 600$ over the $V \sim 10^6\,h^{-3}{\rm Mpc}^3$ CLAMATO volume at $2.1 < z < 2.5$) will be sufficient to detect or rule out the most aggressive alignment models based on halo shape at ∼2-3 σ. However, more realistic models with smaller alignments will require an order of magnitude more coeval galaxies for detection at a similar level. Figure 2.6 also shows that ground-based imaging should be sufficient to measure galaxy spins as long as position angles can be measured with an error $\lesssim 20°$.

Additional measurements besides spin-eigendirection correlations may yield further independent information. For instance, IGM tomography will be able to identify a large number of voids (Stark et al. 2015), allowing measurement of the void-spin correlation (e.g. Trujillo et al. 2006, Slosar & White 2009, Varela et al. 2012). We can also use the eigenvalues to partition our map into voids, sheets, filaments, and nodes (Lee & White 2016) and measure spin-$\hat{e}_1$ alignments only in filaments, or spin-$\hat{e}_3$ alignments only in sheets, where they may be strongest (e.g. Hahn et al. 2007a).

2.4 Conclusions

Intrinsic alignments between galaxies and the underlying cosmic web have been predicted from both DM-only and hydrodynamical simulations, several of which predict increasing alignment strength at higher redshift ($z \gtrsim 1$). At these redshifts, it becomes increasingly expensive to obtain spectroscopic redshifts with sufficiently high number densities to trace the cosmic web. Recently, tomographic reconstruction of the IGM as traced by high area densities of Lyman-α forest sightlines has emerged as a promising method to map the cosmic web at $z \sim 2-3$.

In this paper, we studied the feasibility of IGM tomographic surveys, in conjunction with coeval galaxy redshift samples with measured structural parameters, to place constraints on galaxy-cosmic web alignments at $z \sim 2.5$. Using detailed hydrodynamical simulations based on the Nyx code, we first generated realistic mock data sets reflecting both ongoing and future IGM tomography surveys. The galaxy spin or shape distributions were 'painted on' with respect to the underlying matter tidal tensor field using a simple alignment model parameterized by $\Delta\langle\cos\theta\rangle$, i.e. the non-random excess alignment of the galaxies with respect to the eigenvectors of the matter tidal tensor. Future studies of galaxy-cosmic web alignments at $z \sim 2$ will benefit greatly from simulations combining both realistic IGM physics and galaxy formation (e.g. future versions of the Nyx simulations used in this paper).

First, we showed that IGM tomography with sightline separations of $\langle d_\perp \rangle \leq 5\,h^{-1}\,\mathrm{Mpc}$ should be able to recover the eigenvectors of the tidal tensor, $\hat{e}_1$, $\hat{e}_2$, and $\hat{e}_3$, as determined from the large-scale distribution of matter in the universe (smoothed on $2\,h^{-1}\,\mathrm{Mpc}$ scales). The mean dot products between the eigenvectors as determined by the matter field and the eigenvectors from a mock observation with sightline spacing 2.5 $h^{-1}\,\mathrm{Mpc}$, similar to the ongoing CLAMATO survey, are [0.815, 0.722, 0.838] for $[\hat{e}_1, \hat{e}_2, \hat{e}_3]$. This builds on our previous result showing that IGM tomography can recover eigenvalue cosmic web classifications with a fidelity similar to $z \lesssim 0.7$ surveys (Lee & White 2016).

We then compared the eigenvectors recovered from the IGM tomography with the spins or shapes in coeval galaxy samples as a function of the alignment strength $\Delta\langle\cos\theta\rangle$, and also considered the effect of uncertainties in the measurement of the galaxy position angles, inclinations, and redshift estimation. The largest factor in our ability to constrain the galaxy-cosmic web alignments is the size of the galaxy sample. Assuming a fiducial mean sightline separation of $\langle d_\perp \rangle = 2.5\,h^{-1}\,\mathrm{Mpc}$, redshift errors of $\sigma_v = 500\,\mathrm{kms}^{-1}$, as well as errors of $\sigma_{\mathrm{PA}} = 10^\circ$ and $\sigma_i = 10^\circ$ in the galaxy position angles and inclinations, respectively, we find that the ongoing CLAMATO Survey on the Keck-I Telescope[6], in conjunction with ~ 600 coeval galaxies from zCOSMOS-Deep and other spectroscopic surveys, should be able to place $\sim 3\sigma$ limits on the most extreme alignment models with $\Delta\langle\cos\theta\rangle \sim 0.1$ within the next few years. For most alignment models with $\Delta\langle\cos\theta\rangle < 0.05$, however, coeval samples of at least several thousand galaxies with spectroscopic redshifts would be needed to make a $\sim 3-4\sigma$ detection. These results are not very sensitive to the mean sightline separation

[6]Comoving volume of $V \sim 10^6\,h^{-3}\,\mathrm{Mpc}^3$ over $2.1 < z < 2.5$ within the central square degree of the COSMOS Field.

of the IGM tomography survey so long as $\langle d_\perp \rangle \lesssim 5\,h^{-1}\,\mathrm{Mpc}$, nor on the accuracy of the galaxy structural parameters, although space-based imaging or very good quality ground-based imaging (< 0.5 arcsec seeing) would be desirable for the latter. We find that alignment measurements using photometric redshifts will require samples at least 20 times larger than spectroscopic redshift samples, indicating that spectroscopic samples are preferable.

Since the primary limitation for this alignment measurement is the size of available galaxy redshift samples at $z \sim 2.5$, a relatively wide/shallow strategy would be optimal: at fixed survey magnitude, the galaxy sample size $N_{\rm gal}$ scales linearly with telescope time by expanding survey area. On the other hand, increasing $N_{\rm gal}$ by increasing survey depth within a small survey area would require exponential increases of telescope time. Since the tidal tensor eigenvector recovery does not degrade much with slightly coarser tomographic reconstructions relative to the fiducial $2.5\,h^{-1}\,\mathrm{Mpc}$ sightline spacing in CLAMATO, this argues that near-future wide-field instruments, i.e. Subaru PFS, which cover much larger areas than CLAMATO with the concomitantly larger $N_{\rm gal}$, will deliver significantly improved spin-cosmic web or shape-cosmic web constraints. However, we did find a mean spacing of $\langle d_\perp \rangle < 5\,h^{-1}\,\mathrm{Mpc}$ is required for the Lyα forest sightlines, above which the eigenvector recovery degrades considerably. Since the $2 < z < 3$ LBG component currently planned for the $\sim 20 - 30$ sq deg PFS Galaxy Evolution Survey leads to a "free" IGM tomographic map with $\langle d_\perp \rangle \sim 6.5\,h^{-1}\,\mathrm{Mpc}$, we advocate supplemental PFS spectroscopy to boost the sightline sampling to $\langle d_\perp \rangle \approx 4\,h^{-1}\,\mathrm{Mpc}$. Based on the calculations of Lee et al. (2014a), this should require $\sim 5 - 6$ hrs of additional exposure time per field, or ~ 20 nights over ~ 25 sq deg (including weather/seeing overheads). Such a program, along with the $\sim 10,000$ coeval galaxies also from PFS, should allow 3σ limits on alignments down to $\Delta\langle \cos\theta \rangle \approx 0.03$. Constraints on even smaller $\Delta\langle \cos\theta \rangle$, at the levels predicted by, e.g. Codis et al. (2015), would require even more ambitious surveys. However, it is conceivable that a new generation of massively-multiplexed wide-field spectrographs on >10m-class telescopes could be available by the early 2030s (McConnachie et al. 2016, Dodelson et al. 2016, Najita et al. 2016), in time to provide priors on the intrinsic alignment systematics for the final LSST tomographic weak lensing analyses.

Acknowledgments

We thank Peter Nugent, Alexie Leauthaud, Nadia Zakamska, Sukhdeep Singh, Miguel Aragon-Calvo, Joanne Cohn, and Sedona Price for useful discussions and comments. K.G.L. acknowledges support for this work by NASA through Hubble Fellowship grant HF2-51361 awarded by the Space Telescope Science Institute, which is operated by the Association of Universities for Research in Astronomy, Inc., for NASA, under contract NAS5-26555. ZL and AK were in part supported by the Scientific Discovery through Advanced Computing (SciDAC) program funded by U.S. Department of Energy Office of Advanced Scientific Computing Research and the Office of High Energy Physics. This research was supported by the Exascale Computing Project (ECP), Project Number: 17-SC-20-SC, a collaborative effort of

two DOE organizations, the Office of Science and the National Nuclear Security Administration, responsible for the planning and preparation of a capable exascale ecosystem, including software, applications, hardware, advanced system engineering, and early testbed platforms, in order to support the nation's exascale computing imperative. Calculations presented in this paper used resources of the National Energy Research Scientific Computing Center (NERSC), which is supported by the Office of Science of the U.S. Department of Energy under Contract No. DE-AC02-05CH11231.

Chapter 3

Alignment between filaments and galaxy spins from the MaNGA integral-field survey

Abstract

Halos and galaxies acquire their angular momentum during the collapse of surrounding large-scale structure. This process imprints alignments between galaxy spins and nearby filaments and sheets. Low mass halos grow by accretion onto filaments, aligning their spins with the filaments, whereas high mass halos grow by mergers along filaments, generating spins perpendicular to the filament. We search for this alignment signal using filaments identified with the "Cosmic Web Reconstruction" algorithm applied to the Sloan Digital Sky Survey Main Galaxy Sample and galaxy spins from the MaNGA integral-field unit survey. MaNGA produces a map of the galaxy's rotational velocity, allowing direct measurement of the galaxy's spin direction, or unit angular momentum vector projected onto the sky. We find no evidence for alignment between galaxy spins and filament directions. We do find hints of a mass-dependent alignment signal, which is in 2-3σ tension with the mass-dependent alignment signal in the MassiveBlack-II and Illustris hydrodynamical simulations. However, the tension vanishes when galaxy spin is measured using the Hα emission line velocity rather than stellar velocity. Finally, in simulations we find that the mass-dependent transition from aligned to anti-aligned dark matter halo spins is not necessarily present in stellar spins: we find a stellar spin transition in Illustris but not in MassiveBlack-II, highlighting the sensitivity of spin-filament alignments to feedback prescriptions and subgrid physics.

3.1 Introduction

Dark matter protohalos acquire their angular momentum through tidal torquing by neighboring large scale structure (Peebles 1969, Doroshkevich 1970, White 1984). In the linear

regime, angular momentum grows linearly with time and is aligned along the intermediate eigenvector of the tidal tensor (i.e. the traceless part of the Hessian of the potential Φ). However, tidal torque theory is only qualitatively correct in the nonlinear regime, as nonlinear evolution significantly weakens the spin alignment (Porciani et al. 2002) and drives alignments with other preferred directions. In the Zel'dovich picture of structure formation, collapse occurs sequentially along the eigenvectors of the tidal tensor (Zel'dovich 1970), forming anisotropic structures such as sheets (one direction of collapse and two of expansion) and filaments (two directions of collapse and one of expansion). Halos in filaments therefore acquire spin parallel to the filament, as matter collapses and rotates in the plane perpendicular to the filament (Pichon et al. 2011, Codis et al. 2012). N-body and hydrodynamic simulations have confirmed this result for low-mass halos ($M \lesssim 10^{12}$ $M_\odot$), while finding that mergers align high-mass halo spins perpendicular to filaments by converting motion along the filament into spin (Bailin & Steinmetz 2005, Aragón-Calvo et al. 2007, Hahn et al. 2007a, Codis et al. 2012, Trowland et al. 2013, Aragon-Calvo & Yang 2014, Dubois et al. 2014, Codis et al. 2015, Ganeshaiah Veena et al. 2018, Wang & Kang 2018, Wang et al. 2018).

Observations probe the spin of baryons within the galaxy rather than the spin of dark matter in the host halo. Initially, the baryons and dark matter share the same angular momentum distribution and the baryons conserve angular momentum as they collapse, creating a rotation-supported disk (Fall & Efstathiou 1980, Blumenthal et al. 1986, Mo et al. 1998). The size and profile of the baryonic disk, as computed from the angular momentum profile and dimensionless spin λ of halos in N-body simulations, are roughly consistent with observations (Fall 1983, Bullock et al. 2001). This simple picture cannot be correct in detail, however, since the baryons are subject to different physical processes than the dark matter, including dissipation, disk instabilities, and feedback-driven outflows (Danovich et al. 2015). These processes lead to misalignments between the spins of the dark matter and the baryons (van den Bosch et al. 2002, Bett 2012). As a result, the mass-dependent alignment transition found in simulations, which typically use gravity-only N-body codes (but see Dubois et al. 2014, Codis et al. 2015, Wang et al. 2018; for spin-filament alignments in hydrodynamic simulations), may not be present in observations or hydrodynamic simulations of galaxy alignments.

Alignments between galaxy spins and large-scale structure have been measured using imaging to infer the galaxy's inclination and spin axis from its the axis ratio and position angle. At $z \sim 0$, studies have found suggestive but ultimately not significant evidence for correlations between the chirality of neighboring galaxy spins (Slosar et al. 2009, Lee 2011, Andrae & Jahnke 2011). Studies of alignments between galaxy spins and large-scale structure have reached conflicting conclusions. Early studies from small galaxy samples in photographic plate surveys yielded weak and conflicting results (Gregory et al. 1981, Dekel 1985, Cabanela & Aldering 1998; and references therein). More recent results from larger samples suggested that spiral galaxies are aligned along the intermediate axis of the tidal tensor, in accord with predictions from tidal torque theory (Lee & Pen 2002, Lee & Erdogdu 2007), and are therefore aligned perpendicular to filaments (Jones et al. 2010, Zhang et al. 2015). However, a number of studies within the past few years have found little support for

tidal torque theory predictions and instead suggest that low-mass spiral spins are parallel to filaments while higher mass elliptical or lenticular spins are perpendicular to filaments (Tempel et al. 2013, Tempel & Libeskind 2013, Pahwa et al. 2016).

Alignments between galaxy spins are of particular interest as they are a major source of systematic error for weak lensing shear measurements, particularly for upcoming missions such as LSST (LSST Science Collaboration et al. 2009), WFIRST (Spergel et al. 2015) and EUCLID (Laureijs et al. 2011) that aim to measure the dark energy equation of state (Bridle & King 2007, Kirk et al. 2012). For disk galaxies, galaxy ellipticities arise from galaxy spins and are quadratic in the tidal field under tidal torque theory (Lee & Pen 2000, Catelan et al. 2001), while for elliptical galaxies, ellipticity arises directly from stretching by tidal fields and is linearly related to the tidal field (Hirata & Seljak 2004). As a result, measurements of alignments between galaxy spins and the surrounding tidal field or large-scale structures (clusters, filaments, sheets and voids) can inform physical models of intrinsic alignments, particularly for disk galaxies, whose intrinsic alignment remains poorly constrained (Hirata et al. 2007, Mandelbaum et al. 2011).

We measure spin-filament alignments using galaxy spins determined from integral-field kinematics rather than from galaxy imaging. Our method is complementary to imaging-based spin measurements, as it has very different sources of systematic error. Galaxies often have low-surface brightness features such as spiral arms or tidal tails, and therefore the galaxy shape may depend strongly on the measurement method, e.g. which isophote is used (see Fig. 1 in Kirk et al. 2015). Similarly, galactic bulges can bias shape measurements even for very late-type galaxies (Andrae & Jahnke 2011). While careful modelling including bulge/disk decomposition can alleviate this bias (e.g. Tempel et al. 2013, Tempel & Libeskind 2013), using kinematics to measure galaxy spin eliminates the need for complex models of galaxy morphology and their associated uncertainty.

In this paper, we measure the alignment between filaments identified in the SDSS Main Galaxy Sample and galaxy spins measured from MaNGA kinematics. We use the filament catalog of Chen et al. (2016), which finds filaments as ridges in the density field using the subspace-constrained mean-shift algorithm (Section 5.2). We find no preference for spin-filament alignments in our overall sample of $\sim$2700 galaxies, and we validate our results by finding similar alignments between galaxies and the Bisous model filaments of Tempel et al. (2014) (Section 6.6). We compare our results to spin-filament alignments in hydrodynamical simulations by measuring the mass-dependence of the alignment signal, and find 2-3σ tension when using spins measured from the stellar continuum, but no tension when using spins measured from the Hα emission line (Section 3.4). Finally, we compare our results to previous findings and conclude in Section 6.8.

In this paper we use a flat ΛCDM cosmology with $\Omega_m = 0.3$ and $h = 0.7$. We convert all masses to $M_\odot$ for inter-comparison between observations and simulations.

3.2 Methods and Data

3.2.1 Filament finder

A variety of methods have been used to find filaments in observations and simulations, including approaches identifying filaments as eigenvectors of the deformation tensor (Hahn et al. 2007a, Jasche et al. 2010), velocity shear tensor (Libeskind et al. 2013), or Hessian of the density field (Aragón-Calvo et al. 2007); identification of filaments as ridges in the density field (Sousbie et al. 2008, Chen et al. 2015); and searches for cylindrical arrangements of galaxies (Tempel et al. 2014). For a comprehensive overview, see Cautun et al. (2014).

We use the publicly available *Cosmic Web Reconstruction* filament algorithm[1] (Chen et al. 2016) to identify filaments in the SDSS Main Galaxy Sample. This filament finder identifies filaments as curves in two-dimensional (α, δ) slices of width $\delta z = 0.005 \sim 20$ Mpc. This yields a well-defined orientation for every point on the filament and makes it easy to cross-correlate with the spin of nearby galaxies. The filament finder is explained in detail in Chen et al. (2015), so we only provide a brief description here. Our filament catalog differs slightly from the publicly available catalog of Chen et al. (2015), as it extends to lower redshift and uses slightly different thresholding to remove noisy filaments.

The filament finder operates on a smoothed density field created from the positions of galaxies in the SDSS Main Galaxy Sample (Blanton et al. 2005) and the LOWZ and CMASS samples from BOSS (Alam et al. 2015), with a redshift-dependent Gaussian smoothing kernel that ranges between 5 and 10 Mpc (Fig. 6 in Chen et al. 2016). It identifies filaments as density ridges of the smoothed density field, or local maxima along the second eigenvector of the Hessian of the density field.

The filament finder uses two-dimensional slices of width $\delta z = 0.05$ ($c\delta z = 1500$ km s^{-1} ~ 20 Mpc); in each slice, it finds filaments in an equirectangular projection of equatorial coordinates (α, δ) using only galaxies in the North Galactic Cap (Figure 3.1). We find filaments between $z = 0.02$ and $z = 0.15$, with the lower limit set by the sparsity of SDSS galaxies at $z < 0.02$ and the upper limit set by the maximum redshift of MaNGA galaxies ($z = 0.15$). At these redshifts the filament finder primarily uses galaxies from the Main Galaxy Sample. We eliminate galaxies in the 10% least dense environments, defined using the distance to the 30th-nearest neighbor. This eliminates noisy filaments from very low-density regions without removing too many filaments. Varying the thresholding criteria does not qualitatively change the results in Table 3.1.

We define the filament orientation at each point as the first principal component of the covariance matrix of the positions of the ten nearest neighbor points. We estimate the uncertainty on the filament directions at each point by measuring the local filament orientation for 100 bootstrap resamples of the filament catalog.

Filaments are identified in 2D rather than 3D for ease of interpretation: collapsing along the line of sight eliminates spurious filaments created by redshift-space distortions and allows us to better model the strong redshift dependence of galaxy density, which requires a

[1] https://sites.google.com/site/yenchicr/

redshift-dependent smoothing length (Chen et al. 2016). Furthermore, previous work measuring three-dimensional spin-filament alignments has found that line of sight biases in both galaxy spins and filaments creates strong spurious alignment signals which must be corrected (Tempel et al. 2013, Tempel & Libeskind 2013). From simulations, we expect that using 2D rather than 3D filaments reduces our signal by $\sim 40\%$ (Appendix 3.B); thus we believe the moderate loss in signal is worth the substantial reduction in systematic errors.

In Figure 3.1 we plot the MaNGA galaxy sample (with $z > 0.02$ and distance to filament $d_F < 40$ Mpc) and the *Cosmic Web Reconstruction* filaments in four redshift slices: $z = 0.02 - 0.025$, the lowest-redshift slice, and the slices containing the three quartiles of the redshift distribution, $z = 0.025 - 0.03$, $0.035 - 0.04$ and $0.055 - 0.06$. In Figure 3.1, most galaxies are clearly closest to a single filament, indicating that confusion between filaments will not contribute significantly to noise in the measurement.

To check our results, we measure alignments with the Tempel et al. (2014) filament catalog[2], which was also derived from galaxies in the SDSS Main Galaxy Sample, with $0.009 < z < 0.155$. Tempel et al. (2014) use a very different method from Chen et al. (2015): they find filaments using the Bisous model, a marked point process model which fits the galaxy data to a filamentary network composed of connected cylinders of fixed width. They find filaments in three dimensions, suppressing peculiar velocities by estimating the velocity dispersions for galaxy groups. We measure alignments using galaxies within 20 h^{-1} Mpc of filaments and with a velocity-corrected distance from the Tempel et al. (2014) catalog, yielding a sample of 3028 galaxies. For each galaxy, we consider its alignment with the plane-of-sky projection of the nearest Tempel et al. (2014) filament. We compare the Tempel et al. (2014) and Chen et al. (2015) filaments in Figure 3.1; Tempel et al. (2014) identify significantly smaller-scale filaments, but on larger scales both methods recover similar filaments. Despite the substantial methodological differences between the two filament finders, we find largely similar alignments (Section 6.6).

3.2.2 MaNGA galaxies

Mapping Nearby Galaxies at Apache Point Observatory (MaNGA) is an integral-field survey that aims to obtain spectra of 10,000 nearby galaxies (Bundy et al. 2015). It began in July 2014 as part of SDSS-IV (Blanton et al. 2017) and is planned to continue until 2020. MaNGA uses the 2.5-m SDSS telescope at Apache Point Observatory in New Mexico (Gunn et al. 2006) and the dual fiber-fed BOSS spectrographs (Smee et al. 2013), but rather than allocating a single fiber per galaxy like previous SDSS surveys, each plate contains 17 pluggable Integral Field Units, each of which consists of hexagonal bundles containing between 19 and 127 fibers with typical spatial resolution of 2.5" or 1.8 kpc at $z = 0.03$ (Drory et al. 2015). The dual spectrograph design enables a wavelength coverage of 3600–10000 Å with a velocity resolution of 70 km s^{-1} (Smee et al. 2013). Typical exposure times of 3 hours

[2] Available on Vizier, http://vizier.cfa.harvard.edu/viz-bin/VizieR?-source=J/MNRAS/438/3465, including a filament catalog; catalog of filament points; and catalog of all galaxies used to construct the filament catalog and their velocity-corrected distances.

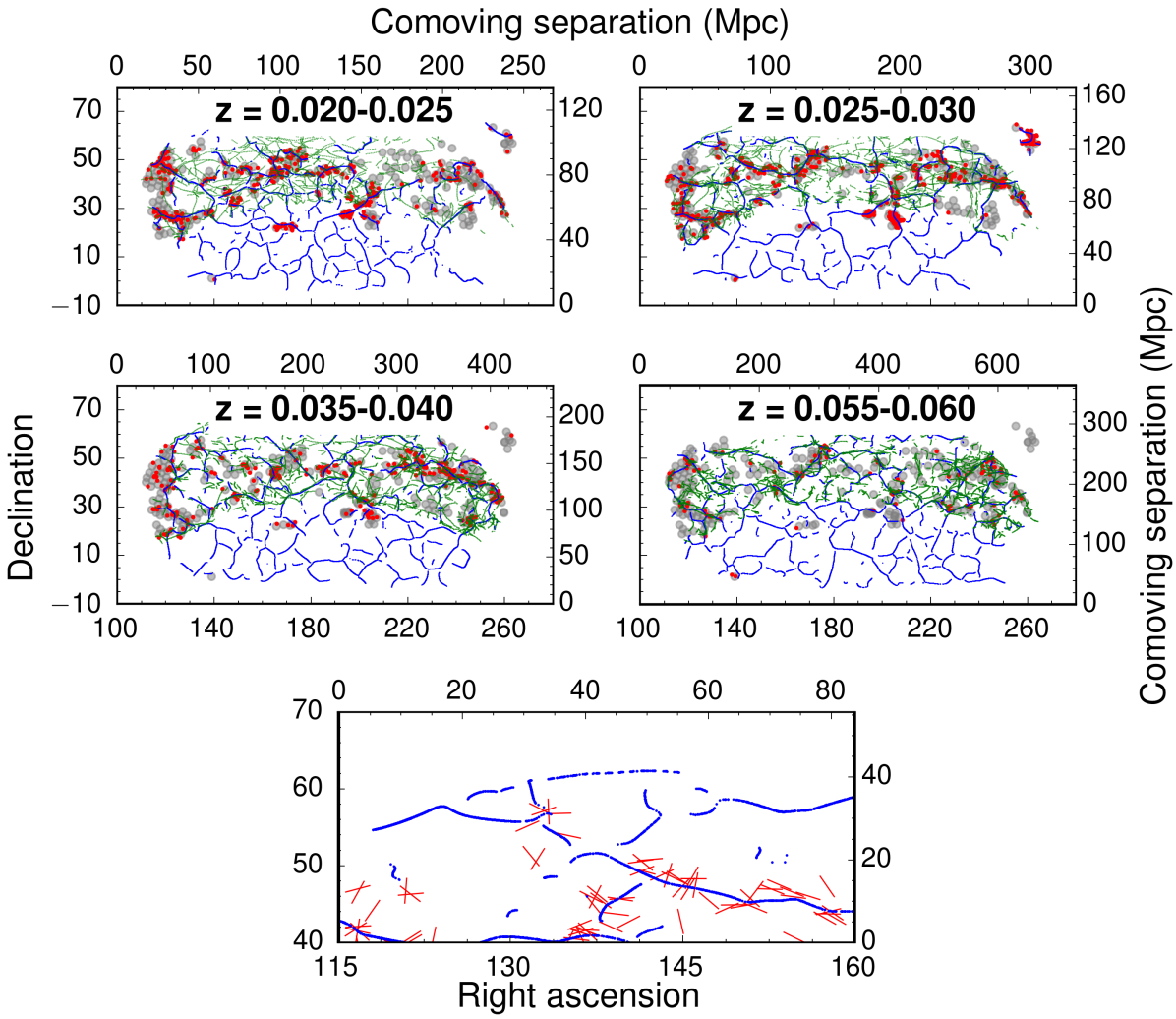

Figure 3.1: *Upper four panels:* MaNGA galaxies (red) located within 40 Mpc of *Cosmic Web Reconstruction* filaments (blue) and Tempel et al. (2014) Bisous filaments (green). Slices were chosen as the lowest redshift slice with filaments ($z = 0.02$) and the three quartiles of the MaNGA galaxy redshift distribution ($z = 0.027$, 0.036, and 0.052). Gray circles indicate MaNGA plates released with MPL-6. *Lower panel:* Comparison between galaxy spins (red lines) and *Cosmic Web Reconstruction* filaments (blue lines) for a section of the sky at $z = 0.025 - 0.03$.

ensured S/N of 5 at the outskirts of targeted galaxies, and much greater towards the center (Law et al. 2015). Spectrophotometric calibration is accurate to $< 5\%$ (Yan et al. 2016b) and the data reduction pipeline is described in Law et al. (2016).

The MaNGA targeting sample consists of 10,000 galaxies with $0.01 < z < 0.15$ (median $z \sim 0.03$). The sample was chosen to have a flat number density distribution in absolute i-band magnitude M_i while maximizing the spatial resolution and ensuring IFU coverage to a few times the half-light radius R_e (Yan et al. 2016a). As a result, stellar mass is highly correlated with redshift for the MaNGA sample, since galaxies of a given mass (and thus radius) are preferentially targeted at a redshift where the IFUs cover a few R_e (Figure 3.2). The double-peaked redshift-mass distribution is a result of the two-tiered MaNGA selection process, consisting of the Primary sample with coverage to $1.5R_e$ and the Secondary sample with coverage to $2.5R_e$. Galaxies are assigned to plates via a tiling algorithm that is unbiased with respect to environment, and to IFUs in a way that maximizes the number of galaxies covered to the appropriate radius (1.5 R_e for Primary sample and 2.5 R_e for the Secondary sample).

We use the MPL-6 data release of MaNGA with v2_3_1 of the Data Reduction Pipeline and v2.1.3 of the Data Analysis Pipeline. MPL-6 contains 4687 galaxy data cubes observed between March 2014 and July 2017, of which 70 are repeat observations. We subsequently reduce our sample to 2736 galaxies via a variety of quality cuts. We remove 85 galaxies with the the CRITICAL DRP3QUAL maskbit set, which indicates a variety of problems ranging from unmasked cosmic rays to IFUs partially falling out of the plate; 426 galaxies targeted as part of ancillary programs, which lack well-defined selection weights; 393 galaxies with $z < 0.02$; and 478 galaxies lying beyond the 40 Mpc radius of influence for galaxy-filament alignments found in Chen et al. (2019). Finally, we remove galaxies with poorly measured spins (see Section 3.2.3): 19 galaxies lacking a sufficient number of points to fit a spin; 170 galaxies with multiple galaxies inside the IFU (Figure 3.4); and 858 galaxies with position angle error $> 5°$, which we find by visual inspection to generally have poorly-defined spins.

We weight each galaxy to create a volume-limited sample (Wake et al. 2017) that is appropriate to compare to simulations. Specifically, we weight each galaxy by the "esrweights" (Equation A12 in Wake et al. 2017), the effective volume over which it could have been observed. The weights are necessary because MaNGA is not a volume-limited sample; the flat distribution in M_i leads to to biases towards higher luminosity at fixed mass, biasing galaxy colors and inclinations (Wake et al. 2017). All results in Sections 6.6 and 3.4 use weighted mean dot products and bootstrap resampling to compute the standard error of the weighted means.

The MaNGA sample is complete to $\log(M_\star/M_\odot) = 9.61$ for the Secondary sample and $\log(M_\star/M_\odot) = 9.10$ for the Primary sample (Wake et al. 2017); thus, we require $\log(M_\star/M_\odot) > 9.6$ for comparison to mass-dependent alignment in simulations (Section 3.4), limiting this comparison to 2551 galaxies. Additionally, the Secondary sample is incomplete for highly inclined galaxies slightly above $\log(M_\star/M_\odot) = 9.61$ (Wake et al. 2017), although such galaxies only constitute a small portion of the sample in the lowest mass bin.

Gross galaxy properties such as absolute magnitude, color, stellar mass, and photometric

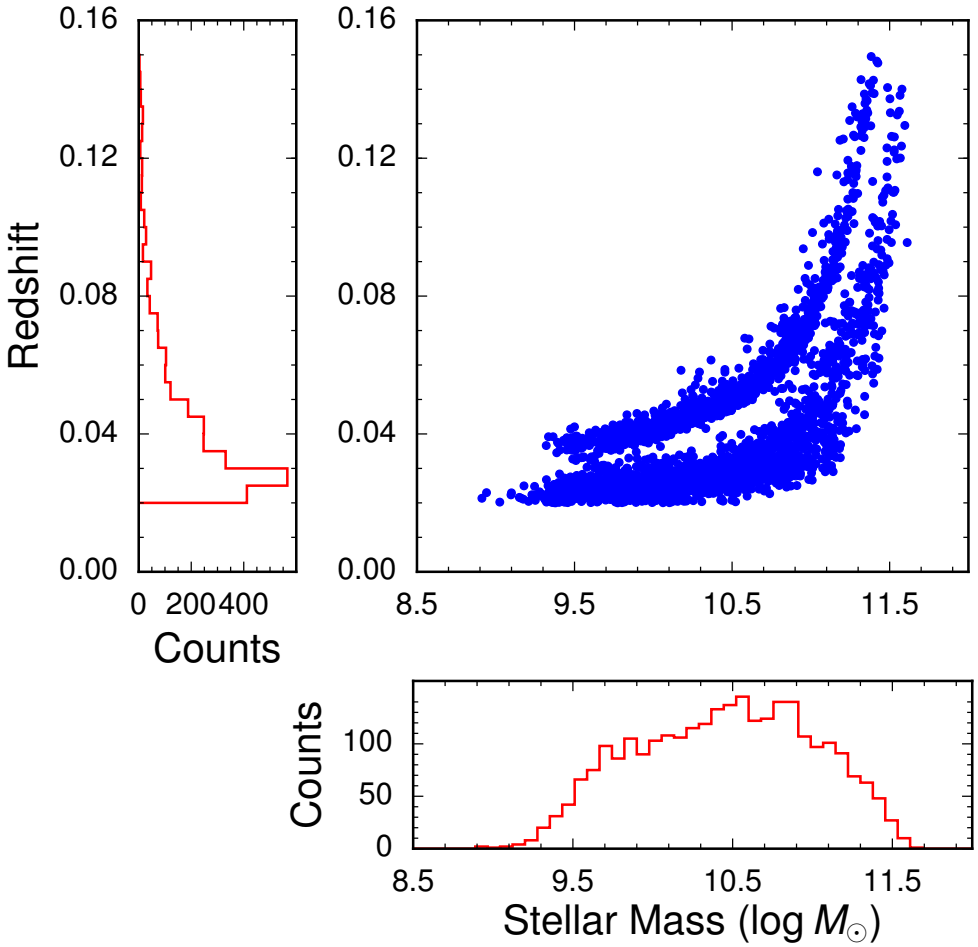

Figure 3.2: Redshift (top) and stellar mass (bottom) distributions of the MaNGA sample of 2736 galaxies (selected according to criteria in Section 3.2.3).

shape are extracted from the MaNGA targeting catalog, v1_0_1 of the NASA-Sloan Atlas (Blanton et al. 2011). This catalog is superior to the SDSS catalog for photometry of bright extended galaxies. We use magnitudes and stellar masses from elliptical Petrosian photometry, recommended as the most reliable photometry in the catalog[3]. We use the Sersic photometry for axis ratios and photometric position angles. The stellar masses and star formation rates are calculated using the K-CORRECT code (Blanton et al. 2003) with a Chabrier (2003) initial mass function. In Figure 3.2, we show the redshift and mass distribution of the final sample of 2736 galaxies.

We use Galaxy Zoo for morphological classification (Lintott et al. 2011), matching each MaNGA galaxy to the nearest Galaxy Zoo source within 0.5". The Galaxy Zoo catalog gives a probability that each galaxy is a spiral (clockwise or counter-clockwise), elliptical, edge-on,

[3]See http://www.sdss.org/dr13/manga/manga-target-selection/nsa/

merger or unknown morphology. To study the morphological dependence of spin-filament alignments, we only use galaxies with a $> 50\%$ probability of any single classification. Edge-on galaxies are defined as galaxies with axis ratio $r < 0.3$ rather than using Galaxy Zoo, since Galaxy Zoo classifies any galaxy with spiral structure as a spiral even if it is nearly edge-on. Our final sample therefore contains 1039 elliptical galaxies, 676 spiral galaxies, and 344 edge-on galaxies, with the rest unclassified.

We use the stellar velocity maps produced by the Data Analysis Pipeline (DAP) for MPL-6 (Westfall et al., in prep), which uses the penalized-pixel fitting method (pPXF) (Cappellari & Emsellem 2004) to determine kinematic parameters. For the spectrum in each spaxel, the DAP first fits the stellar continuum using the MILES stellar library (Sánchez-Blázquez et al. 2006) and masking emission lines. Emission lines are subsequently fit, fixing the stellar continuum to the previously-determined best-fit values.

To check the robustness of our results, we measure galaxy spins from both the stellar continuum and the Hα emission line velocity maps. We apply the same fitting methods (Section 3.2.3) to both velocity maps. These measurements trace different physical components of the galaxy: the stellar continuum traces the stars while the emission line traces the gas.

3.2.3 Galaxy spins

We determine the spin vector for each galaxy by measuring the kinematic position angle using integral-field data from the MaNGA survey. Specifically, the plane-of-sky projection of the spin vector is perpendicular to the kinematic position angle (Figure 3.3). For each galaxy we determine a single global position angle (and thus spin direction) from the full datacube. We apply the FIT_KINEMATIC_PA routine (Krajnović et al. 2006) to determine the kinematic position angle for each galaxy from the stellar velocity maps, using velocities from the unbinned spaxels (see Appendix 3.A for further details). Our method is necessarily two-dimensional, consistent with our two-dimensional filament finder. In accordance with the two-dimensional nature of our measurement, hereafter we refer to the plane-of-sky projection of the spin as the galaxy spin vector. While the three-dimensional spin could be estimated using the galaxy's axis ratio to find the inclination (Haynes & Giovanelli 1984), this method requires an estimate of the galaxy's intrinsic thickness; assumes that the galaxy's shape can be approximated by an oblate spheroid, which may not be valid for elliptical galaxies; and could be biased by the isophote used or the presence of a galactic bulge (Andrae & Jahnke 2011, Kirk et al. 2015). Moreover, estimating the three-dimensional spin from the galaxy's shape necessarily leads to anisotropic errors between the plane of sky and the line of sight and potentially an inhomogeneous distribution of inclinations (e.g. Tempel et al. 2013, Tempel & Libeskind 2013).

We show 6 randomly selected fits in Figure 3.3. The output of FIT_KINEMATIC_PA agrees well with the position angle one would identify by eye. However, FIT_KINEMATIC_PA fails in cases where there are multiple kinematically-distinct galaxies in the IFU. In these cases, FIT_KINEMATIC_PA spuriously identifies the line connecting the galaxies as the position angle (Figure 3.4). We identify these cases by searching

for galaxies with multiple SDSS $r < 20$ sources located within the IFU and visually inspect each image to distinguish contaminants from foreground stars, background galaxies, and errors in SDSS photometry. We find and exclude 171 galaxies with spurious fits due to multiple kinematically-distinct galaxies in the IFU.

Visual inspection shows that the velocity maps become increasingly noisy, with poorly defined rotation, when $\sigma_{\rm PA} > 5^\circ$. As a result, we remove these 858 galaxies from our measurement. Using a stricter cut of $\sigma_{\rm PA} < 3^\circ$ changes the results presented in Table 3.1 by $\lesssim 1\sigma$.

In the bottom panel of Figure 3.1, we plot galaxy spin vectors and filaments for a small region of the sky at $z = 0.025 - 0.03$ to illustrate the alignment measurement. We are searching for a weak alignment identifiable statistically but not visually.

In Figure 3.5, we show that the measurement errors on the filaments (blue) dominate the errors on the galaxy position angles (red). We also plot the distribution of stellar minus emission line position angle; since this dispersion is the quadrature sum of the measurement error on the position angle and the true dispersion between the stellar and emission line spins, it provides an upper bound on the position angle error. This dispersion is still smaller than the filament error, showing that the filament error must be greater than the position angle error.

3.2.4 Mock spins and filament catalogs from hydrodynamical simulations

We compare our results to galaxy alignments measured in two publicly available cosmological hydrodynamical simulations, MassiveBlack-II[4] (Khandai et al. 2015) and Illustris-1[5] (Vogelsberger et al. 2014, Nelson et al. 2015). Since the spin-filament alignment signal is quite subtle, we require large box hydrodynamical simulations ($L \gtrsim 100$ Mpc).

MassiveBlack-II is a cosmological simulation run using the smoothed particle hydrodynamics code GADGET in a 100 h^{-1} Mpc box with $\Omega_m = 0.275$, $h = 0.704$, and $\sigma_8 = 0.816$ (Khandai et al. 2015). The simulation contains 2×1792^3 particles, with dark matter particle mass of $1.1 \times 10^7 h^{-1} M_\odot$ and gas particle mass $2.2 \times 10^6 h^{-1} M_\odot$. MassiveBlack-II includes subgrid models for star formation and black hole feedback. Star formation occurs according to the multiphase model of Springel & Hernquist (2003), and young stars and supernovae provide feedback by heating the Gas is accreted onto black holes following Bondi accretion, limited to twice the Eddington accretion rate, and 5% of the energy radiated by the accreting black hole is deposited as feedback. Halos are identified using a friends-of-friends algorithm with linking length $b = 0.2$, and subhalos are identified using SUBFIND. Halos and subhalos are required to have at least 40 dark matter and gas particles; therefore, the stellar mass limit of the simulation is $1.26 \times 10^8 M_\odot$.

In MassiveBlack-II, the spin for each galaxy is defined as the unit stellar angular momen-

[4] http://mbii.phys.cmu.edu/

[5] http://www.illustris-project.org/data/

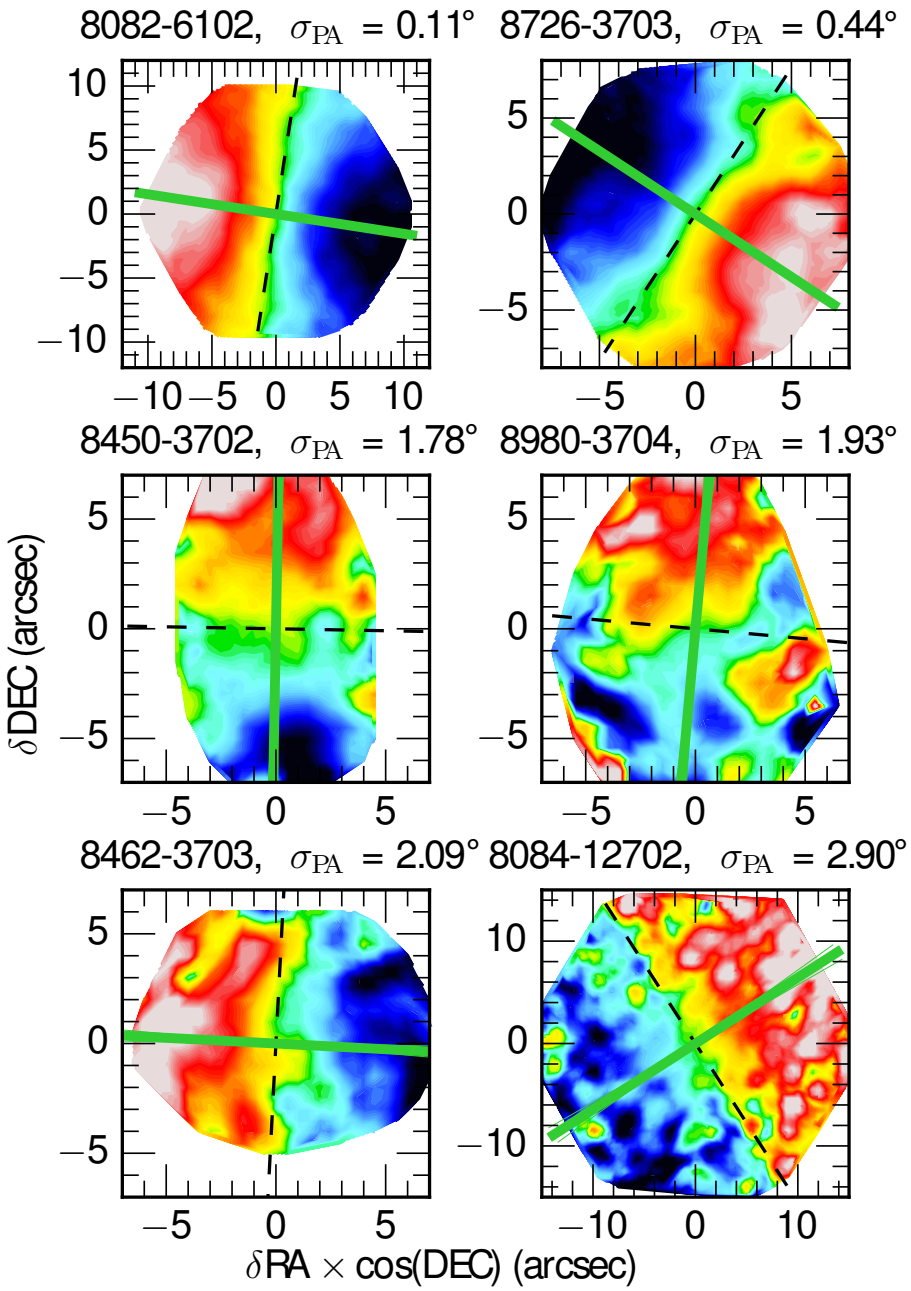

Figure 3.3: 6 randomly selected galaxies with stellar velocity maps and FIT_KINEMATIC_PA fits. The best-fit kinematic position angle is the thick green line and the spin vector is the dashed black line. The thin green lines (often obscured by the thick green line) show the 1-σ uncertainty on the position angle. The title gives the plate and IFU ID uniquely identifying each observation and the error on the PA in degrees.

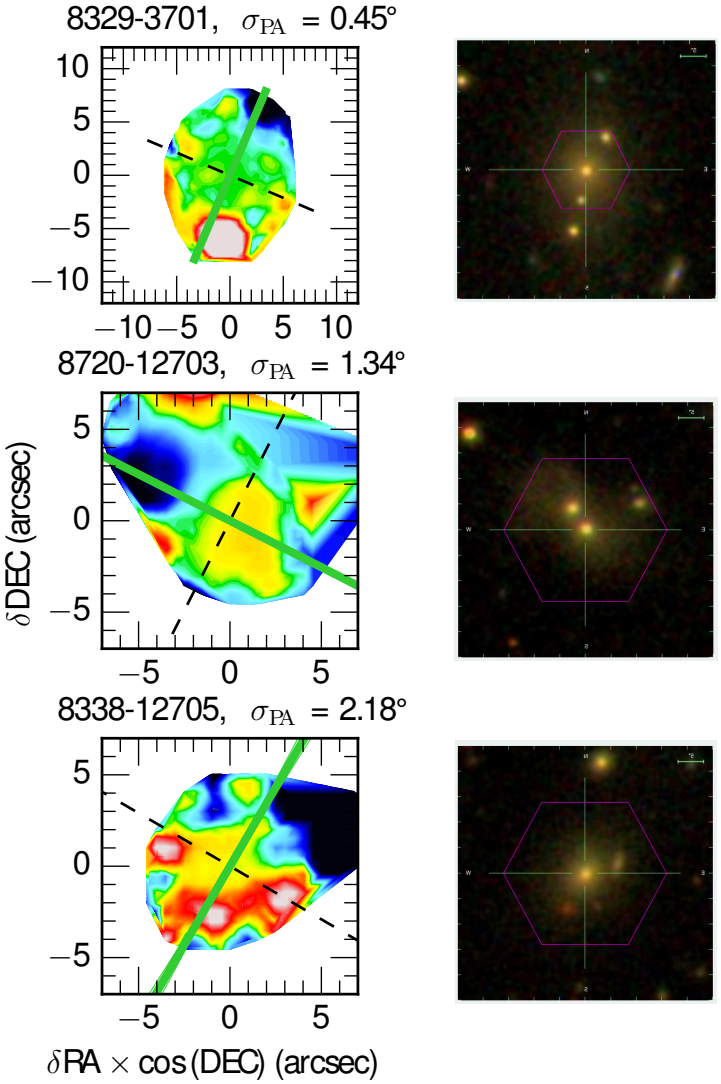

Figure 3.4: 3 randomly selected cases with multiple galaxies inside the IFU. Panels on the left show the stellar velocity maps and FIT_KINEMATIC_PA fits. Panels on the right show the SDSS image with the MaNGA IFU overlaid. Although the fitting errors on these galaxies are formally smaller than the cutoff for poorly measured spins (error $> 5°$), it is clear from comparison to the SDSS images that the fit is spurious due to multiple galaxies in the IFU.

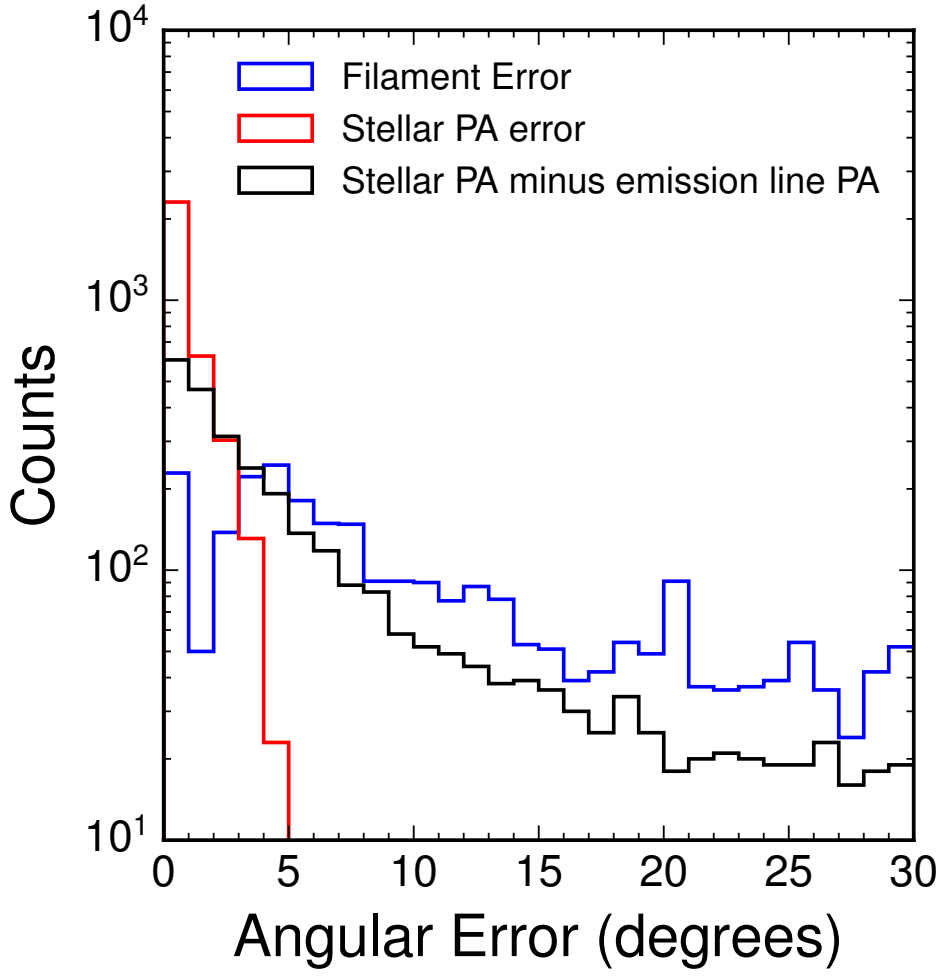

Figure 3.5: Comparison between the error on the filament angle nearest to each galaxy (blue), the error on the stellar position angle (red), and the dispersion between the stellar position angle and the emission line position angle (black).

tum vector. Galaxy spins are only computed for subhalos with at least 1000 dark matter and star particles. This corresponds to a stellar mass limit of $\log(M_\star/M_\odot) = 9.5$ for the sample with measured spins; thus, the spin subsample is complete for the mass range of the MaNGA sample ($\log(M_\star/M_\odot) > 9.6$), confirming the validity of comparing data to simulations over this mass range. We also consider alignments between filaments and gas spins in MassiveBlack-II, where gas spins are computed for subhalos with at least 1000 gas particles.

Illustris-1 is run using the moving-mesh code AREPO in a 75 h^{-1} Mpc box with 1820^3 gas and dark matter particles each for a dark matter particle mass of $6.3 \times 10^6 M_\odot$ and a gas particle mass of $1.3 \times 10^6 M_\odot$. Subhalos are required to have at least 20 particles[6]; therefore, the stellar mass limit is $2.6 \times 10^7 M_\odot$. The cosmological parameters are $\Omega_m = 0.2726$, $h = 0.704$, and $\sigma_8 = 0.809$. The subgrid physics is described extensively in Vogelsberger et al. (2013) and is similar to the subgrid physics in MassiveBlack-II, but somewhat more elaborate: Illustris-1 uses variable wind speeds and mass loading in the Springel & Hernquist (2003) galactic wind model, and Illustris-1 includes radio-mode AGN feedback as well as quasar-mode feedback.

Halos in Illustris-1 are identified using a friends-of-friends algorithm with linking length $b = 0.2$ on the dark matter particles, and subhalos are subsequently identified using SUBFIND. For both MassiveBlack-II and Illustris, the masses quoted in this paper (both dark matter and stellar) are defined as the total mass of all particles bound to a given SUBFIND halo. As in MassiveBlack-II, subhalo spin is defined as the unit stellar angular momentum vector (Zjupa & Springel 2017), summing over all star particles within twice the stellar half-mass radius.

Angular momenta are only calculated for subhalos with more than 300 dark matter particles, yielding a stellar mass limit of $3.8 \times 10^8 M_\odot$ for halos with the cosmic baryon fraction. Therefore, as for MassiveBlack-II, it is valid to compare simulation and data alignments for MaNGA galaxies with $\log(M_\star/M_\odot) > 9.6$.

Since we measure filaments using *Cosmic Web Reconstruction* in two dimensions, some filaments in our catalogs may just be cuts through sheets lying perpendicular to the plane of the sky. Since halo alignments with sheets may be different from halo alignments with filaments (e.g. Aragón-Calvo et al. 2007; find a mass-dependent transition from alignment to anti-alignment with filaments, but mass-independent alignment between halos and sheets), our alignment measurements are not directly comparable to three-dimensional filament alignment measurements in simulations. Therefore, we compare our measurement to mock observations in MassiveBlack-II and Illustris-1 reproducing the two-dimensional filaments used in the observational work.

For both Illustris-I and MassiveBlack-II, we create a mock filament catalog for each of the 26 *Cosmic Web Reconstruction* $\Delta z = 0.005$ slices between $z = 0.02$ and $z = 0.15$. These 26 filament catalogs allow us to create a mock galaxy-filament alignment measurement by matching the redshift distribution of the MaNGA galaxies. For each redshift slice, we select subhalos in descending order of mass to match the number density of SDSS galaxies in that

[6] http://www.illustris-project.org/data/docs/faq/#cat3

Table 3.1: *Cosmic Web Reconstruction* alignments for different subsamples

Sample	N	$\langle\cos\theta\rangle$	SE	Shuffle mean	σ from shuffle
All	2736	0.6452	0.0075	0.6406	0.61
$D_F < 0.6$ Mpc	684	0.6474	0.0144	0.6438	0.25
$0.6 < D_F < 1.4$ Mpc	684	0.6532	0.0148	0.6427	0.71
$1.4 < D_F < 3.0$ Mpc	684	0.6497	0.0146	0.6370	0.87
$D_F > 3.0$ Mpc	684	0.6257	0.0154	0.6365	-0.70
$M_\star < 10.02$	684	0.6601	0.013	0.6406	1.50
$10.02 < M_\star < 10.47$	684	0.6288	0.0120	0.6425	-1.14
$10.47 < M_\star < 10.87$	684	0.6350	0.0125	0.6407	-0.46
$M_\star > 10.87$	684	0.6500	0.0147	0.6358	0.97
$u - r < 1.70$	684	0.6562	0.0139	0.6417	1.04
$1.70 < u - r < 2.09$	684	0.6381	0.0149	0.6409	-0.19
$2.09 < u - r < 2.35$	684	0.6630	0.0130	0.6354	2.12
$u - r > 2.35$	684	0.6072	0.0168	0.6373	-1.79
elliptical	1039	0.6408	0.0130	0.6392	0.12
spiral	676	0.6423	0.0147	0.6399	0.16
edge-on	344	0.6239	0.0186	0.6392	-0.82

Note. — MaNGA spin-*Cosmic Web Reconstruction* filament alignments for the entire sample and sub-samples split by distance to filament (D_F), stellar mass (in units of $\log M_\odot$), $u - r$ color, and morphology. $\langle\cos\theta\rangle$ is the mean dot product between the unit spin vector and the unit filament vector. SE is the standard error of the mean, calculated using 50000 bootstrap resamples of the data. We measure the expectation for random alignments using 50000 shuffles of the data, and compute σ, the deviation between the data and the randoms in units of the standard error.

redshift slice. We define filaments using subhalos rather than halos or dark matter particles because subhalos are generally taken as proxies for galaxies in e.g. comparisons to the galaxy stellar mass function (Khandai et al. 2015, Vogelsberger et al. 2014). Since the completeness of the SDSS Main Galaxy Sample is $> 90\%$ (Strauss et al. 2002), this procedure yields a mock sample representative of MGS. We move the subhalos into redshift space and divide the box into 7 slices along the z axis (width $14h^{-1}\,\mathrm{Mpc} = 20$ Mpc), finding filaments in two dimensions in each slice following the same method as in the data. We generate the smoothed density field from subhalos in the 90% densest environments, match the smoothing bandwidth at each redshift to the bandwidth used in the data, and identify the filament direction using local PCA. We ignore the periodic boundary conditions of the box when finding filaments. With these 26 filament catalogs we can then make a mock observation of galaxy-filament alignment by randomly assigning each galaxy in the simulation to one of the 26 catalogs following the redshift distribution of the data (see Section 3.4 for further details).

3.3 Galaxy-filament alignments of entire sample

After the quality cuts described above and the redshift cut ($0.02 < z < 0.15$), we measure alignments with a sample of 2736 galaxies. We measure alignment using the mean dot product between the unit filament vectors and the unit galaxy spin vectors. A dot product of 1 indicates perfect alignment, 0 indicates perfect anti-alignment, and $2/\pi = 0.6366$ (i.e. the average value of $\cos\theta$ over the range 0 to π) indicates random alignment. All mean dot products are defined as weighted means using the MaNGA weights defined to recover a volume-limited sample (Wake et al. 2017). Error bars are defined for the weighted means using 50000 bootstrap resamples of each galaxy subsample. We compare the measured alignment to a random signal generated from 50000 shuffles of the galaxy and filament catalogs; if there are anisotropies in the galaxy and filament catalogs, the expectation for random alignments will deviate from $2/\pi$. In fact, deviations from $2/\pi$ are modest for all subsamples.

We find no evidence for alignments between galaxy spins and filaments, with a mean dot product of 0.6452 ± 0.0075, an 0.61σ deviation from the shuffled dot product of 0.6406.

In Table 3.1, we split the sample in several ways: four equal-sized groups in each of distance to nearest filament D_F, stellar mass, and $u - r$ color; and spiral, elliptical, and edge-on galaxies. We do not find significant alignments for any of the groups, nor do we find significant linear trends with any of these properties.

We also measure alignments with the Bisous model filaments of Tempel et al. (2014), and find similar results (Table 3.2). While the overall alignments are stronger for the Bisous filaments (1.16σ versus 0.61σ), in neither case are they statistically significant, and we do not find statistically significant alignments with any subsample in mass, color, distance to filament, or morphological type for the Tempel et al. (2014) filaments. The similar alignment results with the two filament finders, despite the drastic methodological differences between the Bisous model and the *Cosmic Web Reconstruction* filaments, bolster our conclusion that

the MaNGA galaxies lack significant alignments with filaments.

Figure 3.6 shows that the distribution of $\cos\theta$ is fully consistent with random alignments. The scatter in $\cos\theta$ is dominated by intrinsic scatter in the alignments between galaxy spins and filaments, rather than measurement error from either the galaxy spins or the filament directions. By measuring the total scatter in the galaxy-filament alignments and subtracting the contribution from measurement error in quadrature, we can estimate the intrinsic scatter in alignments between galaxy spins and filaments. We estimate the contribution from measurement error by creating 50,000 realizations of the alignment dataset in which each filament or position angle is drawn from a Gaussian with standard deviation given by the reported measurement error. We find that the standard deviation of the resulting mean dot product (i.e. the scatter from measurement error) is 0.0044. The total standard error of 0.0075 is slightly higher than the standard error expected if the galaxies and filaments were entirely randomly aligned, 0.0074. Since the standard error cannot extend higher than ~ 0.0074, at this point the quadrature sum of the intrinsic scatter and measurement error may exceed the total scatter, and thus we can only place a lower bound on the intrinsic scatter, $\sigma_i \geq 0.0061$.

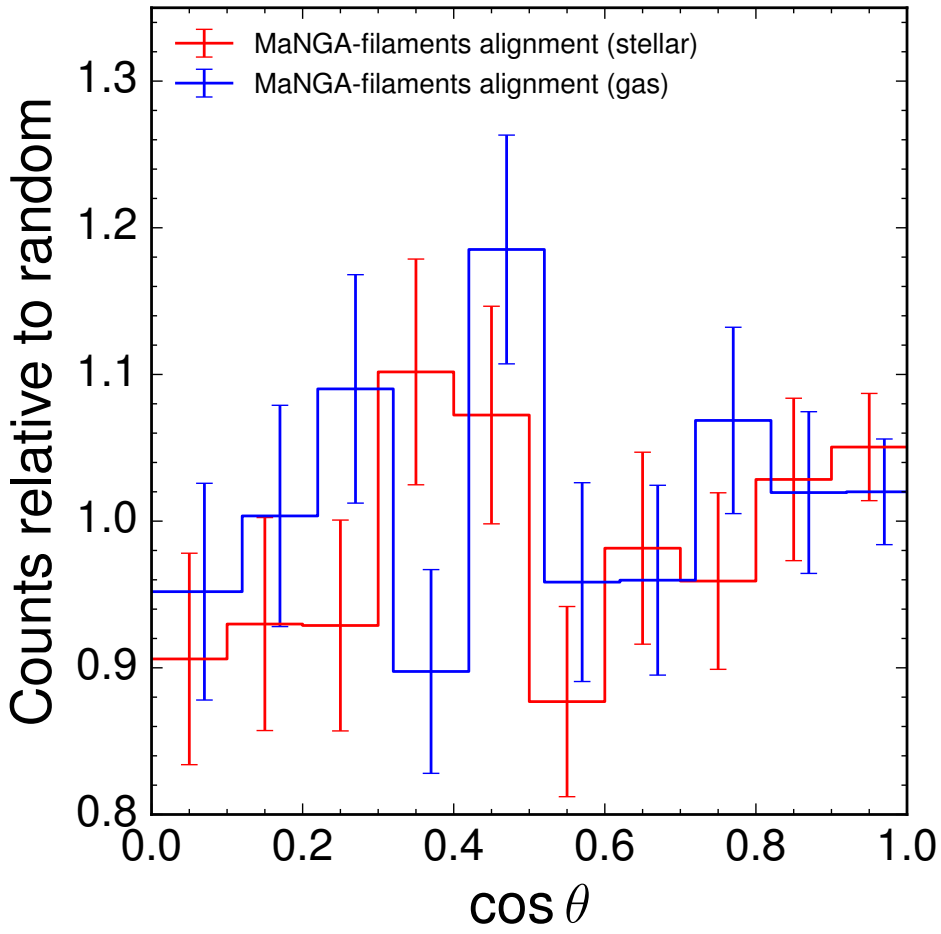

Figure 3.6: Distribution of $\cos\theta$ (angle between galaxy spin and *Cosmic Web Reconstruction* filament direction; red for stellar spins and blue for emission line spins) compared to random alignments. Each histogram is divided by the expectation for random alignments in that bin. Error bars are computed from Poisson statistics and the gas-filament alignment histogram is offset for clarity.

3.4 Mass-dependence of spin-filament alignments

Previous work has found that galaxy spin-filament alignments in N-body and hydrodynamical simulations are mass dependent, with lower mass galaxies showing alignment and higher mass galaxies showing anti-alignment (Bailin & Steinmetz 2005, Aragón-Calvo et al. 2007, Hahn et al. 2007a, Codis et al. 2012, Trowland et al. 2013, Aragon-Calvo & Yang 2014, Dubois et al. 2014, Codis et al. 2015). As a result of this mass dependence, it is possible that a significant alignment signal could be concealed by opposing contributions from high and low mass galaxies. Therefore, we study the mass dependence of the alignment signal and compare it to mass-dependent alignments in the MassiveBlack-II and Illustris-1 simulations. We attempt to mimic the construction of the spin and filament catalogs as closely as possible to present a fair and quantitative comparison between data and simulations.

We separate galaxies in the data and simulations into five bins of $\Delta \log M_\star = 0.5$, with the lower limits of each bin ranging from $10^{9.6} M_\odot$ to $10^{11} M_\odot$ (the lowest bin has $\Delta \log M_\star = 0.4$). We ignore galaxies less massive than $10^{9.6} M_\odot$ because MaNGA is incomplete below this mass, yielding a sample of 2551 MaNGA galaxies. While the individual stellar masses have relatively large uncertainties ($0.2-0.3$ decades; Blanton & Roweis 2007, Conroy 2013), each bin in stellar mass has > 100 galaxies and thus the mass uncertainties are much smaller than the bin sizes.

The redshift distribution of each stellar mass bin is quite different due to the strong correlation between redshift and stellar mass in the MaNGA sample (Figure 3.2). Furthermore, the number density of galaxies in the SDSS Main Galaxy Sample is a strong function of redshift, and thus the fidelity of recovery of the filaments will be better at low redshift than at high redshift. These effects may introduce a spurious mass-dependence into the alignment signal. The hydrodynamical simulation boxes are only 100 h^{-1} Mpc, so we cannot create a lightcone mocking the SDSS Main Galaxy Sample. Instead, we create 26 different realizations of the filament catalogs with filaments found using different subhalo densities (i.e. representing different galaxy densities), corresponding to the redshift slices of the filament catalog, as described in Section 3.2.4. In each realization, we find filaments in two dimensions as in the data. We assign each galaxy to one of the 26 different filament catalogs by drawing from the redshift distribution of the MaNGA galaxies at a given mass, weighted by the MaNGA volume weights. In this way, we assign each galaxy in the simulation to a unique filament, and measure the two-dimensional spin-filament alignment in the same manner as in the data. We estimate error bars using the standard error of the mean of each bin, and average over 100 random draws from the mass-redshift distribution. We assess the discrepancy between data and simulation using χ^2, with errors given by the quadrature sum of the errorbars on the data and errorbars on the simulation.

This methodology yields different spin-filament alignments from the standard picture, with weak anti-alignments seen at all masses, rather than a transition from alignments at low mass to anti-alignments at high mass. This discrepancy arises from the enforced degeneracy between mass and redshift: at high mass the sample is dominated by high redshift galaxies, which are associated with more poorly measured filaments due to the lower number density

Table 3.2: Bisous filament alignments for different subsamples

Sample	N	$\langle\cos\theta\rangle$	SE	Shuffle mean	σ from shuffle
All	2546	0.6462	0.0079	0.6370	1.16
$D_F < 0.3$ Mpc	635	0.6265	0.0178	0.6357	-0.57
$0.3 < D_F < 1.0$ Mpc	637	0.6360	0.0151	0.6375	-0.04
$1.0 < D_F < 1.8$ Mpc	636	0.6493	0.0152	0.6402	0.83
$D_F > 1.8$ Mpc	638	0.6716	0.0150	0.6363	2.32
$M_\star < 9.89$	636	0.6377	0.0137	0.6369	0.08
$9.89 < M_\star < 10.38$	637	0.6619	0.0123	0.6371	2.05
$10.38 < M_\star < 10.82$	636	0.6487	0.0130	0.6388	0.94
$M_\star > 10.82$	637	0.6259	0.0160	0.6363	-0.67
$u - r < 1.65$	636	0.6369	0.0151	0.6367	0.02
$1.65 < u - r < 2.06$	637	0.6679	0.0146	0.6370	2.15
$2.06 < u - r < 2.33$	636	0.6343	0.0142	0.6393	-0.16
$u - r > 2.33$	637	0.6498	0.0159	0.6343	0.83
elliptical	1030	0.6489	0.0122	0.6368	1.01
spiral	667	0.6558	0.0147	0.6361	1.30
edge-on	338	0.6262	0.0211	0.6396	-0.50

Note. — MaNGA spin-Bisous filament alignments for the entire sample and sub-samples split by distance to filament (D_F), stellar mass (in units of $\log M_\odot$), $u - r$ color, and morphology. $\langle\cos\theta\rangle$ is the mean dot product between the unit spin vector and the unit filament vector. SE is the standard error of the mean, calculated using 50000 bootstrap resamples of the data. We measure the expectation for random alignments using 50000 shuffles of the data, and compute σ, the deviation between the data and the randoms in units of the standard error.

in the Main Galaxy Sample at higher redshift. While high mass galaxies show stronger anti-alignments than low mass galaxies at fixed redshift, the strong anti-alignment at high masses is weakened by the degeneracy between mass and redshift. The difference between the simulation curves in Figure 3.7 and the standard picture highlights the importance of constructing a simulation sample that closely mimics the methodology of the data.

For the fiducial case, we find modest tension between the mass-dependence of alignments in the MaNGA sample of 2551 galaxies and the mass-dependence in the hydrodynamical simulations, with $\chi^2 = 14.26$ over 4 degrees of freedom ($p = 0.0065$, equivalent to 2.7σ) for MassiveBlack-II and $\chi^2 = 11.09/4$ dof ($p = 0.026$, equivalent to 2.2σ) for Illustris. We find similar 2-3σ tensions when using different bins, and in fact find a higher $\chi^2 = 15.52$ when using a stricter cut of $\sigma_{\rm PA} < 3^\circ$, indicating that the tension is not an artifact of the binning scheme and cuts used. However, this tension is clearly absent in the mass-dependence of alignments for Hα emission line spins, for which we find $\chi^2 = 2.59$ over 4 degrees of freedom between the data and MassiveBlack-II.

We confirm that the χ^2 test is appropriate for this comparison: the mean dot product in each stellar mass bin is normally distributed, and the covariance between neighboring bins is small compared to the variance of each bin. Using 50,000 bootstrap resamples, we confirm that the distribution of the mean dot product in each mass bin is normally distributed, even in cases where there are only ~ 50 galaxies in the smallest (most-massive) bin. We estimate the covariance by resampling the galaxies in 100 deg^2 blocks rather than re-sampling galaxy by galaxy in order to preserve the source of the covariance, correlations between neighboring galaxy spin-filament dot products arising from galaxy spin correlations, which drop rapidly over $\sim 10\ h^{-1}\,$Mpc (Pen et al. 2000, Lee 2011). We find that computing the χ^2 with this covariance matrix rather than assuming a diagonal covariance matrix makes little difference, and that the resulting covariance matrices are relatively robust to changes in the size of the resampling blocks. Given that MaNGA galaxies are widely distributed over the sky, with the average pair separation greater than the $\sim 10\ h^{-1}\,$Mpc spin correlation length (Figure 3.1), we expect the covariance matrix to be nearly diagonal.

The sample of MaNGA galaxies with well measured spins is not complete: in fact, the completeness varies as a function of mass, with low and high mass galaxies having relatively low completeness of well-measured stellar spins, whereas intermediate-mass galaxies are quite complete (Table 3.3). This incompleteness preferentially selects galaxies with higher specific angular momentum j, for which it is easier to measure a spin direction. This could possibly bias the mass-dependence of spin-filament alignments, if high j galaxies have different alignments than low j galaxies. We attempt to estimate the bias introduced by this incompleteness by removing low j subhalos in the mass bins in the simulation to match the incompleteness of stellar spins in MaNGA. This is a conservative procedure, as incompleteness is likely also caused by low-S/N stellar continuum and plane-of-sky inclinations, which are not related to galaxy-filament alignment stength. Nevertheless, removing low-j subhalos has an extremely modest effect on alignments in the simulations, changing the χ^2 between data and Illustris from 11.09 to 12.57.

These tests suggest that the comparison between data and simulations presented above

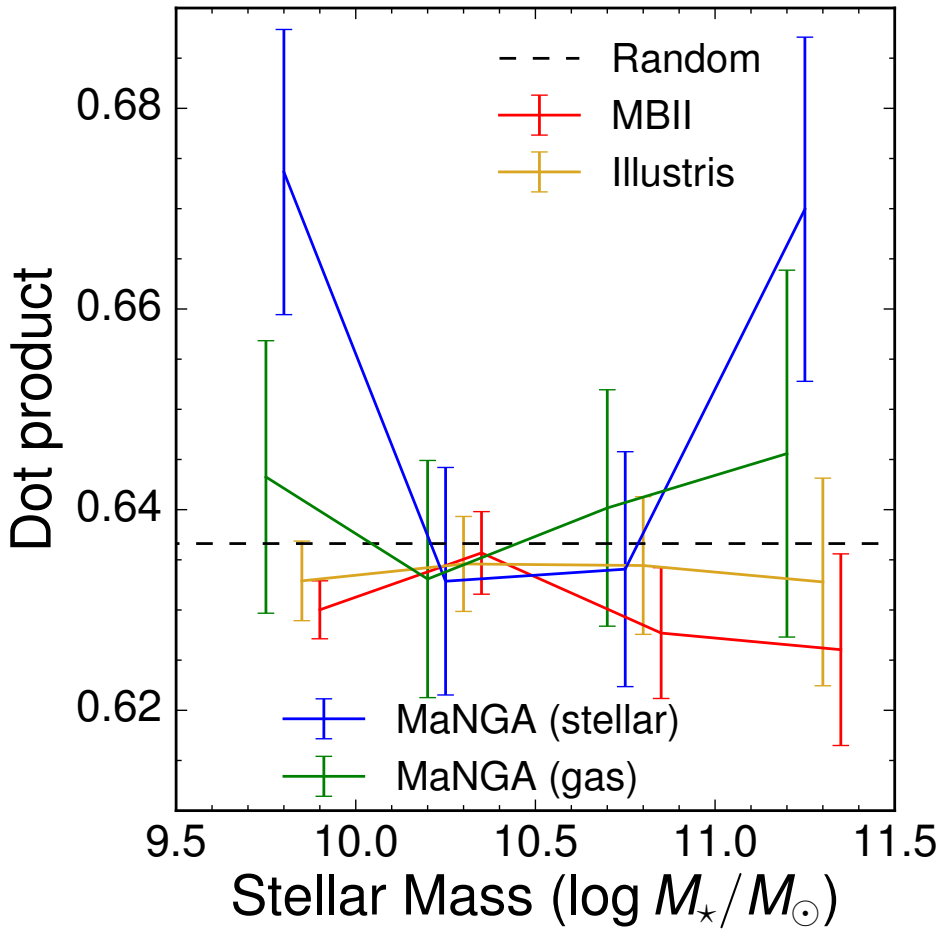

Figure 3.7: Mass-dependence of MaNGA spin-filament alignment, comparing MaNGA alignments using both stellar (blue) and emission line (green) spins to alignments in the MassiveBlack-II (red) and Illustris (orange) simulations. In each bin, points from different samples are offset for clarity.

Table 3.3: Completeness of spin measurement as a function of mass

Bin	Stellar completeness	Emission line completeness
$9.6 < \log h^{-1} M_\odot < 10$	83.7%	91.3%
$10 < \log h^{-1} M_\odot < 10.5$	97.1%	91.3%
$10.5 < \log h^{-1} M_\odot < 11$	95.6%	90.0%
$\log h^{-1} M_\odot > 11$	76.2%	76.2%

Note. — Fraction of MaNGA galaxies with well measured spins (error $< 5°$) in different mass bins.

is not impacted by covariance between the stellar mass bins or incompleteness in the spin measurements. Therefore the discrepancy between the spin-filament alignments in data and simulations remains unresolved.

3.4.1 3D alignments in simulations

While the mass-dependent alignment signal in data is quite modest, more significant differences become apparent if we instead use simulated filaments with no regard to observational constraints, i.e. filaments in three dimensions and filaments measured using all subhalos, rather than only using massive observable galaxies. This allows us to detect galaxy-filament alignments at much higher significance.

Both MassiveBlack-II and Illustris show similar mass-dependence of the alignments between dark matter spins and filaments (Figure 3.8). This transition from aligned at low masses to anti-aligned at higher masses is consistent with previous findings, mostly from dark-matter-only simulations (Bailin & Steinmetz 2005, Aragón-Calvo et al. 2007, Hahn et al. 2007a, Pichon et al. 2011, Codis et al. 2012, Trowland et al. 2013, Aragon-Calvo & Yang 2014, Dubois et al. 2014, Codis et al. 2015, Wang et al. 2018).

In contrast, Illustris and MassiveBlack-II paint opposing pictures of the mass dependence of stellar spin-filament alignments. In Illustris the mass-dependence of the stellar spin alignments is quite similar to the mass-dependence of the dark matter spin alignments, while in MassiveBlack-II the stellar spin alignments show a qualitatively different behavior than the dark matter spin alignments, remaining anti-aligned even at the lowest masses (Figure 3.8). The $z \sim 0$ results in Illustris are consistent with the findings of Dubois et al. (2014) in the Horizon-AGN hydrodynamic simulation at $z = 1.8$, who measured alignments between filaments and stellar angular momentum and found a transition from alignment to anti-alignment at $M_\star \sim 10^{10.5}\ M_\odot$. Additionally, we find very similar mass-dependent alignments to Wang et al. (2018), who also use Illustris to measure alignments between galaxies and the third eigenvector of the deformation tensor, which defines the filament direction within the Zel'dovich approximation.

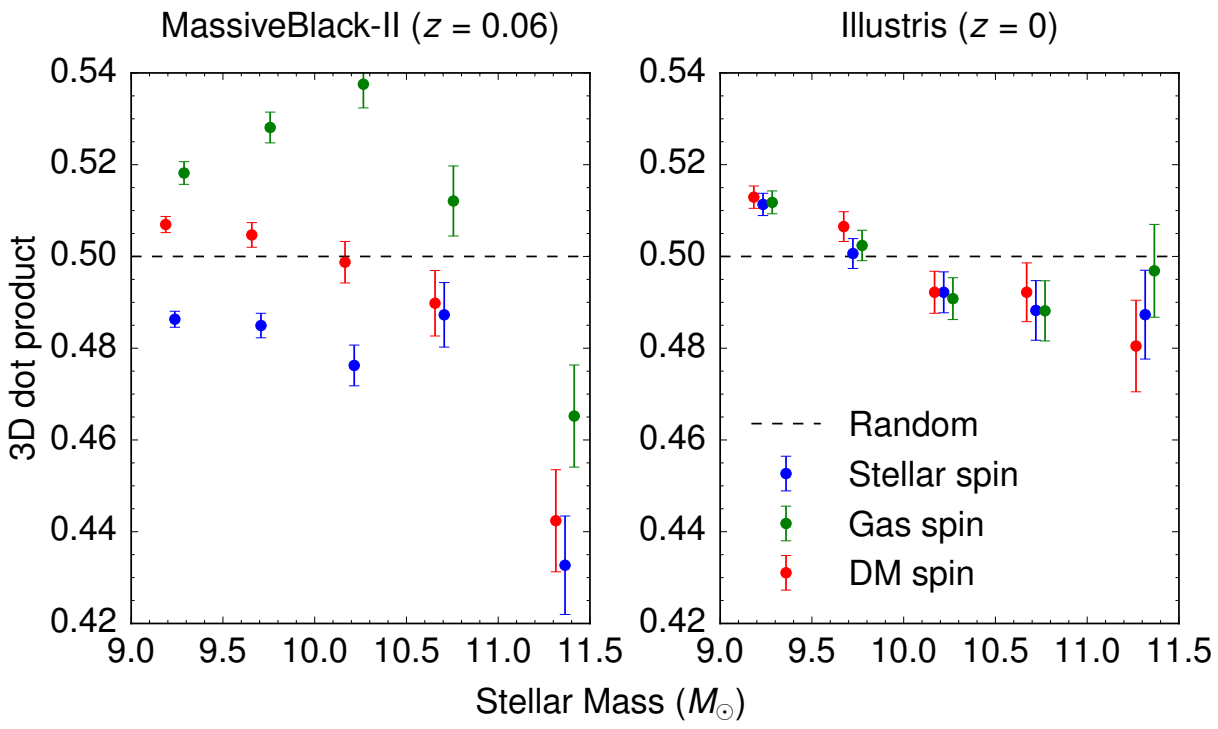

Figure 3.8: 3D alignments between subhalo spins and "ideal" filaments measured using the 500,000 most-massive subhalos in Illustris ($z = 0$) and MassiveBlack-II ($z = 0.06$). In both panels, the black dotted line is the 3D dot product expected for random alignments, the red (blue; green) points are alignments between dark matter (stellar; gas) spins and filaments. Points are offset in mass for clarity.

The mass-dependent trends in gas spin alignments are even more divergent between Illustris and MassiveBlack-II. Gas-filament alignments in Illustris are quite similar to star-filament and dark matter-filament alignments, but gas spins in MassiveBlack-II remain aligned with filaments until $M_\star \sim 10^{11}\ M_\odot$, and the alignments are considerably stronger than low-mass dark matter-filament alignments. While gas spins in MassiveBlack-II are only measured for a subset of galaxies with > 1000 gas particles, this subset has very similar stellar-filament and dark matter-filament alignments as the entire sample, implying that the gas-filament alignments are not significantly impacted by selection bias.

Taken together, these results suggest that while the "transition mass" picture presented in previous work (e.g. Codis et al. 2012) remains valid for dark matter spins, its validity for stellar and gas spins of galaxies is questionable and apparently dependent on subgrid physics and feedback models.

In conclusion, we find modest tension between the mass dependence of galaxy-filament alignments in MaNGA and in the MassiveBlack-II and Illustris simulations. The tension

is present if MaNGA spins are estimated using stellar continuum velocities, although it disappears if we use MaNGA spins measured from the Hα emission line. While we find minimal differences in alignments between MassiveBlack-II and Illustris using a sample of simulated galaxies and filaments selected to mimic the MaNGA and SDSS galaxy samples, an ideal measurement using filaments constructed from all subhalos in the simulations reveals a significant difference in the behavior of spin alignments in Illustris and MassiveBlack-II at low masses. While both simulations find that dark matter spins are aligned with filaments at low mass, in agreement with previous results from N-body simulations, Illustris finds stellar spin-filament alignment at low mass, while MassiveBlack-II finds stellar spin-filament anti-alignment.

3.5 Discussion

We present the first measurement of alignments between filaments and galaxy spins as measured from integral-field kinematics. We find no significant detection of galaxy spin alignments with filaments. We find that the mass dependence of spin-filament alignments from MaNGA are in 2-3σ tension with spin-filament alignments from the MassiveBlack-II and Illustris simulations, although the tension disappears if we instead use galaxy spins measured from the Hα emission line. While the predictions of MassiveBlack-II and Illustris are essentially identical if we use a "mock-observational" sample, three-dimensional filaments measured using all subhalos in the simulation reveal significant differences in alignment behavior at low masses, suggesting that the "transition-mass" picture described in previous works is dependent on details of feedback and subgrid physics.

Previous studies have measured galaxy spin-filament alignments using galaxy shape as a proxy for galaxy spin (Tempel et al. 2013, Tempel & Libeskind 2013, Pahwa et al. 2016, Chen et al. 2019). These studies find a weak dichotomy between spiral and elliptical galaxies, with spirals aligned and ellipticals anti-aligned with filaments. We do not find evidence for this dichotomy, but our error bars are larger than in previous studies and our results are consistent with them.

The results in this work are limited by the relatively small sample size of $\sim$ 2600 MaNGA galaxies with well-measured spins and sufficient proximity to "Cosmic Web Reconstruction" filaments. The error bars on this measurement are dominated by intrinsic scatter rather than measurement error on the spins or the filaments, suggesting that acquiring larger samples of galaxy spins is the most effective way to achieve a more precise measurement. The full MaNGA sample will provide integral-field-unit spectroscopy for 10,000 galaxies, roughly doubling the sample with sufficient spin measurements. This represents a significant step forward, but even larger samples are needed to distinguish the alignment models of different simulations at high significance. The proposed Hector survey on the Anglo-Australian Telescope could deliver integral-field spectroscopy for up to 100,000 galaxies over the next decade (Bryant et al. 2016), offering an unparalleled ability to learn about the relationship between galaxy spin and large-scale structure and the acquisition of galaxies' angular momentum.

Acknowledgments

We thank Simone Ferraro, Joanne Cohn and Shy Genel for helpful comments and discussions.

This research made use of Marvin, a core Python package and web framework for MaNGA data, developed by Brian Cherinka, José Sánchez-Gallego, Brett Andrews, and Joel Brownstein (Cherinka et al. 2018).

Calculations presented in this paper used resources of the National Energy Research Scientific Computing Center (NERSC), which is supported by the Office of Science of the U.S. Department of Energy under Contract No. DE-AC02-05CH11231.

Funding for the Sloan Digital Sky Survey IV has been provided by the Alfred P. Sloan Foundation, the U.S. Department of Energy Office of Science, and the Participating Institutions. SDSS acknowledges support and resources from the Center for High-Performance Computing at the University of Utah. The SDSS web site is www.sdss.org.

SDSS is managed by the Astrophysical Research Consortium for the Participating Institutions of the SDSS Collaboration including the Brazilian Participation Group, the Carnegie Institution for Science, Carnegie Mellon University, the Chilean Participation Group, the French Participation Group, Harvard-Smithsonian Center for Astrophysics, Instituto de Astrofísica de Canarias, The Johns Hopkins University, Kavli Institute for the Physics and Mathematics of the Universe (IPMU) / University of Tokyo, Lawrence Berkeley National Laboratory, Leibniz Institut für Astrophysik Potsdam (AIP), Max-Planck-Institut für Astronomie (MPIA Heidelberg), Max-Planck-Institut für Astrophysik (MPA Garching), Max-Planck-Institut für Extraterrestrische Physik (MPE), National Astronomical Observatories of China, New Mexico State University, New York University, University of Notre Dame, Observatório Nacional / MCTI, The Ohio State University, Pennsylvania State University, Shanghai Astronomical Observatory, United Kingdom Participation Group, Universidad Nacional Autónoma de México, University of Arizona, University of Colorado Boulder, University of Oxford, University of Portsmouth, University of Utah, University of Virginia, University of Washington, University of Wisconsin, Vanderbilt University, and Yale University.

3.A Galaxy spin fitting

We use the FIT_KINEMATIC_PA routine (Krajnović et al. 2006) to determine the kinematic position angle for each galaxy from the stellar velocity maps, using velocities from the unbinned spaxels. We remove low quality or potentially problematic data by masking spaxels with r-band SNR < 5, spaxels with the DONOTUSE or UNRELIABLE bitmasks (Westfall et al., in prep), $|v| > 350$ km s^{-1}, $\sigma_v > 10^3$ km s^{-1}, or a velocity that is more than a 5-σ outlier (i.e. $|v| > 5$ times the standard deviation of v). We also mask all contiguous regions with SNR > 5 that are disconnected from the central part of the galaxy in order to eliminate faint companion galaxies within the IFU. To avoid giving a large weight to any

one spaxel, we set the minimum velocity error to 2 km s^{-1} (Pineda et al. 2017). From visual inspection of the fits, we find that these settings give the best performance. We recenter each galaxy about the unweighted centroid of its unmasked region, since the center of rotation in some galaxies is offset from the center of the IFU. Finally, we perform each fit in curved-sky coordinates ($\alpha \cos\delta$, δ) and convert the resulting position angles to an equirectangular projection for consistency with the filament catalog. We use this method as it fits the position angles in a physical coordinate system.

FIT_KINEMATIC_PA fits a bi-antisymmetric model to a velocity map. For a specified rotation of the xy coordinates relative to the native ($\alpha \cos\delta$,δ) coordinates (i.e. position angle), the bi-antisymmetric model at (x,y) is the average of the velocity at ($\pm x$, $\pm y$), linearly interpolating between neighboring points if need be. The best-fit position angle minimizes χ^2 computed from the data, the bi-antisymmetric model and the MaNGA velocity errors. We initially loop over all PAs between 0° and 180° to ensure that we are near the global minimum, then use Nelder-Mead minimization to find the global minimum χ^2.

To estimate the error on the position angle, we create 100 realizations of the velocity map, drawing the velocity in each spaxel from a Gaussian centered at the measured velocity, with standard deviation equal to the velocity error, and assuming no covariance between neighboring spaxels. We apply the same χ^2 minimization process to each of the 100 realizations, again using the MaNGA velocity errors and the bi-antisymmetric model from FIT_KINEMATIC_PA. We define the position angle as the mean of the ensuing 100 position angles θ_i and the position angle error as the standard deviation of the 100 position angles. We use the circular mean of headless (i.e. spin-2) vectors μ_{180}:

$$\mu_{180}(\vec{\theta}) = \frac{1}{2} \arctan \frac{\sum \sin 2\theta_i}{\sum \cos 2\theta_i} \tag{3.1}$$

The standard deviation is adjusted similarly:

$$\sigma_{180}(\vec{\theta}) = \sqrt{\frac{1}{N} \sum \min^2(\theta_i - \mu_{180}(\vec{\theta}), 180 - \theta_i + \mu_{180}(\vec{\theta}))} \tag{3.2}$$

While this is only an approximate estimate of the position angle error, and may in particular underestimate the error due to nonzero covariance between neighboring spaxels, the position angle errors are not an important contributor to the total error budget on the alignment measurements: they are dominated by the errors on the filament angles (Figure 3.5) and as we show in Section 5.2, the measurement errors are dominated by the intrinsic scatter in galaxy-filament alignments anyway.

3.B 3D vs 2D alignment measurements in simulations

We use measurements of galaxy-filament alignments in the MassiveBlack-II simulation to determine how much signal is lost using two-dimensional rather than three-dimensional

measurements of the filaments. We generate three-dimensional filaments using the redshift-space positions of the top 500,000 subhalos in MBII by total mass ($\log M_h/M_\odot > 9.74$) and applying the Cosmic Web Reconstruction algorithm with a smoothing bandwidth of 1 h^{-1} Mpc. For the two-dimensional sample, we use the same subhalos and bandwidth, but as in Section 3.2.4, we split the box into 7 slices along the z direction ($\Delta z = 0.005 = 20$ Mpc ~ 14 h^{-1} Mpc) and separately find two-dimensional filaments in each slice. In both cases, the number density of subhalos is much greater than the number density achievable in the Main Galaxy Sample; we use these large samples in order to make a high signal-to-noise measurement of three-dimensional and two-dimensional alignment, and assume that the reduction in signal from three-dimensional to two-dimensional will be similar for the realistic lower number-density samples.

We find that the mean dot product between the 3D filaments and the subhalo stellar spins is 0.4882 ± 0.00136 compared to an expectation of 0.5 for random alignments for an alignment strength signal-to-noise of 8.68. For the two-dimensional filaments, we find a mean dot product of 0.6293 ± 0.00145 compared to 0.6366 for random alignments, yielding an alignment strength signal-to-noise of 5.03. We also measure alignments between subhalo spins and "ideal" two-dimensional filaments, which are the projection of the 3D filaments onto the xy plane; here we find a mean dot product of 0.6267 ± 0.00146 and signal-to-noise 6.81. This indicates that most of the reduction in the $\Delta z = 0.005$ case comes from loss of filament information in the z direction and not from the finite Δz of the slices. Therefore, we estimate that using two-dimensional filaments in slices of $\Delta z = 0.005$ reduces the alignment signal strength by 40%. However, it is unlikely that we could realize a 40% improvement in signal by using three-dimensional filaments, since the line-of-sight component of the galaxy spin vector is significantly harder to measure than the transverse component, reducing the signal gain from three-dimensional filaments (Krolewski et al. 2017).

Chapter 4

A Detection of $z \sim 2.3$ Cosmic Voids from 3D Lyman-α Forest Tomography in the COSMOS Field

Abstract

We present the most distant detection of cosmic voids ($z \sim 2.3$) and the first detection of three-dimensional voids in the Lyman-α forest. We used a 3D tomographic map of the absorption with effective comoving spatial resolution of $2.5\,h^{-1}$Mpc and volume of $3.15 \times 10^5\,h^{-3}$Mpc^3, which was reconstructed from moderate-resolution Keck-I/LRIS spectra of 240 background Lyman-break galaxies and quasars in a $0.16\,\mathrm{deg}^2$ footprint in the COSMOS field. Voids were detected using a spherical overdensity finder calibrated from hydrodynamical simulations of the intergalactic medium. This allows us to identify voids in the IGM corresponding to voids in the underlying matter density field, yielding a consistent volume fraction of voids in both data (19.5%) and simulations (18.2%). We fit excursion set models to the void radius function and compare the radially-averaged stacked profiles of large voids ($r > 5\ h^{-1}\,$Mpc) to stacked voids in mock observations and the simulated density field. Comparing with 432 coeval galaxies with spectroscopic redshifts in the same volume as the tomographic map, we find that the tomography-identified voids are underdense in galaxies by 5.95σ compared to random cells.

4.1 Introduction

Cosmic voids offer a laboratory for studying cosmology and galaxy formation in extreme environments. Voids are large (Mpcs to tens of Mpcs), slightly prolate regions nearly devoid of galaxies, which constitute the majority of the universe's volume (van de Weygaert & Platen 2011). Voids are surrounded by the beaded, filamentary network of the cosmic web and expand and evacuate as matter streams onto filaments and collapses into halos (Bond

et al. 1996). Matter streams outward most quickly in the center of voids, where the density is lowest, creating a so-called bucket profile with a uniform inner density ($\delta \sim -0.7 - 0.9$; Hamaus et al. 2014, Sutter et al. 2014a). The exact shape of the profile is dependent on both the void finder and the large-scale environment of the void under consideration: small voids are often subvoids within a large-scale overdensity and are surrounded by a ridge of higher density, while large voids (as well as voids found by spherical overdensity finders; see White & Padmanabhan 2017) typically have a smooth profile approaching the mean density from below (Hamaus et al. 2014, Cai et al. 2016a). While isolated voids become more isotropic over time (Sheth & van de Weygaert 2004), voids in the real universe remain prolate due to external tides and collisions with neighboring sheets and filaments (van de Weygaert & Platen 2011).

Voids are especially useful for studying components of the universe that cluster weakly, such as dark energy (Lee & Park 2009, Lavaux & Wandelt 2012) or massive neutrinos (Villaescusa-Navarro et al. 2013, Massara et al. 2015, Banerjee & Dalal 2016): since voids are underdense in the clustered components of the universe (dark matter and baryons), unclustered components will have a maximal effect on the dynamics within voids (Goldberg & Vogeley 2004). Voids are also sensitive probes of modified gravity theories, which may be screened in higher density regions (Clampitt et al. 2013).

Prospects for void cosmology have been studied using several different observables. Since voids are spherical on average, the Alcock-Paczynski test (Alcock & Paczynski 1979) can be performed on sufficiently large stacks of voids (Ryden 1995, Lavaux & Wandelt 2012). Other sensitive observables include void-galaxy cross-correlations and redshift-space distortions (Cai et al. 2016a, Hamaus et al. 2017); the integrated Sachs-Wolfe effect from stacked voids (Granett et al. 2008, Cai et al. 2017, Kovács et al. 2017); weak lensing of stacked voids (Higuchi et al. 2013, Krause et al. 2013, Melchior et al. 2014, Clampitt & Jain 2015, Barreira et al. 2015, Gruen et al. 2016, Cai et al. 2017); void counts to probe modified gravity (Li et al. 2012, Clampitt et al. 2013, Lam et al. 2015, Cai et al. 2015, Zivick et al. 2015) or dark energy (Pisani et al. 2015, Pollina et al. 2016); and void ellipticities (Park & Lee 2007, Bos et al. 2012). Extending the study of cosmic voids to higher redshifts could allow for better constraints on redshift-dependent models, such as early dark energy (Doran & Robbers 2006).

Studying galaxies in voids can illuminate the influence of environment on galaxy evolution. N-body simulations show that the halo mass function abruptly changes from sheets to voids, leading to a dearth of dwarf galaxies in voids. This is the so-called "void phenomenon," originally identified as a tension with ΛCDM by Peebles (2001) but explained in the context of the halo model by Tinker & Conroy (2009). Comparisons of void galaxies to galaxies in average environments suggest that the change in the stellar mass function plays a dominant role in modifying galaxy properties as compared to the field (Hoyle et al. 2005, Tinker et al. 2008, Alpaslan et al. 2015, Penny et al. 2015, Beygu et al. 2016) and void galaxies show a similar diversity in morphology to field galaxies of the same stellar mass (Beygu et al. 2017). Recently some hints have emerged that void galaxies may have a slightly higher mass-to-light ratio than field galaxies of the same mass (Alpaslan et al. 2015), slightly higher HI masses

at low stellar mass (Beygu et al. 2016) and slightly enhanced star formation rate to HI mass ratio (Kreckel et al. 2012), although these effects remain quite subtle. Since the global star formation rate of the universe is much higher at $z \sim 2$ at $z \sim 0$, it would be interesting to study whether stellar mass remains the primary driver of void galaxy properties at $z \sim 2$, or whether environment begins to play a more significant role.

Observational studies of voids have been limited to low to moderate redshift where sufficiently dense galaxy surveys are available to identify voids. Voids have been identified in 2dF (Ceccarelli et al. 2006), SDSS (Pan et al. 2012, Sutter et al. 2012), VIPERS (Micheletti et al. 2014), BOSS (Mao et al. 2017b), DES (Sánchez et al. 2017), and DEEP2 (Conroy et al. 2005). The SDSS and BOSS voids have also been used for cosmological analyses (Sutter et al. 2014c, Hamaus et al. 2016, Mao et al. 2017a). Finding voids with radius of a few Mpc requires a large-volume galaxy survey with resolution of a few Mpc, which becomes increasingly difficult above $z \sim 1$ (Stark et al. 2015).

At higher redshifts, Lyman-α forest tomography (Pichon et al. 2001, Caucci et al. 2008, Lee et al. 2014a) offers an alternative method for obtaining large-volume, densely spaced surveys of the matter density field. Using spectroscopic observations of closely-spaced quasars and Lyman-break galaxies, Lyman-α forest tomography can reconstruct the 3D intergalactic medium absorption field with resolution of a few Mpc and on cosmological volumes of 10^6 h^{-3} Mpc^3 (Lee et al. 2014a). This technique allows for recovery of the cosmic web with comparable fidelity to $z < 0.5$ galaxy surveys (Lee & White 2016, Krolewski et al. 2017), which requires considerably greater spatial resolution than $z \sim 2$ galaxy surveys can provide. At $z \sim 2.5$, absorption with optical depth unity arises from neutral hydrogen with three times the mean density; thus, the Lyman α forest is ideal for probing underdense structures such as voids. Indeed, Stark et al. (2015) found that a simple spherical overdensity void finder could recover $r \geq 6\ h^{-1}$ Mpc voids in the IGM flux field at 60% fidelity, allowing detection of ~ 100 such voids in a 1 deg^2 survey.

In this paper, we make the first detection of $z \sim 2$ cosmic voids in the 3D Lyman-α forest using the COSMOS Lyman-Alpha Mapping and Tomography Observations (CLAMATO) survey (Lee et al. 2017). CLAMATO is the first survey to systematically use Lyman-break galaxies for Lyman-alpha forest analysis. It has produced a 3D map of the IGM absorption field with resolution 2.5 h^{-1} Mpc and volume 3.15×10^5 h^{-3} Mpc^3, using Keck-I/LRIS observations of the central 0.16 deg^2 of the COSMOS field.

While we are not the first to consider voids in the IGM, this work is distinct from previous observational efforts: Tejos et al. (2012) worked at $z \sim 0$; Rollinde et al. (2003) used only four sightlines, leading to large uncertainties; and Viel et al. (2008b) were limited to analyzing flux in 1D skewers.

The detection of $z \sim 2$ voids extends observational studies of voids to a much higher redshift range. In the future, high-redshift voids could allow for studies of the redshift evolution of void galaxies and void properties over a much larger redshift baseline, and better constraints on redshift-dependent dark energy and modified gravity models.

We begin by describing the data (Section 6.2) and simulations (Section 5.2.1) used in this paper. Next we determine appropriate spherical overdensity thresholds by matching

the void fraction in mock tomographic observations to the fraction of true voids in the density field (Section 4.4.1). We apply these thresholds to data in Section 4.4.2. In Section 4.5, we compare the tomography-identifed voids to the positions of coeval galaxies with spectroscopic redshifts, and find that the voids are $\sim 6\sigma$ underdense in coeval galaxies. We discuss the properties of the voids in Section 4.6 (including the void radius function and stacked void profile) and present our conclusions in Section 6.8.

In this paper we use a flat ΛCDM cosmology with $\Omega_m = 0.31$ and $h = 0.7$. While the simulations use a slightly different cosmology (see Section 5.2.1), the differences are small enough that the discrepancy will have negligible impact on the results presented here.

4.2 Data

We identify voids in the reconstructed IGM tomographic map from the first data release of the CLAMATO survey[1]. The observations are described in detail by Lee et al. (2017), but we briefly summarize the pertinent details here.

The survey targeted $2.3 < z < 3$ background Lyman-break galaxies and quasars with the LRIS spectrograph (Oke et al. 1995, Steidel et al. 2004) on the Keck-I telescope at Maunakea, Hawai'i, to measure the foreground Lyman-α forest absorption. This program targeted the COSMOS field to take advantage of rich existing datasets and achieve a high targeting efficiency. We observed 23 slitmasks (18 regular slitmasks and 5 "special" slitmasks designed to fill in gaps in coverage) with ~ 20 targets per mask. We successfully reduced 437 galaxies and AGN, of which 289 had high-confidence redshifts, and 240 were usable for the Lyman-α forest analysis at our targeted absorption redshift range of $2.05 < z < 2.55$. The primary criterion for the selection of the background spectra was the signal-to-noise ratio on the continuum in the Lyman-α forest (i.e. ratio of estimated continuum to pixel noise; hereafter we refer to this quantity as "S/N"): we required S/N ≥ 1.2 per pixel.

The intrinsic continua of the background sources were estimated using mean-flux regulation (Lee et al. 2012, 2013), which adjusts the mean Lyman-α forest transmission within each sightline to be consistent with $\langle F(z)\rangle$ estimates from the literature — we used Faucher-Giguère et al. (2008). Based on Lee et al. (2012), we estimate that the continuum errors are approximately $\sim 10\%$ rms for the noisiest spectra (S/N ~ 2 per pixel) and improve to $\sim 4\%$ rms for S/N ~ 10 spectra.

From the observed flux density and the fitted continuum, we compute the Lyα forest fluctuations, δ_F:

$$\delta_F = \frac{f}{C\langle F(z)\rangle} - 1 \tag{4.1}$$

where $\langle F(z)\rangle$ is the mean Lyα transmission from Faucher-Giguère et al. (2008) (the power-law fit from Table 5, including metals, with bins of width $\Delta z = 0.1$).

We use these values of δ_F as input for the Wiener-filter tomographic reconstruction. To avoid a flared map geometry, we use a constant conversion between redshift and comoving

[1]We use CLAMATO v4, available here: https://doi.org/10.5281/zenodo.1292459.

distance, $d\chi/dz$, and a constant transverse comoving distance χ, both evaluated at $z = 2.3$. With a fixed angular footprint on the sky, this amounts to a $\sim 20\%$ change in the reconstruction kernel size over the length of the map. While our mocks lack this redshift-dependent reconstruction kernel, we find that our results are virtually unchanged when we use an evolving $\chi(z)$ and $d\chi/dz(z)$. Specifically, the volume fraction of voids drops from 19.5% to 19.2% (0.2σ), the voids remain $\sim 6\sigma$ underdense in coeval galaxies, and the void radius function and void profile change by $< 1\sigma$ at all bins. Thus, we keep the simpler redshift- and angle-distance conversions presented above, but caution that future, more detailed analysis will likely require more accurate coordinate conversions and thus a more complex map geometry.

We define an output grid with cells of comoving size 0.5 h^{-1} Mpc, transverse dimensions 30 h^{-1} Mpc $\times$ 24 h^{-1} Mpc, and line-of-sight length 438 h^{-1} Mpc, corresponding to $2.05 < z < 2.55$. Thus the total comoving volume is 3.15×10^5 h^{-3} Mpc^3 over an survey geometry which is elongated along the line-of-sight (redshift) dimension but considerably smaller across the transverse dimensions. The effective sightline spacing varies along the line of sight from 2.22 h^{-1} Mpc at $z = 2.25$ to 3.15 h^{-1} Mpc at $z = 2.45$.

We use a Wiener filtering algorithm developed by Stark et al. (2015) to reconstruct the 3D IGM absorption field:

$$\delta_F^{\rm rec} = \mathbf{C}_{\rm MD} \cdot (\mathbf{C}_{\rm DD} + \mathbf{N})^{-1} \cdot \delta_F \tag{4.2}$$

where $\mathbf{N}$ is the noise covariance, $\mathbf{C}_{\rm DD}$ is the data-data covariance, and $\mathbf{C}_{\rm MD}$ is the map-data covariance. We assume that the noise covariance is diagonal, with $\mathbf{N}_{ij} = n_i^2 \delta_{ij}$ where n_i is the pixel noise. To avoid weighting any sightlines too heavily, we set a minimum noise level of 0.2. We further assume that $\mathbf{C}_{\rm MD} = \mathbf{C}_{\rm DD} = C$:

$$C = \sigma_F^2 \exp\left[-\frac{\Delta x_\perp^2}{2 l_\perp^2} - \frac{\Delta x_\parallel^2}{2 l_\parallel^2}\right] \tag{4.3}$$

We use $\sigma_F^2 = 0.05$, $l_\perp = \langle d_\perp \rangle = 2.5$ h^{-1} Mpc, and $l_\parallel = 2.0$ h^{-1} Mpc. While in previous works we have additionally Gaussian-smoothed the output tomographic reconstruction, in this paper we apply no additional smoothing to the map, following Stark et al. (2015).

Hereafter we identify voids in the Wiener-filtered map rather than in the pixel-level data. While it should be possible to develop a void finder that can be applied directly to the pixel-level data (a method which could in principle also be extended to the sparsely and irregularly sampled galaxy field), we leave the development of this method to future work.

Figure 4.1 shows the distribution of $\delta_F^{\rm rec}$ in the Wiener-filtered map and overplots a Gaussian distribution with the same mean and standard deviation. Although the distribution of $\delta_F^{\rm rec}$ is reasonably well-approximated by a Gaussian, particularly in the high $\delta_F^{\rm rec}$ region where the voids lie, the underlying density field smoothed on scales of 2.5 h^{-1} Mpc is quite non-Gaussian, indicating that there is cosmological information in the presence and distribution of voids beyond the two-point statistics in the map.

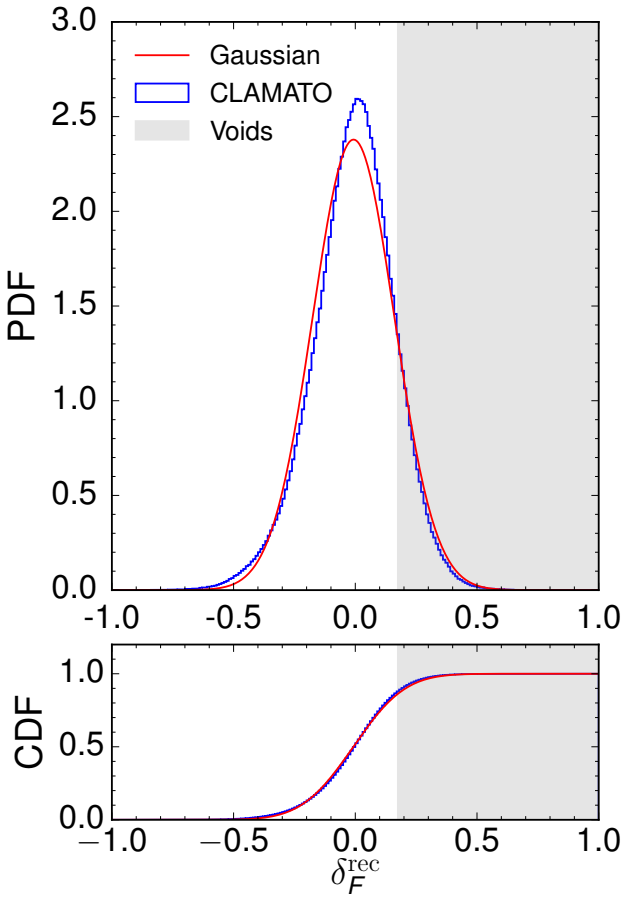

Figure 4.1: Probability density and cumulative distributions of $\delta_F^{\rm rec}$ in the CLAMATO map compared to a Gaussian. The lower edge of the gray shaded region is the threshold for average void density, $\delta_F^{\rm rec} = 0.175$.

4.3 Simulations

We use mock tomographic reconstructions from Lyα forest simulations to both calibrate the thresholds for the spherical overdensity void finder and understand the effects of survey geometry and sample variance on our results. We use both hydrodynamic simulations of the IGM and N-body simulations of the density field with the Lyα forest modeled using the fluctuating Gunn-Peterson approximation. Each simulation has its advantages and disadvantages: the hydrodynamic simulation more accurately models the physics of the IGM but is hampered by a relatively small volume of $(100\ h^{-1}\,\mathrm{Mpc})^3$; the larger $(256\ h^{-1}\,\mathrm{Mpc})^3$ N-body simulation enables us to create many realizations of CLAMATO-like volumes with approximately the correct survey geometry (though considerably shorter along the line of

sight) but its IGM prescription is only approximate. Throughout this paper we use both simulations and wherever possible we endeavor to compare the N-body and hydrodynamic simulation results to ensure robustness to different simulation methods and different included physics.

4.3.1 Hydrodynamical Simulations

The hydrodynamic simulations of the IGM are generated with the N-body plus Eulerian hydrodynamics NYX code (Almgren et al. 2013). It has a 100 h^{-1} Mpc box size with 4096^3 cells and particles, resulting in a dark matter particle mass of $1.02 \times 10^6 h^{-1} M_\odot$ and spatial resolution of 24 h^{-1} kpc. As discussed in Lukić et al. (2015), this resolution is sufficient to resolve the filtering scale below which the IGM is pressure supported and to reproduce the $z = 2.4$ flux statistics to percent accuracy within the range of physics included (we neglect radiative transfer and do not model high column-density systems well). We use a snapshot at $z = 2.4$. This simulation uses a flat ΛCDM cosmology with $\Omega_m = 0.3$, $\Omega_b = 0.047$, $h = 0.685$, $n_s = 0.965$, and $\sigma_8 = 0.8$, consistent with latest Planck measurements (Planck Collaboration et al. 2016a). It uses the ionizing background prescription of Haardt & Madau (1996), producing an IGM temperature-density relationship with $T_0 \sim 10^4$ K and $\gamma \sim 1.55$ at $z = 2$. This simulation does not model star-formation and hence has no feedback from stars, galaxies, or AGNs, but these are expected to have a negligible effect on the Lyα forest statistics (Viel et al. 2013).

We generate 512^2 absorption skewers with a spacing of 0.2 h^{-1} Mpc and sample from these skewers to create mock data. We compute the Lyα forest flux fluctuation along each skewer, then shift to redshift space and Doppler broaden the skewers using the gas temperature. The H 1 optical depths, τ, in the mock spectra are adjusted to match the mean flux from Faucher-Giguère et al. (2008) at $z = 2.3$ ($\langle F \rangle = 0.8189$); we use a single mean flux throughout the entire line of sight direction since neither simulation box is as long as the line-of-sight length of the map. Absorption skewers are randomly selected with mean sightline spacing $\langle d_\perp \rangle = 2.5\ h^{-1}$ Mpc and rebinned along the line of sight with resolution 0.84 h^{-1} Mpc, corresponding to the 1.2 Å LRIS pixels. Using a single sightline spacing is approximate, as the mean transverse separation of CLAMATO sightlines varies with redshift (Lee et al. 2017); our choice of $\langle d_\perp \rangle = 2.5\ h^{-1}$ Mpc is slightly conservative compared to the CLAMATO $\langle d_\perp \rangle = 2.37\ h^{-1}$ Mpc. This difference should not be significant since we use the same correlation lengths for the tomographic reconstructions ($l_\perp$ and $l_\parallel$ in Equation 4.3) in both mocks and data. Finally, the skewers are smoothed with a Gaussian kernel with 2.8 h^{-1} Mpc FWHM (~ 4 Å) to account for the spectral resolution of LRIS at 4000 Å.

We add both random noise and correlated continuum error to each skewer. Random noise is simulated assuming the S/N per pixel is a unique constant for each skewer. To determine S/N for each skewer, we draw from a power-law S/N distribution $\mathrm{d}n_{\mathrm{los}}/\mathrm{dS/N} \propto \mathrm{S/N}^{-\alpha}$ (Stark et al. 2015; hereafter S15b), where S/N ranges between 1.4 and infinity. From S15b, we use $\alpha = 2.7$ for the $\langle d_\perp \rangle = 2.5\ h^{-1}$ Mpc reconstructions. The minimum S/N of 1.4 in

the mock sightlines is slightly higher than the minimum S/N of 1.2 in CLAMATO; the S/N distribution in CLAMATO rolls over below S/N of 1.5, perhaps owing to the difficulty of determining redshifts for low-S/N galaxies. Therefore, a minimum S/N of 1.4 provides the best match to the CLAMATO S/N distribution, with median S/N of 2.1 in CLAMATO and 2.15 in the mock sightlines (Figure 4.2). We then use the S/N for each sightline to determine the pixel noise n (i.e. the error on δ_F):

$$n = \frac{1}{\mathrm{S/N}\langle F \rangle} \tag{4.4}$$

Subsequently, we add a random Gaussian deviate with standard deviation n to the δ_F values in each pixel and use the resulting noisy δ_F and n as input to the Wiener filter (Equation 4.2).

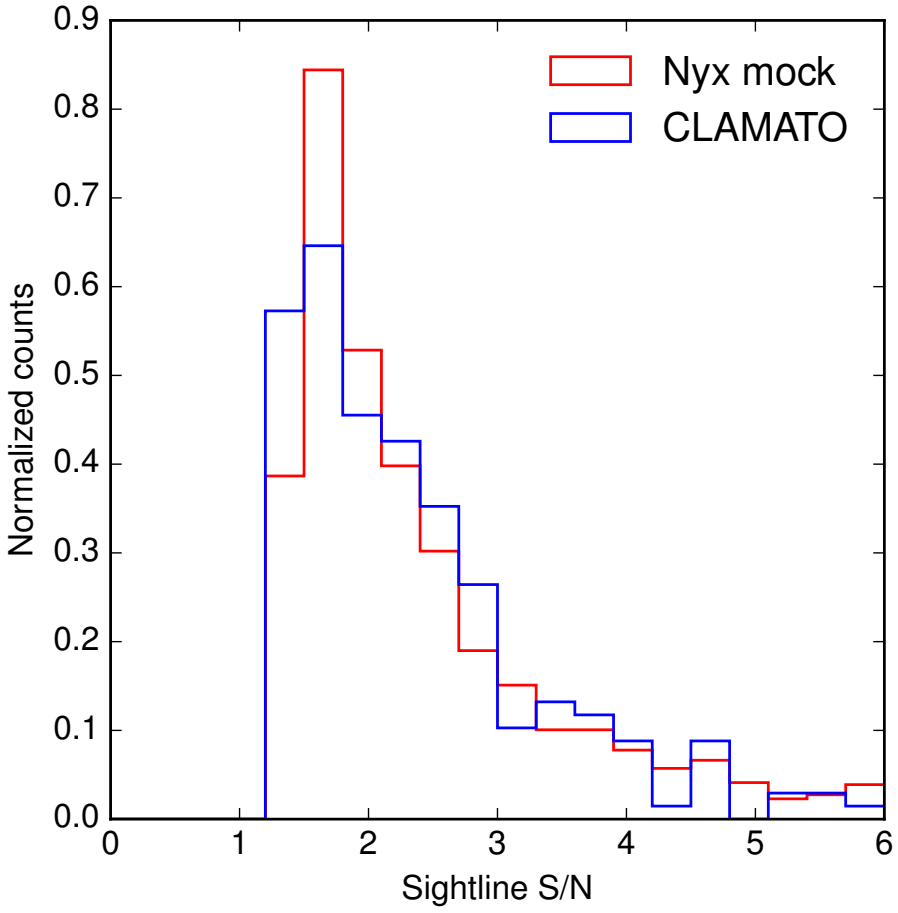

Figure 4.2: Distribution of S/N per pixel for CLAMATO sightlines and Nyx mock sightlines.

We also model continuum-fitting error:

$$F_{\rm obs} = \frac{F_{\rm sim}}{1+\delta_{\rm cont}} \tag{4.5}$$

where $\delta_{\rm cont}$ is a random Gaussian deviate, identical for all pixels within a skewer, with mean 0 and standard deviation $\sigma_{\rm cont}$. Following Lee et al. (2012), $\sigma_{\rm cont}$ is a function of the S/N, with lower S/N spectra having higher continuum error and vice versa. We fit a function to the data points in Figure 8 of Lee et al. (2012) for $z = 2.35$

$$\sigma_{\rm cont} = \frac{a}{S/N} + b \tag{4.6}$$

where $a = 0.2054$ is a free parameter fit to the data and $b = 0.015$ is the rms fitting error in the absence of continuum structure and noise, to which the continuum error should asymptote in the case of infinite signal-to-noise. To be conservative, we cap the continuum error for S/N > 10 at 4%.

We apply the same Wiener-filter interpolation to the mock sightlines as to our data, with the same noise floor of 0.2 as in the data. Just as in the data reconstruction, we use pixels 0.5 h^{-1} Mpc on a side.

4.3.2 Large-Volume N-body Simulations

The hydrodynamical simulation is too small ($L = 100\,h^{-1}$ Mpc) to mimic the elongated CLAMATO survey geometry. To better understand the effect of survey geometry and sample variance on our results, we therefore also use a larger N-body simulation (White et al. 2010). This is a publicly-available simulation used in our previous papers (Lee et al. 2015, Stark et al. 2015, Stark et al. 2015), so we describe it only briefly here.

The N-body simulation uses 2560^3 particles of $8.6\times10^7\ h^{-1}M_\odot$ in a 256 h^{-1} Mpc periodic box. The cosmological parameters are $\Omega_m = 0.31$, $\Omega_b h^2 = 0.022$, $h = 0.677$, $n_s = 0.9611$, $\sigma_8 = 0.83$, and initial conditions are generated using second-order Lagrangian perturbation theory at $z_{ic} = 150$. The particles were evolved forward using the TreePM code of White (2002), and we use output at $z = 2.5$. The Lyα absorption field was generated with the fluctuating Gunn-Peterson approximation assuming a pressure filtering scale of 100 h^{-1} kpc and a power-law temperature-density relationship with $T_0 = 2\times10^4$ K and $\gamma = 1.6$.

Taking advantage of the larger volume of the N-body box, we create both a single mock reconstruction spanning the entire 256^3 box and 64 reconstructed subvolumes each with dimensions $32\,h^{-1}$ Mpc $\times\ 32\,h^{-1}$ Mpc $\times\ 256\,h^{-1}$ Mpc, which roughly match the CLAMATO survey geometry and volume. The exact CLAMATO survey geometry ($30\,h^{-1}$ Mpc $\times$ $24\,h^{-1}$ Mpc $\times\ 438\,h^{-1}$ Mpc) cannot be reproduced even with the 256 h^{-1} Mpc simulation, but it provides at least a rough comparison.

We generated skewers using 640^3 grids of the Lyα absorption field. We followed exactly the same procedures to generate mock CLAMATO observations from the N-body simulations as from the hydrodynamic simulations.

4.4 Void Finding

4.4.1 Calibrating the void finder

To identify cosmic voids in the IGM map, we use the void-finding procedure described in Stark et al. (2015), which is analogous to the spherical overdensity techniques used for halo-finding in N-body simulations but applied to underdensities. While this method cannot fully capture the complex and anisotropic shapes of voids, it is simple, easy to use, and easy to apply to both the density field and flux field. While alternative finders (i.e. watershed methods; Neyrinck 2008) are widely used in the literature, the complexity of these void finders may lead to poor performance in the presence of noise in the tomographic maps (e.g. Stark et al. 2015). Moreover, as this is the first attempt at void detection in a qualitatively new data set, the spherical overdensity finder has an attractive simplicity.

To identify voids, we begin by finding all points with δ_F greater than some threshold[2], or density lower than a separate threshold ("SO threshold"). Spheres are grown around all these points until the average δ_F (density) in the sphere reaches a second threshold ("SO average"). All spheres with $r \leq 2\ h^{-1}$ Mpc are removed and overlapping voids are eliminated by only keeping the void with the largest radius.

The SO threshold and SO average chosen in this paper are motivated by the values given in Table 1 of Stark et al. (2015). However, these thresholds are inapplicable to CLAMATO because they neglect continuum error in the mock sightlines and do not match the mean flux of the observations. Continuum error is particularly important at the high-transmission (high δ_F) end (Lee et al. 2015). By combining Equation 4.1 and Equation 4.5 and Taylor-expanding in the small quantity $\delta_{\rm cont}$, the change in δ_F due to continuum error is $\delta_{\rm cont} F/\langle F \rangle$; thus continuum error is more important at the high-flux end than the low-flux end. Moreover, since continuum error is correlated along a sightline, it will both create spurious voids and erase real voids. Since continuum error increases the spread of $\delta_F^{\rm rec}$ at the high-flux end, adding continuum error will lead to more points with extreme values of $\delta_F^{\rm rec}$ and thus increase the void fraction.

Following Stark et al. (2015), we begin by finding voids in the real and redshift-space density fields. We use the same real space thresholds as Stark et al. (2015), with SO threshold of $\rho = 0.2\bar{\rho}$ and SO average of $\rho = 0.4\bar{\rho}$. The SO threshold is derived from the central density of a void at shell-crossing in the spherical top-hat collapse model (van de Weygaert & Platen 2011); the SO average is less well-motivated, and was chosen by Stark et al. (2015) to best create visually-identified voids surrounded by edges (i.e. the bucket profile). The values of the SO threshold and SO average in the redshift-space density are arbitrary; we use the same values as Stark et al. (2015), $\rho_{\rm red} = 0.15\bar{\rho}$ for the SO threshold and $\rho_{\rm red} = 0.3\bar{\rho}$ for the SO average. We expect the thresholds to be lower in redshift space than in real space due to outflows from voids.

We find similar volume fractions in the N-body and hydrodynamic simulations for voids in the real-space and redshift-space density fields (17-18% in hydrodynamic simulations in

[2]Recall that δ_F has a negative sign convention with respect to overdensities.

Table 4.1: Volume fraction for different void thresholds in simulated catalogs

Field	SO thresh	SO average	Vol. frac.
ρ	$0.2\bar{\rho}$	$0.4\bar{\rho}$	0.180
$\rho_{\rm red}$	$0.15\bar{\rho}$	$0.3\bar{\rho}$	0.173
δ_F	0.192	0.152	0.180
$\delta_F^{\rm rec}$	0.220	0.175	0.180
$\delta_F^{\rm rec}$ (N-body)	0.220	0.175	0.182
CLAMATO	0.220	0.175	0.195

Note. — Comparison of volume fraction of voids in data and simulations (100 h^{-1} Mpc hydrodynamic box and 256 h^{-1} Mpc N-body box). All simulated fields are from the hydrodynamic box unless otherwise noted. The simulated fields include real and redshift-space density fields, the underlying flux δ_F, and the reconstructed flux $\delta_F^{\rm rec}$, with CLAMATO-like sightline spacing and realistic noise and continuum error. Both δ_F and $\delta_F^{\rm rec}$ are adjusted to the mean flux used in CLAMATO at $z = 2.3$.

Table 4.1 compared to 15% in N-body from Table 1 in Stark et al. 2015). The small remaining discrepancies may arise from the slightly different cosmologies of the two simulations and the fact that the N-body simulations neglect baryonic effects.

We choose the SO thresholds in the underlying flux field δ_F and the mock CLAMATO reconstruction $\delta_F^{\rm rec}$ to match the void fraction in the redshift-space density field. These thresholds are listed in Table 4.1. We do not use the same thresholds for δ_F as Stark et al. (2015), since we rescale $\langle F \rangle$ to $\langle F(z = 2.3) \rangle$ from Faucher-Giguère et al. (2008), changing the range of δ_F and necessitating the use of a different threshold. This allows us to apply the same SO thresholds to both the observations and the two simulations. Furthermore, unlike Stark et al. (2015), we do not use the same SO thresholds for δ_F and $\delta_F^{\rm rec}$, since the presence of continuum error substantially broadens the PDF of $\delta_F^{\rm rec}$, yielding a 24% void fraction in $\delta_F^{\rm rec}$ versus 18% void fraction in δ_F for the same SO thresholds. Due to the sensitivity of the void fraction to both the mean flux and the continuum error, we emphasize that picking appropriate thresholds requires realistic mock reconstructions. As a result, these thresholds are only applicable to the data presented in this paper.

In the presence of continuum error, void recovery is slightly poorer than reported in Stark et al. (2015). As in Stark et al. (2015), we characterize the fidelity of void recovery using the volume overlap fraction and match error between redshift-space density field and mock-reconstruction voids. The volume overlap fraction is defined as the fraction of the volume of voids in one catalog that overlap voids in another catalog, while the match error is defined

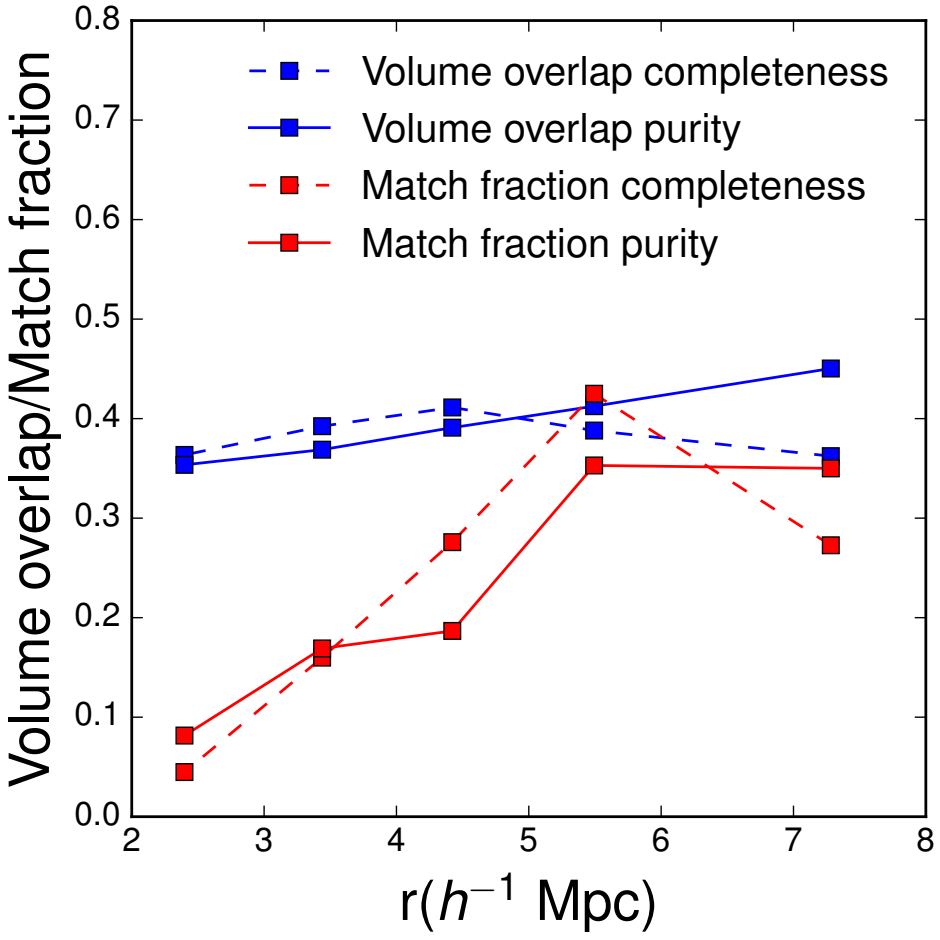

Figure 4.3: Purity and completeness of the volume overlap fraction and match fraction (fraction of voids with $\epsilon < 0.3$, see Equation 4.7) as a function of void radius, measured between voids in the mock CLAMATO-like reconstructions and the redshift-space density field in the Nyx simulation.

for each pair of voids A and B:

$$\epsilon = \frac{\sqrt{(r_A - r_B)^2 + |\vec{x}_A - \vec{x}_B|^2/3^2}}{r_A} \tag{4.7}$$

For each void in catalog A, the match error is the minimum of the match error with all voids in catalog B. Following Stark et al. (2015), two voids are defined as well-matched if $\epsilon < 0.3$; thus the match fraction is the fraction of all voids in a catalog with $\epsilon < 0.3$.

Depending on the comparison sample, these quantities can describe either the purity or the completeness of the void catalog: the completeness is characterized by the (overlap or match) fraction of density voids that are also found in the reconstruction, while the purity is characterized by the fraction of voids in the reconstruction that also exist in the density

field. We find that the completeness and purity drop 5 to 10 points compared to an identical mock observation without continuum error. Overall, we amend the conclusion of Stark et al. (2015) that 60% of $r \geq 5\ h^{-1}$ Mpc voids are recovered by CLAMATO-like IGM tomography, instead finding the recovery of these large voids to be closer to 40-45%.

In Figure 4.3, we plot the completeness and purity of the volume overlap fraction and match fraction compared between voids in mock IGM tomography and the redshift-space density field in the Nyx simulation as a function of void radius. For large voids, the completeness and purity of the match fraction and volume overlap fraction range between 30 and 45% for $r \sim 6\ h^{-1}$ Mpc. For small voids, the match fraction drops rapidly to $\sim 5\%$ for $r \sim 2\ h^{-1}$ Mpc while the volume overlap fraction drops more slowly, to 35% for $r \sim 2\ h^{-1}$ Mpc. The same behavior was seen in Stark et al. (2015), and reflects the fact that small voids may have poor centering and radius estimates due to tomographic noise artificially splitting or joining voids, but the volume overlap fraction may nevertheless remain substantial. We present Figure 4.3 as a guide for using the void catalog (Table 4.2). In Section 4.6, we only use the high-quality $r \geq 5\ h^{-1}$ Mpc sample for studying void profiles, as this sample is less contaminated by noise in the tomographic reconstruction.

4.4.2 Application to data

Applying the SO void finder to the 2017 CLAMATO IGM tomography map (Lee et al. 2017), we identify 355 $r > 2\ h^{-1}$ Mpc cosmic voids, including 48 higher-quality $r \geq 5\ h^{-1}$ Mpc voids which we use for studying the void profile (Section 4.6). These voids fill 19.5% of the tomographic volume. Table 4.2 presents the radii and positions of the voids in both sky coordinates and tomographic map coordinates. In Figure 4.4, we overplot the voids and positions of coeval spectroscopic galaxies from MOSDEF, VUDS, zCOSMOS, and our own survey (see Section 4.5 for descriptions of these surveys). The figure shows slices through the volume, sampled every $2\ h^{-1}$ Mpc in the right ascension or longitudinal direction. While most voids span more than one slice in this plot, for clarity we only show voids in the slice where their respective centers are located. Voids in Figure 4.4 appear largely devoid of galaxies, though a visual evaluation of the galaxy distribution is difficult owing to the very non-uniform selection function of the coeval galaxy spectroscopy. A quantitative analysis of galaxies within the tomography-identified voids is presented in Section 4.5.

Figure 4.5 shows projections onto the plane of the sky for the four largest voids in our volume. In each projection, $\delta_F^{\rm rec}$ is averaged across $20\ h^{-1}$ Mpc along the line of sight (roughly the diameter of these voids). We show all coeval galaxies within this slice; therefore, galaxies with a different redshift from the void center may appear to lie in a void in Figure 4.5 while actually lying outside the void boundaries.

We highlight a complex of several voids between RA 0 and $10\ h^{-1}$ Mpc, declination 0 and $20\ h^{-1}$ Mpc, and $z = 2.32 - 2.37$. While this structure is broken into many voids by the spherical void finder, it is likely that these voids are part of a single structure spanning 10-20 h^{-1} Mpc, including the largest single void in the map, located at $(x, y, z) = (1, 0, 244.5)$ h^{-1} Mpc with radius 9.40 h^{-1} Mpc. As this void is located at the very bottom of the map,

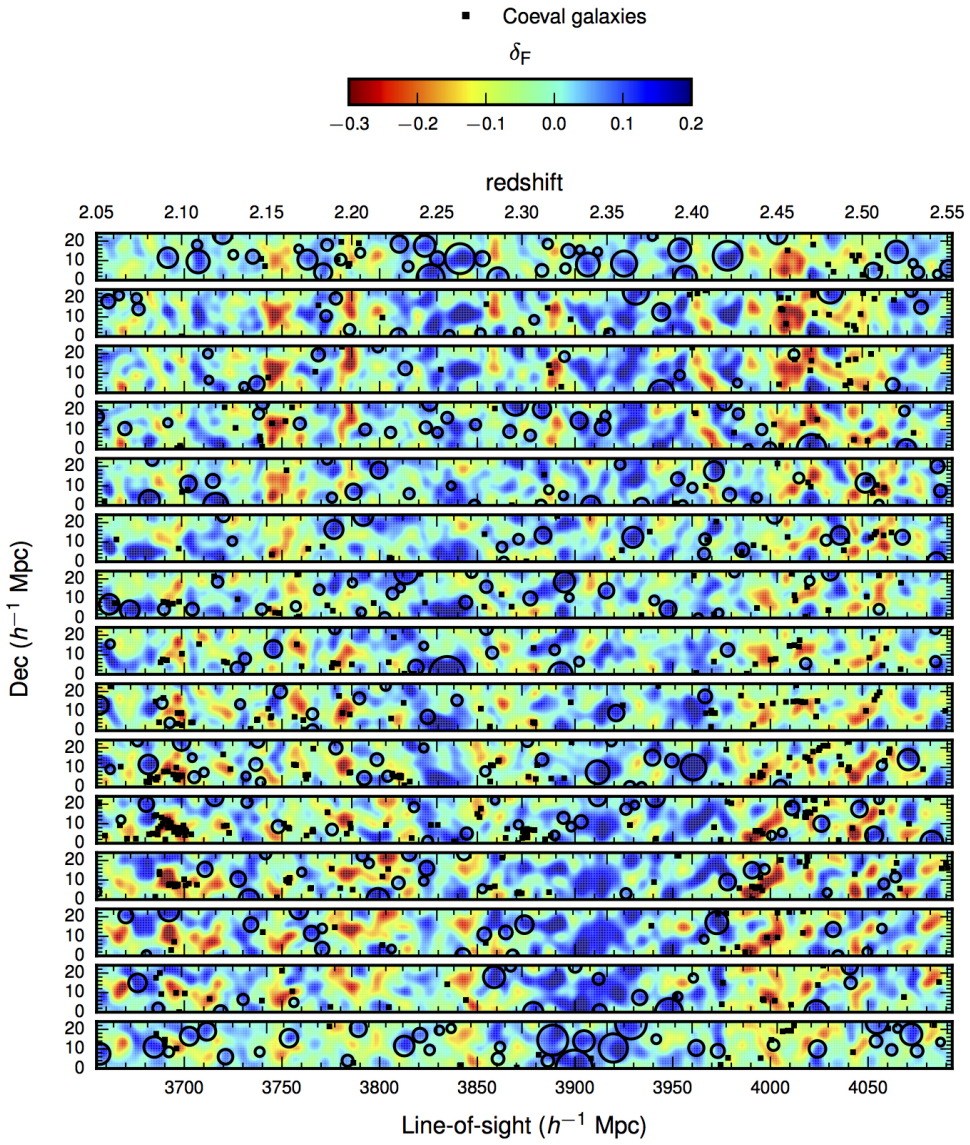

Figure 4.4: Voids (circles) and spectroscopic galaxies (squares) in the 2017 CLAMATO map. Blue indicates regions of low absorption and thus low density and high δ_F, while red indicates regions of high absorption, high density, and low δ_F. Each strip is a slice through the RA direction, spaced by 2 h^{-1} Mpc (strips are centered at RA = 1 h^{-1} Mpc, 3 h^{-1} Mpc, etc.). RA increases from the bottom strip to the top strip and declination increases from bottom to top on each strip. In each strip, we plot voids between 0 and 2 h^{-1} Mpc, 2 and 4 h^{-1} Mpc, etc. Note that we only plot voids on the strip where they are centered, although they may span multiple strips.

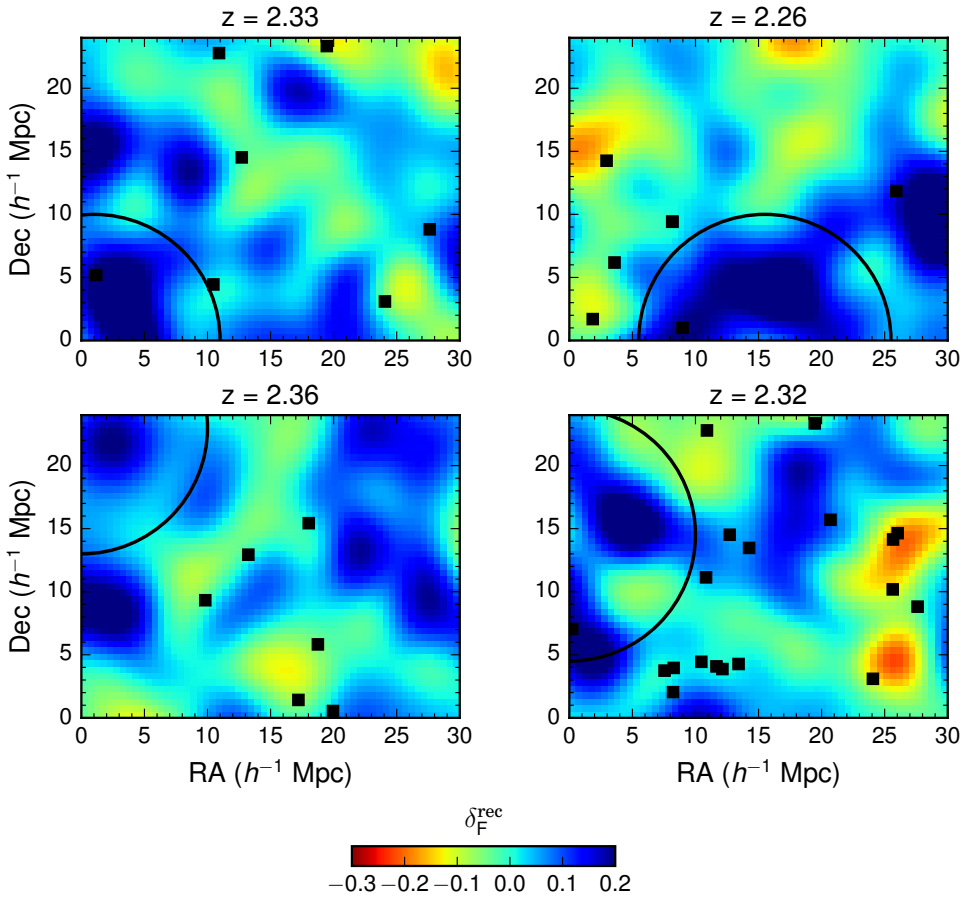

Figure 4.5: Projections of $\delta_F^{\rm rec}$ onto the line of sight for the four largest voids in Table 4.2. In each panel, we plot the mean $\delta_F^{\rm rec}$ averaged along a 20 h^{-1} Mpc length along the line of sight, centered at the redshift of each void. The black circle shows the void and black squares are coeval galaxies within ± 10 h^{-1} Mpc of the void center.

future observations extending the map will better probe this structure.

While the void fraction in CLAMATO (19.5%) is slightly higher than the void fraction in the mocks (18%), this difference can be entirely explained by sample variance. To quantify the impact of sample variance on the void fraction, we compute the void fraction in 64 subvolumes from our 256 h^{-1} Mpc N-body simulation. We find that the void fractions in the subvolumes range from 14.5% to 22.8%, with a mean of 17.9% and a standard deviation of 1.8% (Figure 4.6). The small difference between the mean void fraction of this sample and the void fraction of the full N-body box (18.2%) is attributable to the effects of an elongated geometry on the N-body subvolumes, and suggests that further deviation from the mean void fraction of the subvolumes due to the difference in survey geometry between CLAMATO and the N-body subvolumes is negligible. The void fraction in the CLAMATO

map is thus $\sim 1\sigma$ higher than the void fraction in the N-body and hydrodynamic mocks.

In principle, matching the void fraction and void statistics in the simulation requires matching Lyα statistics such as the flux PDF and the flux power spectrum. In practice, matching the flux PDF especially is notoriously difficult, creating an additional source of systematic error that may lead to disagreement between void-finding in data and in simulations. Moreover, discrepancies between theory and data are especially significant at the high-transmission end of the PDF, $F > 0.8$, where the voids lie (Bolton et al. 2016). The high-transmission end of the flux PDF is particularly sensitive to the slope of the temperature-density relationship γ (White et al. 2010). Early measurements of the flux PDF suggested that $\gamma \lesssim 1$ (Bolton et al. 2008), in contrast to $\gamma \sim 1.6$ used in simulations here, though Lee (2012) pointed out that the effects of continuum error can be degenerate with changing γ. Later measurements of the flux PDF from BOSS with better controlled continuum fitting found $\gamma \sim 1.6$ (Lee et al. 2015), though Rorai et al. (2017) claim that even with improved continuum fitting, high-resolution quasar spectra still favor $\gamma \lesssim 1$, especially in underdense regions. Overall, Lee et al. (2015) showed that careful modeling of noise and systematic errors are critical for interpreting the flux PDF of low-resolution, noisy data such as BOSS or CLAMATO, with spectral resolution, pixel noise and continuum error playing a particularly prominent role. They also find that additional discrepancies remained at high flux, which they solved by varying $\langle F \rangle$. Therefore, we carefully model pixel noise, continuum error, and Gaussian smoothing from the LRIS spectrograph. While we believe our current mocks are sufficiently realistic for an initial void detection and characterization, more careful mocks will be required for future cosmological analyses of IGM cosmic voids.

4.5 Void-Galaxy Counts in Cells

The cosmic voids in the CLAMATO volume are by far the most distant sample of cosmic voids known at the present time. In comparison with the most distant $z \sim 1$ voids previously detected in galaxy redshift surveys (e.g., Conroy et al. 2005, Micheletti et al. 2014), our voids at $z \sim 2.3$ are $\sim 1.7\times$ further in terms of comoving distance. Moreover, since CLAMATO achieves $\gtrsim 3$ times better density field resolution than existing or upcoming galaxy surveys at $z \sim 2$, it represents the best method for detecting high-z voids for the immediate future (although all-sky interferometric 21cm surveys may be able to detect voids at $z \sim 1-2$; White & Padmanabhan 2017).

We validate the void-finding technique by counting coeval spectroscopic galaxies within the tomography-identified voids and comparing these counts to the number of galaxies within random cells with the same radius distribution and volume fraction. Exploiting the rich set of spectroscopic data that already exists within the COSMOS field, we use 110, 109, 118, and 95 galaxies from the VUDS (Le Fèvre et al. 2015), MOSDEF[3] (Kriek et al. 2015), CLAMATO, and zCOSMOS-Deep (Lilly et al. 2007) surveys respectively, which directly overlap with the

[3]We use their 2016 August data release; http://mosdef.astro.berkeley.edu/for-scientists/

Table 4.2: Voids in CLAMATO 2017 Map

Tomographic map position (h^{-1} Mpc)			Void Radius	Sky position		
x	y	z	(h^{-1} Mpc)	α (J2000)	δ (J2000)	redshift
1.0	0.0	244.5	9.40	149.96480	2.15000	2.33
15.5	0.0	179.5	9.10	150.17943	2.15000	2.26
0.0	23.0	273.5	7.90	149.95000	2.49016	2.36
0.0	14.5	233.5	7.70	149.95000	2.36445	2.32
29.5	11.0	186.0	7.65	150.38665	2.31268	2.26
23.0	0.0	366.0	7.45	150.29044	2.15000	2.47
29.5	12.5	323.0	7.40	150.38665	2.33487	2.42
0.0	10.5	264.5	7.25	149.95000	2.30529	2.35
29.5	1.0	171.0	7.00	150.38665	2.16479	2.25
3.5	0.0	293.0	6.95	150.00181	2.15000	2.39

Note. — Table 2 is published in its entirety in the machine-readable format. A portion is shown here for guidance regarding its form and content.

Table 4.3: Significances of galaxy underdensities in voids from IGM tomography

Galaxy survey	N_{gal}	Galaxies in voids	Galaxies in randoms (mean)	Galaxies in randoms (σ)	Significance
VUDS	110	13	20.36	4.29	0.0491
MOSDEF	109	6	18.49	5.45	0.0047
CLAMATO	118	10	22.07	4.67	0.0033
zCOSMOS	95	8	18.63	4.12	0.0035

Note. — Significance of galaxy underdensities in 4 coeval galaxy surveys. CLAMATO uses the galaxies spectroscopically confirmed by our data that lie within the map volume.

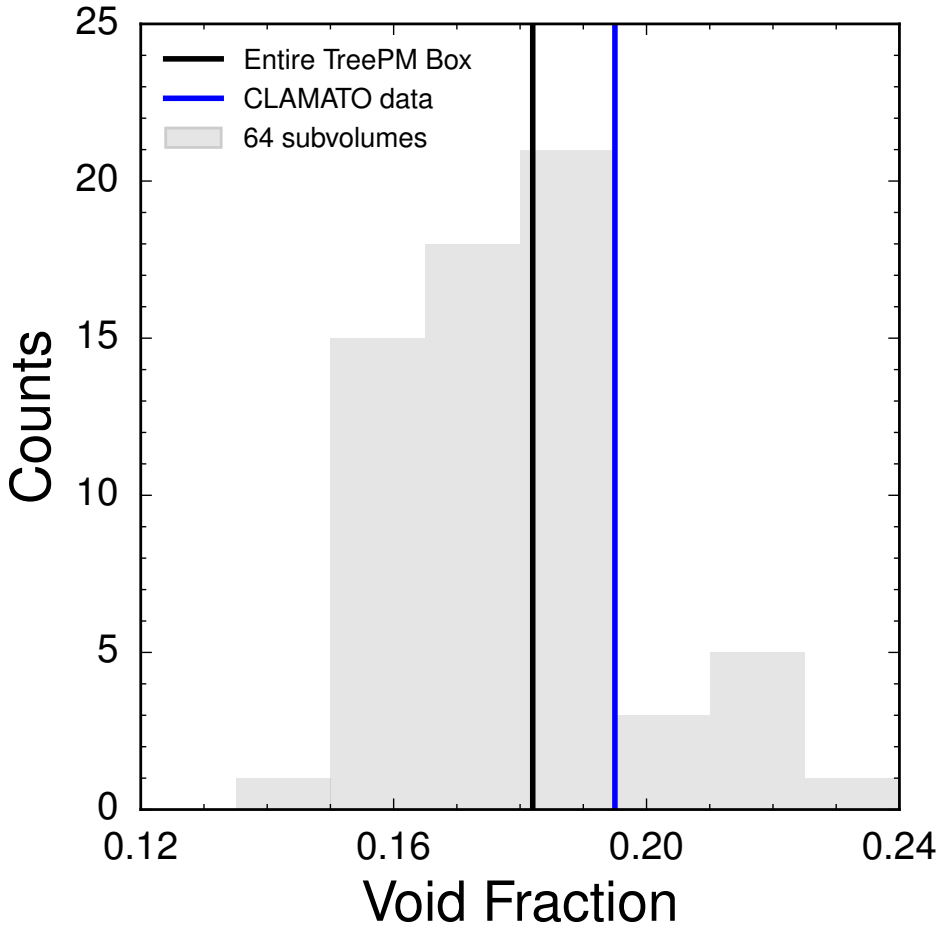

Figure 4.6: Volume fraction of cosmic voids from 64 subvolumes each with dimensions $32 \times 32 \times 256$ h^{-1} Mpc (light gray histogram), extracted from the N-body 256 h^{-1} Mpc simulation box, compared to void fraction from entire box (black) and in CLAMATO data (blue).

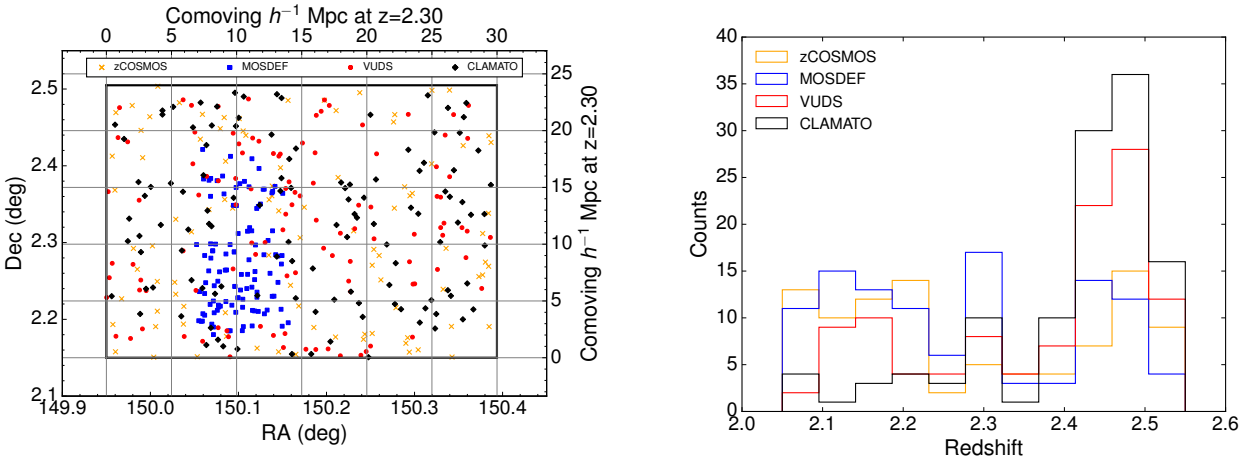

Figure 4.7: *Left:* Positions of galaxies in the COSMOS field with known spectroscopic redshifts that are coeval with the $2.05 < z < 2.55$ CLAMATO map. The black box indicates the footprint of the CLAMATO map. *Right:* Redshift distribution of coeval galaxies.

CLAMATO map volume at $2.05 < z < 2.55$. By CLAMATO, we mean galaxies that were spectroscopically confirmed by CLAMATO to lie inside the map volume, e.g. sightlines for the lower redshift part of the map or galaxies with redshifts too low to be viable sightlines.

In Figure 4.7, we show the redshift distribution of these coeval galaxies and their spatial coverage compared to the CLAMATO area. These surveys differ in their redshift accuracy: the NIR-based redshifts from MOSDEF are most accurate (Steidel et al. 2010; $\sigma_v \sim 60$ km s^{-1}, corresponding to $\sigma_{los} \sim 0.7\ h^{-1}$ Mpc), followed by the optical redshifts from VUDS, CLAMATO, and zCOSMOS (Steidel et al. 2010, Kriek et al. 2015; $\sigma_v \sim 300$ km s^{-1}). For this analysis, we do not include galaxies from two overlapping spectroscopic surveys, 3DHST and ZFIRE. The grism redshifts from 3DHST have redshift uncertainties of $\sigma_v \gtrsim 500$ km s^{-1} (Kriek et al. 2015, Momcheva et al. 2016b) which are comparable to the typical sizes of our voids of a few cMpc. The ZFIRE survey (Nanayakkara et al. 2016) specifically targeted at the $z \sim 2.1$ protocluster (Spitler et al. 2012) and is therefore a poor choice for void validation because the galaxies will not lie in an average environment.

Galaxy positions are converted to x, y, z coordinates with the origin at $z = 2.05$, right ascension 149.95° and declination 2.15° using the transverse comoving distance evaluated at $z = 2.3$. We convert galaxy redshift z_{gal} to coordinate position z using

$$z = (z_{gal} - 2.05) \left.\frac{d\chi}{dz}\right|_{z=2.3} \tag{4.8}$$

Therefore, the conversion between (α, δ, z) and map coordinates (x, y, z) is identical for coeval galaxies and Lyα forest pixels.

`data-releases/`.

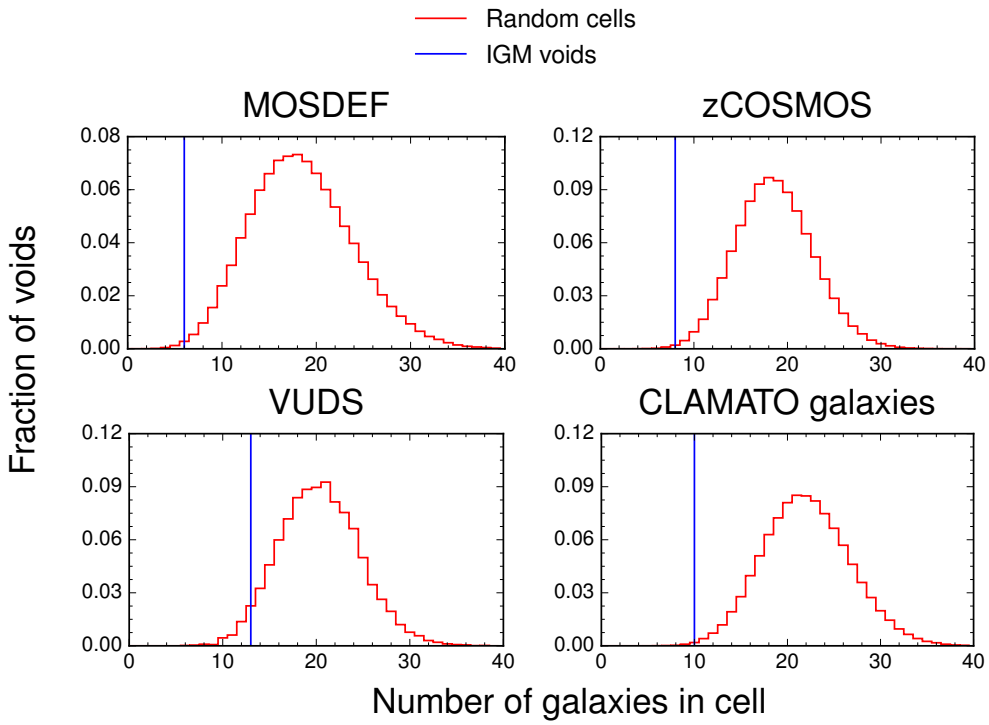

Figure 4.8: Distribution of number of galaxies in random cells (red), compared to number of galaxies in IGM voids (blue line), for 4 galaxy surveys. The p value is the fraction of the red histogram to the left of the blue line.

We emphasize that this comparison is simply a validation of the cosmic void sample, and that the void-finding on the tomographic reconstruction is entirely self-sufficient. Conversely, the spectroscopic redshift galaxy samples within the field are too sparse and incomplete[4] to define cosmic voids, but should be sufficient to falsify a spurious detection of cosmic voids.

To compare the abundance of galaxies in voids with a control sample, we create many realizations of random catalogs with the same radius function as the void catalog. Many of the largest CLAMATO voids are preferentially located near the edge of the CLAMATO volume. Therefore, in order to reproduce the correct volume fraction in the random catalogs, we require each random cell to have the same distance from the boundary as the corresponding void with the same radius.

In detail, for each void in the catalog, we create a random cell with the same radius. If the void is located in a "corner" of the volume (i.e. the distance between both its x and y positions and the box edge is smaller than the void radius), we assign the random's xy position by rotating the void's xy position about the origin by either 0°, 90°, 180°, or 270°. We then randomly assign the z position. For voids not located in a corner, we randomly assign the position along the faces of a rectangular prism with distance to the CLAMATO volume edge equal to the minimum distance between the void center and the box edge. Just like the voids, the random cells are required to be non-overlapping. We find that the random cells fill 18.9% of the CLAMATO volume (on average), compared to 19.5% of the CLAMATO volume filled by voids. As a sanity check that the random cells are indeed unbiased regions, we also find in the random cells an average absorption of $\langle \delta_F^{\rm rec} \rangle = -6.57 \times 10^{-3} \pm 5.1 \times 10^{-3}$ (1σ standard deviation) compared to $\langle \delta_F^{\rm rec} \rangle = -7.23 \times 10^{-3}$ for the entire map. In other words, they are both consistent with zero as would be expected by definition (Equation 4.1).

For MOSDEF, we use separate random catalogs covering the smaller area probed by this survey (Figure 4.7) rather than the entire CLAMATO volume. This allows the random catalogs to accurately reproduce the void fraction within the MOSDEF survey region. We use an area that extends 3 h^{-1} Mpc beyond the approximate MOSDEF footprint: in this case, 150.001° > R.A. > 150.203° and 2.150° > Dec > 2.444°. We include voids that are slightly outside the MOSDEF footprint because these voids may still overlap with MOSDEF galaxies; we choose a 3 h^{-1} Mpc buffer because the average void size is about 3 h^{-1} Mpc. The random cells fill 12.5% of the MOSDEF region volume, compared to 12.6% void fraction in this region, with average $\delta_F^{\rm rec}$ -0.0113 ± 0.0091. The smaller void fraction may be due to the fact that the MOSDEF region is slightly overdense, with $\langle \delta_F^{\rm rec} \rangle = -0.0121 \pm 0.0002$ (standard error of the mean) compared to $\langle \delta_F^{\rm rec} \rangle = -0.0073 \pm 0.0001$ in the entire map.

The significance of the galaxy underdensity in tomographic voids is the probability that the number of galaxies in random cells is less than or equal to the number of galaxies in voids. We calculate this probability by counting the number of realizations of the random catalog with fewer galaxies in the randoms than in the tomographic voids, giving a p value for each galaxy survey. Assuming that the constraints from the different galaxy surveys

[4] We find $n_g \sim 1.1 \times 10^{-3} h^3\,{\rm Mpc}^{-3}$ for VUDS, CLAMATO, and zCOSMOS redshifts combined, compared to $n_g \sim 5 \times 10^{-3} h^3\,{\rm Mpc}^{-3}$ in the VIPERS survey which detected $z \sim 1$ voids.

are independent, the combined constraint is simply the product of the p values for the individual surveys. The distribution of galaxy counts in random cells is neither Gaussian nor Poissonian, particularly as it approaches zero galaxies where the data lies; therefore, calculating p values by direct simulation is essential and we emphasize that the conversion to σ is purely for illustrative purposes. The error on p values computed this way are given by $\sqrt{p(1-p)/N}$. In order to achieve $< 10\%$ errors on p values, we use 10,000 realizations of the random catalog for VUDS, and 300,000 realizations for CLAMATO, MOSDEF, and zCOSMOS.

We report significances in Table 4.3 and compare the number of galaxies in voids to the number of galaxies in random cells in Figure 4.8. Assuming that the galaxy surveys are independent, we find a combined p value of 3×10^{-9}, equivalent to a 5.95σ detection of galaxy underdensities in the tomography-identified voids.

The significance of the galaxy underdensity in the tomographically-identified voids is similar for all four surveys, although modestly lower for VUDS. These galaxies are the faintest of the surveys used ($\langle r \rangle = 24.9$, compared to $\langle r \rangle = 24.1$ for CLAMATO and zCOSMOS and $\langle r \rangle = 24.8$ for the primarily quiescent MOSDEF sample), and are thus likely have lower bias, causing them to cluster towards voids (Conroy et al. 2005).

4.6 Void properties

4.6.1 Void radius function

We compare the void radius function in CLAMATO to the void radius function in mock observations and in the real-space density field (Figure 4.9). Due to edge effects, voids are significantly more likely to be found near the map boundaries of both the CLAMATO data and the 64 subvolumes of the N-body box with roughly CLAMATO-like geometry. As a result, we omit voids found within one void radius of the box edge. To compute the void radius function, we weight each void by the effective volume over which it could have been observed: for a void of radius r, this volume is $(30-2r)(24-2r)438\ h^{-3}\ \mathrm{Mpc}^3$. Omitting voids near the box edge leads to substantially better agreement with the void radius function in both the density field and the full-volume reconstruction. We also overplot the range of void radius functions found in the 64 subvolumes to give an estimate of the impact of sample variance on this measurement; we do not plot the range for large voids where the Poisson errors become large due to the relatively small volume of both the CLAMATO and simulated survey volumes.

We compare the measured void radius function to predictions from excursion set theory (Sheth & van de Weygaert 2004, Jennings et al. 2013). The excursion set model associates voids with spherical regions that have just undergone shell crossing and have thus attained an average density of $0.2\bar{\rho}$. The evolution of voids is modeled as a random walk with two barriers, a lower barrier at $\delta_v = -2.71$, the linear underdensity of shell-crossed voids, and an upper barrier, δ_c, modeling voids squeezed out of existence by surrounding overdensities, ranging

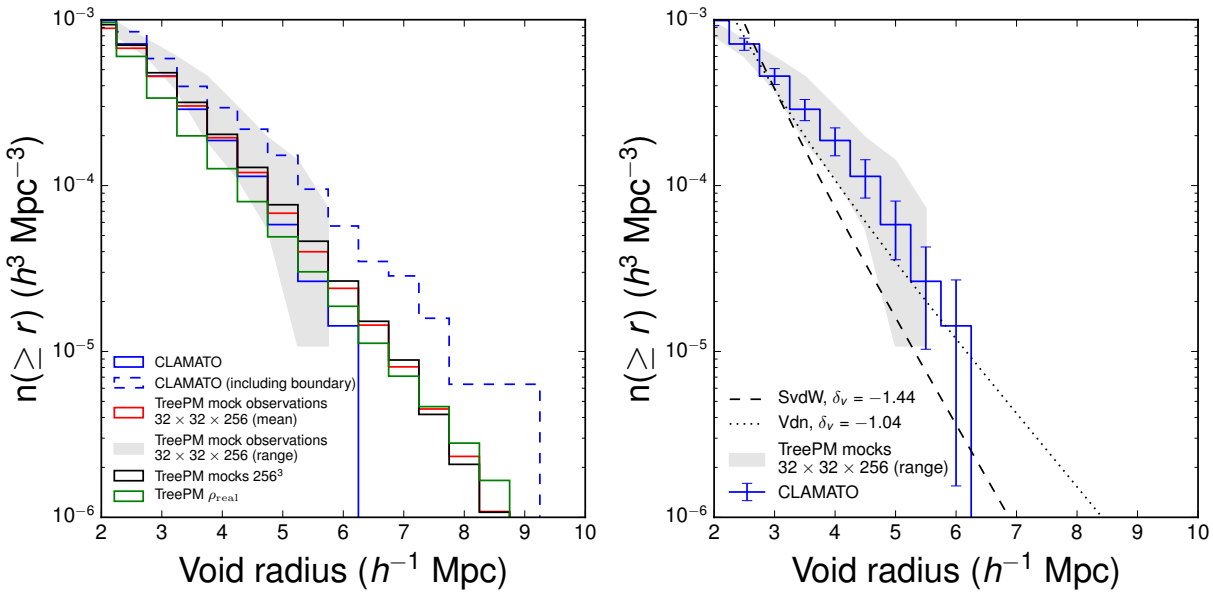

Figure 4.9: *Left:* Comparison of void radius function in CLAMATO to void radius function from the N-body real-space density field; the mean and range of the void radius function from mock observations constructed from 64 $(32 \times 32 \times 256)$ $h^{-3}\,\mathrm{Mpc}^3$ subvolumes of the N-body box; and the void radius function from a mock observation constructed from the full 256^3 $h^{-3}\,\mathrm{Mpc}^3$ box. In all cases we exclude voids with distance to the boundary smaller than the void radius, except for the blue dashed line, which gives the abundance of all CLAMATO voids and thus shows the impact of edge effects on the CLAMATO void abundance. In all cases, we have centered each histogram bin over the corresponding void radius: i.e. the bin centered at 3 $h^{-1}\,\mathrm{Mpc}$ gives the number of voids with radius greater than or equal to 3 $h^{-1}\,\mathrm{Mpc}$. *Right:* Comparison of the CLAMATO void radius function to excursion set models (black lines), with the range of the 64 N-body subvolumes overplotted to give a sense of the error on the measured void radius function. Error bars on the data are Poisson error bars on the counts in each bin, divided by the effective volume of that bin.

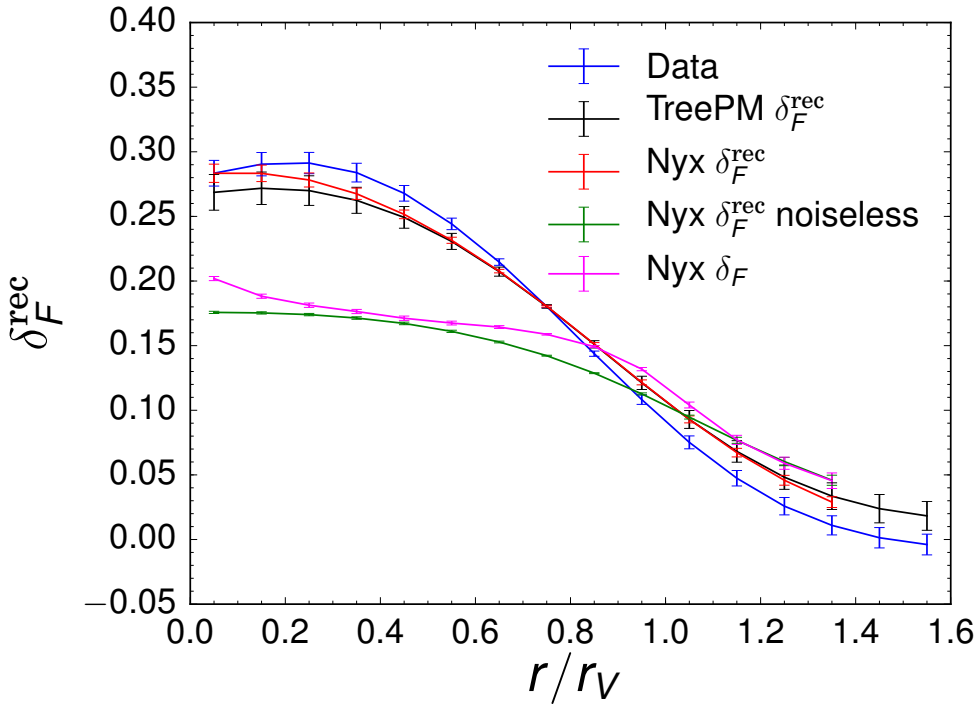

Figure 4.10: Radially-averaged void profiles in data (blue), mock observations (black for N-body box and red for hydrodynamic box), noiseless mock observations (green) and underlying δ_F (magenta), stacked in units of the void radius r_V, for all voids with $r \geq 5\ h^{-1}\,$Mpc. Errorbars for the Nyx profile are estimated using 1000 realizations of the void catalog generated via bootstrap resampling, while errorbars for the TreePM and data profiles are generated from the standard deviation over the 64 subvolumes of the TreePM box.

between 1.06 and 1.69. We fit two excursion set models to the data, the number-density-preserving model of Sheth & van de Weygaert (2004) (SvdW) and the volume-preserving model of Jennings et al. (2013) (Vdn). $\delta_v = -2.71$ provides a poor fit in both cases, so we allow the void threshold to vary as a free parameter, finding $\delta_v = -1.44$ (-1.04) for the SvdW (Vdn) models. We use χ^2 minimization to determine the best-fit δ_v, with error bars given by the Poisson errors on the number of voids in each bin divided by the effective volume of that bin, i.e. $(30 - 2r)(24 - 2r)438\ h^{-3}$ Mpc^3 for a bin at radius r. Owing to the large range in $n(\geq r)$, we minimize χ^2 in log-space rather than linear space. We find that neither model can adequately explain the void radius function at small r ($< 3\ h^{-1}$ Mpc), where the error bars are substantially smaller than at large r. As a result, the best-fit curves for both models are "tilted" relative to the data at $r \geq 3\ h^{-1}$ Mpc due to the smaller errorbars and thus larger impact of the points at small r. While neither model can fit the void radius function at small radii, the Vdn model adequately fits the data at large r, and provides a notably better fit than the SvdW model.

We expect a higher value of δ_v than -2.71 for the void radius function in our work because we use a higher mean overdensity of voids ($\bar{\rho} = 0.4$); indeed, our results are similar to the results of Jennings et al. (2013), who found $\delta_v = -1.24$ for $\bar{\rho} = 0.4$. Our results also lie in the same general range as previous results, which find δ_v between -0.2 and -1.0 (Sutter et al. 2014b, Pisani et al. 2015, Nadathur & Hotchkiss 2015). However, Jennings et al. (2013), working between $z = 0$ and 1, recommend models with considerably smaller void abundance than found here (1/5 the abundance of the Sheth & van de Weygaert (2004) prediction with $\delta_v = -1.24$, about 5 times lower than our data).

4.6.2 Radial void profile

We plot radially-averaged void profiles in Figure 4.10 for all voids with $r \geq 5\ h^{-1}$ Mpc, normalizing each void to its void radius and stacking in units of the void radius r/r_V. There is good agreement between void profiles in data and mock observations, with $\chi^2 = 22.1$ over 16 radial bins between the void profile in CLAMATO and the void profile in mock observations from the N-body simulations. Since each bin is $0.1r_v \sim 0.5\ h^{-1}$ Mpc, much smaller than $\langle d_\perp \rangle = 2.5\ h^{-1}$ Mpc, the void profile is highly correlated between neighboring bins, so we cannot assume a diagonal covariance matrix when computing χ^2 (i.e. the χ^2 quoted above uses the full covariance matrix and is much lower than if this covariance matrix were diagonal). We compute the covariance matrix using the 64 subvolumes of the N-body box and scale down the covariance by 0.8, the volume ratio between the N-body subvolumes and the CLAMATO volume. We also use the unbiased estimator of Hartlap et al. (2007) for the inverse covariance matrix, for the case where the mean is estimated from the data (their Equation 17). The strong agreement between the radial void profile in mock observations and data suggests that approximations in the map-making process (e.g. the distance-redshift and angle-redshift conversion discussed in Section 6.2) make only a minor impact on the void profile.

The void profile in mock observations traces the void profile in the underlying Lyα flux field, δ_F, well for $r > r_V$ but deviates badly inside the void. This deviation is due almost entirely to noise in the spectra, with the profiles in noiseless reconstructions resembling the δ_F profiles much more closely. Unfortunately, the deviation between void profiles in $\delta_F^{\rm rec}$ and δ_F means that void profiles in the reconstruction do not trace void profiles in matter, and thus we do not try to fit a functional form to the void profile (e.g. Ceccarelli et al. 2006, Hamaus et al. 2014, White & Padmanabhan 2017) as it could not be compared with low-redshift results.

Qualitatively, the void profile in the data is missing the "compensation wall" that is present in some low redshift void profiles, particularly voids with $r < 20\ h^{-1}$ Mpc like those discussed here (Hamaus et al. 2014). It is unclear whether the absence of a compensation wall is indicative of physical differences between high and low redshift voids, or is merely an artifact of our void finder and void sample. For instance, while our voids are small at $z \sim 2.3$, they will become much bigger by $z \sim 0$: Sheth & van de Weygaert (2004) find $r_v \propto (1+z)^{-2/(3+n)}$, where $n \sim -1.5$ is the slope of the power spectrum on scales of the void size. Therefore 5 h^{-1} Mpc voids at $z = 2.3$ correspond to 25 h^{-1} Mpc voids at $z = 0$, which generally have a very weak or absent compensation wall (Cai et al. 2015, Hamaus et al. 2016). On the other hand, White & Padmanabhan (2017) suggest that spherical overdensity finders may not find compensation walls, while Cai et al. (2016a) argue that compensation walls are only present in voids found in overdense environments.

We also study the impact of redshift-space distortions on $z \sim 2$ voids. Redshift-space distortions modify the void profile along the line of sight and are often measured using the quadrupole of a correlation function or void profile. Numerical simulations find that for $r \gtrsim r_V$ in uncompensated voids, iso-density contours are flattened along the line of sight in the same sense as the Kaiser (1987) effect for overdensities (Cai et al. 2016a, Nadathur & Percival 2017). On smaller scales, nonlinear effects such as velocity dispersion may lead to extended profiles along the line of sight (Cai et al. 2016a), although the magnitude of these effects is unclear (see discussion in Nadathur & Percival 2017). We replicate these findings for simulated voids at $z \sim 2$ in the underlying flux and density fields for the entire $256^3\ h^{-3}$ Mpc^3 box.

However, we find that when measured in $(32 \times 32 \times 256)\ h^{-3}$ Mpc^3 CLAMATO-like subvolumes, the void quadrupole is significantly distorted by edge effects in the Wiener filter and void finder. We also find that the void quadrupole is significantly distorted by continuum error, since continuum error is correlated along the line of sight. Due to the large impact of these systematic effects, we do not present redshift-space distortion measurements in CLAMATO voids here. Future surveys with larger contiguous area (e.g. an IGM tomography survey on the Subaru Prime Focus Spectrograph over 20 deg^2) will be less impacted by continuum errors: we find very good agreement between the void quadrupole in a $128 \times 128 \times 256\ h^{-3}$ Mpc^3 subvolume and the full TreePM box. However, continuum error will remain a major source of systematic error for modeling redshift-space distortions in Lyα forest voids: either the effects of continuum error must be removed, e.g. by ignoring correlated pixels along the line of sight, or we require accurate end-to-end modeling of the effects of continuum error

on void shapes.

4.7 Conclusions

We present the first detection of cosmic voids at $z \sim 2$ using a spherical overdensity finder applied to a tomographic map of the 3D Lyα absorption field from the CLAMATO survey carried out on the Keck-I telescope. By targeting background LBG and quasar sightlines with mean transverse separation 2.5 h^{-1} Mpc at $z \sim 2.3$, we create a Wiener-filtered map of the neutral hydrogen density on few Mpc scales, which is an excellent tracer of the underlying matter density. This allows us to measure the density field on scales considerably smaller than current galaxy surveys can achieve at this redshift, enabling cosmic void detection at far greater ($\sim 1.7\times$) cosmic distance than hitherto the most distant cosmic voids at $z \sim 1$.

Building on the results of Stark et al. (2015), we use realistic mock observations based on hydrodynamical and N-body simulations to calibrate thresholds for identifying voids in IGM maps. This is necessary to better model the Lyman-α forest and continuum errors in the survey, which were neglected in Stark et al. (2015). Within the simulations, we find worse void recovery from IGM tomography than Stark et al. (2015): $\sim 40\%$ of tomographically-identified voids are well-matched to density-field voids for $r \geq 5$ h^{-1} Mpc.

Using thresholds calibrated from simulations, we apply the void finder to the CLAMATO map to find a 19.5% volume fraction of voids. After removing voids affected by edge effects, we find good agreement between the void radius function in simulations and data. Excursion set models can fit the void radius function only if the excursion set threshold is adjusted considerably from the Sheth & van de Weygaert (2004) prediction of -2.71.

We also study the stacked void profiles for the higher-confidence subsample of large ($r \geq 5$ h^{-1} Mpc) voids. As in Stark et al. (2015), we find no compensation ridge in the radial void profiles, consistent with other spherical overdensity finders (White & Padmanabhan 2017).

We validate the void detection by finding that these voids are $\sim 6\sigma$ underdense in coeval galaxies from the MOSDEF, VUDS, and zCOSMOS spectroscopic redshift surveys, as well as CLAMATO-confirmed galaxies falling within the tomographic volume. While the galaxy catalogs are unable to detect voids on their own, they validate the detection of voids in IGM tomography by showing that our voids have significantly fewer galaxies than random regions with the same radius distribution.

Identifying cosmic voids requires both a large volume and a reasonably dense sampling of the density field. Previous detections of voids from galaxy surveys have extended to $z \sim 1$ (Conroy et al. 2005, Ceccarelli et al. 2006, Sutter et al. 2012, Micheletti et al. 2014, Mao et al. 2017b, Sánchez et al. 2017), while IGM tomography can detect voids at $z \sim 2.3$, providing by far the most distant sample of voids owing to much denser sampling of the density field than galaxy surveys at comparable redshifts. Moreover, upcoming surveys will dramatically increase the number of $z \sim 2.5$ voids detected via IGM tomography. We find 48 voids with $r \geq 5$ h^{-1} Mpc (for which we expect $\geq 45\%$ void recovery); the full CLAMATO survey will cover $\sim 3-5$ times more volume than the data used in this paper and thus we

expect to find > 100 $r \geq 5$ h^{-1} Mpc voids, in line with the estimates in Stark et al. (2015). Moreover, the Prime Focus Spectrograph (PFS) on the Subaru telescope will begin operation by 2020 (Takada et al. 2014); it will allow for surveys covering a much wider area, owing to the much larger field of view of PFS compared to LRIS. A dedicated IGM tomography survey building on the PFS galaxy evolution survey could cover 15-20 deg^2 with sightline separation 3-4 h^{-1} Mpc, i.e. comparable or slightly worse sampling than CLAMATO — the exact parameters are currently under discussion within the PFS collaboration. Thus, such a survey on PFS could find 2000 $z \sim 2.5$ voids (Stark et al. 2015) with comparable fidelity to CLAMATO. The larger area could be particularly crucial to detecting void redshift space distortions at high significance.

At low redshifts, voids have been used for Alcock-Paczynski tests to measure cosmological parameters, since voids are on average spherical in real-space (Sutter et al. 2014c, Mao et al. 2017a). Stark et al. (2015) estimates that a competitive high redshift measurement of the Alcock-Paczynski parameter will require 10,000 voids, which could be achieved by a dedicated 100-night tomography survey on PFS, or by shorter surveys on even more ambitious instruments such as the Maunakea Spectroscopic Explorer (McConnachie et al. 2016) or the Billion Object Apparatus (Dodelson et al. 2016). On the other hand, Stark et al. (2015) find that linear theory accurately predicts the radial velocity profile of voids, suggesting that studying the velocity field either to infer cosmological parameters (e.g. Hamaus et al. 2016; using redshift-space distortions at low redshift) or to test modified gravity theories could be promising avenues of exploration. In particular, Clampitt et al. (2013) estimates that modified gravity theories could alter void profiles in a way that could be observed with samples of 20 voids.

Finally, voids offer an intriguing test-bed for galaxy formation, as they contain halos that have grown primarily by diffuse accretion rather than mergers (Fakhouri & Ma 2009). Existing studies of galaxy formation in voids have been limited to low redshift, where differences in void galaxy properties can be attributed largely to their different stellar masses (Hoyle et al. 2005, Tinker et al. 2008, Alpaslan et al. 2015, Penny et al. 2015, Beygu et al. 2016). However, this may be different at high redshift, particularly since the global star formation rate at $z \sim 2$ is much higher than at $z \sim 0$. In principle, we have already identified 35 galaxies in voids; however, if a tomography-identified void contains a galaxy, it is more likely that it is a fluctuation due to noise than otherwise. Stark et al. (2015) point out that "true" voids are expected to be devoid of such bright galaxies, but that voids could contain faint $L \sim 0.3L_\star$ galaxies that could be observed by the NIRSPEC spectrograph on JWST.

Acknowledgments

We thank Shirley Ho, Uroš Seljak, Joanne Cohn, and Zachary Slepian for helpful comments on this work. K.G.L. acknowledges support for this work by NASA through Hubble Fellowship grant HF2-51361 awarded by the Space Telescope Science Institute, which is operated by the Association of Universities for Research in Astronomy, Inc., for NASA, under

contract NAS5-26555. We are also grateful to the entire COSMOS collaboration for their assistance and helpful discussions. Calculations presented in this paper used resources of the National Energy Research Scientific Computing Center (NERSC), which is supported by the Office of Science of the U.S. Department of Energy under Contract No. DE-AC02-05CH11231. The data presented herein were obtained at the W.M. Keck Observatory, which is operated as a scientific partnership among the California Institute of Technology, the University of California and the National Aeronautics and Space Administration (NASA). The Observatory was made possible by the generous financial support of the W.M. Keck Foundation. The authors thank Yong's Kal-Bi in Waimea, HI, for vital sustenance during our observations. The authors also wish to recognize and acknowledge the very significant cultural role and reverence that the summit of Maunakea has always had within the indigenous Hawai'ian community. We are most fortunate to have the opportunity to conduct observations from this mountain.

4.A Publicly available CLAMATO void catalog

We have made the CLAMATO void catalog (Table 4.2) publicly available on Zenodo (https://doi.org/10.5281/zenodo.1295839). We have also included void catalogs from the mock CLAMATO-like observations in the Nyx and TreePM box, including void catalogs from both the full TreePM box and the 64 subvolumes, and void catalogs from the (real and redshift-space) density fields and underlying flux of the Nyx simulation, corresponding to the void fractions reported in Table 4.1. We have also included the mock CLAMATO maps from these simulations.

Chapter 5

Thermal Sunyaev-Zel'dovich effect from quasar host halos

Abstract

The thermal Sunyaev-Zel'dovich (tSZ) effect is a powerful probe of ionized gas in massive halos. Recent measurements of the tSZ signal around quasars have interpreted it as arising from thermal energy injection via AGN feedback into the gas directly adjacent to the accretion disk, rather than from virialization of hot gas in the host halo. In this paper, we examine the tSZ-quasar cross-correlation. We show that on large scales, the cross-correlation is dominated by the two halo term from correlated halos around the AGN, rather than from hot gas near the AGN or its host halo. In this regime, the tSZ-quasar cross-correlation probes the Compton-y bias of the universe, essentially the amplitude and redshift distribution of the thermal pressure from hot halo gas. Because quasar samples extend over a broad redshift range, the tSZ-quasar cross-correlation is an excellent tomographic probe of the amplitude of the halo gas pressure profile, which is in turn sensitive to details of AGN feedback and cluster formation. On small scales, the tSZ-quasar cross-correlation is highly sensitive to the uncertain halo mass distribution of quasars. We fit physically-motivated quasar models, built from galaxy-black hole and stellar mass-halo mass scaling relations, to luminosity function and clustering data. We then show that the tSZ-quasar cross-correlation is a sensitive discriminant of these models. We argue that the tSZ signal from fainter upcoming quasar samples (i.e. in the DESI survey) is likely dominated by virialization of the host halo rather than thermal energy injection from AGN feedback. Therefore, future small scale quasar-tSZ cross-correlations may play a powerful role in testing quasar formation and evolution.

5.1 Introduction

The thermal Sunyaev-Zel'dovich effect (Sunyaev & Zeldovich 1970, 1972) arises from inverse Compton scattering of CMB photons by hot electrons along the line of sight, distorting

the blackbody spectrum of the CMB. Massive individual clusters have been detected via their tSZ flux (e.g. Carlstrom et al. 2002), while on the other extreme, large-area CMB and large-scale structure surveys have enabled stacking analyses around halos down to $4 \times 10^{12}\ M_\odot$ (Hand et al. 2011, Planck Collaboration et al. 2013b, Greco et al. 2015). Furthermore, detections of the global tSZ signal (Planck Collaboration et al. 2014e) have enabled constraints on σ_8, taking advantage of the scaling $C_\ell^{tSZ} \sim \sigma_8^7$ (Komatsu & Seljak 2002).

The tSZ spectral distortion along a single line of sight is given by

$$\frac{\Delta T}{T_{\rm cmb}} = \left[x \frac{e^x + 1}{e^x - 1} - 4 \right] \ y \tag{5.1}$$

where $x \equiv h\nu / K T_{\rm cmb}$ and y is the dimensionless Compton-y parameter, proportional to the integrated electron pressure along the line of sight. The tSZ distortion is negative at low frequencies and crosses zero at 217 GHz. A more observationally relevant quantity is Y, the Compton-y parameter integrated over some aperture (e.g. the radius of a halo or the beam of a CMB map) and thus with units of solid angle.

Y is proportional to the pressure and is thus sensitive to any source of keV electrons. At cluster masses, the requisite electrons are generated primarily by gravitational heating as they fall into the deep potential well. Since gravity is scale-free and the power spectrum is close to a power law on the relevant scales, this process leads to a nearly power-law relationship between Y and the halo mass $Y \propto M^{5/3} E(z)^{2/3}$ (Kaiser 1986), where $E(z) = H(z)/H_0 = \sqrt{\Omega_m (1+z)^3 + \Omega_\Lambda}$. In the purely gravitational case, deviations from power-law behavior due to the preferred scale of structure formation are modest. Non-gravitational physical processes with preferred length scales (such as radiative cooling, star formation, and feedback) will break the self-similar scaling relation, leading to mass dependence of the temperature and gas density profiles (Kravtsov & Borgani 2012). In general, deviations from self-similarity in simulations are mild and primarily affect the mass-dependence of the scaling, for which deviations are parameterized by α, the logarithmic slope minus 5/3 (Kravtsov & Borgani 2012).

Radiative cooling primarily affects the tSZ scaling relation by reducing the gas fraction at low mass as gas is converted into stars (Kravtsov et al. 2005, Battaglia et al. 2013). Other physical effects of cooling, such as its impact on the entropy profile, are less important than the decrease in gas fraction (da Silva et al. 2004, Reid & Spergel 2006). The induced deviations from self-similarity are thus quite modest, though the impact on the normalization may be larger (da Silva et al. 2004, Nagai 2006). Feedback plays a similar role, breaking self similarity by modifying the gas profile towards flatter outer slopes at low mass (Battaglia et al. 2012b). AGN feedback is thought to be more important at $M > 10^{13}\ M_\odot$ whereas stellar feedback can affect the $Y - M$ slope at smaller masses (van de Voort et al. 2016). Early work also considered the impact of 'pre-heating' on the ICM where a large quantity of heat was injected at high redshift (da Silva et al. 2001, White et al. 2002), but these models are incompatible with high-redshift Lyα forest constraints and star-formation histories (Kravtsov & Borgani 2012). Moreover, simulations suggest AGN feedback is neceessary to resolve the "cooling crisis," or overproduction of stars in simulations with radiative cool-

ing only (McCarthy et al. 2010). Since both feedback and cooling create departures from self-similarity through the gas fraction, Böhringer et al. (2012) proposes that the self-similar scaling relations can be modified to account for hydrodynamics by using a halo mass and redshift-dependent gas fraction.

The presence of radiative cooling is well-established and necessary to account for the presence of stars in a galaxy cluster, but prescriptions for AGN feedback in simulations are more uncertain. To remain agnostic about the details of feedback, we consider two very simplified schemes for feedback: an overall increase or decrease in the tSZ signal from all halos (similar to the approach taken in Efstathiou & Migliaccio (2012), who model the tSZ signal using a universal pressure profile from Arnaud et al. (2010) with adjustable amplitude and redshift evolution); and direct energy injection into the gas surrounding the AGN, proportional to the energy output of the quasar (as used in galaxy formation and evolution models; Springel et al. 2005, Hopkins et al. 2006a).

5.1.1 Review of observational and theoretical literature

AGN feedback both reduces the baryon fraction in groups and small clusters by pushing baryons to large radii and thus decreasing the tSZ signal in the inner part of the profile (Battaglia et al. 2012b, Le Brun et al. 2015); and heats the gas on small scales, potentially enhancing the tSZ signal close to the quasar (Scannapieco & Oh 2004, Scannapieco et al. 2008, Rowe & Silk 2011, Chatterjee & Kosowsky 2007, Chatterjee et al. 2008, Spacek et al. 2017a, Soergel et al. 2017). Sufficiently efficient AGN feedback in simulations causes a break in the $Y - M$ relationship, typically around 10^{13} $M_\odot$ (Henden et al. 2018) or 10^{14} $M_\odot$ (McCarthy et al. 2017, Le Brun et al. 2017), with $\alpha \sim 0.5$ (a steeper slope below the break). However, other simulations with less efficient AGN feedback do not show evidence for a change in logarithmic slope (Planelles et al. 2017). Above 10^{14} $M_\odot$, deviations for self-similarity are milder, $\alpha \sim 0.1 - 0.2$, but nevertheless often measured in simulations (Stanek et al. 2010, Battaglia et al. 2012b, Kay et al. 2012, Planck Collaboration et al. 2014d, Barnes et al. 2017, Gupta et al. 2017). Direct comparisons between simulations and observations yield a consistent slope, suggesting that simulations are sufficiently realistic to interpret data (Jakobs et al. 2017).

While early studies neglecting AGN feedback argued for a universal pressure profile (Nagai et al. 2007, Arnaud et al. 2010), simulations with AGN feedback predict that pressure profiles deviate from self-similarity in both their mass and redshift scalings, with AGN feedback expelling gas from the center of the halo and creating a shallower outer pressure profile (Battaglia et al. 2012b, Kay et al. 2012, Le Brun et al. 2015, Gupta et al. 2017). Despite these deviations from self-similarity, in these simulations integrated Y remains self-similar if integrated over a sufficiently large aperture (Battaglia et al. 2012a). This is because the AGN feedback prescriptions in these simulations does not destroy hot gas altogether but merely pushes it to larger radii. However, it remains possible that other feedback prescriptions not considered in these simulations could increase the amount of hot gas immediately around the quasar (Scannapieco & Oh 2004, Scannapieco et al. 2008)

Observational evidence for the self-similarity of the $Y - M$ relationship has been mixed. Planck Collaboration et al. (2013b) find a self-similar $Y - M$ relation down to 4×10^{12} $M_\odot$, but this result could be consistent with significant deviations from self-similarity in the pressure profile (Greco et al. 2015, Le Brun et al. 2015). At cluster scales ($> 10^{14} M_\odot$), Planck Collaboration et al. (2013a) find that a universal pressure profile is appropriate, though with a shallower outer slope than Arnaud et al. (2010). On the other hand, Tanimura et al. (2020) find that the pressure profile around SDSS LRGs requires AGN feedback in addition to gravitational collapse. Future observations may be able to push to even smaller masses and test different feedback models in the CGM around $\sim 10^{12}$ $M_\odot$ halos, although constraints are likely to be better from X-ray stacks than from tSZ stacks (Singh et al. 2016).

There are other indirect probes of the thermal state of the gas (and thus the impact of AGN feedback) besides stacking on halos. At low masses, the tSZ-halo cross-correlation is dominated by the 2-halo term, which provides information about gas in all halos. Vikram et al. (2017) use the 2-halo tSZ signal around SDSS groups to constrain the bias-weighted electron pressure[1] at $z = 0.15$. Hill et al. (2018) compare this measurement to 2-halo predictions from broken and unbroken power law $Y - M$ relations, and find that a power law broken at 10^{14} $M_\odot$ is moderately (2σ) preferred by the data, in agreement with expectations for AGN feedback. Similarly, Pandey et al. (2019) find that the two-halo term of galaxy-tSZ cross-correlations is consistent with gravitational collapse and shock heating, and is beginning to place interesting constraints on the contribution from AGN feedback. Future measurements with CMB S4/Simons Observatory and the DESI BGS sample will both be able to constrain the pressure profile and to infer the $Y - M$ relationship to constrain simulations of AGN feedback (Pandey et al. 2020). The tSZ-galaxy cross-correlation can also be interpreted to constrain the hydrostatic mass bias (Makiya et al. 2018); i.e. the discrepancy between true cluster masses and the X-ray determined cluster masses used to calibrate the *Planck* pressure profile, which may be due to deviations from hydrostatic equilibrium in the X-ray cluster sample. tSZ measurements of the hydrostatic mass bias are generally consistent with *Planck* cluster counts and do not find evidence for redshift evolution, though they have a relatively restricted redshift range ($z \leq 0.4$) (Koukoufilippas et al. 2020).

The tSZ power spectrum can be used to constrain departures from self-similarity on small angular scales $\ell > 1000$ (Ramos-Ceja et al. 2015), where the power spectrum is dominated by gas at small radii around 10^{14} $M_\odot$ halos, which are more sensitive to feedback. Conversely, the tSZ power spectrum at low ℓ, as measured by Planck, is robust to effects of AGN feedback (McCarthy et al. 2014, Horowitz & Seljak 2017). Nonthermal pressure support can also change the shape of the power spectrum on large scales (Shaw et al. 2010).

Recently, several studies have used the tSZ-lensing cross-power spectrum to both constrain cosmology and ICM parameters. Simulations suggest that most of the tSZ-lensing cross-correlation comes from hot gas in the ICM, rather than gas beyond the virial radius ("missing baryons"), though the ∼20% of the signal from "missing baryons" may still offer

[1]Following Hill & Spergel (2014) we refer to this quantity as the Compton-y bias.

interesting constraints on the diffuse intergalactic medium, which is generally very hard to study (Battaglia et al. 2015, Hojjati et al. 2015, Ma et al. 2015).

Van Waerbeke et al. (2014) detect the first cross-correlation between tSZ and weak lensing maps, interpreting this result as a constraint on the Compton-y bias. Hill & Spergel (2014) consider both cosmology and ICM constraints from the cross-correlation of Planck tSZ and CMB lensing. Their ICM constraints depend on the assumed cosmology but generally favor ICM pressure profiles with AGN feedback over adiabatic ICM profiles with no star formation or feedback. Similarly, Timmons et al. (2017) uses the CMB skewness power spectrum to measure the tSZ-CMB lensing cross-correlation and constrain the shape of the ICM pressure profile. Osato et al. (2018) cross-correlates tSZ with optical weak lensing to place constraints on σ_8 and the nonthermal pressure fraction in the semi-analytic model of Flender et al. (2017). Hojjati et al. (2017) measure the cross-correlation between Planck tSZ and RCSLens weak lensing, and compare their results to simulations with varying levels of AGN feedback. They find modest preference ($1.5-2\sigma$) for AGN feedback simulations over adiabatic simulations, and also point out that the impact of AGN feedback on the tSZ-weak lensing cross-correlation is maximal for $\theta < 30$ arcmin. Battaglia et al. (2015) shows the tSZ-CMB lensing cross-spectrum from simulations with shock heating only; radiative cooling and star formation; and AGN feedback. They find that ongoing and future experiments will be able to constrain the outer slope and normalization of the pressure profile, and the redshift evolution of the normalization. Similarly, Battaglia et al. (2017) finds that future LSS cross tSZ and LSS cross kSZ measurements will be able to constrain non-thermal pressure and AGN feedback efficiency to percent level.

Alternatively, AGN feedback has been directly probed by stacking the tSZ signal around quasars and searching for a small-scale excess tSZ signal (e.g. Chatterjee & Kosowsky 2007, Chatterjee et al. 2008). However the evidence for such an excess remains unclear. Chatterjee et al. (2010) reported 2.5σ evidence for a tSZ decrement in WMAP data around photometric SDSS quasars; however, the limited frequency coverage prevented them from definitively identifying the signal as tSZ. Later, Ruan et al. (2015) reported a strong tSZ signal around SDSS quasars, much larger than would be expected based on reasonable estimates of their halo masses. However, later work pointed out that the signal was also far larger than expectation for quasar feedback (Crichton et al. 2016, Verdier et al. 2016, Soergel et al. 2017) and argued that the signal was due to CIB contamination in the Compton-y maps (by Hill & Spergel 2014) used by Ruan et al. (2015).

An alternative approach is to make a very high-resolution observation of a single system, probing only the innermost part of the AGN where emission from feedback or a wind should be much brighter than emission from gravitational collapse. Lacy et al. (2019) use ALMA to observe the hyperluminous quasar HE 0515-4414, observing SZ emission from the wind with 0.01% of the total radiative energy of the quasar.

Subsequent studies have explicitly modelled CIB emission as well as the tSZ distortion and have come to conflicting conclusions: Crichton et al. (2016) found 3.5σ evidence for a stacked tSZ signal around SDSS quasars using CMB maps from ACT and sub-mm maps from *Herschel*-SPIRE; Verdier et al. (2016), using Planck CMB maps, found evidence for

tSZ signal but only around quasars at $z > 2.5$, and Soergel et al. (2017) found only 1.6σ evidence for an SZ signal using Planck CMB data and AKARI far-infrared maps to constrain CIB emission. All three studies reached significantly different conclusions about the levels of CIB emission, suggesting that different dust models significantly affect the SZ results. Moreover, none of these studies were able to explicitly identify the SZ signal with quasar feedback rather than virialization of the host halos, due to uncertainties in the quasar halo occupation distribution (Dutta Chowdhury & Chatterjee 2017). Indeed, hydrodynamical simulations of the Planck-SDSS measurement performed by Soergel et al. (2017) find that the feedback signal is only 10-20% of the virialization signal. A further challenge arises from two-halo SZ signal from correlated nearby halos; Cen & Safarzadeh (2015) suggests that this two-halo term dominates the SZ signal for the coarse Planck beam.

Perhaps the most robust detection of SZ around AGN comes from Gralla et al. (2014) and Hall et al. (2019). Gralla et al. (2014) find a 5σ detection of SZ signal around radio-loud AGN, corresponding to halo masses of a few 10^{13} $M_\odot$; this measurement agrees with halo masses measured from weak lensing and confirms that radio-loud AGN are more massive than optical AGN. Gralla et al. (2014) find that their SZ measurements are consistent with SZ signal from virialized halo gas only and rule out the most extreme theoretical predictions for the feedback SZ signal. Hall et al. (2019) find a 4-σ tSZ excess using multi-wavelength data from radio to far-infrared, and modelling a multi-component quasar SED. This either comes from quasar host halos with mass 6×10^{12} h^{-1} $M_\odot$, or feedback which deposits 5% of the quasar bolometric luminosity into the IGM over a quasar lifetime of 100 Myr.

Another similar method for probing AGN feedback involves stacking on massive elliptical galaxies, the descendants of $z \sim 2$ quasars. Spacek et al. (2016) finds 3.9σ evidence for SZ signal in SPT using VISTA Hemisphere Survey and Blanco Cosmology Survey galaxies at $0.5 < z < 1.0$; they find no convincing evidence at $1.0 < z < 1.5$, nor do they find a significant SZ signal around WISE-selected SDSS galaxies using ACT data (Spacek et al. 2017b). The WISE galaxies and high redshift VHS/BCS galaxies are consistent with SZ signal from gravitational heating, whereas the low z VHS/BCS galaxies exhibit a 1σ excess consistent with simple AGN feedback models. However, Spacek et al. (2017a) compares these measurements to predictions of hydrodynamic simulations with and without AGN feedback and find a strong preference for no AGN feedback, a constraint driven by the ACT measurement around the more massive $M_\star > 5 \times 10^{11} M_\odot$ WISE galaxies.

In this paper, we study two of the major difficulties with previous quasar-tSZ cross-correlations: contributions from the two-halo term at large scales (which comes from correlated nearby halos and thus is not affected by direct energy injection around the accretion disk); and uncertainty in the small-scale tSZ signal due to the uncertain halo occupation of quasars. We show that the large-scale (two halo) tSZ signal is most useful for constraining AGN feedback, whereas the small-scale signal holds promise for discriminating between quasar halo occupation models.

5.1.2 Outline of this paper

We introduce our methods and simulations in Sec. 5.2. In Sec. 5.3, we use the DarkSky N-body simulation to demonstrate that the large-scale tSZ-quasar cross-correlation is dominated by the two-halo term from correlated matter. In Sec. 5.4.1 and Appendix 5.B, we update the quasar model of Conroy & White (2013) with superior luminosity function and clustering data, and create mock quasar samples appropriate for the DESI survey (Levi et al. 2013, DESI Collaboration et al. 2016). In Sec. 5.5, we show how the small-scale tSZ signal can discriminate between quasar models which otherwise match the observed luminosity function and clustering. While the one-halo signal from virialization is in principle degenerate with the energy injection from feedback, based on past findings we expect the feedback signal to be subdominant for DESI quasars. This is because the feedback signal scales with luminosity and the DESI quasars are $\sim$1 mag fainter than previous samples. Finally, in Sec. 5.6, we show that the two-halo term is easily detectable with DESI and Simons Observatory (The Simons Observatory Collaboration et al. 2018), and can be used to place constraints on the evolution of the Compton-y bias, which in turn is sensitive to AGN feedback. In sum, we argue that the tSZ-quasar cross-correlation is a rich probe of astrophysics. On large scales, it can constrain global modifications to the tSZ signal arising from AGN feedback, and on small scales, it can break degeneracies between quasar halo occupation models.

5.2 Methods and simulations

5.2.1 Simulations

To look at the domain of validity of our analytic results we compare to the `DarkSky` N-body simulation suite[2], specifically simulation `ds14_a` (Skillman et al. 2014). This simulation used the `2HOT` code of Warren (2013) to evolve 10240^3 particles in an $8\,h^{-1}$Gpc volume to model the growth of structure in a ΛCDM cosmology with $\Omega_M = 1 - \Omega_\Lambda = 0.295$, $h = 0.688$, $n_s = 0.968$ and $\sigma_8 = 0.835$. Initial conditions were generated from a glass using $2^{\rm nd}$ order Lagrangian perturbation theory at $z = 93$. Halos were found using the `Rockstar` code (Behroozi et al. 2013). The mass resolution is $3.9 \times 10^{10}\ h^{-1}\ \mathrm{M}_\odot$, yielding a minimum halo mass of $10^{12}\ M_\odot$ at 20 particles per halo. We use the output lightcone in this work, which extends to $z = 2.38$. Consistent with the mass defintions in Battaglia et al. (2012b), all halo masses are defined as M_{200c}, that is the mass enclosing a spherical overdensity of 200 times the critical density.

5.2.2 Compton-y model

We paint Compton-y on to the lightcone using the Battaglia et al. (2012b) pressure profiles, cut off at a radius of 4 Mpc. While Battaglia et al. (2012b) only determine the

[2]http://darksky.slac.stanford.edu

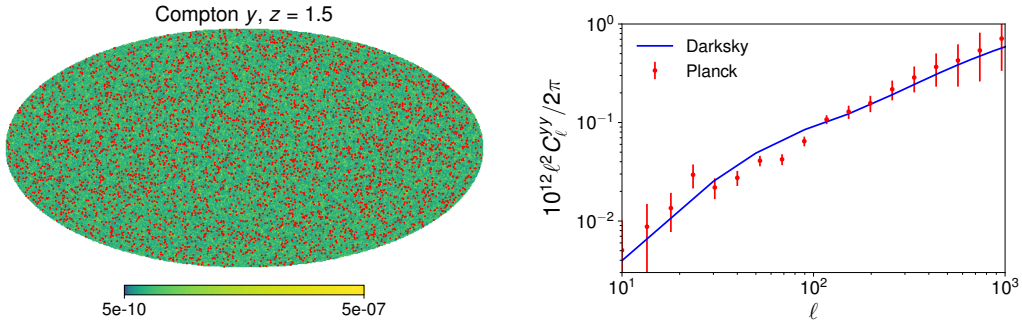

Figure 5.1: *Left:* Darksky Compton-y map from halos with $1.4 < z < 1.6$. Red dots are 5000 quasars randomly selected from halos following Eq. 5.2 with $\sigma = 0.5$ dex. *Right:* Comparison of tSZ power spectrum for Darksky and Planck Collaboration et al. (2014e).

pressure profile for halos at $M_{200c} > 5 \times 10^{13}\ M_\odot$ and $z < 1.5$, we extrapolate their fits to higher redshift and mass.

In Fig. 5.1, we show the Compton-y map from the Darksky simulation (§5.2.2) in a narrow redshift bin, $1.4 < z < 1.6$, with simulated quasars overplotted. We also show that the tSZ power spectrum in Darksky matches the Planck Collaboration et al. (2014e) quite well except near $\ell = 100$; at these angular scales the tSZ power spectrum is dominated by the nearest clusters and such a disagreement could be driven by sample variance in the nearby universe.

5.3 Quasar-tSZ Cross-correlation with uncertain HOD

Quasar autocorrelations and cross-correlations have measured quasar bias from $z = 0$ to 4 (Croom et al. 2005, Shen et al. 2009, White et al. 2012, Shen et al. 2013, Laurent et al. 2017). Most of these studies measure quasar clustering on large scales (the two-halo term) (though see Hennawi et al. 2006; for small-scale quasar clustering). These measurements yield an estimate of the mean halo mass of quasars (though with large spread between different measurements; Porciani et al. 2004, Croom et al. 2005, Richardson et al. 2012, White et al. 2012, Shen et al. 2013), but the width remains largely unconstrained, in large part due to the unknown duty cycle, which prevents us from constraining the quasar halo occupation using the space density. Other, indirect constraints on the HOD width still provide a large range of possibilities. Models in which quasars occupy a very narrow range in halo mass are disfavored by the scatter observed in the local $M - \sigma$ relations (Magorrian et al. 1998, Gebhardt et al. 2000, Ferrarese & Merritt 2000, Marconi & Hunt 2003) and their extensions to $M_{\rm BH} - M_h$ relations (Ferrarese 2002); given typical factor of two scatter in the $M_{\rm BH} - M_\star$ relation and in the $M_\star - M_h$ relation (Moster et al. 2010, Behroozi et al. 2013), quasars must occupy a nonzero range in halo mass. On the other hand, while the strong clustering at high

redshifts limits the scatter in the halo mass at $z > 3$ (White et al. 2008, Shankar et al. 2010, Degraf et al. 2011), no such constraint exists at lower mass. Tight constraints on the HOD form must come from additional modeling assumptions.

Since both the 1-halo and 2-halo contributions to the tSZ signal are non-linear functions of the halo mass, this uncertainty in the HOD translates into a large uncertainty in the predicted signal.

5.3.1 Lognormal quasar Halo Occupation Model

To illustrate these points, we first consider a toy model of the quasar halo occupation distribution, specifically that the probability of a halo hosting an active QSO is lognormal in the halo mass. While it has only weak physical motivation, it has qualitatively the right behavior compared to more complex models and is useful for cleanly establishing two points: the dominance of the two-halo clustering term at $\ell \lesssim 2000$ and the uncertainty in the one-halo term arising from the poorly constrained quasar HOD width at fixed bias. We take the probability of a halo hosting a quasar to be Gaussian in log halo mass $m \equiv \log_{10} M_{200c}$:

$$p_{\rm qso}(m) \propto \exp\left[-\frac{(m-\mu)^2}{2\sigma^2}\right] \tag{5.2}$$

where the normalization is proportional to the quasar duty cycle and is adjusted to match the observed quasar number density. Given σ, we adjust μ to match the clustering of quasars. Therefore, we use σ to parameterize the range of allowed halo occupation models. We generalize p_{qso} to a wide range in redshift by holding σ fixed and re-fitting μ at each redshift.

We adjust the log-normal model to impose "physical priors" on the quasar halo occupation. We begin by computing the number density of quasars brighter than $M_g(z = 2) = -23$, using the luminosity function of Palanque-Delabrouille et al. (2016a) (PLE plus LEDE model). We then require the duty cycle be 10% or less by capping p_{qso} at 0.1 and iteratively and uniformly adjusting p_{qso} upwards outside of the capped region to match the normalization. This duty cycle is consistent with the largest estimates of the quasar lifetime, $t_Q \lesssim 10^8$ yr (Yu & Tremaine 2002, Martini 2004, Schmidt et al. 2017, Davies et al. 2018). We also require that all quasars live in halos with galaxy mass greater than 10^9 $M_\odot$, using the Moster et al. (2010) stellar mass to halo mass relation to assign stellar masses. We use 10^9 $M_\odot$ as the lower limit host galaxy mass since that is the mass at which a $M_i(z = 2) = -23$ quasar emitting at the Eddington limit has a black hole mass 1% of the host galaxy mass, roughly the upper bound seen in the local universe(McConnell & Ma 2013).

We show the resulting quasar halo mass functions in Fig. 5.2. We compute quasar HODs both using the Tinker et al. (2008) mass function and using the halos in the Darksky simulation, which are incomplete below 10^{12} $M_\odot$. The low-mass cutoff is apparent on the left side of the plot, and the saturation at duty cycle of 10% leads to a cuspy behavior particularly prevalent at high redshift. The restricted scatter in halo mass at high redshift pointed out by White et al. (2008), Shankar et al. (2010), Degraf et al. (2011) also becomes apparent at $z > 2$.

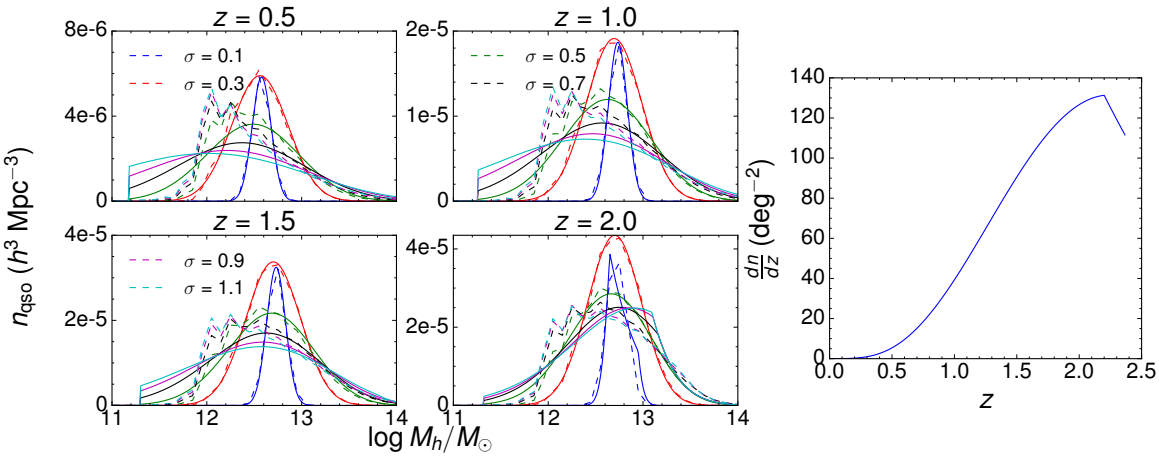

Figure 5.2: *Left:* Quasar number density from lognormal quasar halo occupation model from $z = 0.5$ to 2 and from $\sigma = 0.1$ to 1.0 dex. Solid lines use the Tinker et al. (2008) mass function and dashed lines use halos from the Darksky simulation, which is incomplete below $\sim 10^{12}$ $M_\odot$. *Right:* Redshift distribution for the lognormal model, computed by integrating the Palanque-Delabrouille et al. (2016a) luminosity function down to $M_g(z-2) = -23$. For ease of display we divide the $\sigma = 0.1$ curve by 3 in all 4 panels.

We match quasar clustering observations by matching the mean bias:

$$\langle b_{\rm qso}(z)\rangle = \frac{\int_0^\infty dM\ \frac{dn(M,z)}{dM}\ b(M,z)\ p_{\rm qso}(M,z)}{\int_0^\infty dM\ p_{\rm qso}(M,z)\ \frac{dn(M,z)}{dM}} \tag{5.3}$$

where we use halo bias $b(M,z)$ from Tinker et al. (2010). Again, we perform this step twice, both with the halo mass function dn/dM from Tinker et al. (2008) and with the halos from the Darksky simulation. We convert from M_{200m} presented in Tinker et al. (2008) to M_{200c} by multiplying by a constant factor, $\sqrt{\Delta_{200c}/\Delta_{200m}}$. This assumes that $\rho \propto R^{-2}$ in the outer halo profile. We match to the quasar bias from Laurent et al. (2017),

$$\langle b_{\rm qso}(z)\rangle = 0.278((1+z)^2 - 6.565) + 2.393 \tag{5.4}$$

Note that while this bias measurement is appropriate to the eBOSS survey, the observed independence of bias with luminosity (Shen et al. 2013, Zhang et al. 2013, Krolewski & Eisenstein 2015) implies that this bias evolution is also valid for deeper quasar samples.

5.3.2 One Halo tSZ

Following the procedure described in Sec. 5.3.1, we determine μ for each σ with $0 < z < 3$. Since we have incorporated observational constraints on the duty cycle and the host stellar mass into the lognormal model, σ is a completely free parameter. The large allowed range

in σ maps to a large range in the tSZ signal, since the tSZ signal scales as $M^{5/3}$ and is thus very sensitive to the high-mass end of the halo occupation.

We show this explicitly in the right panel of Fig. 5.3. Over $0 < z < 3$, we compare the scaling of the tSZ signal to its value at $\sigma = 0.5$ dex; that is, we compute the ratio of $\langle Y(\sigma)\rangle$ to $\langle Y(\sigma = 0.5)\rangle$:

$$\frac{Y(\sigma, z)}{Y(\sigma = 0.5, z)} = \frac{\int_0^\infty dM\ M^{5/3}\ p_{\rm qso}(M, \sigma, z)\ \frac{dn(M,z)}{dM}}{\int_0^\infty dM\ p_{\rm qso}(M, 0.5, z)\ \frac{dn(M,z)}{dM}} \tag{5.5}$$

This ratio can be computed at any redshift, since $p_{\rm qso}$ varies with redshift. We therefore also determine the redshift-integrated ratio, using dN/dz from the Palanque-Delabrouille et al. (2016a) luminosity function Φ integrated over absolute magnitude M_g:

$$Y(\sigma) \propto \int_0^3 dz\ Y(\sigma, z) E(z)^{2/3} \int_{-\infty}^{-23} dM_g\ \Phi(M_g, z) \tag{5.6}$$

and we can likewise determine the ratio $Y(\sigma)/Y(0.5)$ in the same manner as Eq. 5.5.

We find nearly an order of magnitude spread in $Y/Y(\sigma = 0.5)$ at $z = 0.5$, compared to a spread of only 60% at $z = 2.5$. This reflects the increasingly constrained halo occupation at higher redshift, since the quasar bias is increasing as the number of high-mass halos is exponentially dropping. This reflects the observations of White et al. (2008) and Shankar et al. (2010) that the spread in the quasar halo occupation must be limited at high z. Averaged over the entire redshift range $0 < z < 3$, we find a factor of 5 change in Y as σ varies from 0.1 to 1.0. Even if we restrict $\sigma > 0.5$, Y is still uncertain by 50% due to the uncertainty in the quasar halo occupation. This implies that the relatively mild enhancement expected from AGN feedback ($\sim$ 20% Soergel et al. 2017) will be completely undetectable given the uncertainty in the quasar HOD.

5.3.3 Two halo term

We measure the cross-correlation between quasars and Compton-y, C_ℓ^{yq}, for our entire quasar sample as a function of the quasar HOD parameter σ. We use anafast to measure the cross-power spectrum between quasar and Compton-y Healpix (Górski et al. 2005) maps. To minimize sample variance, the quasar map is the weighted mean of the halo map, weighted by p_{qso}. We display the binned cross-correlations with bins of width $\Delta\ell = 100$.

On large scales, C_ℓ^{yq} is dominated by the two-halo term and is thus entirely determined by the quasar and Compton-y biases (or equivalently the distribution of Compton-y as a function of halo mass) (left panel of Fig. 5.3). At $\ell > 1000$, C_ℓ^{yq} transitions to the one-halo regime described in Sec. 5.3.2, where the uncertainty in σ maps into a large range of possible amplitudes of C_ℓ^{yq} at fixed quasar bias.

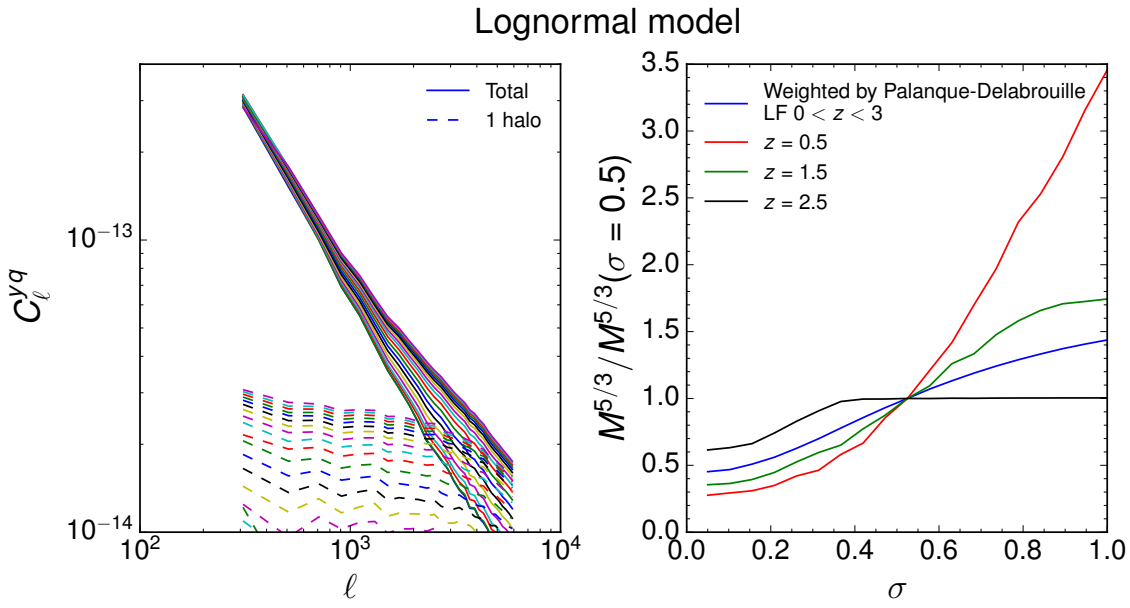

Figure 5.3: *Left:* C_ℓ^{yq} for all quasars ($0 < z < 2.38$) in the DarkSky simulation using the lognormal model with different values of σ (colored lines) ranging from 0.1 dex on bottom to 1.0 dex on top. Solid curve is C_ℓ^{yq} and dashed is C_ℓ^{yq} with scrambled halo positions, i.e. no clustering. *Right:* Ratio of $M^{5/3}$ to $M^{5/3}$ (i.e. the scaling of the 1-halo signal) at $\sigma = 0.5$ decades for lognormal quasar HODs with the halo mass function given by Tinker et al. (2008).

5.4 Empirical quasar halo occupation model

In the previous section, we showed that a one-parameter family of lognormal models, characterized by the width of the quasar HOD σ, can reproduce the quasar clustering exactly while varying wildly in the one-halo tSZ signal. However, it is difficult to physically interpret σ in the context of quasar formation and triggering. Therefore, in this section we use a set of empirically-motivated quasar models both to discuss the constraints those measurements would give on different models of black hole triggering and growth (Sec. 5.5) and to forecast future tSZ-quasar cross-correlations (Sec. 5.6).

5.4.1 Empirical quasar halo occupation model

We use a set of empirically-motivated quasar halo occupation models based on Conroy & White (2013). This model connects halo mass to galaxy stellar mass via empirical models (e.g. Moster et al. 2010, Behroozi et al. 2013, 2018) and galaxy mass to black hole mass through a simple relation inspired by local black hole-galaxy relations. We use Behroozi et al. (2018) as our fiducial stellar mass-halo mass relation and find little difference if we use Moster et al. (2010) instead.

While Conroy & White (2013) found that a linear black hole-galaxy relation was sufficient to reproduce both the luminosity function and quasar function, we find that updates to the stellar mass-halo mass relation and better quasar clustering data disfavor this simple model (Appendix 5.B). To reproduce both the luminosity function and quasar clustering, we instead use a piecewise-linear relationship

$$\log M_{\rm BH} = \begin{cases} \alpha + \log(1+z)^2 + \beta_1 \log M_{\rm gal} & \log M_{\rm gal,*} < 11 \\ \alpha_2 + \log(1+z)^2 + \beta_2 \log M_{\rm gal} & \log M_{\rm gal,*} > 11 \end{cases} \tag{5.7}$$

where α_2 is chosen to ensure continuity. We use $\beta_1 = 1$ and $\beta_2 = 2$. This is motivated by low-redshift black hole scaling relations, which generally measure the $M_{\rm BH}$-$M_{\rm bulge,*}$ relation rather than $M_{\rm BH}$-$M_{\rm gal,*}$. Since bulges are more prominent in high-mass galaxies, the steeper slope for high-mass galaxies accounts for the transition between high-mass bulge-dominated galaxies and low-mass galaxies with small bulges (Khochfar et al. 2011, Mendel et al. 2014, Kormendy 2016, Bentz & Manne-Nicholas 2018).

The abundance of black holes of a given mass is then a fixed fraction $f_{\rm on}$ (the duty cycle) of the abundance of halos of that mass, which can be converted to a quasar lifetime $t_{\rm Q} = f_{\rm on} t_{\rm Hub}$.

Black hole mass is then related to quasar luminosity through an assumed Eddington ratio distribution:

$$L_Q = 3.3 \times 10^4 \eta \frac{M_{BH}}{M_\odot} L_\odot \tag{5.8}$$

In the simplest model, the Eddington ratio distribution is lognormal, corresponding to a

"scattered lightbulb" model of quasar triggering:

$$P_{\rm LN}(\eta) = \frac{f_{\rm on}}{\sigma\sqrt{2\pi}} \exp\left(\frac{-(\log\eta - \log\eta_0)^2}{2\sigma^2}\right) \tag{5.9}$$

Assuming that the scatters in each relation are independent, the width of the lognormal is the quadrature sum of the scatter in the galaxy-halo, galaxy-black hole, and Eddington ratio distributions.

This model can then be fit to the quasar luminosity function. It has two free parameters, α and $f_{\rm on}$. The mean Eddington ratio $\eta_0(z)$ is a fixed function; following Conroy & White (2013), we consider both a model with constant $\eta_0 = 0.1$ and a model with a linear ramp in η_0 from 0.1 at $z = 0.5$ to 1.0 at $z = 3.5$.

We describe fits to the AGN UV luminosity function data of Kulkarni et al. (2018) in Appendix 5.B. We use α and $f_{\rm on}$ for a model with a fiducial scatter of 0.52 dex, corresponding to 0.3 dex of scatter in each of the galaxy-black hole mass, galaxy-halo and Eddington ratio distributions.

We also consider two variations on the fiducial model to illustrate the range of 1-halo tSZ signal from different quasar models. First, we consider a model where the Eddington ratio distribution is a power law rather than log-normal (e.g. Veale et al. 2014):

$$P_{\rm PL}(\eta) = f_{\rm on} \frac{\ln 10\,(\eta/\eta_0)^{-\beta} \exp\left(-\eta/\eta_0\right)}{\Gamma(-\beta, \eta_{\rm min}/\eta_0)} \tag{5.10}$$

where Γ is the incomplete gamma function, and $f_{\rm on}$ is the duty cycle as before. Both Equations 5.9 and 5.10 are normalized such that $\int P d\log\eta = 1$. The slope of the faint-end (power-law) slope β lies between 0 and 1, and we define the distribution from $\eta_{\rm min}$ to ∞. Following Veale et al. (2014), we hold $\eta_{\rm min}$ fixed at 10^{-3}; since $\eta_{\rm min}$ only affects very low-luminosity quasars, it is essentially only degenerate with $f_{\rm on}$ with no other effects on the quasar luminosity function or tSZ signal. As in the lognormal model, the free parameters are α and $f_{\rm on}$, with the characteristic Eddington ratio η_0 a fixed function of redshift and β playing the role of σ in Eq. 5.9. Following Hopkins & Hernquist (2009), who directly measure the distribution of η using quasar luminosities and virial masses, we fix $\eta_0(z = 0)$ to 0.4. At higher redshifts we tune $\eta_0(z)$ to generate consistent BH growth histories by using a linear ramp from 0.4 to 4.0 between $z = 0.5$ and $z = 3.5$.

The power-law model leads to a luminosity-dependent quasar lifetime (Hopkins & Hernquist 2009), and is motivated by both theoretical expectations for a luminosity-dependent lifetime (Hopkins et al. 2006b, Novak et al. 2011) and by measurements of the Eddington ratio distribution, which generally favor luminosity-dependent lifetime models over "scattered lightbulb" models (Kauffmann & Heckman 2009, Hopkins & Hernquist 2009, Aird et al. 2012, Bongiorno et al. 2012, Kelly & Shen 2013) and see compilation in Hickox et al. (2014).

As in Veale et al. (2014), we find that the power law model fits the data similarly well as the scattered lightbulb model. Unlike the scattered lightbulb model, for which σ is fairly well-constrained by the data, we find that a wide range of β fits the data well, and thus we take two representative values of β for the power-law model, $\beta = 0.2$, and $\beta = 0.6$.

In the power law model, the quasar lifetime is mass independent but varies with luminosity due to the shape of the Eddington ratio distribution. We also consider a model where the Eddington ratio distribution remains lognormal, but the lifetime is explicitly mass-dependent:

$$P_{\rm MDL}(\eta) = \frac{f_{\rm on}\left(\frac{M_{\rm BH}}{10^8 M_\odot}\right)^{-\gamma}}{\sigma\sqrt{2\pi}} \exp\left(\frac{-(\log\eta - \log\eta_0)^2}{2\sigma^2}\right) \tag{5.11}$$

This model is motivated by the observational results and modelling of Hopkins & Hernquist (2009), which suggests an explicitly mass-dependent lifetime with more massive quasars having a shorter lifetime (see their figure 9). As in the lognormal model, we use the varying η_0 model with a linear ramp between 0.1 and 1.0 between $z = 0.5$ and 3.5 to ensure consistent BH growth. For the mass-dependent lifetime model, we find that $\gamma = 0.3$ and $\sigma = 0.52$ are able to adequately fit the luminosity function data.

Matching quasar clustering requires adjusting the stellar mass-halo mass relation for the power-law and mass-dependent lifetime quasar models. We find that decreasing the stellar mass by 0.3 dex from the Behroozi et al. (2018) relation yields a better match to quasar clustering for these models. This is well within the uncertainty in the $z \sim 1$ SM-HM relation (Fig. 35 in Behroozi et al. (2018)).

For each of the four models under consideration (lognormal, power-law with $\beta = 0.2$ and 0.6, and mass-dependent lifetime), we fit the luminosity function in 12 bins of redshift between $0 < z < 7$, as described in Appendix 5.B. We linearly interpolate between α at different redshifts (and log-linearly interpolate $f_{\rm on}$) to assign black hole masses and abundances at each redshift.

5.4.2 Creating a DESI-like sample

We then apply an observational flux cut to mimic the DESI selection function (N. Palanque-Delabrouille, priv. comm.). The selection function is estimated by applying DESI quasar cuts to deep imaging, and comparing the resulting redshift and r-band magnitude distribution to expectations from a complete, variability-selected luminosity function (Palanque-Delabrouille et al. 2016a,b).[3] This allows us to derive the probability of DESI observing a quasar as a function of r magnitude and redshift. The quasar cuts are a Random Forest selection (Kitanidis et al. 2019) applied to deep DES imaging in Stripe 82 from the Legacy Survey (Dey et al. 2019). This is the fiducial procedure for determining the magnitude and redshift distribution of DESI quasars.

This yields the resulting selection functions in r magnitude and z, i.e. the fraction of all

[3]The luminosity is slightly different from the corrected version in Palanque-Delabrouille et al. (2016b), with a very minor change at the faint end of the luminosity function (Palanque-Delabrouille et al., in prep).

optical quasars passing DESI target selection

$$P(r) = \begin{cases} 0 & r \leq 17.5 \\ 1 & 17 \leq r \leq 21 \\ 1 - \frac{0.2}{1.25}(r - 21) & 21 \leq r \leq 22.25 \\ 0.8 - \frac{0.3}{0.45}(r - 22.25) & 22.25 \leq r \leq 22.7 \\ 0 & r \geq 22.7 \end{cases} \tag{5.12}$$

and in redshift

$$P(z) = \begin{cases} 0.8 - \frac{0.8}{0.5}(0.5 - z) & z \leq 0.625 \\ 1 & 0.625 \leq z \leq 2.5 \\ 1 - 0.5(z - 2.5) & 2.5 \leq z \leq 4.5 \\ 0 & z > 4.5 \end{cases} \tag{5.13}$$

Applying this selection function requires us to relate L_Q to r magnitude; we use the relation from Shen et al. (2009) to relate L_Q to $M_i(z = 2)$:

$$M_i(z = 2) = 72.5 - 2.5 \log L_Q \tag{5.14}$$

the Richards et al. (2006) K-correction to translate from $M_i(z = 2)$ to i magnitude, and a 5th order polynomial fit to the dereddened $r - i$ distribution of SDSS and BOSS quasars in narrow redshift bins for $0.5 < z < 3.5$:

$$r - i(z) = \begin{cases} 0.2177 & z \leq 0.5 \\ -0.1482z^5 + 1.636z^4 - 6.716z^3 & \\ +12.55z^2 - 10.39z + 3.017 & 0.5 \leq z \leq 3.5 \\ 0.1058 & z \geq 3.5 \end{cases} \tag{5.15}$$

5.5 Constraining quasar models from small-scale tSZ

While Planck lacks the necessary resolution to detect the one-halo term at high significance, such a detection will be well within reach for SO owing to its much smaller beam. Because the tSZ signal scales as $M^{5/3}$, it is a sensitive probe of the quasar halo mass distribution, discriminating between models with similar predictions for the quasar auto-correlation. Moreover, while in principle the one-halo signal is degenerate with extra contributions from AGN energy injection around the accretion disk, we expect the feedback signal to be subdominant to the halo virialization signal for DESI quasars, since they are less luminous than previous samples.

We compare the bias and tSZ energy from the four quasar models described in Sec. 5.4.1. We average the tSZ energy (both from feedback and virialization) and bias over the quasar models using the Tinker et al. (2008) mass function and Tinker et al. (2010) mass-bias

relation. We use the analytic mass function to include contribution from halos below the DarkSky resolution limit.

We compute the thermal energy from virialization $E_{\rm thermal}$ following Crichton et al. (2016), Hall et al. (2019), which is in turn based on the empirical relation from Planck Collaboration et al. (2013b):

$$\frac{\int P_e dV}{10^{60}\ {\rm erg}} = 0.011 E(z)^{2/3} \left(\frac{M_h}{10^{12}\ M_\odot} \right)^{5/3} \tag{5.16}$$

$$E_{\rm thermal} = \frac{3}{2} \left(\frac{\mu_e}{\mu} \right) \int P_e dV \tag{5.17}$$

where $\mu_e = 1.17$ and $\mu = 0.61$ are appropriate for solar abundances and a fully ionized gas.

We compare the virialization energy to energy injection from feedback

$$E_{\rm feedback} = f L_{\rm bol} \tau \tag{5.18}$$

where $L_{\rm bol}$ is the quasar luminosity and τ is the lifetime. following the prescription in Crichton et al. (2016), Hall et al. (2019). This assumes that some fixed fraction of the total energy emitted by the quasar is deposited as feedback into the surrounding gas. Simulations generally require $\sim 5\%$ of the quasar's radiative energy to be deposited in the surrounding medium (Hopkins et al. 2006a), in rough agreement with observational results (Crichton et al. 2016, Hall et al. 2019).

Figure 5.4 shows that even quasar models with very similar bias evolution can yield drastically different tSZ signals. As a result, the one halo tSZ-quasar cross-correlation is very promising for constraining models of quasar growth and behavior.

We also find that for a DESI-like quasar sample, the virialization signal is generally much larger than the feedback signal. Thus, a one-halo measurement of the DESI quasar-tSZ cross-correlation can likely be interpreted solely in terms of the virialization energy of the quasar host halo.

This result is in some tension with the previous observational literature, which generally finds that the feedback signal is equal to or even exceeds the virialization signal (Ruan et al. 2015, Crichton et al. 2016, Verdier et al. 2016, Hall et al. 2019), although Soergel et al. (2017) argue the feedback signal should be subdominant to virialization. However, the DESI-like quasar sample considered here is ~ 1 magnitude fainter than the faintest sample used in previous work (eBOSS), since DESI extends to fainter magnitudes than eBOSS. At $z = 2$, the DESI-like sample considered here has mean $M_i(z = 2) = -24.06$, compared to mean $M_i(z = 2) = -25.14$ for the DR14 quasar sample at $1.8 < z < 2.2$ (Pâris et al. 2018). This decreases the feedback signal by a factor of 3, but barely affects the virialization signal, since quasar luminosity is very weakly dependent on host halo mass. Previous work has generally also studied quasars at $z \sim 2$, where the feedback signal is larger compared to virialization, because halos at high redshift are less massive. In constrast to BOSS and eBOSS, which focus on higher-redshift quasars, DESI aims to use quasars to trace matter clustering at $0.8 < z < 2$. By probing both fainter and lower redshift quasars, Fig. 5.4 shows that in DESI, virialization of the host halo will dominate over energy injection from AGN feedback.

Thus, DESI is more suitable for measuring the host halo virialization signal than previous samples.

Nevertheless, the thermal energy from feedback depends also on the parameters f and τ, which are also very uncertain. Thus it is possible that Fig. 5.4 underestimates the feedback contribution. However, τ is unlikely to exceed the fiducial value of 10^8 yr by a substantial amount. Indeed, our models favor a considerably smaller τ, closer to 10^7 yr (Fig. 5.9), although we keep $\tau = 10^8$ yr in Fig. 5.4 for consistency with past work.

Thus, for the feedback energy to match the virialization energy at $z \sim 2$, the efficiency of energy injection needs to be considerably higher, $\sim 20\%$, which is in tension with expectations. Given the large uncertainty in AGN feedback, efficiencies of 20% are disfavored but cannot be ruled out.

Another way to distinguish feedback from virialization energy is the luminosity dependence of the signal. At $z = 2$, changing the quasar luminosity by an order of magnitude will change the feedback signal by an order of magnitude, but only increase the virialization signal by 50%. Thus, splitting the sample by luminosity can isolate the two signals: the lowest-luminosity subsample is dominated by the virialization signal, while the highest-luminosity subsample may be dominated by the feedback signal.

5.6 Forecasts for large-scale tSZ constraints

We predict C_ℓ^{yq} for the cross-correlation of DESI quasars with tSZ, using the fiducial CW13 model described in Sec. 5.4.1 (Fig. 5.5). We forecast the detection significance from both current Planck data and future data from the Simons Observatory.

To determine the detection significance we compute the noise as follows:

$$(N_\ell^{yq})^2 = \frac{1}{f_{\rm sky}(2\ell+1)} \left[(C_\ell^{yq})^2 + (C_\ell^{yy} + N_\ell^{yy})(C_\ell^{qq} + N_\ell^{qq})\right] \exp(\ell^2\theta_{\rm beam}^2) \tag{5.19}$$

where $f_{\rm sky}$ is the fraction of sky covered (fiducially 0.3 for Planck and 0.23 for SO cross-correlation); N_ℓ^{yy} is the noise on the tSZ map; N_ℓ^{qq} is the noise on the quasar map arising from Poisson fluctuations, $N_\ell^{qq} = 1/\overline{n}_q$, where $\overline{n}_q$ is the mean number density over the sky; and the final term corrects for the degradation of the signal by the finite beam size assuming a Gaussian beam with width $\theta_{\rm beam}$ (1.4' FWHM for SO and 10' FWHM for Planck). We directly measure $C_\ell^{qq} + N_\ell^{qq}$ from the simulation by creating a realization of the quasar catalog with the proper number density and measuring the autocorrelation of this catalog.

We use the homogeneous noise spectrum for the MILCA maps from Planck Collaboration et al. (2016f). Planck Collaboration et al. (2016f) present noise curves from both the NILC and MILCA methods; we conservatively use the MILCA noise curves, which are slightly higher on large scales. However, using MILCA reduces the expected detection significance by $\sim 0.5\sigma$ compared to NILC.

The Simons Observatory tSZ noise curves (The Simons Observatory Collaboration et al. 2018) are computed using a harmonic-space internal linear combination method from their

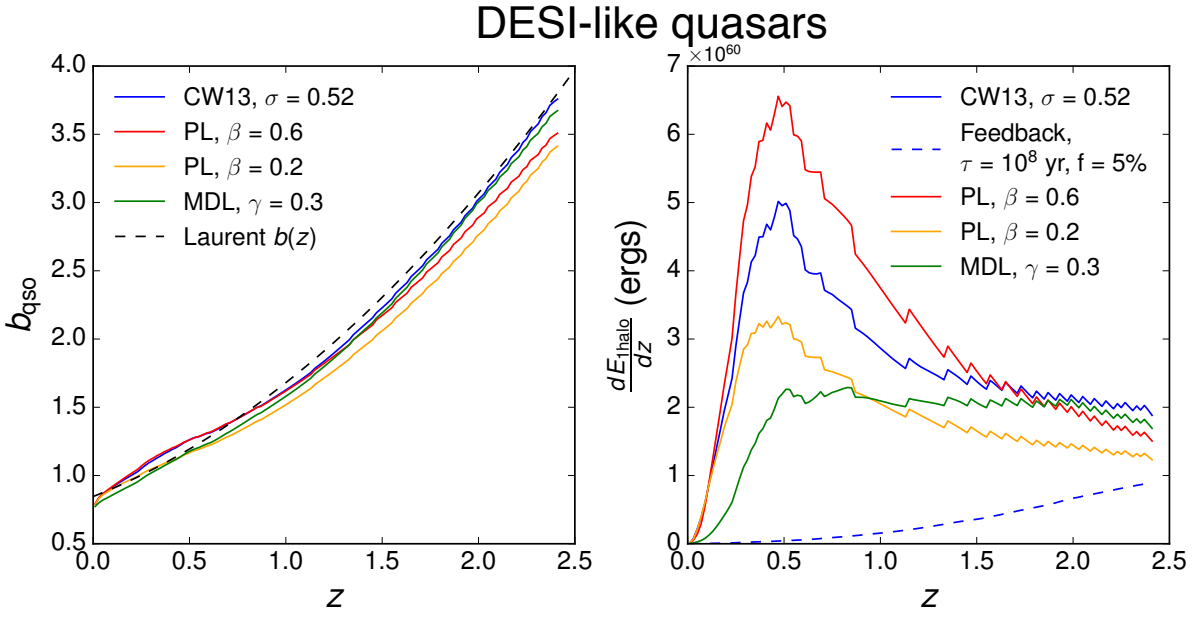

Figure 5.4: *Left:* $b_{\rm qso}(z)$ for DESI-like samples with different quasar models, compared to $b_{\rm qso}(z)$ from eBOSS (Laurent et al. 2017), which is appropriate for the fainter DESI quasar sample because of the weak dependence of quasar bias on luminosity. *Right:* Fractional one-halo thermal energy signal from virialization (solid lines) in bins of redshift, $\frac{dE_{\rm 1halo}}{dz}$, for different quasar models. Dashed line gives the feedback signal for the fiducial values of the quasar lifetime and fractional energy injection. Quasar models with similar clustering produce dramatically different tSZ signals, and because DESI quasars are fainter than previous samples, the feedback signal is likely smaller than the virialization signal.

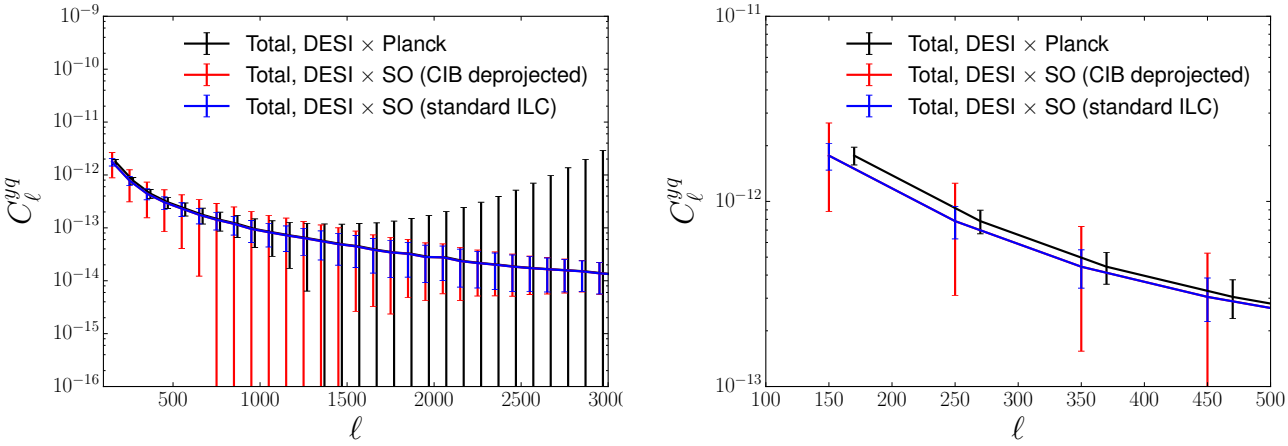

Figure 5.5: *Left:* C_ℓ^{yq} forecasts for Simons Observatory and Planck cross-correlations with DarkSky quasars across the entire redshift range ($0 < z < 2.38$) populated according to the CW13 model and the DESI flux cut. Planck errorbars are offset for clarity. *Right:* same as left panel but zoomed in on the range $100 < \ell < 500$, to show that Planck achieves lower noise on large scales due to its greater sky coverage.

fiducial sky and noise model. In this work we use their "standard ILC" noise from the full 16000 deg^2 survey with baseline sensitivity. We also show the noise curve with CIB deprojected to show the impact of CIB uncertainties, since this is a major systematic in previous tSZ-quasar cross-correlations (Verdier et al. 2016, Soergel et al. 2017, Hall et al. 2019).

We find that given the coarse Planck beam, any quasar-tSZ cross-correlation using Planck will be dominated by the two-halo term. This implies the quasar-tSZ cross-correlation can only constrain energy injection (e.g. from AGN feedback) across all halos, rather than energy injection from a particular quasar into its host halo (i.e. Ruan et al. 2015, Crichton et al. 2016). Moreover, this implies that Planck cross-correlations cannot differentiate between quasar models due to the poor resolution of the one-halo term.

We also forecast the sensitivity of the tSZ cross-spectrum between DESI and Simons Observatory tSZ measurements, using a 1.4' FWHM beam. Here we find similar errorbars but a higher expected significance owing to the much smaller beam. As a result, the SO-DESI measurement is much more sensitive to the one-halo term.

The two-halo cross-correlation is directly proportional to the product of the quasar bias b_Q, the Compton-y bias b_y and the redshift distribution of total y in the universe, dy/dz (Komatsu & Kitayama 1999) In Appendix 5.A, we show this explicitly by writing down the equations for a halo model of the tSZ-quasar cross correlation. We can therefore directly translate forecasts for the tSZ-quasar cross-correlation in the two-halo regime to constraints on $b_y\ dy/dz$, given a fiducial 5% uncertainty in the quasar bias (Laurent et al. 2017). In Fig. 5.6, we show that $b_y\ dy/dz$ can be measured to $\sim 20\%$ in $\Delta z = 0.25$ bins using either

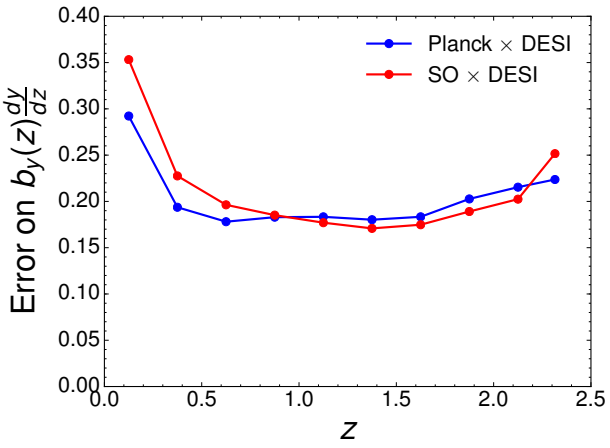

Figure 5.6: Error on $b_y(z)\ dy/dz$ as a function of redshift, using $\Delta z = 0.25$ bins and 5% error on the quasar bias.

Planck or SO, if we conservatively cut at $\ell_{\rm max} = 2000$ to eliminate any possible one-halo contamination. In fact, the constraints are slightly worse for SO than for Planck, since Planck has slightly lower noise on the large scales over which the 2-halo term will be measured and a slightly larger area overlap with DESI. Using the CIB deprojected noise curves rather than the standard ILC for SO reduces the detection significance by 40%, suggesting that CIB uncertainties may increase the fractional error on $b_y dy/dz$ to ∼30%, and will not destroy the constraining power of the measurement.

Under the assumption of fixed cosmology, these constraints may be further translated to direct constraints on ICM physics. $b_y\ dy/dz$ is directly proportional to the amplitude of the $Y - M$ relationship (Appendix 5.A), so assuming a fixed pressure profile shape, these constraints can be directly translated to 20-30% constraints on P_0, the amplitude of the pressure profile, in $\Delta z = 0.25$ redshift bins, or a 5% constraint on a redshift-independent P_0. This is quite competitive with existing constraints, including a 5% measurement of P_0 at $z \sim 0.15$ from the SDSS group sample (Hill et al. 2018), a 5% constraint from the tSZ auto spectrum (Hill & Spergel 2014) and a 20% constraint from the tSZ-lensing cross spectrum (Hill & Spergel 2014). However, due to the strong dependence of the tSZ power spectrum on σ_8, all of these one-halo constraints on P_0 are near the bound (5-10%) set by the uncertainty in σ_8. In contrast, two-halo measurements of P_0 are much less sensitive to σ_8 ($\propto \sigma_8^2$ rather than σ_8^7) and so offer better hope for higher-precision measurements of P_0.

5.7 Conclusions

In this paper we have studied how the combination of large redshift surveys and future CMB experiments can be used to study quasar models and hot halo gas through measurements of the Sunyaev-Zeldovich effect in stacked QSO samples.

We argue that the large-scale two-halo term from the quasar-tSZ cross-correlation is the cleanest probe of AGN feedback. The two-halo term depends only on the large-scale quasar and Compton-y biases, and is insensitive to the highly uncertain details of the quasar halo occupation. AGN feedback can modify the total thermal energy in all halos (or a mass-selected subset, if it creates a break in the $Y-M$ relation), thus changing the Compton-y bias. The large scale quasar-tSZ cross-correlation is a particularly powerful probe of the Compton-y bias because quasars have an extended redshift distribution, so they can tomographically map the history of ionized gas throughout the universe.

As part of this project we have developed and calibrated a technique for making mock catalogs of QSOs. These catalogs reproduce the luminosity functions and clustering of optical Type I QSOs over the redshift range of interest for surveys such as DESI ($0.5 < z < 2$). This is a substantial update to the quasar model of Conroy & White (2013), as we re-fit the model with the updated UV luminosity function of Kulkarni et al. (2018) and also present two generalizations of the model with varying lifetimes and Eddington ratio distributions.

We show how the small-scale tSZ signal can discriminate between these quasar models, which otherwise match the luminosity function and clustering data. We argue that because DESI quasars are fainter than previous quasar samples, they are more sensitive to tSZ from halo virialization and less sensitive to energy injection from AGN feedback. As a result, large scales offer the best prospects for learning about AGN feedback from the two halo term of the tSZ-quasar cross-correlation, whereas small scales are most useful for constraining quasars' halo occupation, informing models of quasar triggering and evolution.

acknowledgments

M.W. is supported by the U.S. Department of Energy and by NSF grant number 1713791. This research used resources of the National Energy Research Scientific Computing Center (NERSC), a U.S. Department of Energy Office of Science User Facility operated under Contract No. DE-AC02-05CH11231. This work also made extensive use of the NASA Astrophysics Data System and of the `astro-ph` preprint archive at `arXiv.org`.

5.A Analytics

While all of our quantitative forecasts in the main text are based on simulated maps, we derive here some expressions using an analytical halo model in order to give intuition on the unique information obtainable by cross-correlating Compton-y with a spectroscopic sample on large scales.

5.A.1 Mean y-distortion

The mean value of y is obtained by summing the contribution of halos over mass and redshift,

$$y = \int dz V_c(z) \int dm \frac{dn}{dm} Y(m,z), \tag{5.20}$$

where $V_c(z) \equiv 4\pi\chi^2(z)d\chi/dz$, the total sky-averaged contribution to y from a halo at mass M and redshift z is

$$Y(m,z) \equiv \left(\frac{\sigma_T}{m_e c^2}\right) \frac{(1+z)^2}{\chi^2(z)} E_{th}(m,z), \tag{5.21}$$

and the total thermal energy in electrons is

$$E_{th}(m,z) \equiv 4\pi \int r^2 dr P_e(r|m,z). \tag{5.22}$$

A useful quantity to define is the contribution to the mean y-distortion per unit redshift,

$$\frac{dy}{dz} \equiv V_c(z) \int dm \frac{dn}{dm} Y(m,z). \tag{5.23}$$

5.A.2 Cross-correlation with linearly biased tracer

The cross-correlation between Compton-y and a linearly biased tracer is the sum of one-halo

$$C_\ell^{1h-yq} = \int dz V_c(z) \int dm \frac{dn}{dm} p_{\rm qso}(m,z) Y(m,z) u_\ell^y(m,z), \tag{5.24}$$

and two-halo

$$C_\ell^{2h-yq} = \int dz V_c(z) P(\ell/\chi, z) \tag{5.25}$$

$$\times \int dm \frac{dn}{dm} b_h(m,z) Y(m,z) u_\ell^y(m,z) \tag{5.26}$$

$$\times \int dm \frac{dn}{dm} b_h(m,z) p_{\rm qso}(m,z), \tag{5.27}$$

terms, where

$$u_\ell^y(m,z) \equiv \frac{4\pi}{E_{th}(m,z)} \int dr r^2 P_e(r|m,z) \frac{\sin(r\ell/\chi)}{r\ell/\chi} \tag{5.28}$$

is the Fourier transform of the projected pressure profile, normalized such that as $\ell \to 0$, $u_\ell^y \to 1$, $p_{\rm qso}(m,z)$ encapsulates the redshift-selection and halo occupation probability, and

$$n_{\rm qso}(z) = \int dm \frac{dn}{dm} p_{\rm qso}(m,z). \tag{5.29}$$

5.A.3 Large-scale Compton bias and $P_0(z)$

On angular scales much larger than individual objects,

$$C_\ell^{2h-yq} \approx \int dz b_q(z) b_y(z) n_{\rm qso}(z) \frac{dy}{dz} P(\ell/\chi, z), \tag{5.30}$$

where the bias of the tracers is

$$b_q(z) \equiv n_{\rm qso}^{-1}(z) \int dm \frac{dn}{dm} b_h(m,z) p_{\rm qso}(m,z) \tag{5.31}$$

and the Compton bias is

$$b_y(z) \equiv \left(\frac{dy}{dz}\right)^{-1} V_c(z) \int dm \frac{dn}{dm} b_h(m,z) Y(m,z). \tag{5.32}$$

Using a distant spectroscopic sample with a narrow redshift distribution allows for a accurate measurement of the quantity $b_y(z)dy/dz$ since, for a uniform sample in a redshift bin of width Δz, equation (5.30) becomes

$$C_\ell^{2h-yq} \approx b_y(z) \frac{dy}{dz} n_{\rm qso}(z) b_q(z) P(\ell/\chi, z) \Delta z, \tag{5.33}$$

and $n_{\rm qso}(z)$ and $b_q(z)P(\ell/\chi, z)$ are known from the clustering properties and abundance of the sample, independent of the cross-correlation measurement. No assumption about the quasar duty cycle or halo occupation distribution needs to be made in this case.

Additionally, because on large scales the shape of the pressure profile does not enter, there is no degeneracy with its overall normalization, unlike for cross-correlation with lensing in which the large-scale contribution from individual massive objects at lower redshift cannot be separated out due to projection affects associated with the lensing kernel. Specifically,

$$b_y(z)\frac{dy}{dz} = P_0(z) \int dm \frac{dn}{dm} b_h(m,z) Y_{\rm fid}(m,z) = P_0(z) \left[b_y(z)\frac{dy}{dz}\right]_{\rm fid}, \tag{5.34}$$

where

$$P_0(z) \equiv \frac{Y(m,z)}{Y_{\rm fid}(m,z)}. \tag{5.35}$$

5.B Quasar model: fits to luminosity function

We update the fits of Conroy & White (2013) for our fiducial quasar model for forecasting purposes. Compared to Conroy & White (2013), we incorporate three major changes to the quasar model: we use a broken power-law relationship between $M_{\rm BH}$ and $M_{\rm gal,*}$ (Eq. 5.7); we use the updated stellar mass to halo mass relation of Behroozi et al. (2018); and we use the updated, homogenized quasar UV luminosity function data from Kulkarni et al. (2018).

Following Kulkarni et al. (2018), we present the luminosity function in units of M_{1450}, the absolute magnitude at 1450 Å, rather than $M_i(z = 2)$ as in Conroy & White (2013). As an additional minor change, we use the cosmology of the DarkSky N-body simulation.

We start with the halo mass functions of Tinker et al. (2008), and convert from M_{200c} to $M_{\rm vir}$ assuming an NFW profile with the concentration given by the Duffy et al. (2008) concentration-mass relation. We use the updated Behroozi et al. (2018) relation to relate halo mass to stellar mass. Stellar mass is related to black hole mass through Eq. 5.7,[4] and the intercept α varied as a free parameter. We then assume that quasars radiate at some fraction of the Eddington luminosity, η, and convert quasar luminosity to M_{1450} using Eqs. 3-8 in Conroy & White (2013)[5]. As in Conroy & White (2013), we find that a model with $\eta_0(z = 0) = 0.1$ and a linear ramp to $\eta_0 = 1$ from $z = 0.5$ to 3.5 produces self-consistent black hole growth, while a model with constant $\eta_0 = 0.1$ fails to do so; as a result we favor the varying Eddington ratio as our fiducial model (Fig. 5.10).

We also fit several models to the quasar luminosity function beyond the "scattered lightbulb" model of Conroy & White (2013). For the scattered lightbulb model, we find that fiducial 0.52 dex scatter (0.3 decades scatter in each of the galaxy-halo, galaxy-black hole, and Eddington ratio distributions) is in better agreement with the data than either a high-scatter (0.7 dex) or low-scatter (0.3 dex) case for $z < 2.4$; at higher redshifts the three cases fit the data equally well. For the power law Eddington ratio model (Eq. 5.10) we find that $\beta = 0.2$ or 0.6 fit the data similarly well as the scattered lightbulb model. Likewise, we find that for the mass-dependent lifetime model (Eq. 5.11), $\gamma = 0.3$ provides an adequate fit to the data[6]. Similarly to the scattered lightbulb model, a linear ramp in η_0 is required to produce consistent black hole growth for the power-law and mass-dependent lifetime models (Fig. 5.10), although as described in Section 5.4.1, the linear ramp for η_0 in the power law model is from $\eta_0 = 0.4$ at $z = 0.5$ to $\eta_0 = 4$ at $z = 3.5$. To match the clustering, we must lower $M_{\rm gal,*}$ by 0.3 dex for the power-law and mass-dependent-lifetime models; this is roughly the 1-σ uncertainty on the stellar mass-halo mass relation at $z \sim 1$ (Behroozi et al. 2018).

These models have two free parameters, α and the quasar duty cycle f_{on} (which can be recast into a quasar lifetime $t_Q = f_{\rm on} t_H$), and we adjust these two parameters to fit the luminosity function by minimizing χ^2. We fit the models in 12 bins of redshift over $0 < z < 7$.

[4]Eq. 1 in Conroy & White (2013), with the logarithmic slope β fixed to one, fits the luminosity function equally well, but under-predicts the clustering. Other slopes, such as $\beta = 1.5$ or $\beta = 1.33$, fit the luminosity function equally well but under-predict the clustering if a non-broken galaxy-black hole relationship is used. Several recent works argue that the $M_{\rm BH} - M_{\rm bulge,\star}$ relation is not universal (Graham & Scott 2015, Savorgnan et al. 2016) and therefore may be nonlinear for all galaxies (Bentz & Manne-Nicholas 2018), motivating the broken galaxy mass-black hole mass relation.

[5]There is a typo in Eq. 7 in Conroy & White (2013) translating $M_i(z = 2)$ to M_{1450}. The correct conversions can be found in Eq. 3 of Richards et al. (2006) or Eq. B8 of Ross et al. (2013), $M_{1450} = M_i(z = 2) + 1.486$.

[6]In all cases, at $z < 3$ the χ^2 for the models is formally quite different. However, as discussed the formal errors on the luminosity function are likely grossly underestimated, so the χ^2 differences are not meaningful. Qualitatively, all four models yield similarly good fits to the data.

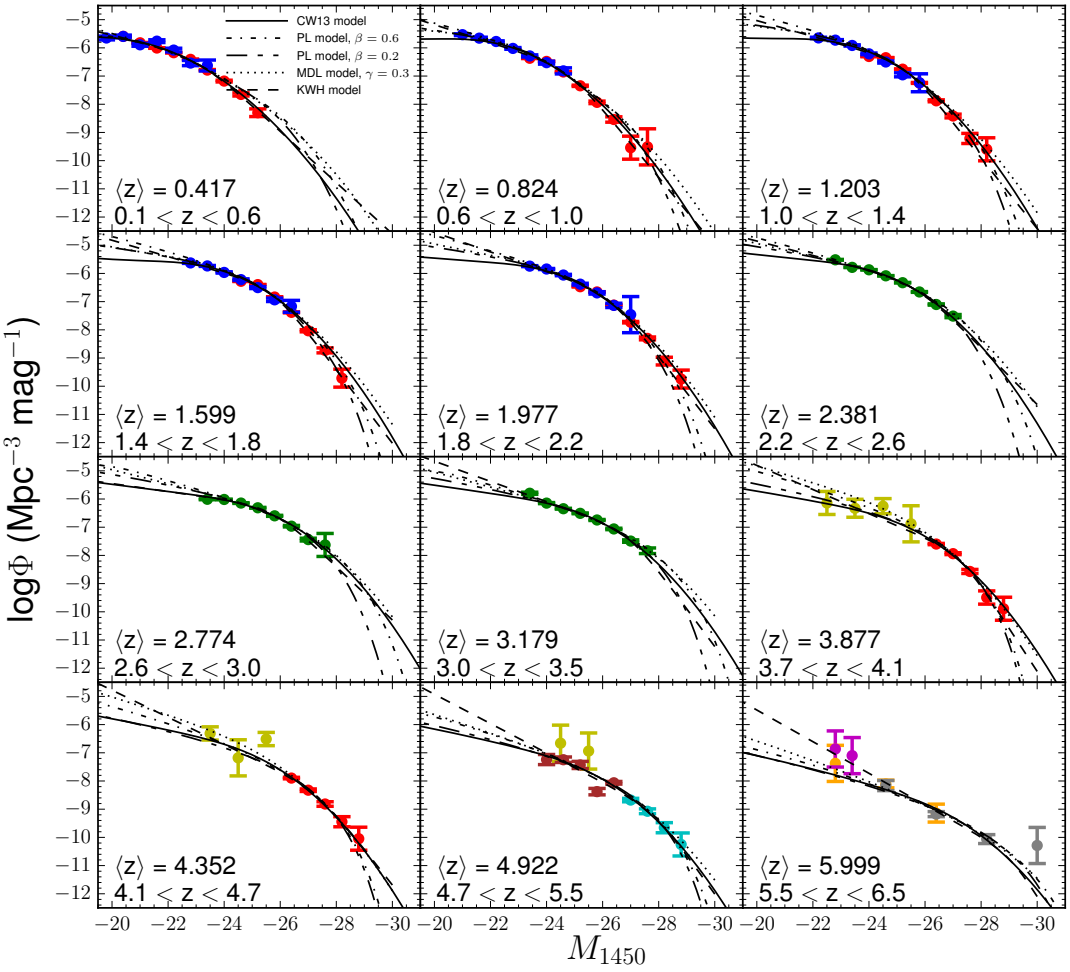

Figure 5.7: Homogenized quasar luminosity function data from Kulkarni et al. (2018) compared to Kulkarni et al. (2018) double power-law fits (dashed) and physical quasar models: the "scattered lightbulb" model of Conroy & White (2013) with a lognormal Eddington ratio distribution; the same model but with a power-law Eddington ratio distribution, either with $\beta = 0.2$ or 0.6 (Eq. 5.10); and a "scattered lightbulb" model with an explicitly mass-dependent lifetime, with $f_{\rm on} \propto M_{\rm BH}^{-0.3}$. Data from SDSS DR7 (Schneider et al. 2010) (red); 2SLAQ (Croom et al. 2009) (blue), BOSS (Ross et al. 2013) (green), Glikman et al. (2011) (yellow), McGreer et al. (2013) (brown), Yang et al. (2016) (light blue), Kashikawa et al. (2015) (magenta), Willott et al. (2010) (orange), and Jiang et al. (2016) (gray).

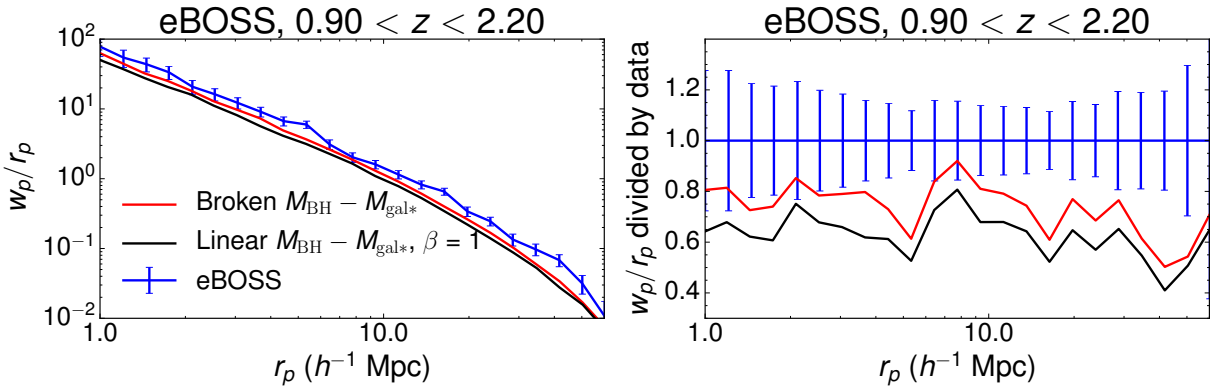

Figure 5.8: comparison to $w_p(r_p)$ in eBOSS quasars as measured by Rodríguez-Torres et al. (2017). Right panel shows ratio of the mock w_p to the data w_p. We find that a broken $M_{\rm BH}$-$M_{\rm gal,*}$ better reproduces the eBOSS clustering than the linear $M_{\rm BH}$-$M_{\rm gal,*}$ from Conroy & White (2013). The remaining discrepancy is likely due to the incompleteness of the DarkSky simulation at small halo masses.

In Fig. 5.7 we show the luminosity function in these 12 bins and in Fig. 5.9 we show the evolution of α and $f_{\rm on}$ with redshift. We find generally smooth redshift evolution in α and t_Q. To compare the models, we show the distribution of halo masses for DESI-like quasar samples selected according to Sec. 5.4.2 in Fig. 5.11.

We also compare these models to quasar clustering measurements (Fig. 5.8). We focus on quasar clustering from the eBOSS survey, since it has a much higher signal-to-noise than previous quasar clustering measurements. We compare to w_p measurements from Rodríguez-Torres et al. (2017). In our DarkSky mock, we move the quasars into redshift space, match $\pi_{\rm max} = 60\ h^{-1}$ Mpc, impose a flux cut of $r < 22$ to match the eBOSS quasar selection, and down-sample quasars to match the observed eBOSS dN/dz. We find that using a linear $M_{\rm BH}$-$M_{\rm gal,*}$ relation, as in Conroy & White (2013), leads to clustering 30-40% too low in the simulation. Instead using a broken $M_{\rm BH}$-$M_{\rm gal,*}$ relation leads to considerably better agreement, although the clustering in the mock is still 20% too low. However, since we can match the large-scale bias of eBOSS (Laurent et al. 2017) using analytic mass and bias functions from Tinker et al. (2008, 2010), we suspect that the discrepancy is due to incompleteness in the DarkSky simulation in halos below $10^{12}\ M_\odot$, which still contain some quasars (Fig. 5.11). We tried a number of other fixes for the clustering, including increasing the scatter to 0.7 dex, changing from the default varying Eddington ratio distribution to a constant Eddington ratio, changing the slope β of the $M_{\rm BH}$-$M_{\rm gal,*}$ relation, using Moster et al. (2010) SM-HM relation rather than Behroozi et al. (2018), modifying the flux cut, and scaling down the input halo masses. The only other change that makes a substantial difference is scaling the input halo masses; however, the amount of scaling required is inconsistent with uncertainties in the SM-HM relation or halo mass definitions. Therefore, we favor changing

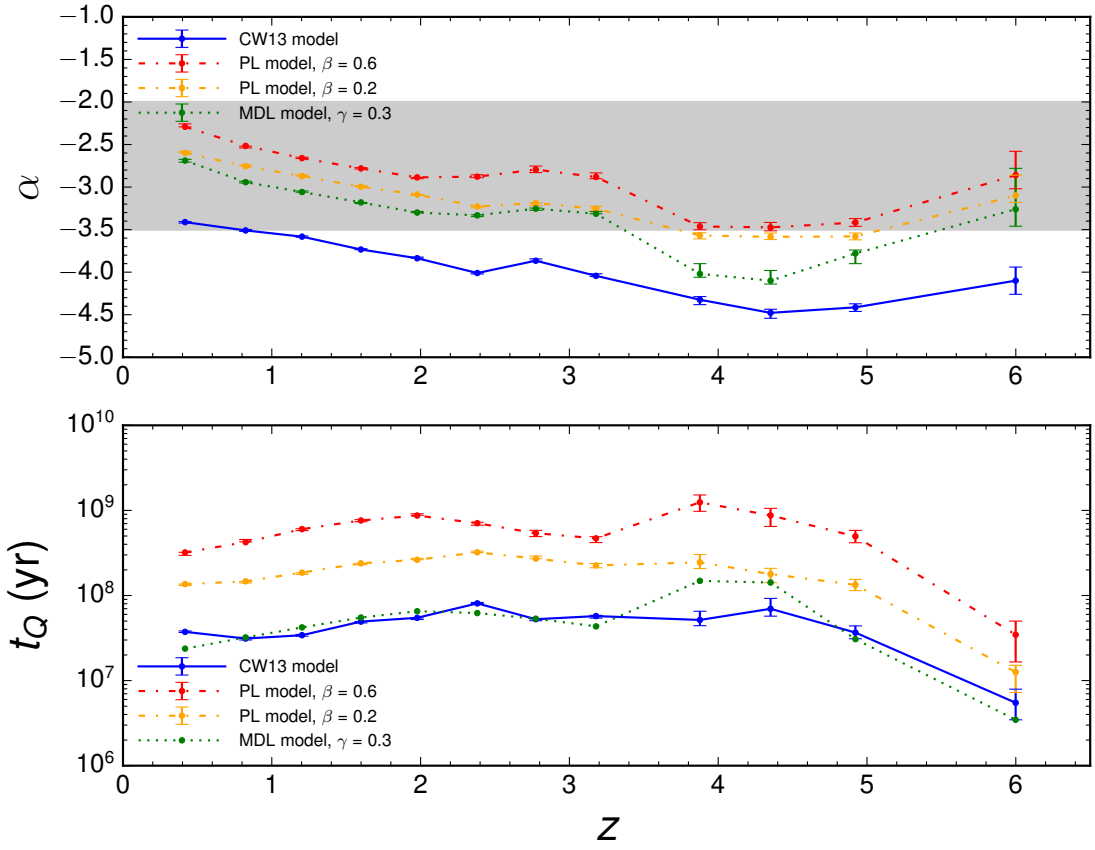

Figure 5.9: Parameters α and t_Q as a function of redshift. Shaded band is the range of local normalization measurements. For the mass-dependent lifetime, t_Q is the lifetime of a quasar with black hole mass $10^8\ M_\odot$.

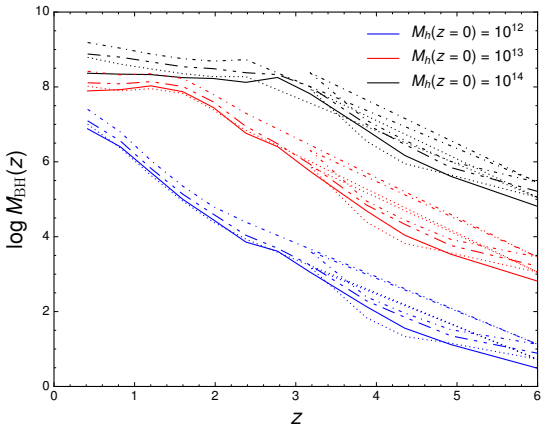

Figure 5.10: Black hole mass as a function of redshift for halos of a given $z = 0$ halo mass, using Behroozi et al. (2013) accretion rates. Line styles for the four quasar models match Fig. 5.7.

to a broken $M_{\rm BH}$-$M_{\rm gal,*}$.

As in Conroy & White (2013), we find that at $z < 4$ the lifetime is redshift-independent, and at higher redshifts it drops. While we caution that the errors on t_Q are underestimates, since the corresponding errors on the luminosity function are only Poisson uncertainties, the drop in t_Q at $z > 4$ is consistent with lifetime estimates of 10^5-10^7 yrs from quasar proximity zones and IGM damping wings at z ∼6-7 (Eilers et al. 2017, Davies et al. 2018). At lower redshifts, the constraints on the quasar lifetime are consistent with alternative measurements of $t_Q \lesssim 10^8$ yr (Yu & Tremaine 2002, Martini 2004, Schmidt et al. 2017).

We find that the normalization α is 0.5 dex lower than Conroy & White (2013) for the "scattered ligthbulb" model, although the other models are more nearly consistent with the Conroy & White (2013) normalization. We found that this discrepancy persists if we use either the stellar mass-halo mass relation or the luminosity function data from Conroy & White (2013); thus both changes drive α to a lower value. For the scattered lightbulb model, α is degenerate with the assumed scatter (Fig. 2 in Conroy & White 2013), but very low values of the scatter (< 0.3 dex) are required to bring α into agreement with Conroy & White (2013). These values of the scatter are both highly disfavored by the luminosity function data and in conflict with constraints on the $M_{\rm BH} - M_{\rm gal,\star}$ scatter (Kormendy & Ho 2013) and the stellar mass-halo mass scatter (Tinker et al. 2017). Systematics in the low-redshift luminosity function data are also likely not the culprit for the discrepancy: Kulkarni et al. (2018) argue that an increase in the faint-end slope of their double power-law model at $z < 0.6$ is a spurious, driven by systematic errors in the completeness due to host galaxy contamination. However, scaling the low-luminosity data at $z = 0.417$ to match the faint-end slope at higher redshifts reduces α by only 0.2 decades (and in fact exacerbates the tension with local measurements and Conroy & White 2013). We also find a consistently low value of α in the $z > 0.8$ bins, suggesting that any mismeasured completeness in the lowest redshift

bin ($z = 0.417$) does not have a significant effect on α.

For all four models, the best-fit $z = 0$ normalization lies on the low end of local measurements, which range from -2 to -3.5 (Merritt & Ferrarese 2001, Kormendy & Gebhardt 2001, McLure & Dunlop 2002, Marconi & Hunt 2003, Häring & Rix 2004, Kormendy & Bender 2009, Jahnke et al. 2009, Kormendy & Ho 2013, McConnell & Ma 2013, Marleau et al. 2013, Reines & Volonteri 2015, Bentz & Manne-Nicholas 2018). Our models only constrain the sum $\log \eta_0 + \alpha$, so the discrepancy could be trivially resolved by reducing $\eta_0(z = 0)$. However, this would conflict with direct determinations of the Eddington ratio distribution using quasars with virial black hole mass estimates (Kollmeier et al. 2006, Shen et al. 2008), which favor $\eta_0 \sim 0.1$. Therefore, we disfavor modifications to our fiducial Eddington ratio model.

Local estimates of the normalization are subject to a variety of systematic effects and caveats. Most obviously, most local estimates measure the normalization of the $M_{\rm BH} - M_{\rm bulge,\star}$ relation (but see Bentz & Manne-Nicholas (2018) and Reines & Volonteri (2015) for local measurements of $M_{\rm BH} - M_{\rm gal,\star}$ normalization), which is equivalent to the normalization of $M_{\rm BH} - M_{\rm gal,\star}$ relation only for high-mass bulge-dominated systems and would thus naturally lead to a lower normalization in the $M_{\rm BH} - M_{\rm gal,\star}$ relation. Moreover, uncertainties in the mass-to-light ratios and IMFs can drive significant changes in both the slope and normalization (Bentz & Manne-Nicholas 2018), while the normalization may be biased high by up to a factor of 3 for directly-measured inactive black holes in early type galaxies, due to the requirement that the black hole sphere of influence be resolved (Shankar et al. 2016). Our results favor lower values of the normalization, although given the large error bars and systematics associated with the local normalization measurements, we do not ascribe too much significance to the discrepancy.

In conclusion, we use the fiducial varying Eddington ratio model as our quasar model, with α, t_Q and luminosity functions given in Fig. 5.9. Specifically, at each redshift we assign α and t_Q using a linear interpolation between the points in Fig. 5.9.

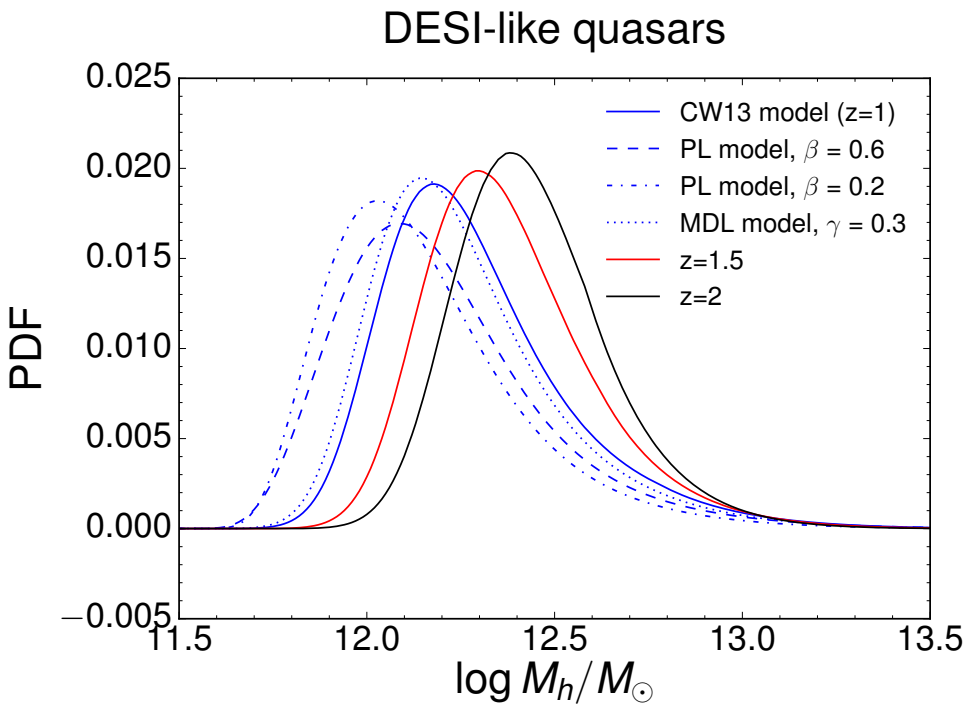

Figure 5.11: Distribution of halo masses for DESI-like quasar samples assigned according to the CW13 model, PL models with $\beta = 0.6$ and $\beta = 0.2$, and MDL model with $\gamma = 0.3$.

Chapter 6

unWISE tomography of Planck CMB lensing

Abstract

CMB lensing tomography, or the cross-correlation between CMB lensing maps and large-scale structure tracers over a well-defined redshift range, has the potential to map the amplitude and growth of structure over cosmic time, provide some of the most stringent tests of gravity, and break important degeneracies between cosmological parameters. In this work, we use the unWISE galaxy catalog to provide three samples at median redshifts $z \sim 0.6, 1.1$ and 1.5, fully spanning the Dark Energy dominated era, together with the most recent Planck CMB lensing maps. We obtain a combined cross-correlation significance $S/N = 79.3$ over the range of scales $100 < \ell < 1000$. We measure the redshift distribution of unWISE sources by a combination of cross-matching with the COSMOS photometric catalog and cross-correlation with BOSS galaxies and quasars and eBOSS quasars. We also show that magnification bias must be included in our analysis and perform a number of null tests. In a companion paper, we explore the derived cosmological parameters by modeling the non-linearities and propagating the redshift distribution uncertainties.

6.1 Introduction

As they travel from the surface of last scattering to the Earth, Cosmic Microwave Background (CMB) photons are deflected by the gravitational potentials associated with large-scale structure (LSS), providing a probe of late-time physics directly in the CMB sky (see Lewis & Challinor 2006, Hanson et al. 2010; for reviews). The lensing effect is dominated by structures on Mpc scales over a very broad range of redshifts from $z < 1$ to $z \sim 10$. By cross-correlating the lensing map with another tracer of large-scale structure which spans a narrower range in redshift, we can simultaneously increase the signal-to-noise ratio and isolate particular redshifts of interest. Doing this on multiple lens redshift planes ("CMB lensing

tomography") breaks important degeneracies between the expansion history and the growth of perturbations, as well as providing greater control over systematics (Hu 1999, 2002). The first detections of CMB lensing were obtained in cross-correlation between galaxy samples and WMAP data (Smith et al. 2007, Hirata et al. 2008), and some of the early work employing cross-correlations with ACT, SPT and Planck are presented in Sherwin et al. (2012), Bleem et al. (2012), Planck Collaboration et al. (2014c) respectively. Since then, there have been a large number of cross-correlation analysis with a wide variety of samples (see for example Omori & Holder 2015, Allison et al. 2015b, Bianchini et al. 2015, Baxter et al. 2016, Giannantonio et al. 2016, Omori et al. 2018, Marques & Bernui 2019).

In this work, we use galaxies from the unWISE catalog (Schlafly et al. 2019), containing angular positions and magnitudes of over two billion objects observed by the Wide-field Infrared Survey Explorer (WISE, (Wright et al. 2010)) mission. The unWISE catalog builds upon earlier WISE-based catalogs by including additional data from the post-hibernation NEOWISE mission, and is the largest full-sky galaxy catalog currently available (Schlafly et al. 2019), containing over half a billion galaxies across the full sky. We further divide the catalog based on magnitude and color and reject stars based on Gaia data (Gaia Collaboration et al. 2016), creating three samples, referred here as "blue", "green" and "red," at median redshifts $\sim 0.6, 1.1$ and 1.5, respectively, allowing a tomographic analysis of the amplitude of fluctuations in the Dark Energy dominated era. Previous cross-correlations between WISE-derived catalogs and CMB lensing were presented in Planck Collaboration et al. (2014c), Ferraro et al. (2015), Ferraro et al. (2016), Hill et al. (2016), Shajib & Wright (2016), Peacock & Bilicki (2018), Marques & Bernui (2019).

In this paper, we present the auto correlation of the galaxy samples and their cross-correlation with the Planck CMB lensing maps (Planck Collaboration et al. 2018f). We also measure the redshift distribution of the unWISE galaxies, which is crucial for the cosmological interpretation of the signal. While obtaining photometric redshifts from the two WISE colors alone is not feasible, cross-matching sources with the COSMOS photometric catalog as well as cross correlation with a number of spectroscopic surveys allows us to determine the ensemble redshift distribution of our samples, together with an estimate of its uncertainty.

The outline of the paper is as follows: In Section 6.2 we summarize the data used and in Section 6.3 we describe our modelling. In Section 6.4 we discuss the auto and cross correlation measurements and in Section 6.5, we measure the redshift distribution of the unWISE sample and characterize its uncertainties. The results are presented in Section 6.6. Possible systematics and null tests are explored in Section 6.7, and in Section 6.8 we summarize our results. This paper is focused on the measurement of the cross-correlation. In a companion paper (Krolewski et al. 2020), we will extract cosmological information by modeling the non-linearities in the signal and marginalizing over uncertainties in the stellar contamination fraction and the galaxy redshift distribution.

Where necessary we assume a fiducial ΛCDM cosmology with the Planck 2018 maximum likelihood parameters (the final column in Table 2 in Planck Collaboration et al. (2018e)). We quote magnitudes in the Vega system, noting that we can easily convert these to AB magnitudes with AB = Vega + 2.699, 3.339 in W1, W2, respectively.

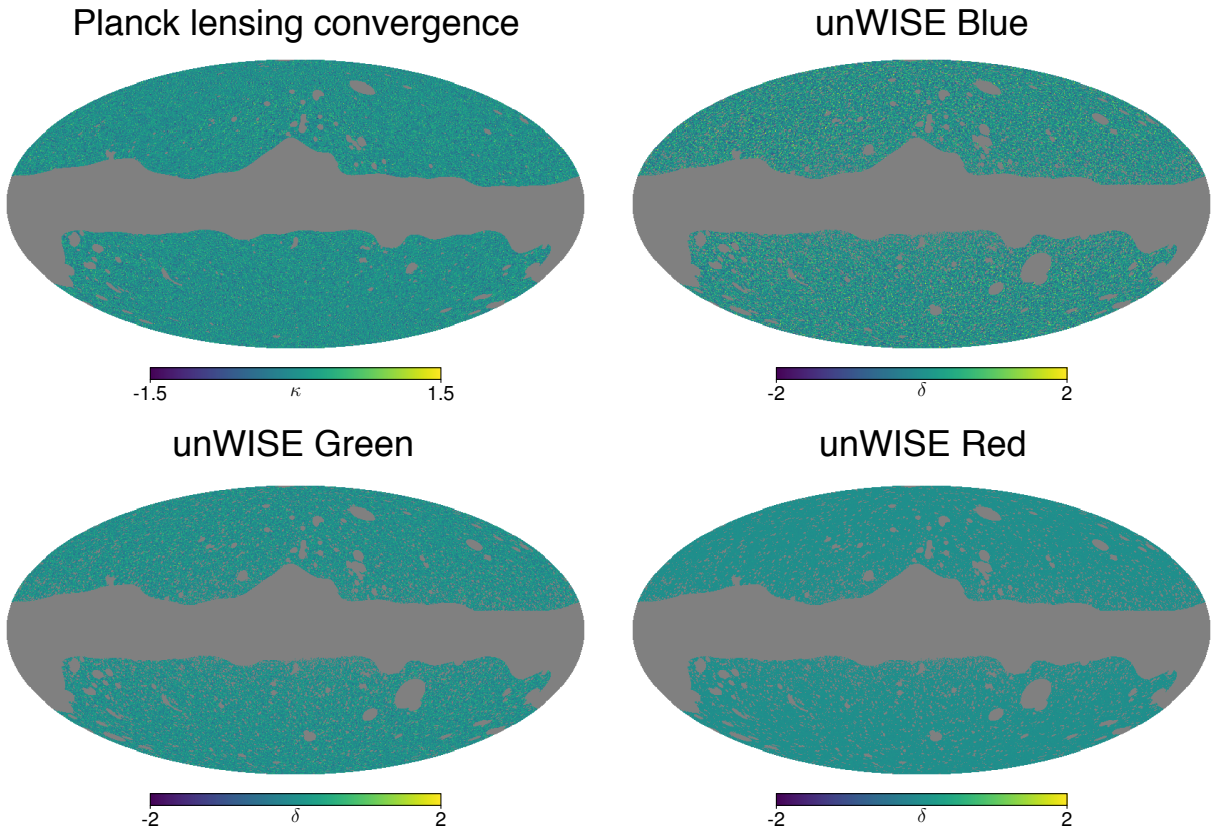

Figure 6.1: Plot of the maps used in the analysis (κ for Planck lensing convergence and density contrast δ for the galaxy samples). The maps have been filtered to only contain the range of scales used in this analysis, i.e. $\ell_{\rm min} = 100$ and $\ell_{\rm max} = 1000$, and this explains the lack of large-scale power.

6.2 The data

6.2.1 Planck CMB lensing maps

Gravitational lensing of the CMB remaps the temperature and polarization fields, altering their statistics in a well-defined way (Lewis & Challinor 2006). By searching for these statistical patterns it is possible to reconstruct the lensing convergence, κ, from quadratic combinations of the foreground-cleaned maps (Hu & Okamoto 2002). We use the latest CMB lensing maps from the Planck 2018 release (Planck Collaboration et al. 2018f) and their associated masks, downloaded from the Planck Legacy Archive.[1] These maps are provided as spherical harmonic coefficients of the convergence, $\kappa_{\ell m}$, in HEALPix format (Górski et al. 2005) and with $\ell_{\rm max} = 4096$. In particular, for our fiducial analysis we use the minimum-variance (MV) estimate obtained from both temperature and polarization, based on the `SMICA` foreground-reduced CMB map. Since the MV reconstruction is dominated by temperature, residual galactic and extragalactic foregrounds may contaminate the signal. Extensive testing has been performed by the Planck team, indicating no significant problems at the current statistical level. Nonetheless, thermal Sunyaev-Zel'dovich (tSZ) contamination has been shown to be one of the largest potential contaminants to cross correlations with tracers of large-scale structure in other analyses (Schaan & Ferraro 2019, Madhavacheril & Hill 2018, van Engelen et al. 2014, Osborne et al. 2014). For this reason, as a test, we shall repeat the analysis with a lensing reconstruction on `SMICA` foreground-reduced maps where tSZ has been explicitly deprojected (Planck Collaboration et al. 2018f), and we will refer to this analysis as "tSZ-free." Possible foreground contamination is discussed more in detail in Section 6.7.2.

6.2.2 unWISE

The WISE mission mapped the entire sky at 3.4, 4.6, 12, and 22 μm (W1, W2, W3, and W4) with angular resolutions of 6.1″, 6.4″, 6.5″ and 12″, respectively (Wright et al. 2010). The AllWISE data release encompassed the full WISE cryogenic mission as well as the initial NEOWISE post-cryogenic mission, from 2010 January to 2011 February, after which the instrument was placed into hibernation (Mainzer et al. 2011, Cutri et al. 2013). The W1 and W2 bands do not require cryogen to operate efficiently, motivating reactivation of WISE in December 2013 (Mainzer et al. 2014). Observations from the continuing NEOWISE mission have been incorporated into increasingly deep "unWISE" coadded images of the sky (Meisner et al. 2017b,a, 2018), which now feature more than 4× longer exposure times than were available for the AllWISE data release. In the future, at least another two years of NEOWISE data will be available (NEO5 and NEO6), which would further increase the depth by ∼0.2 magnitudes.

The deeper imaging coupled with the ∼ 6.5″ angular resolution leads to crowded images with many overlapping sources, requiring a new approach to the analysis of the WISE

[1] PLA: `https://pla.esac.esa.int/`

Label	$\mathrm{W1}-\mathrm{W2} > x$	$\mathrm{W1}-\mathrm{W2} < x$	$\mathrm{W2} < x$	$\bar{z}$	δz	$\bar{n}$	s
Blue		$(17-\mathrm{W2})/4+0.3$	16.7	0.6	0.3	3409	0.455
Green	$(17-\mathrm{W2})/4+0.3$	$(17-\mathrm{W2})/4+0.8$	16.7	1.1	0.4	1846	0.648
Red	$(17-\mathrm{W2})/4+0.8$		16.2	1.5	0.4	144	0.842

Table 6.1: Color and magnitude cuts for selecting galaxies of different redshifts, together with the mean redshift, $\bar{z}$, and the width of the redshift distribution, δz (as measured by matching to objects with photometric redshifts on the COSMOS field (Laigle et al. 2016)), number density per deg^2 within the unWISE mask, $\bar{n}$, and response of the number density to magnification, $s \equiv d\log_{10} N/dm$. Galaxies are additionally required to have $\mathrm{W2} > 15.5$, to be undetected or not pointlike in Gaia (see §6.2.3), and to not be flagged as diffraction spikes, latents or ghosts. s is measured using galaxies at ecliptic latitude $|\lambda| > 60°$, where WISE reaches fainter limiting magnitudes due to increased depth of coverage (see Appendix 6.C).

coadded images. The `crowdsource` crowded field photometry pipeline (Schlafly et al. 2018), originally designed for surveys of the Galactic plane, was employed to generate a new catalog based on the deep unWISE coadded images (Schlafly et al. 2019). The resulting catalog provides a sample of > 500 million galaxies with $0 < z < 2$ and improves the uniformity of the depth and photometric calibration of the WISE survey.

6.2.3 Galaxy selection

Galaxies are selected on the basis of their WISE W1 and W2 magnitudes. Inspection of the average colors of galaxies detected in WISE as a function of redshift shows a clear trend in which fainter and redder galaxies tend to be at higher redshift. Accordingly we made three selections of galaxies in $\mathrm{W1}-\mathrm{W2}$ color, with a sliding cut on color with magnitude reflecting that fainter galaxies tend to be at higher redshifts. Table 6.1 gives the adopted color selection for the three samples considered in this work, which we term the blue, green, and red samples (Schlafly et al. 2019). Table 6.1 also summarizes important properties of each sample including the redshift distribution, the number density, and the response of number density to galaxy magnification $s \equiv d\log_{10} N/dm$. We measure s using galaxies with ecliptic latitude $|\lambda| > 60°$, where the WISE depth of coverage is greater and thus the measurement of s is less affected by incompleteness. We describe the measurement of s in Appendix 6.C.

We require that the blue and green samples have $15.5 < \mathrm{W2} < 16.7$, and the red sample has $15.5 < \mathrm{W2} < 16.2$. If we allow the red sample to include sources with $16.2 < \mathrm{W2} < 16.7$, we find that the red-blue cross-correlation is inconsistent at the 2-3σ level with the expected cross-correlation given the bias measured from the CMB-cross spectra (Appendix 6.D). The fainter red samples also exhibit a decrease in number density closer to the Galactic plane, and may have more angular variation in dN/dz. As a result, we suspect that the fainter red sample is more affected by stellar contamination or systematics-driven fluctuations, and exclude it from our fiducial definition of the red sample.

Each of the samples is required to be either undetected or not pointlike in Gaia. Here a source is taken as "pointlike" if

$$\text{pointlike}(G, A) = \begin{cases} \log_{10} A < 0.5 & \text{if } G < 19.25 \\ \log_{10} A < 0.5 + \frac{5}{16}(G - 19.25) & \text{otherwise}\,, \end{cases} \tag{6.1}$$

where G is the Gaia G band magnitude and A is `astrometric_excess_noise` from Gaia DR2 (Gaia Collaboration et al. 2018). A source is considered "undetected" in Gaia if there is no Gaia DR2 source within 2.75″ of the location of the WISE source. High `astrometric_excess_noise` indicates that the Gaia astrometry of a source was more uncertain than typical for resolved sources; this cut essentially takes advantage of the 0.1″ angular resolution of Gaia to morphologically separate point sources from galaxies. We additionally remove sources classified as diffraction spikes, first or second latents, or ghosts in either W1 or W2, corresponding to "unWISE flags" 1, 2, 3, 4 or 7.[2]

6.2.4 Masks

For the lensing map, we use the official 2018 Planck lensing mask, provided together with the other data products (Planck Collaboration et al. 2018f). This is created using a combination of the `SMICA` 70% Galactic mask, retaining the cleanest 70% of the sky, together with the 143 and 217 GHz point source masks and the tSZ-detected clusters with $S/N > 5$ (Planck Collaboration et al. 2018f). We additionally masked a small region of the sky with $|b| < 10°$ that was unmasked in the Planck map. Overall, this leaves an unmasked sky fraction $f_{\rm sky} = 0.670$ for the lensing map. As a test of Galactic contamination we also use the 60 and 40% temperature masks from the Planck 2018 data release[3], masking an increasing fraction of the Galactic plane. The impact on the results is discussed in Section 6.7.3.

For WISE, we found it convenient to use the Planck lensing mask as an effective galactic mask, to avoid excessive stellar contamination close to the galactic plane. We additionally mask stars, galaxies, planetary nebulae, and `NSIDE` = 2048 HEALPix pixels with substantial area lost due to sub-pixel unWISE masks (e.g. for diffraction spikes from bright stars).

We mask the 6678 brightest stars in the infrared sky (6156 at $|b| > 20°$) with W1 < 2.5 or W2 < 2 or K < 2 (where the WISE magnitude is the brighter of the AllWISE or unWISE magnitudes). We use the bright star list provided by the CatWISE team (Eisenhardt et al., in prep)[4] for these objects.[5] We find that a disk of radius 0.5° is adequate to prevent contamination due to spurious detections around the majority of these bright sources. For the very brightest stars, diffraction spikes extend beyond the $\sim 1°$ extent of the diffraction spike mask; we therefore use a 1.5° radius around 32 stars with $-3 <$ W2 < -2 and a

[2] See Table 5 here: `http://catalog.unwise.me/files/unwise_bitmask_writeup-03Dec2018.pdf`

[3] Always multiplied by the original lensing mask.

[4] `catwise.github.io`

[5] We additionally add the carbon star IRC+20326, which had problematic photometry in both AllWISE and unWISE.

3° radius around 11 stars with W2 < -3. Finally, we mask 0.2° around 6212 stars with $2 <$ W2 < 2.5, W1 > 2.5, and K > 2, where we find that in rare cases, the unWISE PSF model does not extend far enough into the wings of the star, leading to spurious sources at the edge of the modeled region.

We also mask bright galaxies using the LSLGA catalog[6], selecting 715 galaxies from Hyperleda (Makarov et al. 2014) with magnitudes < 13 (almost always in the B filter, though in rare cases the K or I filter), diameter $D_{25} > 3$ arcmin, and surface brightness within D_{25} of < 26 mag/arcsec^2. Using the position angle and ellipticity in the catalog we mask ellipses around each galaxy out to $1.5R_{25}$, and we visually confirm that this radius removes the impact of galaxies on our samples.

We also find that planetary nebulae can contaminate our samples, particularly the red sample. We mask 1143 planetary nebulae (Acker et al. 1992), masking out to twice the optical radius of each planetary nebula.

In all three cases (stars, galaxies, and planetary nebulae) we create a binary mask on an `NSIDE` $= 2048$ HEALPix map, masking all pixels within the specified distance of the source. For the planetary nebulae, we additionally use the "inclusive=True" option in the HEALPix QUERY_DISC command since the pixels in our map are often larger than the mask radius.

Finally, we correct for area lost in each (`NSIDE` $= 2048$) HEALPix pixel from sub-pixel masking. Sub-pixel masking arises from two sources: foreground Galactic stars from Gaia, which will mask any unWISE source within 2.75″ due to our Gaia point-source exclusion, and unWISE masking of diffraction spikes, latents and ghosts around bright stars[7]. We apply a binary mask to remove all pixels with more than 20% area lost due to sub-pixel masking, and we correct the density in the remaining pixels by dividing by the fractional unmasked area of each pixel.

We apodize the Planck lensing mask (with additional exclusion of $|b| < 10°$) with a 1° FWHM Gaussian. We do not apodize the stellar, large galaxy, planetary nebulae or area lost masks. We use the apodized Planck lensing mask for the CMB lensing map and the product of the apodized lensing mask and the unapodized stellar, large galaxy, planetary nebulae and area-lost masks for the unWISE galaxy map. This yields $f_{\rm sky} = 0.586$ for the unWISE galaxy map.

6.3 Model

6.3.1 Angular Clustering

Both the CMB lensing convergence κ and the unWISE projected galaxy density are projections of 3D density fields. We define the projection through kernels $W(\chi)$, where χ is the line-of-sight comoving distance. Given two such fields X, Y on the sky their angular

[6] https://github.com/moustakas/LSLGA

[7] http://catalog.unwise.me/files/unwise_bitmask_writeup-03Dec2018.pdf

cross-power spectrum is

$$C_\ell^{XY} = \frac{2}{\pi}\int_0^\infty d\chi_1\, d\chi_2\; W^X(\chi_1)W^Y(\chi_2)\int_0^\infty k^2\, dk\; P_{XY}(k; z_1, z_2) j_\ell(k\chi_1) j_\ell(k\chi_2) \quad . \tag{6.2}$$

On small angular scales (high ℓ) one may make the Limber approximation (Limber 1953), under which C_ℓ reduces to a single integral of the equal-time, real-space power spectrum:

$$C_\ell^{XY} = \int d\chi\; \frac{W^X(\chi)W^Y(\chi)}{\chi^2}\; P_{XY}\left(k_\perp = \frac{\ell+1/2}{\chi}, k_z = 0\right) \tag{6.3}$$

where we have included the lowest order correction to the Limber approximation, $\ell \to \ell+1/2$, to increase the accuracy to $\mathcal{O}(\ell^{-2})$ (Loverde & Afshordi 2008).

Lensing is sourced by the Weyl potential, which is related to the total matter power spectrum (including neutrinos) by the Poisson equation. Writing C_ℓ in terms of the galaxy-matter and matter-matter power spectra $P_{\rm mg}$ and $P_{\rm gg}$, the weight functions $W(\chi)$ are

$$W^\kappa(\chi) = \frac{3}{2}(\Omega_m+\Omega_\nu)H_0^2(1+z)\;\frac{\chi(\chi_\star-\chi)}{\chi_\star} \quad , \quad W^g(\chi) = b(z)H(z)\,\frac{dN}{dz} \tag{6.4}$$

with $\chi_\star$ the distance to last scattering and $\int dz\; dN/dz = 1$.

Besides density-density and density-lensing correlations, there are also correlations induced by lensing magnification of background sources:

$$C_\ell^{\kappa g} \to C_\ell^{\kappa g} + C_\ell^{\kappa\mu} \tag{6.5}$$

$$C_\ell^{g_1 g_2} \to C_\ell^{g_1 g_2} + C_\ell^{g_1\mu_2} + C_\ell^{g_2\mu_1} + C_\ell^{\mu_1\mu_2} \tag{6.6}$$

where

$$W^{\mu,i}(\chi) = (5s-2)\,\frac{3}{2}(\Omega_m+\Omega_\nu)H_0^2(1+z)g_i(\chi) \tag{6.7}$$

$$g_i(\chi) = \int_\chi^{\chi_\star} d\chi'\;\frac{\chi(\chi'-\chi)}{\chi'}\;H(z')\;\frac{dN_i}{dz'} \tag{6.8}$$

where $s \equiv d\log_{10} N/dm$ is the response of the number density to a multiplicative change in brightness. Given our complex selection function, we measure the response by finite difference, artificially changing each magnitude by the same amount (in analogy to lensing magnification) and measuring the change in number of galaxies satisfying our selection criteria. This procedure is discussed in detail in Appendix 6.C for both the unWISE galaxies (necessary for modeling the angular power spectra) and for the spectroscopic samples (necessary for determining magnification bias contamination to the clustering redshifts). For the color-selected unWISE samples, the response s may be significantly different from the slope of the luminosity function at the magnitude limit because the color cut is magnitude dependent.

6.3.2 HaloFit model

In order to compute C_ℓ we need to model $P_{\rm gg}(k,z)$, $P_{\rm mg}(k,z)$ and $P_{\rm mm}(k,z)$. In this paper, we do not explore the cosmological implications of our measurement, but rather seek to characterize the unWISE samples and their redshift distribution, and present a measurement of the cross-correlations. For this purpose, a phenomenological fit will be sufficient, and we choose to model the auto and cross correlation in terms of a linear bias, multiplied by the "HaloFit" fitting function (Takahashi et al. 2012) to the non-linear matter power spectrum as implemented in the CLASS code (Blas et al. 2011):

$$P_{\rm mg}(k,z) = b_{\rm lin}(z) P_{\rm mm}(k,z) \quad , \quad P_{\rm gg}(k,z) = b^2_{\rm lin}(z) P_{\rm mm}(k,z) + \text{Shot Noise} \tag{6.9}$$

This procedure has been shown to produce fairly reasonable phenomenological fits to the auto and cross correlations.[8] While the fit may be good, Modi et al. (2017) has shown that the value of the inferred cosmological parameters can be significantly biased if HaloFit is used, and for this reason we will explore a more sophisticated bias model to better model non-linearities in our cosmological analysis in Krolewski et al. (2020).

Since the galaxy field responds to dark matter and baryons only (Costanzi et al. 2013, Villaescusa-Navarro et al. 2014, Castorina et al. 2014, 2015, Vagnozzi et al. 2018), $P_{\rm gg}$ is the power spectrum of non-neutrino density fluctuations. Although lensing responds to the power spectrum of total fluctuations, on the scales of interest here the neutrinos cause a scale-independent suppression of power. Therefore, using the non-neutrino power spectrum throughout and substituting $\Omega_m + \Omega_\nu \to \Omega_m$ greatly simplifies the modelling and makes less than 1% difference compared to the exact calculation.

6.4 Angular clustering

In this section we discuss our method of estimating the auto and cross spectra, as well as their covariance matrix.

6.4.1 Angular power spectra estimation

In order to estimate the binned cross and auto power spectra, we use a pseudo-C_ℓ estimator Hivon et al. (2002) based on the harmonic coefficients of the galaxy and lensing fields. The measured pseudo-C_ℓ on the cut sky are calculated as

$$\tilde{C}^{XY}_\ell = \frac{1}{2\ell+1} \sum_m X_{\ell m} Y^\star_{\ell m} \tag{6.10}$$

[8] For the magnification bias terms, each ℓ maps to higher k than for the clustering terms; therefore the linear bias times Halofit model is less adequate for $C^{\mu g}_\ell$. However, the magnification bias terms are subdominant compared to the clustering terms, so inaccuracy in modeling $C^{\mu g}_\ell$ is not significant.

where $X, Y \in \{g_1, g_2, g_3, \kappa\}$ are the observed fields on the cut sky. Because of the mask, these differ from the true C_ℓ that are calculated from theory, but their expectation value is related through a mode-coupling matrix, $M_{\ell\ell'}$, such that

$$\langle \tilde{C}_\ell \rangle = \sum_{\ell'} M_{\ell\ell'} C_{\ell'} \tag{6.11}$$

The matrix $M_{\ell\ell'}$ is purely geometric and can be computed from the power spectrum of the mask itself. While Eq. (7.11) is not directly invertible for all ℓ, the MASTER algorithm (Hivon et al. 2002) provides an efficient method to do so assuming that the power spectrum is piecewise constant in a number of discrete bins, b. Defining a "binned" mode-coupling matrix, $\mathcal{M}_{bb'}$ (Alonso et al. 2018), we can recover unbiased binned bandpowers

$$C_b = \sum_{b'} \mathcal{M}^{-1}_{bb'} \tilde{C}_{b'} \quad . \tag{6.12}$$

We use the implementation in the code `NaMaster`[9] (Alonso et al. 2018). Finally, the theory curve must be binned in the same way as the data when comparing theory and measurements. Since the true C_ℓ are not piecewise constant, this involves the following steps (Alonso et al. 2018): First, the theory curve is convolved with $M_{\ell\ell'}$ using Eq. (7.11). Then the convolved theory, $\tilde{C}_\ell^{\rm theory}$, is binned in the same bins, b, as the data to form bandpowers, $\tilde{C}_b^{\rm theory}$, and finally the bandpowers are decoupled using Eq. (7.12) to obtain $C_b^{\rm theory}$. While for simplicity the plots show unbinned theory curves, all of the calculations are performed with binned quantities.

In short, our pipeline works as follows: first, we mask the Planck lensing map with the mask provided by the Planck team, apodized with a Gaussian smoothing kernel with FWHM 1 deg. For the unWISE galaxies, we use the custom-made mask described in Section 6.2.4, which includes different apodization schemes for the wide Galactic mask and point sources. In addition, we have to consider that Galactic stars can mask galaxies behind them or in their vicinity, a problem that becomes more severe closer to the galactic plane. To correct for this, we create an "area lost" mask (described in Section 6.2.4) and divide the observed galaxy number count by the area available in each pixel, to obtain an unbiased estimate of the local number of galaxies. Then a galaxy overdensity field is created, and cross-correlated with the CMB lensing maps using `NaMaster`. Finally, we need to correct for the pixel window function, due to the assignment of galaxies to discrete pixels: we divide $C_\ell^{\kappa g}$ by the HEALPix pixel window function at the center of each bandpower. The procedure is more complicated for C_ℓ^{gg}: a shot-noise power spectrum has correlation length zero and thus does not need to be corrected for the pixel window function, whereas the signal part of C_ℓ^{gg} should be divided by the square of the pixel window function. Therefore, we first subtract the estimated shot noise from C_ℓ^{gg} using $\bar{n}$ from Table 1, then divide by the squared pixel window function, and then add the estimated shot noise back.

[9] https://github.com/LSSTDESC/NaMaster

We tested this pipeline on Gaussian realizations of the CMB lensing and galaxy fields, and noted that the final "deconvolved" C_ℓ are rather sensitive to the choice of apodization scale, especially for the CMB lensing map, but are not affected by the inclusion of unapodized components in the galaxy mask. Our choice of smoothing was determined by optimizing the recovered power spectrum in simulations with known input angular correlation. In particular, we use the above `NaMaster` pipeline to measure C_ℓ for 100 simulated Gaussian lensing and galaxy maps (generated with the correct cross-correlation). We find significant biases of several percent due to power leakage outside the measured range, if the $\ell_{\rm max}^{\rm NaMaster}$ used in `NaMaster` is close to the $\ell_{\rm max} = 1000$ used in our analysis. To remedy this, we run `NaMaster` with $\ell_{\rm max}^{\rm NaMaster} = 6000$, before extracting the bandpowers in our analysis range and discarding the higher ℓ ones.

With the Gaussian simulations, we also find biases of several percent in the recovery of the galaxy auto-spectrum at $\ell < 300$ (Figure 6.2). Mask-induced mode coupling causes $\ell < 50$ systematic power in the auto-spectrum to leak to considerably higher ℓ. We find that if we turn off the extra low-ℓ power by using the theory prediction rather than the measured C_ℓ^{gg} as the input power spectrum, we can recover C_ℓ^{gg} with no bias.

We therefore filter all modes with $\ell < 20$ in the unmasked galaxy map. To do this, we take the spherical harmonic transform of the raw galaxy map (before applying the mask), apply a sharp cut setting all modes with $\ell < 20$ to zero, and apply the inverse transform to recover the filtered map. We then use the filtered map as input for our NaMaster pipeline. We find this procedure leads to considerably less biased recovery of the auto-spectrum (Figure 6.2). Other approaches (i.e. setting the edge of the smallest-ℓ bin to $\ell_{\rm min}^{\rm NaMaster} = 20$ or filtering $\ell < 50$ modes instead) also recover the unbiased auto and cross-spectra. We correct the auto-spectra for the residual mask-transfer bias. Since the residual bias is $\leq 1\%$, smaller than the statistical errors on the cross spectrum or the statistical errors from uncertain dN/dz, this correction has only a small impact on our results (compare the "no transfer function" row to the fiducial row in Figure 6.12).

We conclude that with our pipeline we can measure all of the auto and cross-correlations between the different samples with sub-percent accuracy over the whole range of scales considered, once the input maps have been filtered and the mask-deconvolution transfer function has been applied.

6.4.2 Covariance matrix

While an exact computation of the covariance matrix after applying the MASTER algorithm for a Gaussian random field is possible, it is computationally very demanding, involving $\mathcal{O}(\ell_{\rm max}^6)$ operations. Efstathiou (2004), García-García et al. (2019) have proposed an approximate method to estimate the Gaussian part of the covariance matrix that makes it as computationally expensive as the power spectrum itself. This procedure has been validated on simulations and shown to work extremely well (García-García et al. 2019). This algorithm is implemented in `NaMaster`, and takes as input the true auto and cross spectra (for example, from the theory curves with the correct value of parameters including the galaxy bias). Since

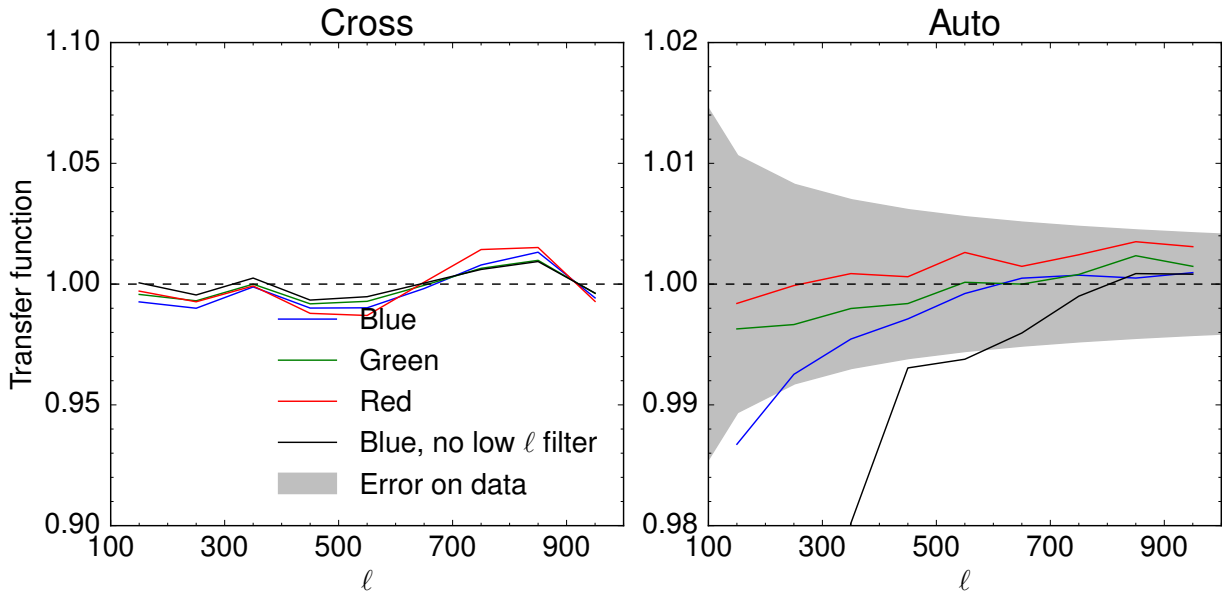

Figure 6.2: Mask deconvolution transfer function for the CMB lensing cross-spectra (left) and galaxy auto spectra (right), i.e. comparison between input power spectrum and output after masking, pseudo-C_ℓ estimation, and mask deconvolution. Maps were generated from power spectra assuming a Gaussian field. Colored curves are transfer functions for different samples after filtering $\ell < 20$ modes from the unmasked map, whereas no filtering was applied to black curves. Recovery of the cross-spectrum is unbiased even without filtering, but recovery of the auto-spectrum requires filtering $\ell < 20$ modes. To ensure sub-percent accuracy, we additionally correct the auto-spectrum by the transfer function displayed here.

measuring the bias requires a covariance matrix to start with, an iterative approach may be used. For computational simplicity, we adopt a further approximation which will assume the decoupled covariance matrix to be diagonal, and where the on-diagonal elements for binned bandpowers of width $\Delta\ell$ are given by Hivon et al. (2002):

$$\mathrm{Cov}(C_\ell^{XY}, C_{\ell'}^{XY}) = \sigma^2(C_\ell^{XY})\delta_{\ell,\ell'} = \frac{\left[C_\ell^{XX}C_\ell^{YY} + \left(C_\ell^{XY}\right)^2\right]_{\mathrm{measured}}}{f_{\mathrm{sky}}(2\ell+1)\Delta\ell}\,\frac{w_4}{w_2^2}\delta_{\ell,\ell'} \tag{6.13}$$

Here the weights w_2 and w_4 are defined in terms of the arbitrary mask weights $W(\hat{\boldsymbol{n}})$ as:

$$w_i f_{\mathrm{sky}} = \frac{1}{4\pi}\int_{4\pi} d\Omega_{\hat{\boldsymbol{n}}} W^i(\hat{\boldsymbol{n}}) \tag{6.14}$$

with $w_1 f_{\mathrm{sky}} = f_{\mathrm{sky}}$. If $X \neq Y$ and the fields have different masks, we take w_2 and w_4 to be the geometric means of the ones computed with each of the individual masks.

Using the method for analytic Gaussian pseudo-C_ℓ covariance in Efstathiou (2004), García-García et al. (2019), we have checked that the largest off-diagonal correlation between bandpowers is 4% for the two lowest ℓ bins, and that the on-diagonal elements agree to percent level. Therefore we conclude that the approximation in Equation 6.13 is adequate for our purposes. Furthermore, we neglect any non-Gaussian contribution to the covariance matrix, since we will only model scales that are in the linear or mildly non-linear regimes, where these corrections are expected to be small.

6.5 Galaxy redshift distribution

Since the unWISE galaxy sample is selected from two-band imaging, dN/dz cannot be determined by photometric redshifts. We instead measure dN/dz using cross-correlations with large-area spectroscopic surveys (Newman 2008, McQuinn & White 2013, Ménard et al. 2013), supplemented by redshifts from cross-matching to deep multi-band photometry in a small field. Cross-correlation redshifts measure $b(z)dN/dz$ (in the absence of a small contribution from magnification bias), which is the relevant kernel for modeling $C_\ell^{\kappa g}$ and C_ℓ^{gg} (Section 6.3). Therefore, unlike previous work, we are not concerned with disentangling dN/dz from the bias evolution of the unWISE galaxies. $C_\ell^{\kappa g}$ and C_ℓ^{gg} do contain a subdominant contribution from magnification bias, which depends on dN/dz alone; in this context, we use dN/dz measured from cross matches to the COSMOS photometric catalog. Consistency between the cross-match dN/dz and cross-correlation $b(z)dN/dz$ requires that the bias increase strongly with redshift. In Appendix 6.B, we show that a simple halo occupation distribution of the unWISE galaxies exhibits a similar increase in bias, demonstrating that our approach is self-consistent.

In Sections 6.5.1 and 6.5.2 we describe our methodology for measuring the cross-correlation and cross-match redshifts and estimating their uncertainties, which constitute a substantial portion of the error budget in modeling the angular power spectra. In Figure 6.3 we list

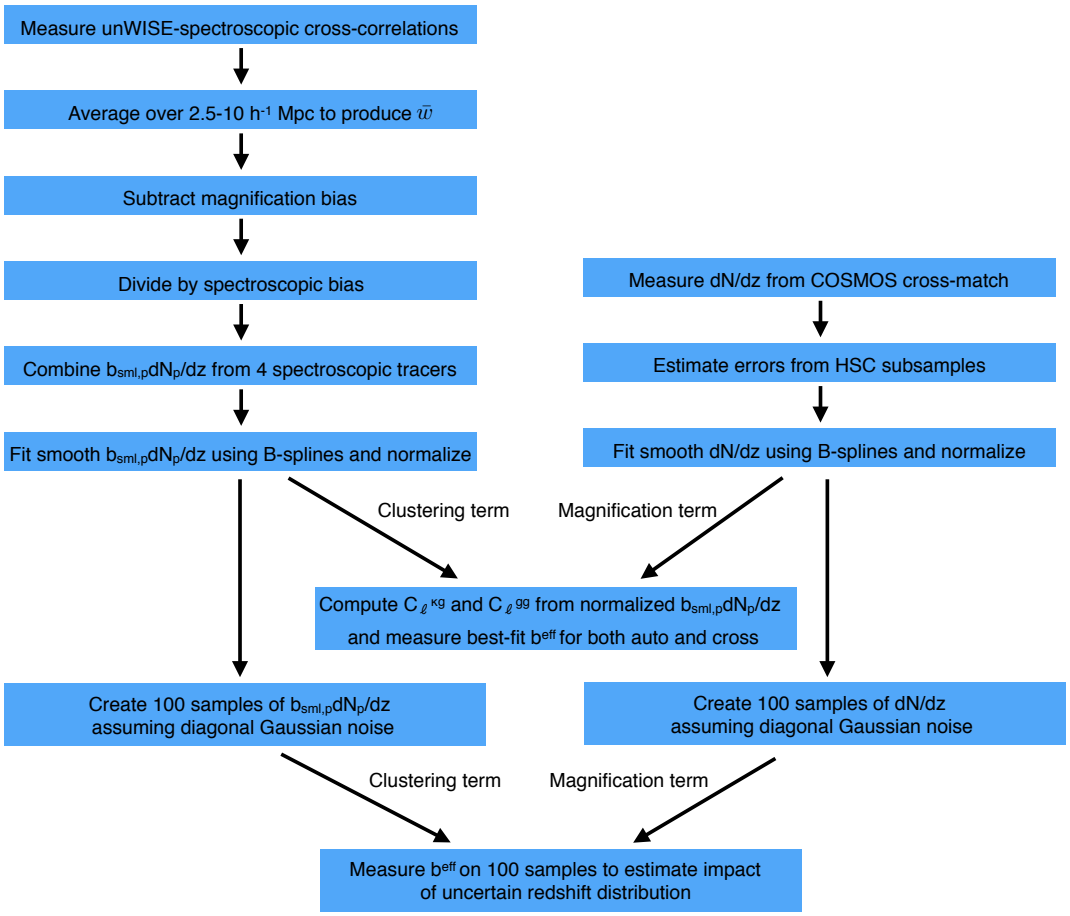

Figure 6.3: An outline of the steps required to interpret the angular clustering of the unWISE samples: estimate the redshift distribution, fit a linear bias to $C_\ell^{\kappa g}$ and C_ℓ^{gg}, and estimate the impact of uncertainty in the redshift distribution on the fitted biases.

the steps outlined in Sections 6.5 and 6.6 to interpret the clustering of the unWISE samples: estimate the redshift distribution, determine the best-fit linear bias of each sample, and estimate the uncertainty on the bias due to uncertain redshift distribution. Throughout Sections 6.5 and 6.7, we quantify systematic errors in terms of their impact on the best-fit bias to the CMB cross ($C_\ell^{\kappa g}$) and galaxy auto power spectra (C_ℓ^{gg}) of the unWISE samples.

6.5.1 Cross-match redshifts

One estimate of dN/dz can be obtained by matching the unWISE samples to deep catalogs with photometric redshifts. The deepest sample of well-measured photometric redshifts comes from the COSMOS field, where deep photometry in many bands spanning the ultraviolet through infrared allows precise photometric redshifts for all sources detected by

WISE with $\Delta z/(1+z) = 0.007$ (Laigle et al. 2016). We first trim the COSMOS catalog to include only objects brighter than 20.7 (19.2) Vega mag at 3.6 (4.2) μm. These depths are roughly 2.5 mag fainter than the 50% completeness limit for the unWISE catalog (Schlafly et al. 2019), so excluding fainter objects removes no objects that WISE could conceivably detect. We then match COSMOS sources to unWISE sources at a radius of 2.75″ over the 2 deg^2 overlap, considering the closest COSMOS source within 2.75″ to be the true match.

The COSMOS catalog marks many bright stars as galaxies, so we additionally edit the COSMOS catalog so that bright objects which Gaia identifies as pointlike are classified as stars, as long as those objects are not X-ray selected. We find that stellar contamination of the unWISE samples is very low, with 1.8%, 1.6%, and likely $< 1\%$ [10] of the blue, green and red samples classified as stars.

For each source, we use the redshift corresponding to the median of the likelihood distribution ("photoz" in the COSMOS catalog). If the SED is better fit by an AGN template than a galaxy template, we instead use the redshift from the AGN template fit ("zq" in the catalog); we find 19%, 30% and 41% of the blue, green and red sample are classified as AGN by this criterion. However, for these objects "zq" and "photoz" are very similar.

Due to the small area of the COSMOS field, sample variance can be larger than the Poisson variance on dN/dz. We therefore estimate uncertainty on dN/dz by constructing 44 subsamples, each of $\sim$2 deg^2, from the HSC SSP survey (Aihara et al. 2018, Tanaka et al. 2018). Compared to COSMOS, HSC is slightly shallower but covers a much larger area ($\sim$120 deg^2). However, the HSC photometric redshifts are less accurate than COSMOS and become biased at $z > 1.5$,[11] where a substantial fraction of galaxies scatter to $z_{\rm HSC} \sim 1$, biasing $dN/dz_{\rm HSC}$ at $z \geq 1$ compared to $dN/dz_{\rm COSMOS}$. As a result, we restrict the HSC comparison to $z < 1$. We use the DEmP photometric redshifts, as these are the most accurate redshifts available for all "primary" HSC objects (Tanaka et al. 2018). We require that the HSC objects have clean photometry: we only use "primary" sources, and remove sources with pixel flags indicating saturated or interpolated pixels, bad pixels, cosmic ray hits, suspect and clipped pixels, and poor centroid measurements. We also require that the objects are classified as extended sources or have $i > 23$, where the star-galaxy classification performs poorly. As with COSMOS, we use the closest match within 2.75″.

We find that the dN/dz errors are larger than Poisson statistics would indicate, by roughly redshift-independent factors of 3.8, 1.9 and 1.1 for the blue, green and red samples at $z < 1$. Since we cannot use HSC to determine dN/dz errors at $z > 1$, where the DEmP photometric redshifts become significantly biased, we extrapolate the dN/dz uncertainty to higher redshift by multiplying the Poisson error bars by a constant factor of 3.8, 1.9 and 1.1 for blue, green and red samples. This extrapolation yields error bars appropriate for the

[10] The red sample only has 188 matches to the COSMOS photometric catalog and none of them are stars; the error on the stellar contamination fraction may therefore be quite large. For the fainter red samples reaching to W2 = 16.5 or 16.7, we find stellar contamination of 0.6% and 0.8%, respectively.

[11] See page A5 in https://hsc-release.mtk.nao.ac.jp/doc/wp-content/uploads/2017/02/s16a_demp_median.pdf, which plots bias, scatter, and outlier fraction as a function of reference redshift for the training set used by HSC.

Color	Median z (b-weighted)	Std	Percentile (5%-95%)	Median z $\ell < 155°$	Median z $\ell > 155°$	Median z	Std	Percentile (5%-95%)
Blue	0.72	0.031	0.11	0.75	0.72	0.63	0.022	0.06
Green	1.38	0.026	0.09	1.35	1.38	1.09	0.019	0.06
Red	1.70	0.064	0.23	1.71	1.68	1.46	0.030	0.09

Table 6.2: Summary statistics of the redshift distribution of the WISE sample. Statistics on the left are computed from samples of $b_{\rm sml,p} dN_{\rm p}/dz$ (i.e. clustering redshifts), while statistics on the right are computed from samples of the cross-match dN/dz. Std gives the standard deviation of the medians of the 100 dN/dz samples. Galactic longitude 155° approximately splits the sky in half, so the $\ell = 155°$ split provides another estimate of the uncertainty on the clustering redshifts.

cosmic variance contribution alone; in Section 6.7.4 we discuss the impact of photometric redshift errors on dN/dz and on our bias results.

We give summary statistics for the cross-match dN/dz in Table 6.2 and plot the cross-match dN/dz in Figure 6.7. Even at low redshift, there is a systematic shift between the COSMOS and HSC dN/dz for the red sample; this may be due to errors in the $z < 1$ HSC redshifts. The impact of this shift is limited because the cross-match dN/dz is only used to model the magnification bias term. Therefore, even the $\Delta z = 0.3$ shift required to reconcile the COSMOS and HSC dN/dz for the red sample makes $\lesssim 0.7\sigma$ difference on the bias fitted to the auto and cross-correlation.

6.5.2 Cross-correlation redshifts

Another method for determining dN/dz is through cross-correlation with a spectroscopic sample. This is an old method has been revived in several recent works (Newman 2008, Ménard et al. 2013, McQuinn & White 2013, Schmidt et al. 2013, 2015, Rahman et al. 2015, 2016b,a, Scottez et al. 2016, 2018, Johnson et al. 2017, Davis et al. 2018, Cawthon et al. 2018, Gatti et al. 2018, Bates et al. 2019) (including validation against spectroscopic redshifts in Rahman et al. (2015)), but here we present one of its first applications to modeling galaxy power spectra. We therefore discuss and quantify several sources of systematic error, including nonlinear clustering and nonlinear bias evolution; magnification bias contribution to the photometric-spectroscopic cross-correlation; and bias evolution of the various spectroscopic samples as required to combine cross-correlations with multiple spectroscopic samples.

In the Limber approximation the cross-correlation of a photometric survey with scale-independent bias $b_{\rm sml,p}(z)$ and redshift distribution $dN_{\rm p}/dz$, and a spectroscopic survey with bias $b_{\rm sml,s}(z)$, in a narrow bin between $z_{\rm min}$ and $z_{\rm max}$ is

$$C_\ell^{\rm p-s\ cross} = b_{\rm sml,s}(z)\, b_{\rm sml,p}(z)\, H(z) \frac{dN_{\rm p}}{dz} \int_{z_{\rm min}}^{z_{\rm max}} dz \frac{dN_{\rm s}}{dz} \frac{P_{\rm mm}\left(k = (\ell + \frac{1}{2})/\chi, z\right)}{\chi^2} + C_\ell^{\rm mag} \quad (6.15)$$

where $C_\ell^{\rm mag}$ includes the contributions from the three lensing magnification bias terms; we assume the bin is sufficiently narrow that the biases and $dN_{\rm p}/d\chi$ are constant across the bin;

and both biases are assumed to be scale-independent.

We refer to the biases here as $b_{\rm sml}$ to emphasize that they are defined on relatively small scales ($2.5 - 10\ h^{-1}$ Mpc) on which we measure the spectroscopic-photometric cross-correlations. This is in contrast to the large-scale bias, $b_{\rm lin}$, relevant to the modeling of the angular power spectrum in Section 6.3. However, as discussed below and in Section 6.7, $b_{\rm sml}$ and $b_{\rm lin}$ are within 15% of each other for all of the unWISE samples, and the systematic error from the discrepancy between $b_{\rm sml}$ and $b_{\rm lin}$ is subdominant to the statistical error from uncertainty in $b\,dN/dz$.

We have implemented a cross-correlation dN/dz estimate in both harmonic and configuration space, obtaining consistent results. It is convenient, and consistent with past results, to first present the spectroscopic-photometric cross-correlations in configuration space. We use the estimator of Ménard et al. (2013), in which the correlation function is weighted by r^{-1} to increase the signal-to-noise ratio and integrated over a range of scales:

$$\bar{w}_{\rm sp}(z) = \sum_i r_i^{-1}\,\Delta r_i\,w_{\rm sp,binned}(r_i, z) \tag{6.16}$$

where we use three log-spaced bins in r between 2.5 and 10 h^{-1} Mpc. The binned correlation function is given by

$$w_{\rm sp,binned}(r_i, z) = \int \frac{\ell d\ell}{2\pi}\,C_\ell^{\rm p-s\ cross}\,\frac{1}{\pi(r^2_{\rm max,i} - r^2_{\rm min,i})}\int_{r_{\rm min,i}}^{r_{\rm max,i}} 2\pi r dr\,J_0(\ell\theta) \tag{6.17}$$

Noticing that $\theta = r/\chi$[12] and switching integration variables from ℓ to k we can write

$$\bar{w}_{\rm sp}(z) = b_{\rm sml,s}(z)\,b_{\rm sml,p}(z)\,H(z)\,\frac{dN_{\rm p}}{dz}\,I(z) + \bar{w}_{\rm mag}(z) \tag{6.18}$$

with

$$I(z) = \int \frac{k\ dk}{2\pi}\int_{z_{\rm min}}^{z_{\rm max}} dz\frac{dN_{\rm s}}{dz}\,P_{\rm mm}(k, z)\sum_{r_i}\frac{r_i^{-1}\,\Delta r_i}{\pi r^2_{\rm max,i} - \pi r^2_{\rm min,i}}\int_{r_{\rm min,i}}^{r_{\rm max,i}} 2\pi r\,J_0(kr)\,dr \tag{6.19}$$

In the linear regime $I(z)$ is equal to $D^2(z)$ times a redshift-independent integral, which is degenerate with the normalization of $dN_{\rm p}/dz$. On our scales of interest, $I(z)$ deviates only slightly from $D^2(z)$ ($\sim 5\%$ at $z = 2$). To compute $I(z)$ we use the HaloFit nonlinear matter power spectrum from Mead et al. (2015) for $P_{\rm mm}(k, z)$ and continue to assume scale-independent bias. While the $I(z)$ term introduces a cosmology dependence into the clustering redshifts, normalizing the clustering redshifts eliminates the relationship between redshift distribution and power spectrum amplitude, allowing us to constrain the power spectrum amplitude (i.e. $\sigma_8(z)$) averaged over the redshift distribution of each unWISE sample.

[12] When measuring $w(\theta)$, we count pairs in angular bins with $\theta_i = r_i/\chi_{\rm central}$, where $\chi_{\rm central}$ is the comoving distance to the center of the sub-bin. Therefore, within each sub-bin, $r = \theta\chi_{\rm central}$, which is well approximated by $r = \theta\chi$ because the sub-bins are narrow. This simplifies the triple integral in Equation 6.19 by allowing the r integral to be redshift-independent.

Lensing magnification can correlate samples widely separated in redshift and therefore bias clustering redshifts in the tails of the distribution (McQuinn & White 2013, Gatti et al. 2018). We estimate the contribution of magnification bias $\bar{w}_{\rm mag}(z)$ using the COSMOS cross-match dN/dz and the measured s for unWISE and the spectroscopic samples (Appendix 6.C), and assuming a scale-independent bias times the HaloFit power spectrum. We use the following form for the bias evolution of each sample:

$$b_{\rm sml,p}(z) = 0.8 + 1.2z \qquad \text{Blue} \qquad (6.20a)$$
$$b_{\rm sml,p}(z) = \max\left(1.6z^2, 1\right) \qquad \text{Green} \qquad (6.20b)$$
$$b_{\rm sml,p}(z) = \max\left(2z^{1.5}, 1\right) \qquad \text{Red} \qquad (6.20c)$$

with $\max(a, b)$ meaning the larger of a and b. This form is roughly consistent both with the observed clustering given the cross-match dN/dz and the expected bias evolution from a simple HOD of the unWISE samples (Figure 6.19). Since the unWISE bias evolution is only required to model the magnification bias correction to the cross-correlation redshifts, more quantitative agreement with the observed clustering is not needed. If we instead use $b_{\rm sml,p}(z)$ from the cross-correlation redshifts after the initial magnification bias correction, the bias fitted to $C_\ell^{\kappa g}$ and C_ℓ^{gg} changes by $< 0.4\sigma$.

We show $\bar{w}$ and the magnification bias correction in Figure 6.5. Magnification bias has the largest impact on the blue sample, with CMASS galaxies at $z > 0.6$ showing the largest impacts.

We can invert Equation 6.18 to derive $b_{\rm p,sml} dN_{\rm p}/dz$ given a measurement of $\bar{w}_{\rm sp}$. We measure the binned correlation function using the estimator of Davis & Peebles (1983)

$$\hat{w}_{\rm sp,binned}(\theta) = \frac{D_{\rm s}D_{\rm p}}{D_{\rm s}R_{\rm p}}\frac{N_{\rm R}}{N_{\rm D}} - 1 \qquad (6.21)$$

using three log-spaced bins between[13] 2.5 and $10\,h^{-1}$ Mpc, with the inner radius set to reduce the contributions from scale-dependent bias and "1-halo" effects. Since the unWISE galaxy density varies across the sky (slightly decreasing towards the Galactic center), we measure the normalization $N_{\rm R}/N_{\rm D}(\theta)$ in `NSIDE` $= 8$ HEALPix pixels. If the annulus in which we count pair straddles two `NSIDE` $= 8$ pixels, we average the normalization in the two pixels. Our correlation function code is publicly available at `https://github.com/akrolewski/BallTreeXcorrZ` and has been tested to ensure that the correlation function as measured on the curved sky is correct.

We cross-correlate the unWISE photometric galaxies with spectroscopic quasars from BOSS DR12 (Pâris et al. 2017) and eBOSS DR14 (Ata et al. 2018)[14] and galaxies from

[13] At all redshifts, the lower limit corresponds to much larger angular scales than those affected by the WISE PSF and suppression by nearby bright sources; see Fig. 25 in `http://wise2.ipac.caltech.edu/docs/release/allsky/expsup/sec6_2.html#brt_stars` for estimation of this scale.

[14] While the BOSS and SDSS quasar catalogs are independent, eBOSS includes previously observed quasars. We remove these quasars to create an independent sample; they comprise 45% of the northern eBOSS catalog.

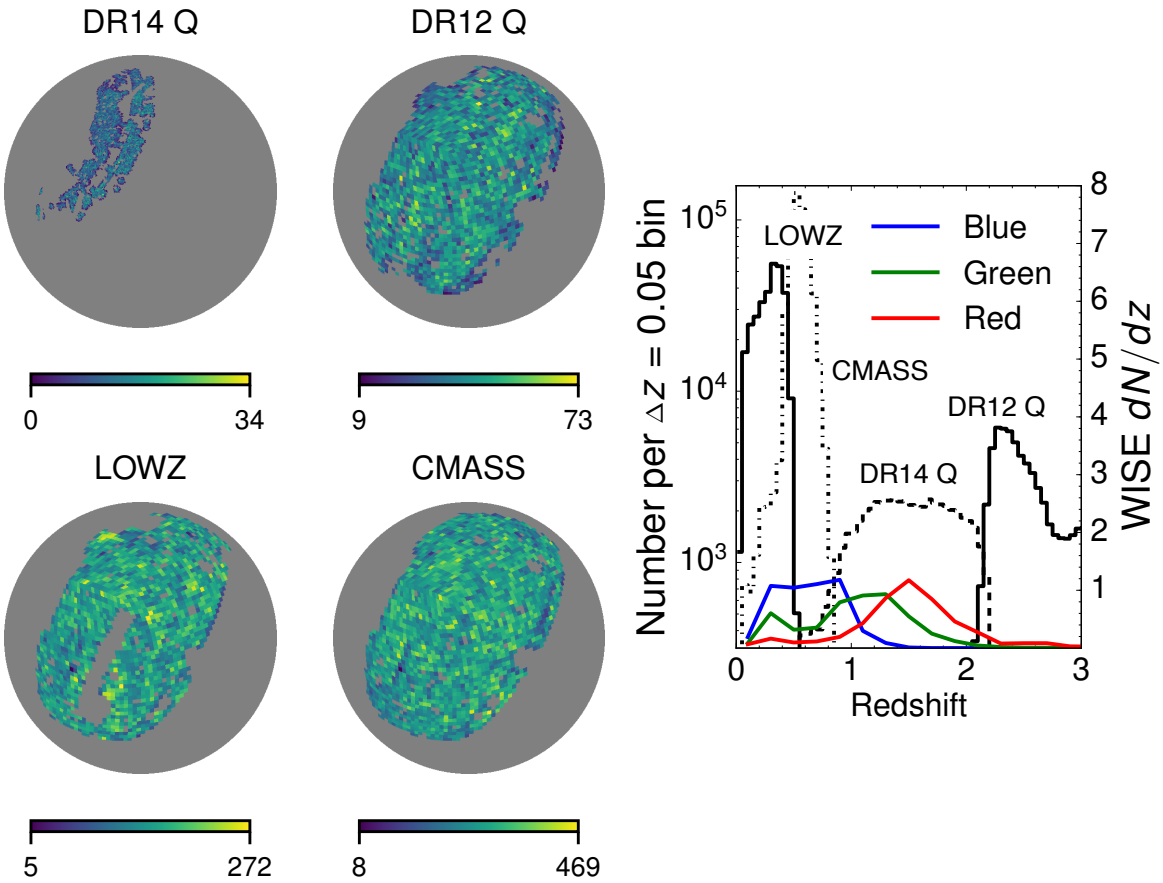

Figure 6.4: *Left:* Sky maps of spectroscopic samples used for cross-correlation redshifts in Galactic coordinates. *Right:* Redshift distributions of spectroscopic samples (black curves) used for cross-correlation redshifts. unWISE galaxy distributions (colored curves) are overplotted with arbitrary amplitude.

BOSS CMASS and LOWZ (Reid et al. 2016). We plot the redshift and sky distributions of the spectroscopic samples used for the clustering redshifts in Figure 6.4.

We split the spectroscopic samples into bins of width $\Delta z = 0.05$ at $z < 0.8$ and $\Delta z = 0.2$ at $z > 0.8$ where the errorbars become much larger due to the sparser quasar samples. As Δz becomes narrower, the signal-to-noise in each individual bin decreases, but the total signal-to-noise of dN/dz increases modestly (by $\sim 35\%$ as Δz changes from 0.1 to 0.02). We prefer having a relatively high signal-to-noise in the individual bins, particularly at high redshift where dN/dz is nearly zero but our errorbars are also relatively large.

We restrict the BOSS quasars to the "CORE"-like sample from Eftekharzadeh et al. (2015) (similar to the "QSO_CORE_MAIN" targeting flag, but only including quasars that would have been selected by the XDQSO method (Bovy et al. 2011),[15] and removing quasars lying in regions where the targeting completeness is $< 75\%$), as was done in previous quasar clustering analyses (White et al. 2012, Eftekharzadeh et al. 2015). We remove all objects in the southern galactic cap (SGC), which are a small fraction of the total spectroscopic sample. Differences in photometric calibration between the SGC and NGC lead to slightly different galaxy samples (Alam et al. 2017, Ross et al. 2017), unexplained differences in quasar clustering between NGC and SGC (White et al. 2012, Eftekharzadeh et al. 2015, Myers et al. 2015), and differences in $\hat{w}_{\rm sp}$, possilby resulting from the different spectroscopic bias evolution. We remove DR12 quasars at $z < 2$, DR14 quasars at $z > 2.2$, and DR14 quasars at $z < 0.8$, since these objects are outliers with redshifts different from each survey's target redshift range and thus may have different clustering properties than the sample as a whole (indeed, we find somewhat discrepant measurements of $\bar{w}_{\rm sp}$ when comparing to BOSS and eBOSS quasars outside their primary redshift ranges). We also remove CMASS galaxies at $z > 0.8$ and $z < 0.1$ and LOWZ galaxies at $z > 0.5$, where the spectroscopic samples become too sparse to measure $b_{\rm sml,s}$ (see below). We summarize the key properties of these samples in Table 6.3.

We apply the corresponding spectroscopic mask to each sample. For eBOSS we use the BOSS veto masks (Reid et al. 2016), pixelized to `NSIDE` = 256 HEALPix pixels, and we also mask `NSIDE` = 128 pixels where more than 80% of eBOSS quasars are in DR7 or DR12. For DR12 quasars, we apply the BOSS veto masks (Reid et al. 2016) and remove `NSIDE` = 256 pixels with $< 75\%$ completeness as computed from the BOSSQSOMASK software[16] (White et al. 2012, Eftekharzadeh et al. 2015). For CMASS and LOWZ we use the corresponding BOSS DR12 LSS catalog masks.[17] We also apply the same WISE masks that we use for the cross-correlation analysis. For the spectroscopic cross-correlations, we threshold all masks by setting pixels with mask value < 0.9 to zero and > 0.9 to one.

We use jackknife[18] resampling to estimate errors on $\bar{w}_{\rm sp}$. We start by splitting the sky into

[15] https://xdqso.readthedocs.io/en/latest/

[16] http://faraday.uwyo.edu/~admyers/bossqsomask/

[17] https://data.sdss.org/sas/dr12/boss/lss/

[18] We also investigated bootstrap resampling to estimate the covariance matrix of $w(\theta)$, and found that on scales smaller than the resampling pixel size (which is always larger than $\theta_{\rm max}$), jackknife errors agree well with errors from the "marked bootstrap" of Loh & Stein (2004), Loh (2008). We prefer jackknife errors to

Sample	$z_{\rm min}$	$z_{\rm max}$	N	Jackknife regions	Area (deg^2)
DR14 Q	0.8	2.2	54708	29	1178
DR12 Q	2.0	4.0	67175	34	6030
LOWZ	0.0	0.5	273549	31	5656
CMASS	0.1	0.8	544308	37	6670

Table 6.3: Properties of the spectroscopic samples used for cross-correlation redshifts.

`NSIDE` = 4 HEALPix pixels[19] and then combine neighboring pixels until the unmasked area within each region reaches a threshold, which we vary between 80 and 120% of the maximum pixel area, choosing the threshold that minimizes the difference between the largest and smallest regions. We list the number of regions used for each sample in Table 6.3. The error on $\bar{w}_{\rm sp}$ is then

$$\sigma^2_{\bar{w}}(z) = \sum_{L=1}^{N} \frac{R_{[L]}}{R} \left(\bar{w}_{[L]}(z) - \langle \bar{w}(z) \rangle\right)^2 \tag{6.22}$$

where R refers to the number of randoms, the subscript $[L]$ indicates that we exclude the Lth region, and $\langle \bar{w}(z) \rangle$ is the average over all N jackknife resamples $\bar{w}_{[L]}(z)$. The replacement of the conventional factor $(N-1)/N$ with $R_{[L]}/R$ is an empirical correction for the fact that the regions have different areas (equation 5 in Myers et al. (2005)).

Combining multiple spectroscopic tracers (as is necessary in our case, due to the broad dN/dz of the unWISE samples) requires a measurement of $b_{\rm sml,s}(z)$. We measure $b_{\rm sml,s}(z)$ by fitting a scale-independent bias times Halofit to the measured $w(\theta)$ between 2.5 and 10 h^{-1} Mpc:

$$w_{\rm auto,s}(\theta, z) = b^2_{\rm sml,s}(z) \int_0^\infty k\, dk\, P_{\rm mm}(k) \int_{\chi_{\rm min}}^{\chi_{\rm max}} \frac{d\chi}{2\pi}\, J_0(k\chi\theta) \left(\frac{dN_{\rm s}}{d\chi}\right)^2 \tag{6.23}$$

where the integral over χ ranges between the lower and upper boundaries of each redshift bin. We omit SDSS DR7 quasars from our spectroscopic samples due to their poorly measured autocorrelation (Ross et al. 2009). For BOSS galaxies and eBOSS quasars we use publicly available galaxy and random catalogs,[20] and for DR12 quasars we generate randoms using

bootstrap errors because sampling a pixel more than once double-counts all pairs in that pixel and is not a reasonable physical situation. Moreover, it leads to ambiguities in the situation where a spectroscopic source lies in pixel i and a photometric source lies in pixel j. In a naive implementation of the bootstrap, intra-pixel pairs are resampled $0, 1, 2...N$ times while cross-pixel pairs are resampled $0, 1, 4...N \times M$ times, leading to larger variance on all scales than jackknife or marked bootstrap. The marked bootstrap avoids this issue by resampling only one of the tracers. We also find very little difference between leave-one-out jackknife resampling and leave-two-out jackknife, so we opt for leave-one-out jackknife in the interest of simplicity.

[19] We use `NSIDE` = 8 pixels for the smaller-area eBOSS samples. We find that using too small pixels can underestimate the errorbars (as argued in Norberg et al. (2009)), so we set the size of the resampling pixels so that ~ 30 are available for each sample.

[20] `https://data.sdss.org/sas/dr12/boss/lss/` for BOSS and `https://data.sdss.org/sas/dr14/eboss/lss/catalogs/` for eBOSS.

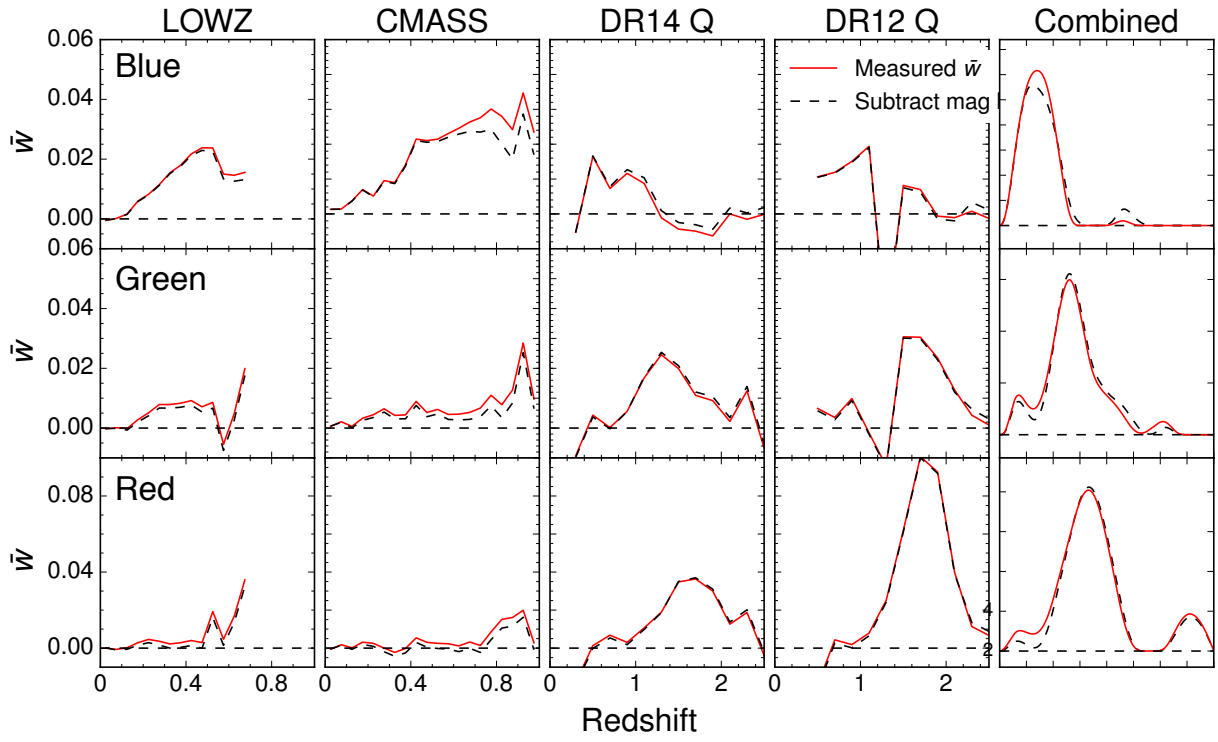

Figure 6.5: Measured $\bar{w}$ without (black dashed) and with (red solid) magnification bias subtracted for unWISE galaxies crossed with our spectroscopic samples (labeled above each column), and for all samples combined (right-most panel).

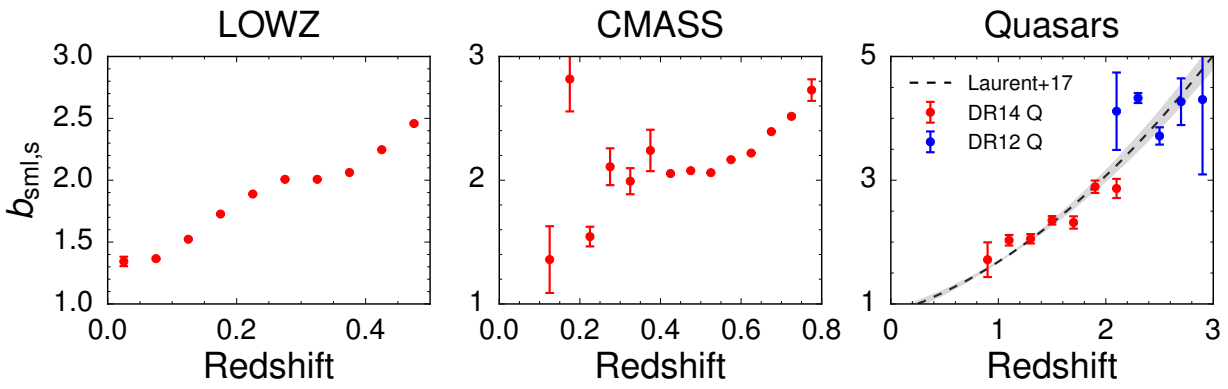

Figure 6.6: Measured bias, $b_{\rm sml,s}$, of spectroscopic samples as a function of redshift. The dashed line in the right panel corresponds to the fit from Laurent et al. (2017) (with the gray band giving uncertainty in the fit). See Table 6.7 for a tabulated compilation.

BOSSQSOMASK. For BOSS galaxies and eBOSS quasars we weight each object by the combined angular systematics, fiber collision and redshift failure weight (Equation 50 in Reid et al. (2016)), and for BOSS quasars we weight by the inverse of the targeting completeness (White et al. 2012, Eftekharzadeh et al. 2015). Note that the 55″ SDSS fiber collision radius is smaller than our inner bin of $2.5\,h^{-1}$Mpc at all redshifts that we consider. Previous work has shown that application of these systematics weights allows unbiased recovery of the correct cosmological clustering (Ross et al. 2012a, 2014, Eftekharzadeh et al. 2015, Ross et al. 2017, Laurent et al. 2017).

While previous measurements of the clustering exist for all spectroscopic samples, measurements for BOSS galaxies have generally been made in coarse redshift bins over a somewhat restricted redshift range ($0.2 < z < 0.6$) (Chuang et al. 2017, Tojeiro et al. 2012, Zhai et al. 2017), so we use our measured bias values (Figure 6.6 and Table 6.7) to ensure that the scales used and redshift bins are consistent with the clustering redshifts. We check our results by replacing our BOSS galaxy spectroscopic bias measurements with those from Figure 12 in Chiang & Ménard (2019) (who measure the bias in similar redshift bins, to measure clustering redshift distributions for Galactic dust maps), and find this makes $\lesssim 0.1\sigma$ difference in the bias fitted to C_ℓ^{gg} and $C_\ell^{\kappa g}$. We also propagate the fitting error on the spectroscopic bias to our clustering dN/dz measurement, although this is almost always subdominant to the statistical error on the cross-correlation.

For quasars, we find that the fitting function of Laurent et al. (2017) provides a very good approximation to the measured bias evolution:

$$b_{\rm sml,s}(z) = (0.278 \pm 0.018)\left[(1+z)^2 - 6.565\right] + (2.393 \pm 0.042) \tag{6.24}$$

Once we have measured the spectroscopic bias, we can divide $\bar{w}$ by $b_{\rm sml,s}$ (as in equation 6.18) to obtain dN_p/dz for each spectroscopic tracer (quasars, CMASS and LOWZ galaxies). We then combine dN_p/dz for the different tracers by inverse-variance weighting

in each redshift bin. We find good agreement between the clustering redshift measurements from CMASS and LOWZ in the redshift range where they overlap ($0 < z < 0.5$) with $\chi^2 = 12.1$ over 10 dof (7.7/10, 2.8/10) for the blue (green, red) samples. We plot the final redshift distributions in Fig. 6.7, along with samples drawn from the uncertainty in the redshift distribution.

To model the angular power spectra, the redshift distribution must satisfy physical constraints ($b_{\rm sml,p} dN_p/dz > 0$ and $b_{\rm sml,p} dN_p/dz|_{z=0} = 0$))[21] and have well-characterized uncertainties. To create a smooth and physical dN_p/dz, we therefore model $b_{\rm sml,p} dN_p/dz$ using cubic B-splines with the spline coefficients required to be positive, satisfying the positivity constraint on $b_{\rm sml,p} dN_p/dz$. Considering the penalized χ^2:

$$\chi^2 = \sum_i \left(\frac{\hat{y}_i - y_i}{\sigma_i} \right)^2 + \lambda \int dx \, [\hat{y}''(x)]^2 \tag{6.25}$$

we determine λ by minimizing χ^2 using cross-validation (Craven & Wahba 1978). This method is sufficiently flexible to fit almost any shape of $b_{\rm sml,p} dN_p/dz$, while satisfying our constraints. We use knots evenly spaced between $z = 0.1$ and $z = 3.5$ with $\Delta z = 0.2$.

By requiring $\hat{y}$ to be positive, this procedure introduces a bias into the theory predictions for C_ℓ, since in regions of nearly zero dN/dz, we will fit to positive noise fluctuations but not negative noise fluctuations. Moreover, the magnitude of this bias is different for $C_\ell^{\kappa g}$ and C_ℓ^{gg}. We find that the differential bias is generally small ($< 5\%$) and therefore do not consider it further in this paper. However, cosmological parameter constraints from these data will require a more careful approach (Krolewski et al. 2020), such as simulating the C_ℓ and dN/dz measurement given some known input cosmology and dN/dz, and subtracting the contribution to C_ℓ from the bias in dN/dz.

We create smooth dN/dz in a similar fashion for the cross-match redshifts. Here we use bins of $\Delta z = 0.06$ instead, as we find that more knots are required to accurately represent the shape of the cross-match dN/dz.

We propagate errors on dN/dz by drawing 100 samples from the data (assuming uncorrelated Gaussian errors between redshift bins), finding the best-fit dN/dz, and using it to model the auto and cross-power spectra. Additionally, we test the assumptions behind the jackknife dN/dz errors by splitting the sky in half at Galactic $\ell = 155°$ and measuring dN/dz separately for each half. Summary statistics for both the cross-correlation and cross-match redshifts are given in Table 6.2.

6.5.3 Systematic errors in the cross-correlation dN/dz

One source of systematic error in the measurement of dN/dz is the discrepancy between $b_{\rm sml,p}$, as measured by the configuration space photometric-spectroscopic cross-correlations, and $b_{\rm lin,p}$, as required to model the autospectra and CMB cross-spectra. Exactly matching the

[21] The number of galaxies per area per comoving distance, $dN/d\chi$, is related to the comoving number density $\bar{n}$ as $dN/d\chi(\chi) = \bar{n} 4\pi\chi^2$ so at $\chi = 0$, $dN/d\chi$ and therefore dN/dz must go to zero.

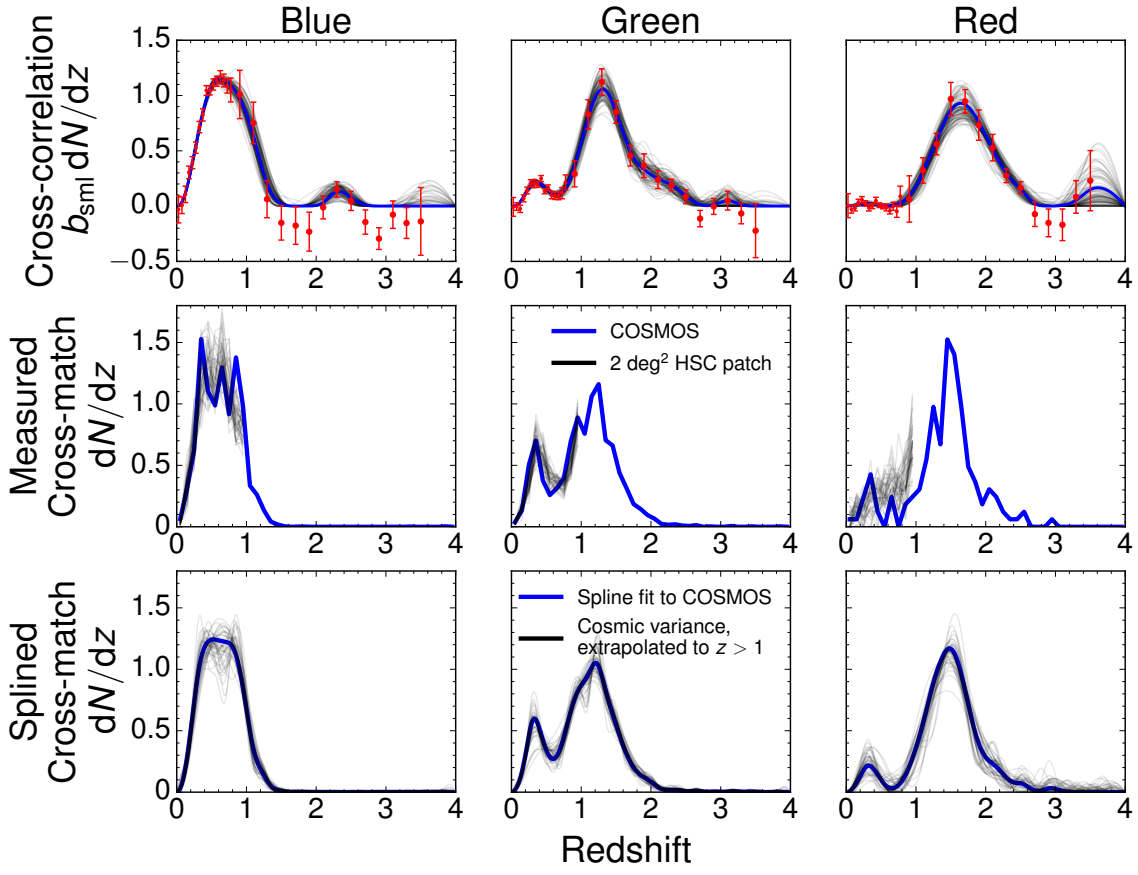

Figure 6.7: *Top*: $b_{\rm sml,p} dN_{\rm p}/dz$ combined for all tracers, with best-fit spline plotted in blue and 100 splined samples drawn from diagonal Gaussian realizations of the noise overplotted in gray. The difference in dN/dz between the two halves of the sky (split at $\ell = 155°$; not shown) is comparable to the range of the 100 spline realizations. *Middle*: dN/dz from the COSMOS cross-matches (thick solid lines) compared to dN/dz from 44 COSMOS-like $\sim$2deg^2 patches of HSC (gray lines). While HSC is deep enough to contain nearly all of the WISE objects, its photometric redshifts become biased at $z > 1$ and therefore we do not display them in this range. *Bottom*: Spline fit to the COSMOS dN/dz (thick solid line) compared to 44 realizations of the noise assuming diagonal Gaussian errors (thin gray lines). To account for cosmic variance, the standard deviation is a fixed multiple of the Poisson error set to match the observed scatter from the 44 HSC patches at $z < 1$, as described in Section 6.5.1.

scales used for the cross-correlation redshifts and the CMB cross-correlations is undesirable because it would push the cross-correlation redshifts to large scales where the signal-to-noise is lower and the potential impact of observational systematics is larger (Ménard et al. 2013); indeed, previous work uses scales of several Mpc at most (Ménard et al. 2013, Schmidt et al. 2013, Rahman et al. 2015, 2016b,a, Davis et al. 2018, Cawthon et al. 2018, Gatti et al. 2018). Conversely working on very small scales can be problematic, as the cross-correlation could depend upon galaxy formation physics in addition to the redshift distribution.

To study potential deviations between $b_{\rm sml,p}$ and $b_{\rm lin,p}$, we populate an N-body simulation with a simple HOD model for the WISE galaxies (Appendix 6.B), which is roughly consistent with the spectroscopic cross-clustering given the cross-match dN/dz (Figure 6.19). We then measure $b_{\rm sml}$ and $b_{\rm lin}$ from the autocorrelation of halos in the simulation at four representative redshifts ($z = 0.41$, 1.00, 1.27 and 1.78; Figure 6.17). At $z = 0.41$, $b_{\rm sml}$ is 0.7% (1.7%, 2.5%) greater than $b_{\rm lin}$ for halos representative of the blue (green, red) samples. At $z = 1.78$, $b_{\rm sml}$ is 7.2% (15.3%) greater than $b_{\rm lin}$ for green (red) halos; and at $z = 1.00$, $b_{\rm sml}$ is 1.6% greater than $b_{\rm lin}$ for blue halos. We discuss the implications of these discrepancies between $b_{\rm sml,p}$ and $b_{\rm lin,p}$ in Section 6.7; we find that their impact is subdominant to the statistical uncertainty on dN/dz.

We also compare the fiducial real-space $b_{\rm sml,p}dN_{\rm p}/dz$ to $b_{\rm lin,p}dN_{\rm p}/dz$ measured in Fourier space using Eq. 6.15 on the same angular scales ($\ell = 100$ to 1000) as the CMB lensing cross-correlation.[22] We find good agreement for bdN/dz in both configuration and harmonic space (Figure 6.8), suggesting that discrepancies between $b_{\rm sml,p}dN_{\rm p}/dz$ and $b_{\rm lin,p}dN_{\rm p}/dz$ are minor.

We test the sensitivity of the dN/dz results to the presence of angular systematics in the spectroscopic data by measuring the weighted cross-correlation, using the combined angular systematics, fiber collision and redshift failure weights for BOSS galaxies and eBOSS; and the inverse of the targeting completeness for BOSS quasars. We also create and apply systematics weights for the unWISE samples, following the methodology of Ross et al. (2017) for the BOSS and eBOSS samples. We construct `nside`=128 maps of the unWISE density (correcting for sub-pixel masking) and of several systematics: stellar density from Gaia (Gaia Collaboration et al. 2018), 5σ limiting magnitude in W2, and $N_{\rm HI}$ column density from the HI4PI 21 cm survey (HI4PI Collaboration et al. 2016). We fit piecewise linear functions to the relationship between density and systematic, using stellar density and W2 limiting magnitude for the green and blue samples, and stellar density and $N_{\rm HI}$ for the red sample (other maps are not significantly correlated with galaxy density). We then define the weights for each systematic as the inverse of the predicted density.

We found $< 0.8\sigma$ change between the weighted and unweighted cross-correlations among all bins in redshift, spectroscopic and photometric tracers; this suggests that angular systematics correlated with unWISE fluctuations do not significantly affect our results.

We also compare the observed cross-correlation in a given redshift bin to the cross-

[22] At $z < 0.3$, $\ell_{\rm max} = 1000$ corresponds to $k_{\rm max} > 1\ h\ {\rm Mpc}^{-1}$, and the scale-independent bias assumption begins to break down. As a result, we set $\ell_{\rm max} = \min(1000, {\rm k_{max}}\chi)$, where χ is the comoving distance to the redshift bin center and $k_{\rm max} = 2.5\ h\ {\rm Mpc}^{-1}$.

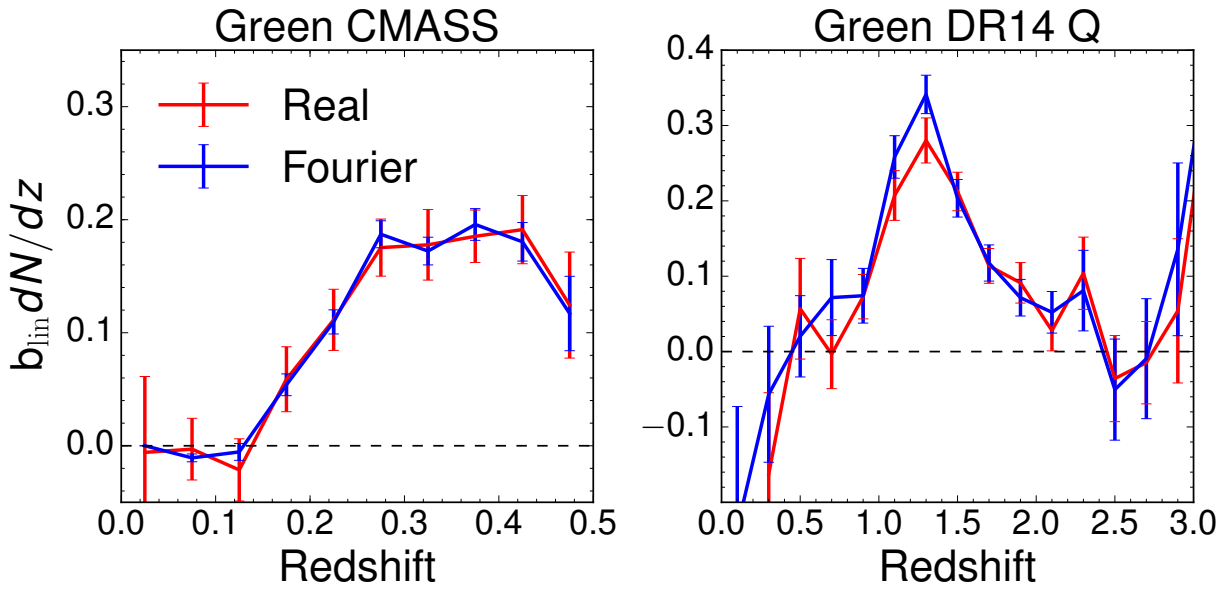

Figure 6.8: Comparison between the fiducial $b_{\rm sml,p} dN_{\rm p}/dz$ measured in configuration space (Equation 6.18) and $b_{\rm lin,p} dN_{\rm p}/dz$ measured in harmonic space using the pipeline described in Section 6.4, with $100 < \ell < 1000$.

correlation between Gaia stars and the spectroscopic sample. Since $\sim 2\%$ of all unWISE samples are stars, star-driven fluctuations in the spectroscopic sample may lead to spurious correlations between unWISE and spectroscopic samples. We find that the LOWZ-Gaia cross-correlation, times a fiducial stellar contamination fraction of 2%, is $< 5\%$ of the LOWZ-unWISE cross-correlation at $z > 0.15$, but comparable to the LOWZ-unWISE cross-correlation at $z < 0.15$ (for all three colors), although the error bars on the LOWZ-Gaia cross-correlation are comparable to the measured cross-correlation at these redshifts.

6.6 Galaxy-lensing auto and cross-spectra

In this section we present our measurements. We parameterize the amplitude of the correlations by a single effective linear bias

$$b^{\rm eff} = \int dz\, b_{\rm lin,p}(z) \frac{dN_{\rm p}}{dz} \tag{6.26}$$

where we follow our convention of $\int dz\ dN/dz = 1$. For our theory model, we use the cross-correlation redshifts, $b_{\rm sml,p} dN_p/dz$, to approximate $b^{\rm eff}$

$$b^{\rm eff} \approx \int dz\, b_{\rm sml,p}(z) \frac{dN_{\rm p}}{dz} \tag{6.27}$$

We insert the normalized cross-correlation redshifts, $f(z)dN_p/dz$

$$f(z)\frac{dN_{\rm p}}{dz} \equiv \frac{b_{\rm sml,p}(z)\frac{dN_{\rm p}}{dz}}{b^{\rm eff}} \tag{6.28}$$

into equation 6.3, and allow the amplitude $b^{\rm eff}$ to vary to match the data:

$$C_\ell^{\kappa g} = b^{\rm eff}\int d\chi \frac{W^\kappa(\chi)}{\chi^2}H(z)\left[f(z)\frac{dN_p}{dz}\right]P(k\chi=\ell+1/2) + \int d\chi\frac{W^\kappa(\chi)W^\mu(\chi)}{\chi^2}P(k\chi=\ell+1/2) \tag{6.29}$$

$$C_\ell^{gg} = (b^{\rm eff})^2\int d\chi\frac{1}{\chi^2}H(z)^2\left[f(z)\frac{dN_p}{dz}\right]^2 P(k\chi=\ell+1/2) + b^{\rm eff}\int d\chi\frac{W^\mu(\chi)}{\chi^2}H(z)\left[f(z)\frac{dN_p}{dz}\right]P(k\chi=\ell+1/2) + \int d\chi\frac{W^\mu(\chi)W^\mu(\chi)}{\chi^2}P(k\chi=\ell+1/2) \tag{6.30}$$

For the magnification bias term $W^\mu(\chi)$, we take the cross-matched dN/dz, and the values of s from Appendix 6.C.

Figure 6.9 shows the auto correlation of our three galaxy samples as well as their cross-correlation with the CMB lensing convergence, κ. Table 6.4 summarizes the results. We quote both statistical and dN/dz error bars on $b^{\rm eff}$; the statistical errors are from the errors on C_ℓ^{gg} and $C_\ell^{\kappa g}$ using the fiducial dN/dz, whereas the dN/dz error bars are the standard deviation of $b^{\rm eff}$ from fitting C_ℓ^{gg} and $C_\ell^{\kappa g}$ to 100 samples of dN/dz with uncorrelated Gaussian error added (as described earlier).

Over the range of scales that we model ($100 < \ell < 1000$), we obtain cross-correlation $S/N = \sqrt{\chi^2_{\rm null} - \chi^2_{\rm cross}}$ of 59.2, 68.5 and 41.4 for the blue, green and red samples, respectively. The combined cross-correlation S/N for the sample as a whole (taking into account the covariance between the three galaxy samples) is 79.3.

6.7 Systematics in the cross-correlation and null tests

In this section we explore the impact of stellar contamination, foregrounds in the CMB maps and the galactic latitude dependence of the signal.

6.7.1 Stellar Contamination

Due to the photometric nature of the catalog, with only two broad-band filters available, some fraction of the objects in our catalog will be stars or other non-cosmological sources

WISE sample	$b^{\rm eff}_{\rm auto}$	Shot Noise ($\times 10^7$)	σ_b from dN/dz	$\chi^2_{\rm auto}$/dof	$b^{\rm eff}_{\rm cross}$	σ_b from dN/dz	$\chi^2_{\rm cross}$/dof
Blue	1.74 ± 0.0052	0.92 ± 0.012	0.0865	24.3/4	1.56 ± 0.0276	0.0355	6.11/5
Green	2.44 ± 0.0083	1.81 ± 0.012	0.0793	8.69/4	2.23 ± 0.0352	0.0308	2.93/5
Red	3.47 ± 0.0383	29.6 ± 0.09	0.2435	8.21/4	3.29 ± 0.090	0.1541	4.56/5

Table 6.4: Results from fitting a constant bias times HaloFit power spectrum (using cross-correlation dN/dz). Note that the value of χ^2 here is for a *fixed* fiducial dN/dz and for a linear bias model with HaloFit power spectrum. A high χ^2 value indicates the need to marginalize over the redshift distribution for any cosmological interpretation, and highlights the importance of going beyond linear bias. In the follow up paper (Krolewski et al. 2020), we fully marginalize over the uncertainty in dN/dz and a non-linear model for galaxy biasing, obtaining a good fit.

such as nebulae or artifacts in the images. For simplicity, below we shall refer to any non-cosmological source that is uncorrelated with the true galaxies in our samples as "stars." On scales where stars can be considered unclustered, i.e. where their clustering power is negligible compared to the galaxies, their effect is to lower both the auto and cross correlations in a way that is completely degenerate with the galaxy bias, and hence can be marginalized over in a cosmological analysis. To see this, let's assume that average number density of objects in our catalog, $\bar{n}$, is the sum of galaxies, $\bar{n}_g$, and "stars", $\bar{n}_s$. The observed "galaxy overdensity" necessarily includes both

$$g^{\rm obs} = \frac{\delta n_g}{\bar{n}_g + \bar{n}_s} + \frac{\delta n_s}{\bar{n}_g + \bar{n}_s} \tag{6.31}$$

We expect the second term to be uncorrelated with CMB lensing, given its non-cosmological origin. This is an important assumption that can be violated, for example, if galactic dust emission affects CMB lensing reconstruction, and at the same time modulates the number density of galaxies observed in WISE. We test this in the next section by applying different galactic cuts. Assuming the second term is uncorrelated with κ, we can write

$$\langle \kappa \; g^{\rm obs} \rangle = \langle \kappa \; g^{\rm true} \rangle \frac{\bar{n}_g}{\bar{n}_g + \bar{n}_s} = \langle \kappa \; g^{\rm true} \rangle \frac{1}{1+\epsilon_s} \tag{6.32}$$

where we have defined $\epsilon_s = \bar{n}_s/\bar{n}_g$ to be the stellar contamination fraction. Similarly, on scales where stars are approximately unclustered (see below),

$$\langle g^{\rm obs} \; g^{\rm obs} \rangle = \langle g^{\rm true} \; g^{\rm true} \rangle \left(\frac{1}{1+\epsilon_s} \right)^2 \tag{6.33}$$

From the argument above, we can see that the effect of stellar contamination is to lower the auto and cross correlations in a scale-independent way. Since $\langle \kappa \; g^{\rm true} \rangle \propto b_g$ and $\langle g^{\rm true} \; g^{\rm true} \rangle \propto b_g^2$, we conclude that unclustered stellar contamination is completely degenerate with a scale-independent galaxy bias and that our analysis actually measures the "effective bias"

$$b^{\rm eff} = b^{\rm true} \frac{1}{1+\epsilon_s} \tag{6.34}$$

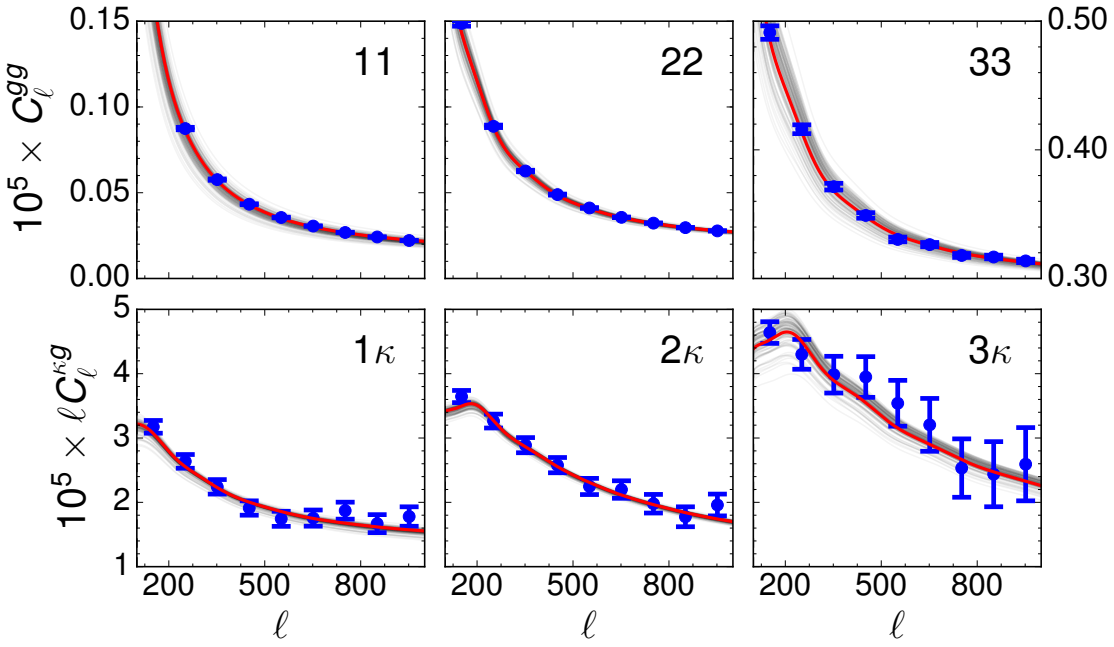

Figure 6.9: Auto correlation (top) and cross correlation between the unWISE catalog and Planck CMB lensing (bottom); numbers label the samples (1: blue, 2: green, 3: red). The best-fit theory curve assuming a constant bias times HaloFit is shown as a solid red line and the uncertainty in the model from the uncertainty in dN/dz is given by the gray lines. We fit angular scales to the right of the dashed line. Magnification bias is a few times larger than the errorbars in the auto-spectra, and $\sim 50\%$ of the errorbars in the CMB cross-spectra.

so that marginalization over galaxy bias will automatically also marginalize over the (in general unknown) amount of stellar contamination. We further note that the ratio

$$\frac{(C_\ell^{\kappa g})^2}{C_\ell^{gg}} \sim \frac{(b_g^{\rm eff})^2 \sigma_8^4}{(b_g^{\rm eff})^2 \sigma_8^2} \sim \sigma_8^2 \tag{6.35}$$

is proportional to σ_8^2 in linear theory, and is therefore independent of $b^{\rm eff}$ on linear scales.

The power spectrum of galactic contaminants such as stars is typically very large on large scales, falling off steeply with increasing ℓ (faster than the typical galaxy power spectrum). For example, we have checked that if the stellar contamination in unWISE traces a Gaia stellar map[23] with stellar contamination fraction $\sim 1\%$ (as expected from the cross-match to COSMOS), the stellar power in the lowest-ℓ bin used in the analysis is $< 0.5\%$ of the galaxy clustering power on the same scale, ensuring that the argument above holds.

[23]We also find a similar power spectrum for Gaia stars that meet our blue or green WISE color selection.

6.7.2 Foreground contamination to CMB lensing cross-correlations

The Minimum Variance (MV) reconstruction we use in the fiducial analysis is dominated by CMB temperature (rather than polarization), and is therefore subject to possible contamination by both galactic and extragalactic foregrounds. When these foregrounds are correlated with the galaxy sample of interest, they can lead to biases in the cross-correlation (Schaan & Ferraro 2019, Madhavacheril & Hill 2018, Ferraro & Hill 2018, van Engelen et al. 2014, Osborne et al. 2014).

Regarding galactic foregrounds, we expect the largest contaminant to be galactic dust, seen in emission in the CMB maps, and causing reddening and/or extinction on most galaxy catalogs. Imperfect foreground separation can impact the CMB lensing maps. While we expect the IR-selected unWISE sources not to be directly affected by galactic dust, nonetheless their local density can be dependent on (for example) stellar density, which is itself correlated with galactic dust. The Planck team Planck Collaboration et al. (2018f) performed a large number of null tests regarding the reconstructed map, and find general stability of the baseline reconstruction on the `SMICA` component separated temperature map. Importantly, the reconstruction is stable with respect to choice of galactic mask, with variations consistent with those expected from the change in area. Most of the null test tensions come from the reconstruction on the 217 GHz frequency map, which may contain non-negligible galactic contamination. We caution that the tSZ-free map has larger weight given to the 217 GHz channel and may therefore have a larger dust contamination.

Regarding extragalactic foregrounds, the effect on the lensing auto-power spectrum has been thoroughly investigated in Section 4.5 of Planck Collaboration et al. (2018f). The Planck team has found that at lensing $\ell < 1000$, both tSZ and CIB biases are expected to be a small fraction of 1%, significantly below the statistical errors. The effect of kSZ biases for the Planck SMICA map has been calculated in Ferraro & Hill (2018) and shown to be negligible. Calculating the bias to the cross-correlation with galaxies is more difficult, since it depends on the particular sample, its redshift distribution, HOD and IR luminosity function. Using realistic correlated CMB and large-scale structure simulations, Schaan & Ferraro (2019), Ferraro & Hill (2018) have found that for a galaxy sample with median redshift ≈ 0.8 and $b(z) \approx 1 + 0.84z$, the size of the biases in auto and cross-correlations are very comparable. This sample is rather similar in redshift distribution and bias (and hence mass) to the WISE blue and green samples, and therefore we expect that the biases in cross be the same order of magnitude of the ones in the CMB lensing auto-spectrum, and hence safely sub-percent. While this argument only provides a rough estimate, it appears very likely that any extragalactic source of bias will be well below the statistical significance of our cross-correlations.

As a further test, we repeat the cross-correlation with the Planck 2018 lensing reconstructed from tSZ-deprojected temperature maps, shown in Table 6.5. Apart from removing the possible tSZ contamination, the CIB contribution will be significantly different due to the different weighting of the single-frequency channels. While the absence of tSZ bias could in principle be partly compensated by a larger CIB-induced bias, the consistency between

the fiducial and tSZ-free cross-correlations provides further confidence that foreground contamination is subdominant to our other sources of uncertainty.

WISE sample	$b^{\rm eff}_{\rm cross}$	$\chi^2_{\rm cross}/{\rm dof}$	$b^{\rm eff}_{\rm cross,tSZ-free}$	$\chi^2_{\rm cross,tSZ-free}/{\rm dof}$
Blue	1.56 ± 0.0276	$6.11/5$	1.54 ± 0.0305	$9.34/5$
Green	2.23 ± 0.0352	$2.93/5$	2.19 ± 0.0389	$3.87/5$
Red 16.2	3.29 ± 0.090	$4.56/5$	3.25 ± 0.102	$6.03/5$

Table 6.5: Comparison between fiducial $b^{\rm eff}_{\rm cross}$ (reproducing Table 6.4) and $b^{\rm eff}_{\rm cross}$ for the tSZ free sample.

6.7.3 Galactic mask dependence of the sample properties

If the redshift distribution varies across the sky, the clustering dN/dz measured in the SDSS region could be unrepresentative of the true dN/dz across the entire WISE mask. We test this possibility by restricting the C^{gg}_ℓ and $C^{\kappa g}_\ell$ measurement to the SDSS footprint used to measure dN/dz and repeating our measurements. We find good agreement between the biases measured in the SDSS region and the biases measured across the full sky (Table 6.6). We also find that the galaxy-galaxy cross-spectra (i.e. Fig. 6.22) are quite similar in the SDSS region as in the full unWISE footprint, changing by $< 10\%$.

WISE sample	$b^{\rm eff}_{\rm auto}$	$10^7\times$ Shot Noise	$\chi^2_{\rm auto}/{\rm dof}$	$b^{\rm eff}_{\rm cross}$	$\chi^2_{\rm cross}/{\rm dof}$
Blue	1.76 ± 0.0117	0.87 ± 0.027	$10.3/4$	1.55 ± 0.0632	$12.7/5$
Green	2.42 ± 0.0188	1.78 ± 0.027	$10.1/4$	2.19 ± 0.0797	$11.8/5$
Red 16.2	3.60 ± 0.0845	28.9 ± 0.21	$7.27/4$	3.27 ± 0.206	$5.73/5$

Table 6.6: Results from fitting a constant bias times HaloFit power spectrum (using cross-correlation dN/dz), restricting measurements to the CMASS area.

We further test the impact of restricting our sample to higher Galactic latitudes by sequentially applying the Planck 60%, 40% and 20% Galactic masks (retaining the "cleanest" 60, 40 and 20% of the extragalactic sky)[24] in addition to the standard WISE masks described in Section 6.2.4. We find no significant change in $C^{\kappa g}_\ell$ as the Galactic masking is changed. In contrast, we find changes of several percent with differing Galactic masks in the $\ell < 100$ bin; consequently, we only fit the bias to $\ell > 100$. At $\ell > 100$, we find a mild scale-independent trend in the amplitude of C^{gg}_ℓ with Galactic latitude, which may be caused by changes in the galaxy population due to changing selection function at higher Galactic latitudes (modifying both the bias and dN/dz). This should not affect our cosmological constraints

[24] Available at https://irsa.ipac.caltech.edu/data/Planck/release_2/ancillary-data/masks/HFI_Mask_GalPlane-apo0_2048_R2.00.fits

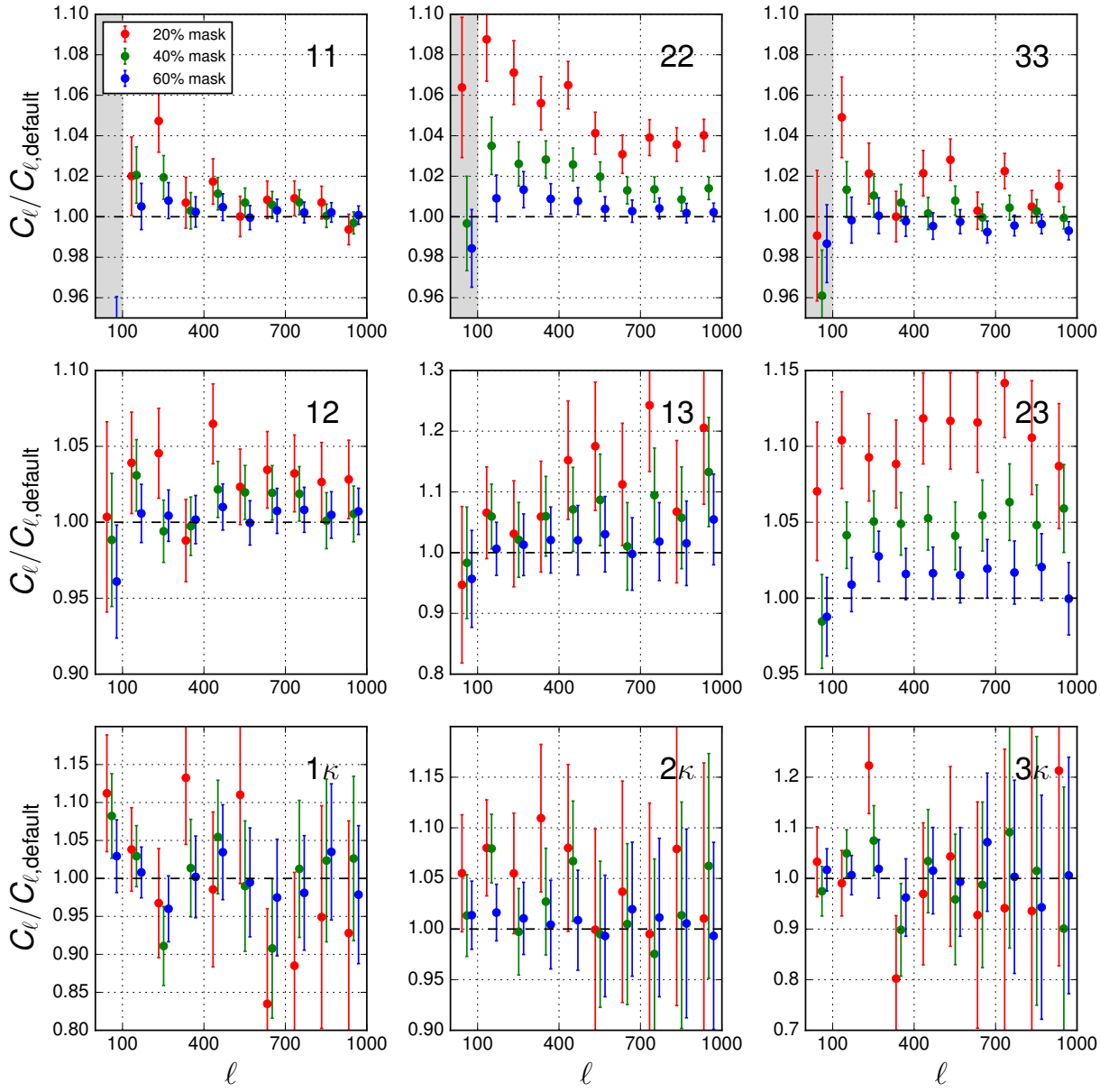

Figure 6.10: Change in clustering when masking is changed from the default Planck and WISE masks to the Planck 20%, 40% and 60% Galactic masks. Top row shows galaxy auto-spectra, middle row shows galaxy-galaxy cross-spectra, and bottom row gives galaxy-CMB cross spectra. Gray regions indicate scales excluded ($\ell < 100$) because the power depends too strongly on the Galactic mask.

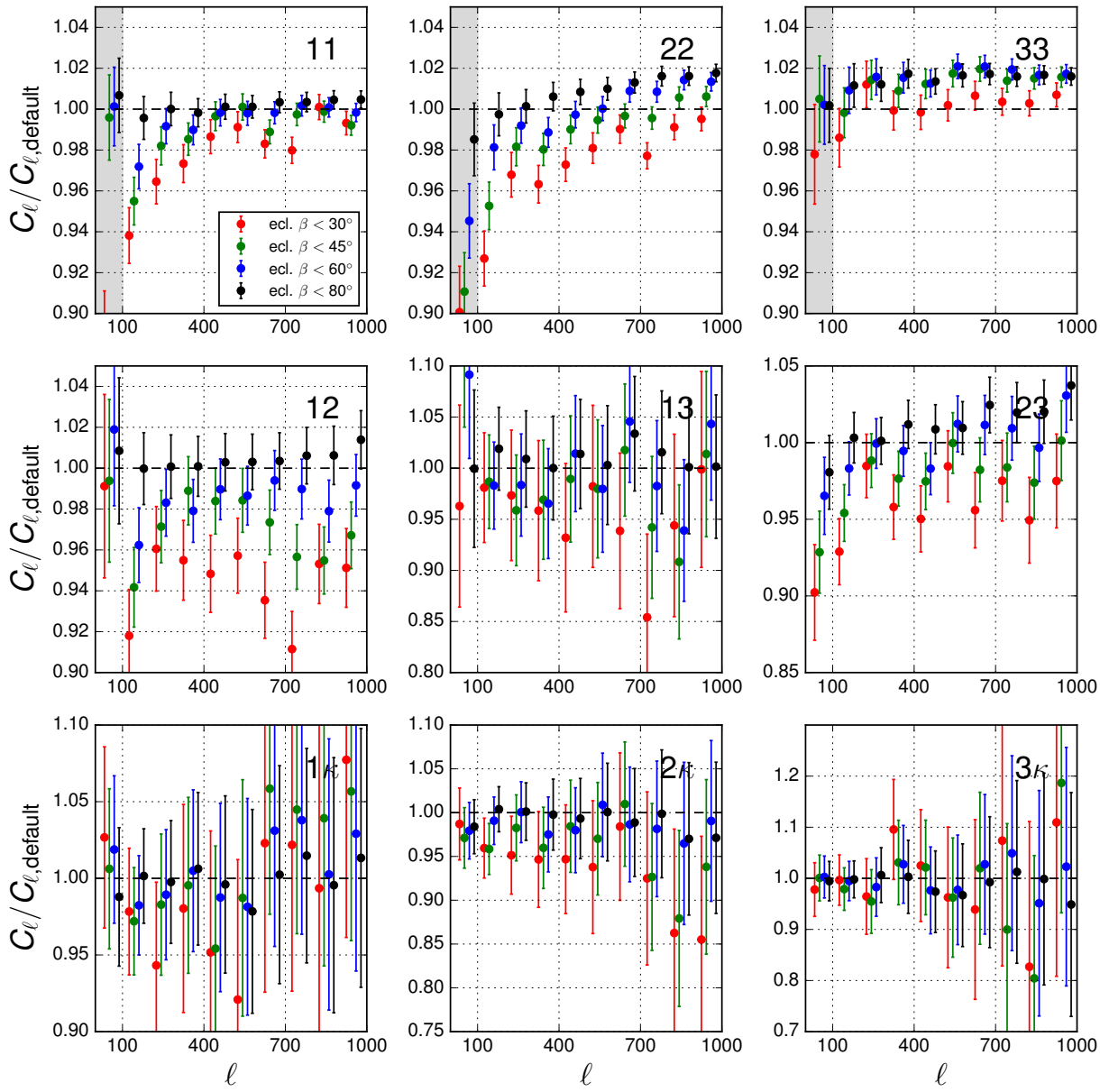

Figure 6.11: Change in clustering when masking is changed from the default Planck and WISE masks to cover more of the ecliptic. We sequentially exclude the sky at ecliptic latitude $\beta < 30°$, 40°, 60°, and 80° (i.e. black points include the smallest fraction of the sky, near the Ecliptic poles). Since the WISE depth of coverage is highest at the ecliptic poles, the black points are the deepest and the red points are the shallowest. Top row shows galaxy auto-spectra, middle row shows galaxy-galaxy cross-spectra, and bottom row gives galaxy-CMB cross spectra. Gray regions indicate scales excluded ($\ell < 100$) because the power depends too strongly on the Galactic mask.

as long as the area over which we measure dN/dz and the auto and cross correlations are the same. In practice, we prefer not to restrict the dN/dz measurement to the footprint of the spectroscopic samples ($f_{\rm sky} = 0.15$) and find that measuring $b^{\rm eff}$ over the spectroscopic footprint leads to variations $< 1\sigma$, suggesting dN/dz varying on the sky is not a major systematic.

Changes in the galaxy-galaxy cross-spectra with Galactic latitude suggest that dN/dz does vary on the sky in addition to the bias. If only the bias were changing as we changed the Galactic masks, the increase in the cross-spectrum would go as the geometric mean of the increase in the individual galaxy auto-spectra, but the red-blue and red-green cross-correlations increase by $\sim 5-10\%$ more than the geometric mean, implying a varying dN/dz[25] or more complex bias.

We perform a similar test for masking the ecliptic plane below $\beta = 30°$, $45°$, $60°$ and $80°$ (Figure 6.11). Similarly, we find only mildly scale-dependent trends, with deviations of $\sim$5% in the auto-spectrum at $\ell > 100$.

We also find that doubling the WISE stellar masking radius changes $b^{\rm eff}$ by less than 1 σ. Similarly, applying the more conservative masks of Kitanidis et al. (2019) (both the QSO and ELG masks, equation 20, which mask around considerably fainter stars than our mask) changes $b^{\rm eff}$ by less than 0.5 σ.

6.7.4 Systematic uncertainties in the redshift distribution

Due to the 6″ WISE PSF, blending is a source of systematic error in the cross-match redshifts, as it could lead to spurious matches with COSMOS. Many of our sources are blended, and it is possible that the low-redshift tails in the red and green samples result from source blending rather than from the presence of low-redshift sources. However, because we only use the cross-match redshifts in the magnification bias term, we expect blending to have a negligible impact on $b^{\rm eff}_{\rm auto}$ and $b^{\rm eff}_{\rm cross}$. If we replace all unWISE magnitudes in the cross-match with Spitzer 3.6 and 4.5 μm magnitudes (reducing the possibility of source confusion due to the 2" resolution of Spitzer) and replace the cross-match dN/dz with the Spitzer dN/dz, we find shifts of $< 0.5\sigma$ in the fitted biases.

Systematic errors in the COSMOS dN/dz may also impact our results, and are an important systematic in cosmic shear (Wright et al. 2019, Hildebrandt et al. 2020). Again, because we only use the COSMOS dN/dz in the magnification term, the impact of this systematic shift on our results is limited. Because our redshift bins are broad, the impact of scatter in the photometric redshifts should be minimal, as the scatter is $\Delta z < 0.1$ for the three samples, compared to the $\Delta z \sim 0.5$ redshift bins. Catastrophic errors may have a more significant impact; from Figures 11 and 12 in Laigle et al. (2016), we conservatively estimate 10% catastrophic errors for the higher-redshift $i \lesssim 24$ red and green samples, and 1% catastrophic errors for the $i \lesssim 22$ blue samples. The maximum impact of these errors

[25]Using fainter red samples (e.g. with a faint cut at W2 = 16.5 or 16.7) leads to even larger variation in red cross blue compared to red and blue separately, suggesting that dN/dz variations are more severe for the fainter red samples.

would be to create a population of galaxies with $\Delta z \sim 1$ redshift errors. We therefore create two dN/dz for the green and red samples where 10% of the galaxies are scattered uniformly into a $0 < z < 1$ tail or a $2 < z < 3$ tail. We find that using these dN/dz instead of the fiducial dN/dz makes $\lesssim 0.5\sigma$ difference in our results.

We study the impact of a discrepancy between $b_{\rm sml,p}$ and $b_{\rm lin,p}$ using $b_{\rm sml}$ and $b_{\rm lin}$ from the autocorrelation of WISE-like samples in an N-body simulation (Appendix 6.B). We parameterize $b_{\rm sml}/b_{\rm lin} = 1 + Az^2$ (smooth curves in Figure 6.18), allowing A to vary between zero and twice its fiducial value, $A_{\rm fid}$. We pick $1 + Az^2$ because it has roughly the right functional form. Since the HODs are approximate anyway, quantitative agreement with the N-body results is not required. Indeed, the $1+Az^2$ fitting function is somewhat conservative, as it predicts a slightly larger increase in $b_{\rm sml}/b_{\rm lin}$ than indicated by the N-body simulations (compare the N-body simulations to the fitting function at $z \sim 0.4$). We show the impact of using both the fiducial value, $A_{\rm fid} = 0.025$, 0.025, 0.05 for blue, green and red, and the maximal value, $A_{\rm max} = 0.1$, 0.15, 0.2 for blue, green and red, for the most extreme bias evolution allowed by the data.

We summarize the impact of different systematics on $b^{\rm eff}_{\rm auto}$ and $b^{\rm eff}_{\rm cross}$ for the green sample in Figure 6.12. The analogous plots for the blue and red samples look similar; in fact, green is the only sample to have $> 1\sigma$ discrepancies from the fiducial value (measured using the quadrature sum of the dN/dz error and the statistical error), with a 1.3σ discrepancy when using $A_{\rm max}$ to correct for nonlinear bias evolution and a 1.3σ discrepancy when the cross-match dN/dz uses $r_{\rm p,min} = 4\ h^{-1}$ Mpc (where $r_{\rm p,min}$ indicates the minimum separation bin used in the clustering redshifts, fiducially 2.5 h^{-1} Mpc). For the $r_{\rm p,min} = 4\ h^{-1}$ Mpc dN/dz, we use the error for the $r_{\rm p,min} = 4\ h^{-1}$ Mpc dN/dz for σ rather than the quadrature sum of this error and the error from the fiducial $r_{\rm p,min} = 2.5\ h^{-1}$ Mpc dN/dz, because the two dN/dz errors are highly correlated.

6.8 Conclusions and lessons learned

We have presented a tomographic measurement of the cross-correlation of the unWISE galaxies and CMB lensing. We report a combined detection significance of 55.1, which is the highest-significance detection of lensing by large-scale structure to date.

One of the greatest challenges was the characterization of the redshift distribution for the three samples. Since for most galaxies only the W1 and W2 magnitudes were available, we did not attempt to assign individual photometric redshifts, but just split the full catalog into three samples with different mean redshifts, but with non-negligible overlap between them. We use two techniques to measure the redshift distribution.

First, we cross-match our objects with the COSMOS catalog, obtaining a direct measurement of the redshift distribution dN/dz. A direct cross-match is insensitive to modeling assumptions and measures dN/dz, required to calculate the magnification bias contribution. If used to predict clustering, assumptions on the redshift evolution of the bias evolution are necessary. One disadvantage is the high completeness required of the survey, which limits the

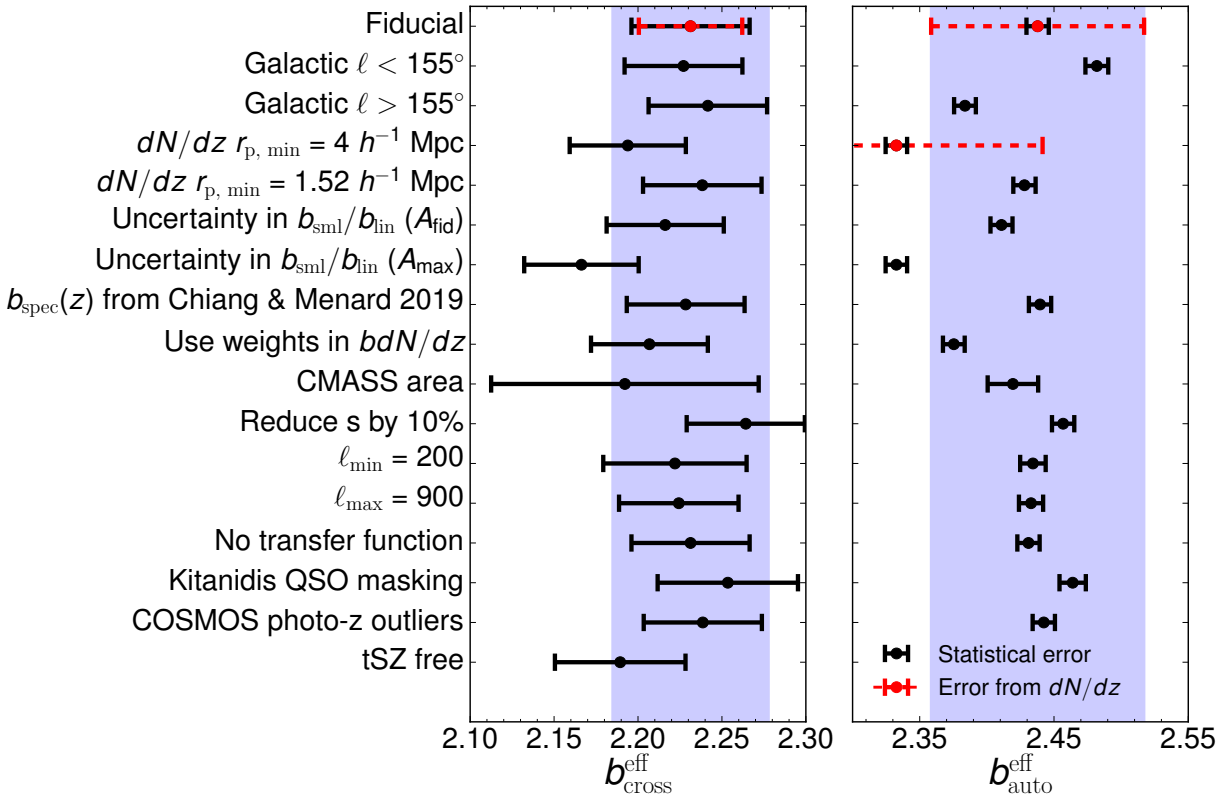

Figure 6.12: Impact of systematic errors on $b^{\rm eff}$ for the green sample. Black errorbars give the statistical uncertainty, red dashed errorbars give the systematic uncertainty from errors in dN/dz (only plotted for the fiducial values), and the blue band displays their quadrature sum. We also plot the uncertainty from dN/dz error for the $r_{\rm p,min} = 4\ h^{-1}$ Mpc dN/dz, to emphasize that this point is only 1.3σ discrepant if we define σ using the dN/dz errors. Top row gives fiducial value matching Table 6.4. The next two rows show $b^{\rm eff}$ for the split-sky sample, giving an estimate of uncertainty due to uncertain dN/dz. The next four rows are concerned with nonlinear bias evolution; either by increasing/decreasing $r_{\rm p,min}$ to be more/less robust against nonlinear bias; or using the parameterized function from Appendix 6.B, $b_{\rm sml,p}/b_{\rm lin,p} = (1 + Az^2)$ with $A_{\rm fid}$ ($A_{\rm max}$) = 0.025 (0.1), 0.025, (0.15), 0.05 (0.2) for blue, green and red. The next row shows the impact of changing the CMASS and LOWZ spectroscopic bias evolution used in the clustering redshifts from the measured values of Table 6.7 to values from Fig. 12 of Chiang & Ménard (2019). The next rows show the impact of using weights in the cross-correlation redshifts, restricting to the CMASS footprint (Table 6.6), reducing magnification bias response s by 10%, changing scale cuts for the auto- and CMB-cross power spectra, using the tSZ-free lensing map, using stricter stellar masking from Kitanidis et al. (2019), and the impact of COSMOS photo-z catastrophic errors adding a spurious low-z tail to dN/dz.

area available. Another disadvantage is source blending, which could lead to spurious cross-matches and thus modify dN/dz. The small overlap area (2 square degrees) not only limits the measurement statistically, but given the inhomogeneous depth of the WISE survey and possible spatial dependence of the selection function, the results may not be representative of the full WISE footprint. While we take steps to ensure that our catalogs are magnitude limited over the whole footprint by applying appropriate magnitude cuts, residual effects such as blending and background subtraction can potentially lead to inhomogeneity in the selection function. The mild trends in bias with respect to Galactic mask observed in Figure 6.10 may be an indication of this.

Second, we cross-correlate the unWISE samples with a number of overlapping spectroscopic samples, thus determining the product of the bias and redshift distribution. This can be advantageous when calculating the clustering signal, since it is this product that enters the auto-correlation and the cross-correlation with CMB lensing. Another advantage is the typically large overlap area (important for when the selection function is inhomogeneous), and the fact that there are no completeness requirements on the spectroscopic sample. However, assumptions on the redshift evolution of the bias are necessary when calculating the magnification bias contribution, and the impact of magnification needs to be taken into account in the spectroscopic-photometric cross-correlation. Moreover, this measurement is subject to the usual modeling challenges such as non-linearities in clustering and bias.

As discussed in Appendix 6.B, the two measurements of dN/dz are consistent with each other when assuming a simple model for bias evolution. Further, the consistency of the unWISE bias measured on the CMASS overlap region (Table 6.6) compared to the whole unWISE footprint (Table 6.4) indicates that the cross-correlation redshifts should be unaffected by spatial variations in the selection function. In the fiducial analysis, we use the cross-correlation result to predict the clustering and the cross-matched distribution to predict magnification bias and therefore we don't need to assume a redshift evolution of the bias.

Once the redshift distribution is known (or the uncertainties appropriately marginalized over), theoretical modeling of the signal on intermediate to small scales is the next challenge. Non-linear corrections to both clustering and bias become important at ℓ of few hundred, where the statistical S/N is still large in each bandpower. This implies that even if dN/dz were known perfectly, our ability to extract cosmological information could still be limited by our theoretical models. We defer consideration of modeling the signal to future work (Krolewski et al. 2020).

In conclusion, we believe that the cross-correlations presented here are an extremely sensitive probe of late-time cosmology. A spectroscopic followup of a subsample of the sources as well as improved modeling of intermediate and small scales can lead to sub-percent measurement, with important possible applications for tests of gravity, measurement of neutrino masses and the properties of Dark Energy.

Acknowledgments

We thank David Alonso, Enea Di Dio, Yu Feng, Julien Guy, Colin Hill, Ellie Kitanidis, Alexie Leauthaud, Thibaut Louis, Emmanuel Schaan, David Schlegel, Uros Seljak, Blake Sherwin, Zachary Slepian, David Spergel, Katherine Suess and Michael Wilson for very useful discussions. S.F. is supported by the Physics Division at Lawrence Berkeley National Laboratory. M.W. is supported by the U.S. Department of Energy and by NSF grant number 1713791. This research used resources of the National Energy Research Scientific Computing Center (NERSC), a U.S. Department of Energy Office of Science User Facility operated under Contract No. DE-AC02-05CH11231. This work made extensive use of the NASA Astrophysics Data System and of the `astro-ph` preprint archive at `arXiv.org`.

6.A Optical properties of unWISE samples and prospects for spectroscopic followup

In this section, we describe the optical properties of the unWISE galaxies from archival photometric and spectroscopic data. We also discuss the prospects and requirements for spectroscopic followup of the unWISE samples to better determine dN/dz.

While the full unWISE sample only has infrared fluxes, by cross-matching to COSMOS we can determine the optical colors and properties of unWISE. In Figure 6.13, we show the distribution of Subaru i^+ for the unWISE galaxies, and the relationship between i^+ and the WISE bands. For the blue sample a 90% completeness is achieved at $i^+ \simeq 22$ while for the green and red samples 90% completeness occurs at $i^+ \simeq 24$.

We also show the stellar mass and star formation rates of unWISE galaxies from COSMOS broad-band photometry. All three unWISE samples have similar stellar masses (with $\log_{10}(M/M_\odot) = 10.80$, 10.78, and 10.87 for the blue, green and red samples) but the star-formation rates of the green and red samples ($\log_{10} \mathrm{SFR}/M_\odot \mathrm{yr}^{-1} = 1.03$, 1.61) are significantly higher than the star-formation rate of the blue sample ($\log_{10} \mathrm{SFR}/M_\odot \mathrm{yr}^{-1} = 0.12$).

Some of the galaxies in the unWISE samples have been observed in the VVDS survey (Le Fèvre et al. 2013) using VIMOS on VLT, allowing us to both better characterize the galaxy samples and understand the feasibility of spectroscopic followup. The VVDS-Deep survey has a simple selection function, uniformly targeting galaxies at $17.5 < I < 24$. Not every $17.5 < I < 24$ galaxy is targeted; to determine the completeness of the unWISE galaxies in VVDS, we must divide the number of matches by the VVDS targeting selection rate (typically 20-30%) and then compare to the number of unWISE galaxies lying within the VVDS spectroscopic mask.[26] We find 444, 261 and 13 VVDS matches to the blue, green and red samples (418, 191 and 10 with high confidence redshifts, ZFLAGS >= 2), implying

[26] As with the COSMOS matches, we additionally remove VVDS galaxies with Spitzer-SWIRE (Lonsdale et al. 2003) 4.5 μm magnitude > 19.2 (18.7 for red sample), although relatively few VVDS galaxies have SWIRE matches so this cut makes little difference.

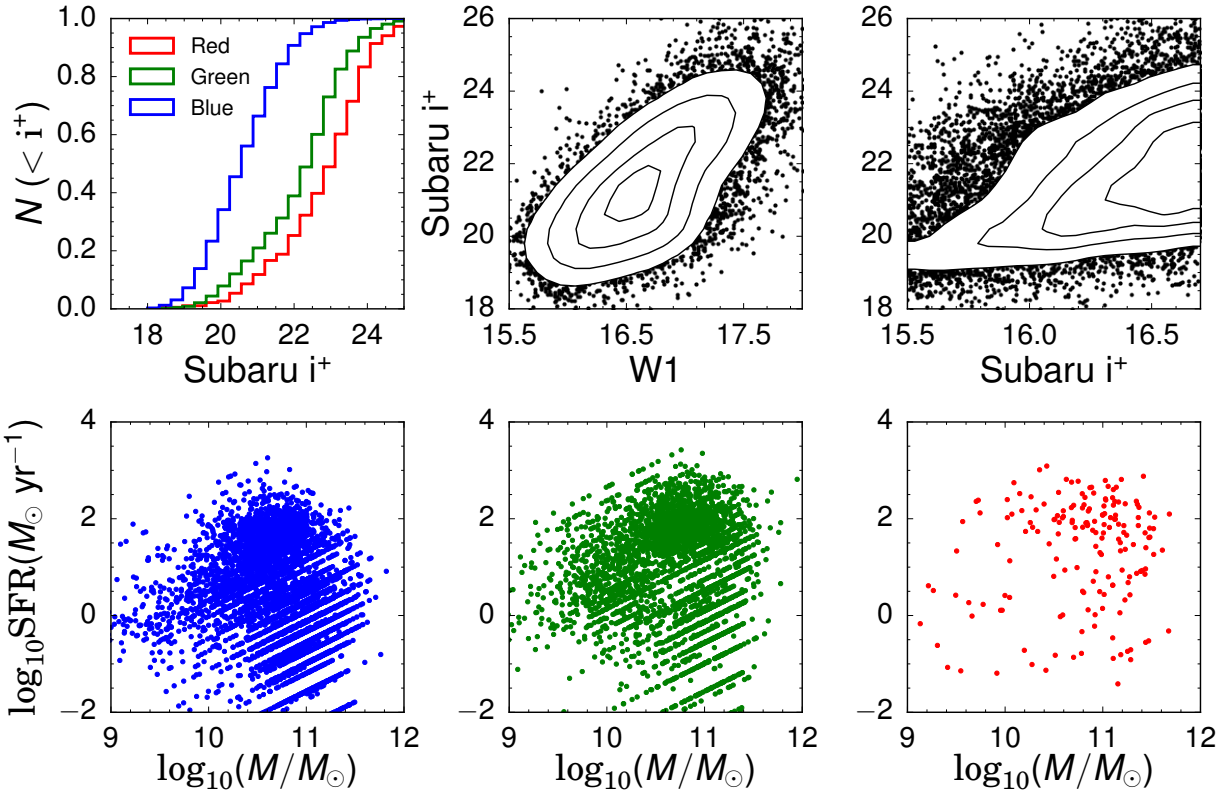

Figure 6.13: *Top left:* Distribution of Subaru i^+ magnitudes ("mag_auto," measured in flexible elliptical apertures, as in Kron (1980)) from unWISE matched to COSMOS. *Top center and right:* Subaru i^+ versus WISE W1 and W2 magnitudes for the combined red, green and blue samples in COSMOS. We show 20%, 40%, 60% and 80% iso-contours of the cumulative distribution function (Gaussian smoothed with $\sigma = 1$ mag) of galaxies in i^+ and W1/W2. *Bottom:* Distribution of stellar mass and star formation rate for each of the three samples, from COSMOS broad-band photometry.

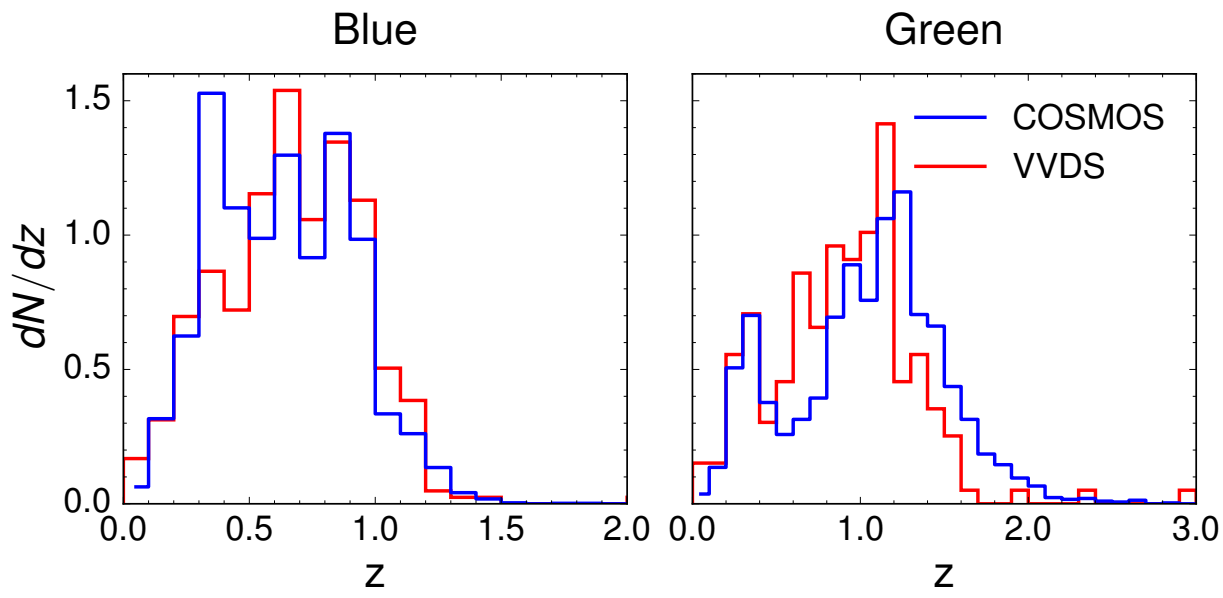

Figure 6.14: Comparison of dN/dz for COSMOS photometric (blue) and VVDS spectroscopic (red) matches for the blue and green samples (including spectra from VVDS-Deep and VVDS-UltraDeep). The red sample has too few VVDS matches to compare the two dN/dz. While VVDS is largely complete for the blue sample, incompleteness at the faint, high redshift end of the green sample may bias dN/dz relative to COSMOS.

101.3%,[27] 89.6% and 70.0% of the blue, green and red samples yield a VVDS spectrum. This agrees well with the fraction of galaxies with I < 24, which is 99.6% (91.8%, 84.5%) for the three samples, implying that within the range of galaxies that could have been targeted, 97.8%, 69.0% and 59.4% of blue, green and red galaxies received a high-confidence VVDS redshift. VVDS-Deep exposure times are 4.5 hr on a $R \sim 230$ spectrograph, suggesting that spectroscopic followup of the unWISE samples is feasible on 8-10 m class telescopes (and perhaps smaller telescopes for the brighter blue sample).

We also incorporate galaxies from the VVDS UltraDeep survey, which includes 12, 19, and 1 galaxies from the blue, green and red samples (10, 11, and 1 with ZFLAGS >= 2). The redshift distribution of blue galaxies with redshifts from VVDS is quite similar to the COSMOS dN/dz (Figure 6.14); for the green sample, the VVDS dN/dz is suppressed relative to COSMOS at $z > 1.6$, possibly because of increased redshift failures at high redshifts where the [OII] line redshifts beyond the red end of the spectrograph.

We display three spectra from each sample in Figure 6.15, representing each sample at low, medium and high redshift. Blending presents a similar challenge for the VVDS cross-match as for COSMOS, so we only display galaxies that are well-isolated in optical imaging.

[27] Completeness higher than 100% likely indicates that the targeting selection rate is somewhat underestimated.

Due to the paucity of red spectra, the red sources at $z = 0.477$ and $z = 2.27$ are blends, although in both cases only one of the two potential optical matches has a VVDS spectrum.

In Figure 6.16, we plot the distribution of redshift and rest frame [OII] 3727 Å EW for the green and blue samples from VVDS spectra, as well as $D_n(4000)$ versus [OII] 3727 Å EW, to separate star-forming from quiescent galaxies as in Franzetti et al. (2007). We find median rest frame [OII] 3727 Å EW of 6.4 (11.8) Å in emission for the blue (green) sample, and from the star-forming versus quiescent cut from Franzetti et al. (2007), 29.0% (60.3%) of blue (green) galaxies are star-forming.

A direct measurement of dN/dz with smaller errors than the COSMOS cross-match dN/dz would allow for improved modeling of the unWISE samples and better control of systematic errors. Even with improved cross-match dN/dz, we would still require the photometric-spectroscopic cross-correlations to determine $b_{\rm lin}(z)$, but we could greatly improve the simple HOD modeling in Appendix 6.B and Fig. 6.19, allowing for better understanding of $b_{\rm lin}(z)$ and potentially better control of systematics such as nonlinear bias evolution. With observations in several fields, we could also better understand the variation in dN/dz on the sky. Finally, we could better understand the impact of blending in our sample by re-targeting both (or all) galaxies blended together by the 6″ WISE PSF.

If the errors on dN/dz were much smaller than the errors on the photometric-spectroscopic clustering measurement, we could neglect dN/dz errors and better model the unWISE galaxy population. This is not the case in Fig. 6.19; at $z < 0.2$ and $z \sim 0.5$ in the blue sample, the error from uncertain dN/dz (gray band) is larger than the statistical error on the clustering (blue errorbars). However, this is driven by the HSC-derived cosmic variance correction, which is a factor of 3.8 for the blue sample (Section 6.5.1). If instead of measuring dN/dz on a single field, we measured dN/dz in multiple fields spread across the sky, the errors would be dominated by Poisson rather than cosmic variance, and no such correction would be necessary. Indeed, if we divide out this correction in the dN/dz errors in Figure 6.19, we find that dN/dz errors are at most 80% of the statistical errors for blue and green (peaking at $z \sim 0.3 - 0.5$); for red, the dN/dz errors are larger at low redshift, 150% of the statistical errors at $z \sim 0.5$. Scaling from the number of galaxies with secure COSMOS redshifts (5557, 3024, and 164 for blue, green and red), we estimate that achieving dN/dz errors that are at most 50% of the statistical errors will require 14000, 7500, and 1500 spectra for the blue, green and red samples. However, a smaller effort focused solely at low redshift could be just as effective for the red sample, since the low redshift tail is much more uncertain than the higher redshift dN/dz.

By measuring dN/dz across multiple fields, a spectroscopic followup program could constrain variations in dN/dz on the sky. Using the standard deviation of the COSMOS cross-match dN/dz, we estimate that we could measure a 5% shift in the mean dN/dz at 3σ with 1000 spectra per field for both the blue and green samples. For the red sample, with 400 spectra per field we could measure a 10% shift at 3σ.

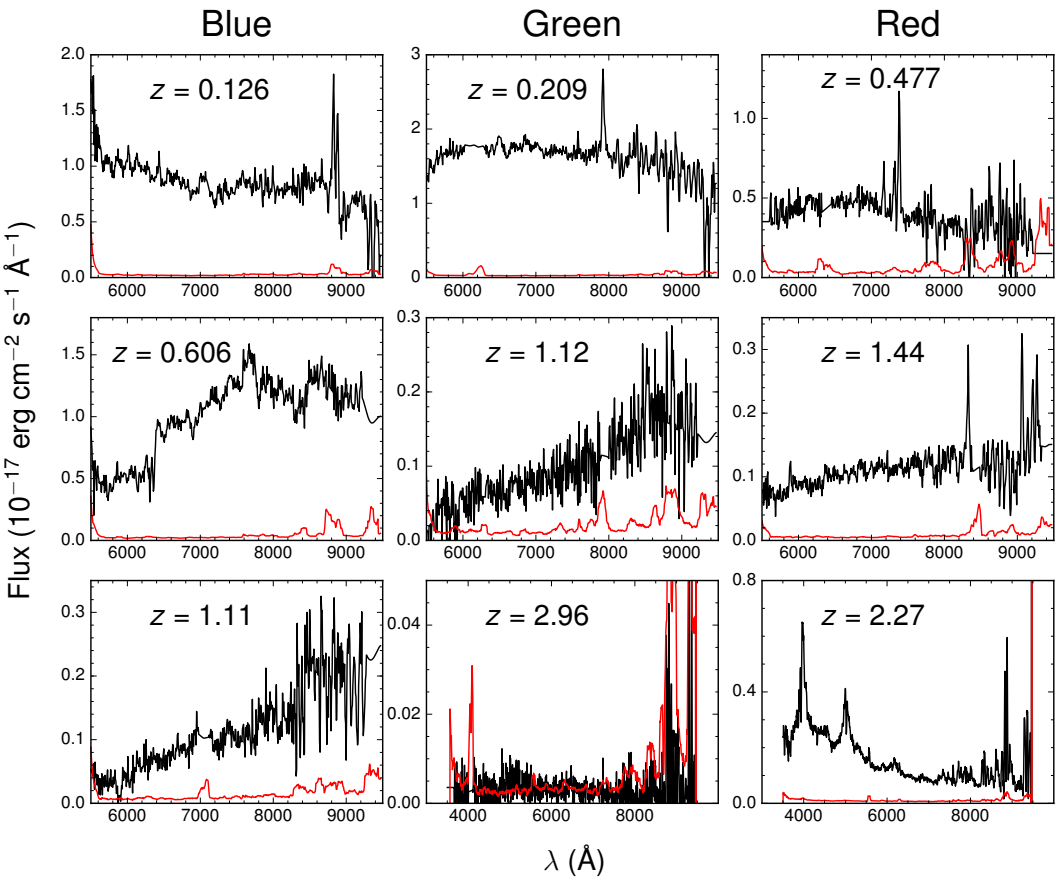

Figure 6.15: VVDS spectra from each of the three unWISE samples, with spectra in black and noise in red. For each of the three samples we display galaxies representative of the low, medium, and high portion of the redshift distribution. The highest redshift green and red galaxies are from VVDS-UltraDeep, which took spectra in both the blue and red grisms of VIMOS; all other galaxies are from VVDS-Deep, which only observed using the red grism.

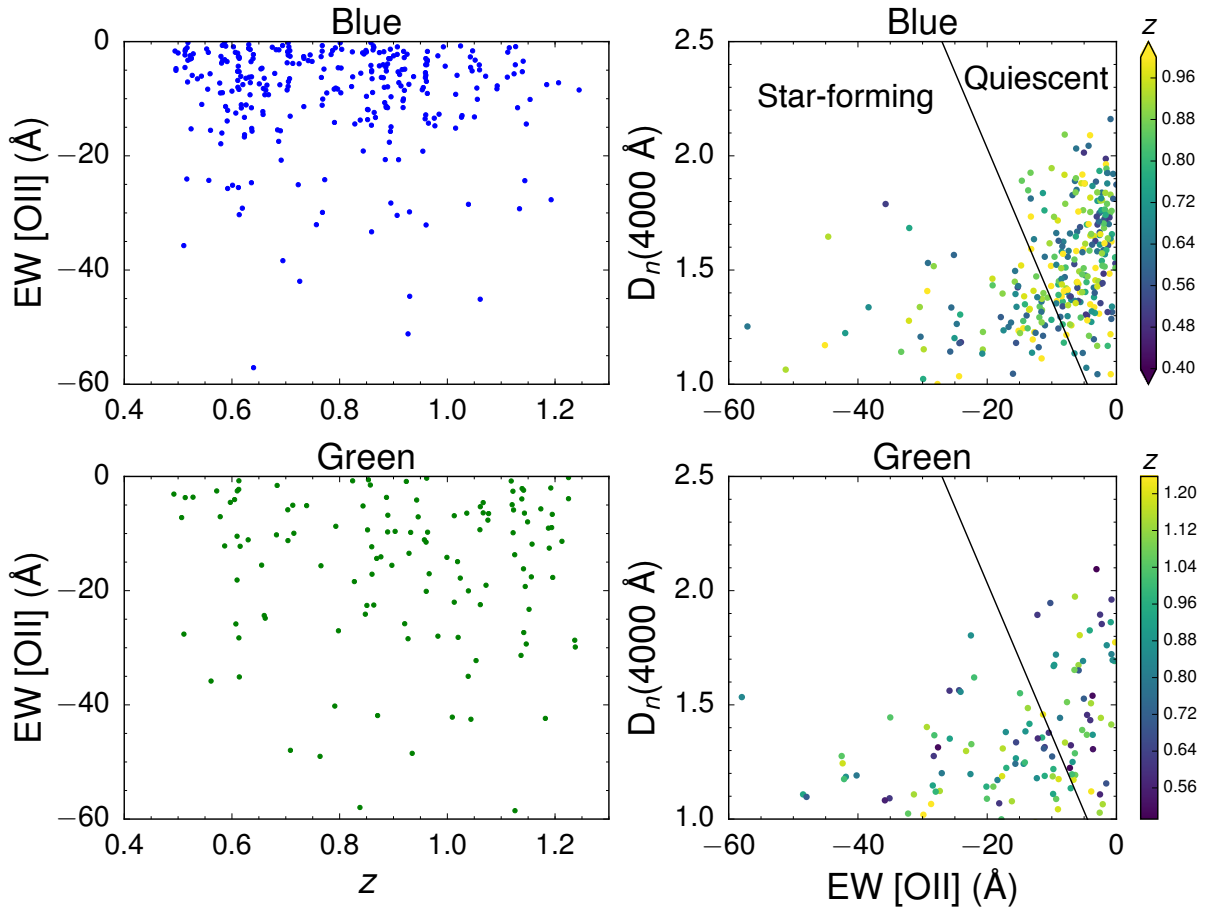

Figure 6.16: *Left:* From VVDS spectra, distribution of rest frame [OII] 3727 Å EW versus redshift for the blue sample (top) and green sample (bottom). *Right:* Distribution of [OII] 3727 Å EW versus $D_n(4000)$ to separate star forming and quiescent galaxies as in Franzetti et al. (2007). Points are color-coded to represent redshift.

		LOWZ		CMASS				eBOSS Q		BOSS Q	
$z_{\rm min}$	$z_{\rm max}$	$b_{\rm sml,s}$	σ_b	$b_{\rm sml,s}$	σ_b	$z_{\rm min}$	$z_{\rm max}$	$b_{\rm sml,s}$	σ_b	$b_{\rm sml,s}$	σ_b
0.00	0.05	1.34	0.0381			0.00	0.20				
0.05	0.10	1.37	0.0077			0.20	0.40				
0.10	0.15	1.52	0.0037	1.36	0.2698	0.40	0.60				
0.15	0.20	1.73	0.0045	2.82	0.2615	0.60	0.80				
0.20	0.25	1.89	0.0039	1.54	0.0796	0.80	1.00	1.72	0.2803		
0.25	0.30	2.01	0.0018	2.11	0.1489	1.00	1.20	2.03	0.0851		
0.30	0.35	2.01	0.0021	1.99	0.1054	1.20	1.40	2.05	0.0759		
0.35	0.40	2.06	0.0019	2.24	0.1674	1.40	1.60	2.35	0.0683		
0.40	0.45	2.25	0.0017	2.05	0.0020	1.60	1.80	2.32	0.0992		
0.45	0.50	2.46	0.0079	2.08	0.0006	1.80	2.00	2.89	0.1004		
0.50	0.55			2.06	0.0008	2.00	2.20	2.87	0.1548		
0.55	0.60			2.17	0.0007	2.20	2.40			4.33	0.0808
0.60	0.65			2.22	0.0010	2.40	2.60			3.72	0.1394
0.65	0.70			2.39	0.0022	2.60	2.80			4.27	0.3772
0.70	0.75			2.52	0.0090	2.80	3.00			4.30	1.2109
0.75	0.80			2.73	0.0872	3.00	3.20			4.30	1.1164
						3.20	3.40			5.33	1.9984

Table 6.7: Bias of the spectroscopic samples and the 1-σ error bar, as defined in Equation 6.23.

6.B Simple HOD model for unWISE samples

When computing dN/dz using cross-correlations we assumed a scale-independent bias, and we found that in order for the cross-match and cross-correlation dN/dz to match, the biases needed to evolve relatively rapidly with redshift. In this Appendix we check whether this assumption and its implications are consistent with expectations from simple models of the manner in which galaxies populate dark matter halos.

A scale-independent bias is likely to be true on large, linear scales, but the extent to which this approximation is valid on the scales used in the dN/dz analysis is unclear. If the bias is scale-dependent, the redshift evolution of $b_{\rm sml,p}$ may not match the redshift evolution of $b_{\rm lin,p}$ (relevant for $C_\ell^{\kappa g}$ and C_ℓ^{gg}), potentially introducing a systematic bias. To investigate this issue we model the unWISE galaxies using a simple HOD applied to dark matter halos in N-body simulations, allowing us to study the scale and redshift dependence of the unWISE galaxy bias. Since our goal is modest, we simply use a 1-parameter family[28] of HODs based

[28]There is some evidence that HOD parameters scale approximately universally with number density, e.g. Brown et al. (2008). A similar assumption is at the root of the 'SHAM' approximation (Conroy et al. 2006).

on Zheng et al. (2005) with

$$\langle N_{\rm cen}\rangle = \frac{1}{2}\left[1+{\rm erf}\left(\frac{\log_{10}M-\log_{10}M_{\rm cut}}{\sqrt{2}\sigma_{\log_{10}M}}\right)\right] \quad ; \quad \sigma_{\log_{10}M}=0.25 \tag{6.36}$$

and

$$\langle N_{\rm sat}\rangle = \left[\frac{M-0.1M_{\rm cut}}{15M_{\rm cut}}\right]^{0.8} \quad . \tag{6.37}$$

The values of $\sigma_{\log_{10}M}$, and the power-law index and denominator in $\langle N_{\rm sat}\rangle$ are typical of magnitude-selected galaxy samples and our final results are not very sensitive to them. The number density and large- and small-scale biases $b_{\rm HOD}(z)$ can then be computed as a function of $\log_{10}M_{\rm cut}$. We compute the comoving number density of unWISE galaxies from the COSMOS cross-match dN/dz (Section 6.5.1) and choose the cutoff mass M_c to match the abundance of each sample at all redshifts. The results are given in Table 6.8.

	Blue		Green		Red	
z	$\log_{10}(M_{\rm cut})$	Abundance (h^3 Mpc^{-3})	$\log_{10}(M_{\rm cut})$	Abundance (h^3 Mpc^{-3})	$\log_{10}(M_{\rm cut})$	Abundance (h^3 Mpc^{-3})
0.41	12.25	3.44×10^{-3}	13.00	5.57×10^{-4}	13.50	1.39×10^{-4}
1.00	12.50	1.43×10^{-3}	12.75	7.19×10^{-4}	13.50	6.55×10^{-5}
1.27	13.25	1.11×10^{-4}	12.75	5.71×10^{-4}	13.50	4.26×10^{-5}
1.78			13.00	5.57×10^{-4}	13.50	1.39×10^{-4}

Table 6.8: Halos populated with the HOD of Eq. 6.36 and Eq. 6.37, at four output times. All HODs use $\sigma_{\log_{10}M}=0.25$ decades, and $\log_{10}M_{\rm cut}$ is then selected to roughly match the abundance of each unWISE sample at the specified redshift.

To reduce scatter, we averaged the results from halo catalogs generated from 4 simulations, each with 1280^3 particles in a $640\,h^{-1}$Mpc box, assuming ΛCDM with Planck 2014 cosmological parameters (Planck Collaboration et al. 2014b). The simulations use the TreePM code of White et al. (2002), are described in section 2.1 of Stark et al. (2015), and are validated in Heitmann et al. (2008). We consider friends-of-friends halos with linking length 0.168 of the mean interparticle spacing at four representative redshifts $z=0.41$, 1.00, 1.27 and 1.78. At each redshift we adjusted $\log_{10}M_{\rm cut}$ as in Table 6.8 and measured the real-space correlation function by direct pair counting of the halos, hence obtaining the projected correlation function, $w_p(R)$. We define the real-space bias as a function of scale

$$b(R)=\sqrt{w_p(R)/w_{p,{\rm HF}}(R)} \tag{6.38}$$

define $b_{\rm sml}$ with the same R^{-1} weighting as in Eq. 6.16:

$$b_{\rm sml}=\int_{r_{\rm min}}^{r_{\rm max}} dR\,R^{-1}\,b(R)\Big/\int_{r_{\rm min}}^{r_{\rm max}} dR\,R^{-1} \tag{6.39}$$

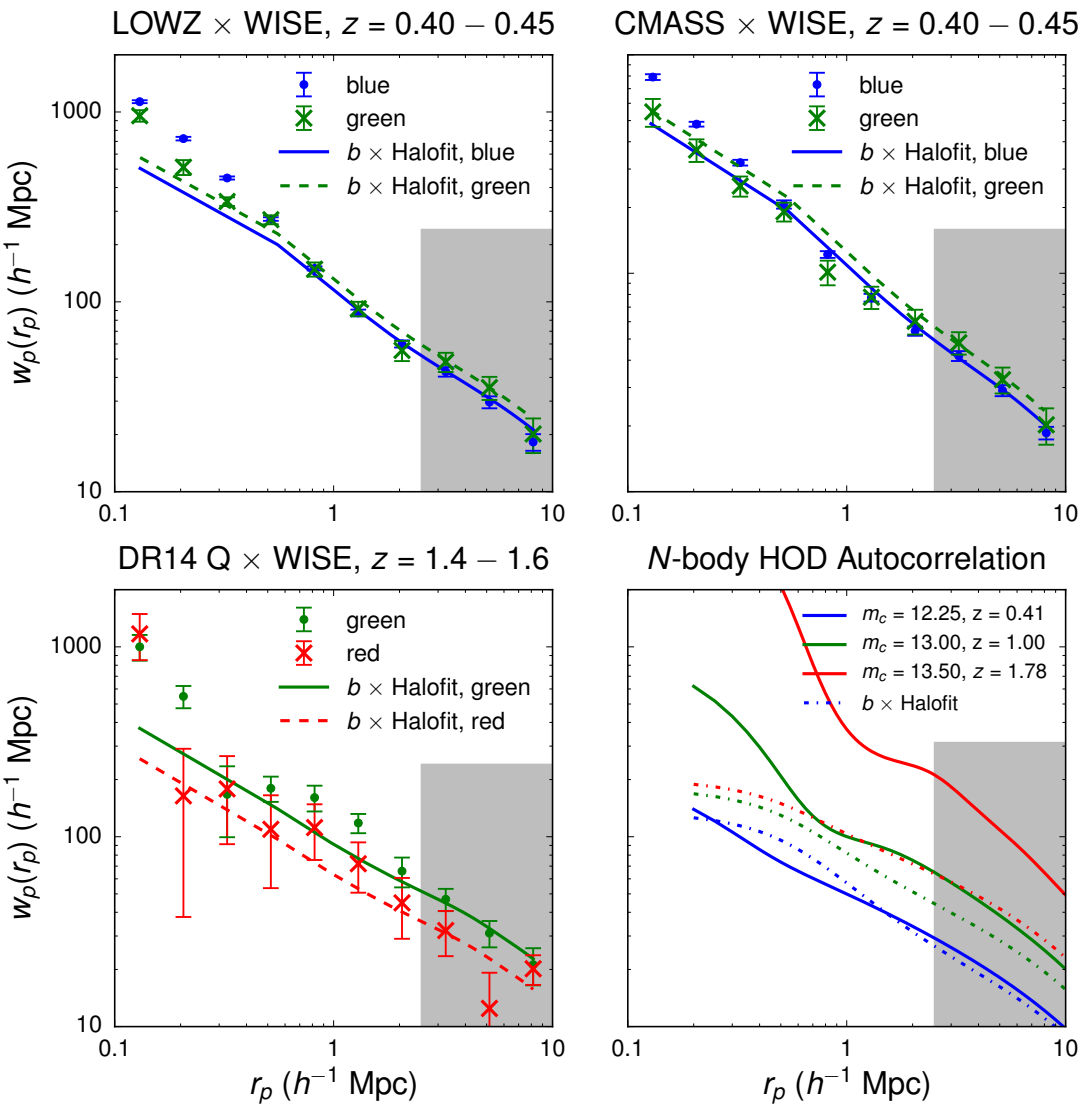

Figure 6.17: Cross-correlations between spectroscopic tracers and the unWISE galaxy samples, compared to a scale-independent bias times nonlinear correlation function fit to the points with $2.5 < r_p < 10\ h^{-1}$ Mpc (shaded region). Deviations from scale-independent bias are seen at $r_p < 2.5\,h^{-1}$Mpc, justifying our decision to use $2.5 < r_p < 10\,h^{-1}$Mpc for the cross-correlation redshifts. *Lower right*: autocorrelation of galaxies populating halos in an N-body simulation according to Eq. 6.36 and 6.37 with $\sigma_{\log_{10} M} = 0.25$ decades. Redshifts and number densities are chosen to be roughly representative of the three unWISE samples. Since the lower right panel is an autocorrelation ($\propto b^2_{\rm unWISE}$) while the other panels are cross-correlations ($\propto b_{\rm unWISE}$), it has a much stronger scale-dependent bias at $z \sim 1.5$ (since the unWISE galaxies have larger and thus more scale-dependent bias than the quasars).

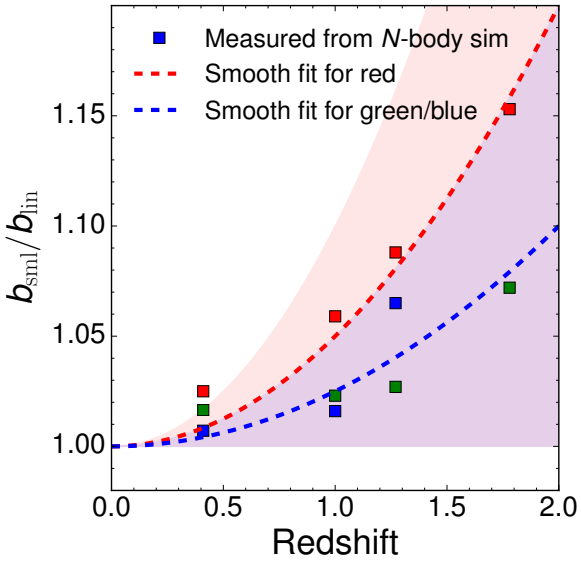

Figure 6.18: Ratio between $b_{\rm sml}$ and $b_{\rm lin}$ for HODs matched to the three unWISE samples at four representative redshifts in the N-body simulation. Dashed lines give interpolating functions $b_{\rm sml}/b_{\rm lin} = 1 + Az^2$ with separate values of A for red and blue/green; shaded regions represent uncertainty on A, accounting for uncertainty in the halo occupation of the unWISE galaxies.

and define $b_{\rm lin} \equiv b(r = 40\,h^{-1}{\rm Mpc})$.

We find only mild departures from scale-independent bias at $2.5 < r_p < 10\ h^{-1}$ Mpc, but more significant deviations at smaller scales, in qualitative agreement with the spectroscopic cross-correlations (Figure 6.17). From the HOD-populated N-body autocorrelations, we find $b_{\rm sml}/b_{\rm lin} = 1.153$ for red at $z = 1.78$, the most massive and highest-redshift sample (Figure 6.18). To interpolate between the four measured points, we use a function of the form $b_{\rm sml}/b_{\rm lin} = 1 + Az^2$, with $A = 0.05$ for red and $A = 0.025$ for green and blue. The HOD has a milder bias evolution than the data for the green and red samples (Figure 6.19). If we match the $z = 1.9$ clustering with a free number density, we find somewhat larger $b_{\rm sml}/b_{\rm lin}$ at $z = 1.9$, corresponding to $A \sim 0.15$ and 0.2 for green and red, respectively. When estimating the impact of this systematic in Section 6.7 and Figure 6.12, we therefore test both the fiducial value of A, $A_{\rm fid} = 0.025$, 0.025, 0.1 for blue, green and red; and the maximal value of A, $A_{\rm max} = 0.1$, 0.15, 0.2 for blue, green and red.

To assess the compatiblity of the cross-correlation and cross-match dN/dz, we compare the bias evolution of galaxies in the HOD, $b_{\rm HOD}(z)$, to the observed bias evolution of the unWISE galaxies, $b_{\rm sml,p}(z)$, in Figure 6.19. Using Equation 6.18, the COSMOS dN/dz, and s from Appendix 6.C, we fit $b_{\rm sml,p}(z)$ to $w(\theta)$ between 2.5 and $10\,h^{-1}$Mpc. Consistency between the cross-match dN/dz and photometric-spectroscopic clustering (from which the cross-correlation dN/dz is derived) requires a steeply evolving galaxy bias (colored lines in Figure 6.19). In fact, the simple abundance-matched HOD yields a galaxy bias that is

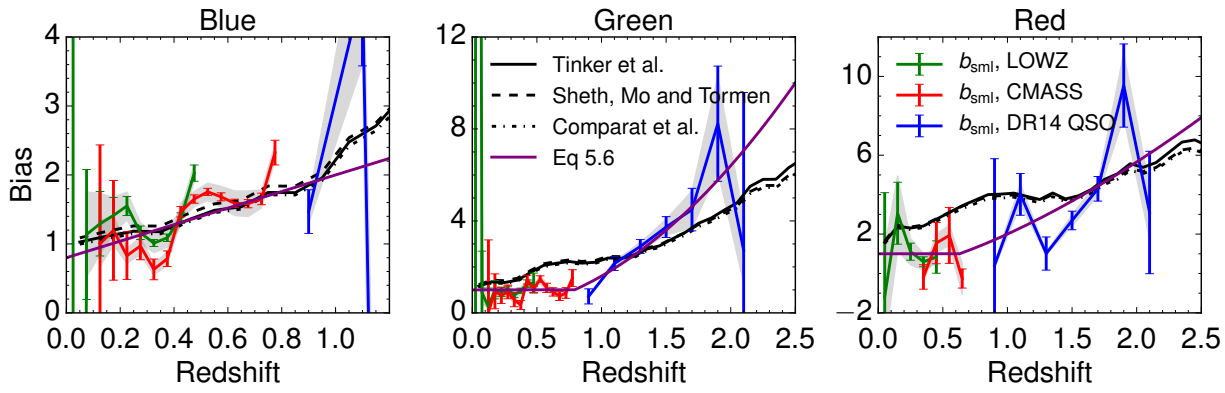

Figure 6.19: Bias, derived from $w(\theta)$ at $2.5 < r < 10\,h^{-1}$Mpc using Equation 6.18 and the COSMOS cross-match redshift distribution. Colored lines give the measured bias; black lines give the bias evolution for an HOD abundance-matched to the density of the WISE samples, with different line styles corresponding to different bias-number density prescriptions from the literature. Errorbars on the colored lines are from measurement errors on $w(\theta)$; the gray bands give the additional uncertainty from uncertain dN/dz, quantified by the 16th-84th percentile range from 100 samples of dN/dz. All fits to clustering include magnification bias using the fiducial values in Table 6.1 and Fig. 6.21.

nearly as steep (Figure 6.19). We compare $b_{\rm sml,p}(z)$ to $b_{\rm HOD}(z)$ using the HOD above and one of three different mass function/mass-bias relationships (Tinker et al., (Tinker et al. 2008, 2010), Sheth, Mo and Tormen (Sheth & Tormen 1999, Sheth et al. 2001), and Comparat et al. (Comparat et al. 2017)). We consider both statistical errors on $b_{\rm sml,p}$ from errors on the cross-correlation (errorbars in Figure 6.19), and errors on $b_{\rm sml,p}$ from the uncertain dN/dz (gray band, giving 16th-84th percentile range from 100 draws from dN/dz). While the uncertainty in dN/dz will also affect the bias evolution of the abundance-matched halos by changing their comoving number density, this effect is smaller than the impact of uncertain dN/dz on $b_{\rm sml,p}(z)$ because the bias is a shallow function of halo mass and thus number density.

For the blue sample, and for the red and green samples at $z > 1$, the measured bias evolution roughly agrees with the HOD prediction within the uncertainty from dN/dz. At $z < 1$, the bias of the red and green samples is significantly lower than the expectation from the HOD. However, both the red and green samples are bimodal, and it is possible that their low-redshift tails are not well-described by the HOD above. For instance, the low-redshift tails could consist of star-forming galaxies occupying halos with a duty cycle well below unity, such that at fixed abundance, the cutoff halo mass is much lower than the HOD above would predict, thus lowering the bias.

The rough agreement between $b_{\rm sml,p}(z)$ and $b_{\rm HOD}(z)$ for the abundance-matched halos shows that the combination of cross-correlation and cross-match redshifts yields a reasonable bias evolution. This result justifies our use of both the cross-correlation and cross-match

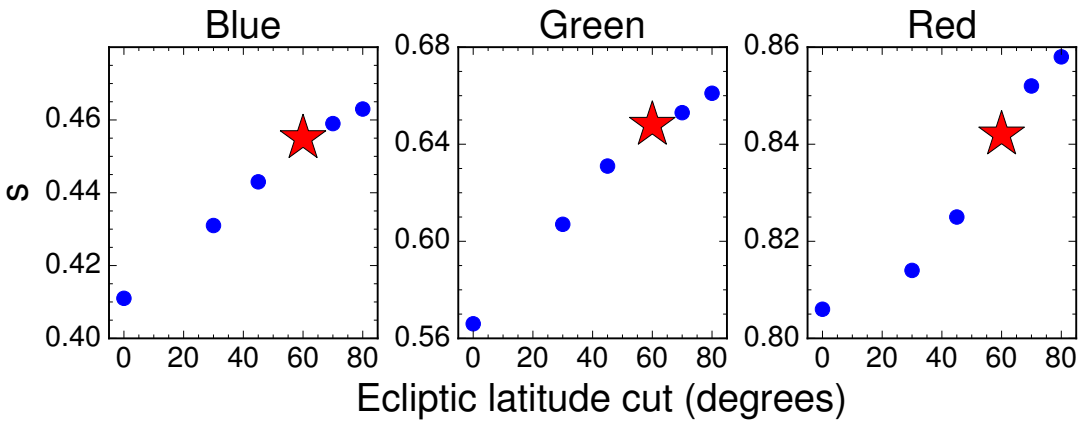

Figure 6.20: Dependence of s for the unWISE samples on ecliptic latitude. Each point shows $s(\lambda_{\rm min})$ measured using galaxies with ecliptic $|\lambda| > \lambda_{\rm min}$. The starred point gives the fiducial value of s, using $\lambda_{\rm min} = 60°$.

redshifts in modelling $C_\ell^{\kappa g}$ and C_ℓ^{gg}, as it suggests they are consistent with each other.

6.C Response of the number density to magnification bias

The amplitude of the magnification bias term depends on the response of the galaxy density to magnification bias, $s \equiv d\log_{10} N/dm$, at the limiting magnitude of the survey. Since the completeness of WISE drops over a relatively large range, measurements of s are affected by incompleteness in WISE. This can be mitigated by restricting the sample to high ecliptic latitude, where the greater depth of coverage results in a fainter limiting magnitude.

Since the WISE galaxies are selected via a magnitude-dependent color cut, one cannot simply histogram them in W2 to determine s. Instead, we compute s by shifting the magnitudes of all WISE objects by 0.02 magnitudes and re-applying our selection criteria.

In Figure 6.20, we show s as a function of $\lambda_{\rm min}$, where we sequentially remove all galaxies with $|\lambda| < \lambda_{\rm min}$. We set the fiducial value of s at $\lambda_{\rm min} = 60°$.

We also require s for each of the spectroscopic samples in order to subtract the magnification bias contribution from $\bar{w}_{\rm sp}$. We measure s by making all galaxies or quasars in the sample fainter by 0.1 magnitudes, applying the relevant selection criteria and measuring the change in number counts.

For LOWZ and CMASS, we use the color cuts described in Reid et al. (2016). This procedure assumes that every galaxy in the spectroscopic sample with perturbed photometry was also in the original sample; this is true for both CMASS and LOWZ (see Figures 3 and 4 in Reid et al. (2016) for color-magnitude plots for LOWZ and CMASS, respectively).

DR12 quasars are selected as point sources with $g < 22$ or $r < 21.85$, $i > 17.8$, and XDQSO "mid-z" quasar probability (i.e. probability the object is a $2.2 < z < 3.5$ quasar)

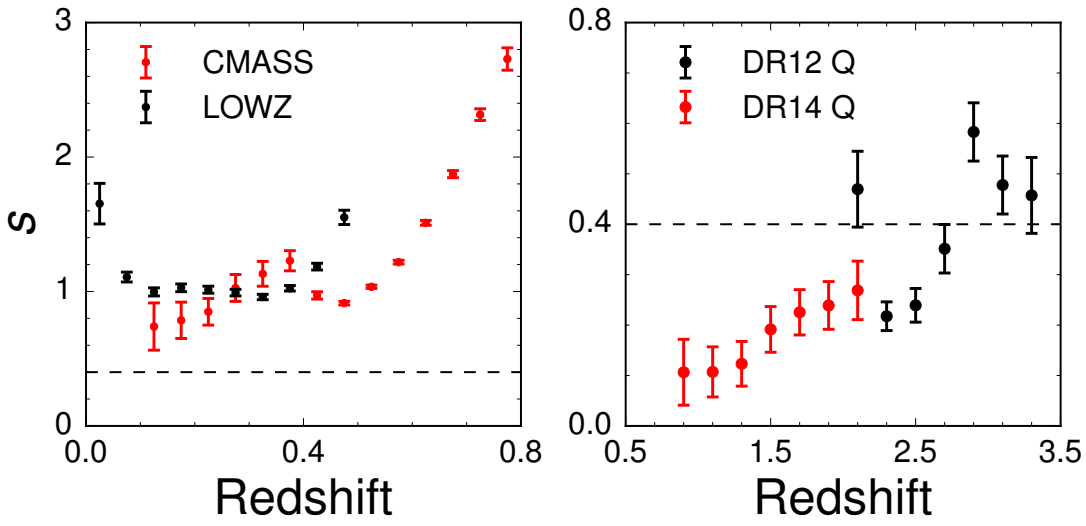

Figure 6.21: Response of galaxy number density to magnification for spectroscopic samples. Error bars are computed as $\Delta s = (\log_{10} N - \log_{10}(N - \sqrt{N}))/\Delta m$. Dashed line indicates $s = 0.4$, where magnification bias makes no contribution to the observed clustering.

> 0.424 (Bovy et al. 2012, Ross et al. 2012b). When we make the quasars fainter by 0.1 magnitudes, we estimate the number of quasars that would be spuriously categorized as extended using the completeness of SDSS star-galaxy separation as a function of r band magnitude(Strauss et al. 2002).[29] Unlike the color cuts used for the BOSS galaxies, with the more complicated XDQSO color cut it is possible that quasars could be excluded from the original targeting but included when the photometry is made fainter by 0.1 magnitudes. To estimate the occurrence of such objects, we use the BOSS BONUS sample of non-uniformly-selected quasars, which are not suitable for quasar clustering analyses but are $\sim 2\times$ as abundant as the CORE sample that we do use. Since BONUS quasars are not selected using XDQSO, they may have mid-z quasar probability < 0.424 but "scatter into" our fainter sample.

For DR14 quasars, we follow a similar procedure as for DR12 quasars, applying the selection criteria of Myers et al. (2015). However, we lack a similarly deep quasar sample (like BONUS in DR12) to determine the number of quasars that scatter into the DR14 selection criteria when the quasar photometry becomes fainter. Based on the number of quasars that scattered into the DR12 quasar selection, we estimate an additional systematic error of $\Delta s \sim 0.1 - 0.2$ for the DR14 quasars.

We plot the resulting s in Figure 6.21, and use them to remove magnification bias from $\bar{w}$. For z beyond the range shown in Figure 6.21, we assume s is a constant function, using the nearest point for which we have a measurement of s.

[29] https://classic.sdss.org/dr7/products/general/stargalsep.html

6.D Galaxy-galaxy cross spectra

In Figure 6.22 we show the cross-spectra between the different galaxy samples. We use the fiducial cross-correlation dN/dz and $b^{\rm eff}_{\rm cross}$ for the theory calculation. Additionally, we fit a shot-noise term, and find good agreement between the expectation and the data once the uncertainty on dN/dz is taken into account. For red cross blue the shot noise term is negligible, but for blue cross green and blue cross red, we find shot noise values of 6.22×10^{-9} and 4.67×10^{-8}, respectively. Shot noise can arise in a cross-correlation if some of the objects in the two samples occupy the same halo, with density $\bar{n}_{\rm common}$. The cross shot-noise is then given by

$$\text{Shot Noise} = \frac{\bar{n}_{\rm common}}{\bar{n}_1\bar{n}_2} \tag{6.40}$$

Using the fitted shot noise for each sample from Table 6.4, we find $\bar{n}_{\rm common} = 130$ deg^{-2} for blue cross green and 41 deg^{-2} for green cross red. This implies that 3.8% (7.0%) of the blue (green) sample lives in the same halo as a green (blue) object, and 2.2% (28.5%) of the green (red) sample lives in the same halo as a red (green) object.

We create a simple "joint HOD" to understand the cross shot-noise. Rather than assume that every halo well above $M_{\rm cut}$ hosts a central galaxy, we instead assume that some halos host red centrals and other halos host green centrals; i.e. we multiply $N_{\rm cen}$ by $f_{\rm green}$ or $f_{\rm red}$ where $f_{\rm green} + f_{\rm red} = 1$, and do not modify $N_{\rm sat}$. We then ask what fraction of red galaxies host a green satellite. If $f_{\rm green} = f_{\rm red} = 0.5$, we find that 26.3% of red galaxies host at least one green satellite. The common fraction remains similar at 15-25% if we change some aspects of this toy model (i.e. increase $f_{\rm green}$ to 0.9; add a linear ramp where halos transition from hosting green galaxies at low redshift to red galaxies at high redshift; or multiply $N_{\rm sat}$ by 0.5 for both green and red to preserve the total number of satellites).

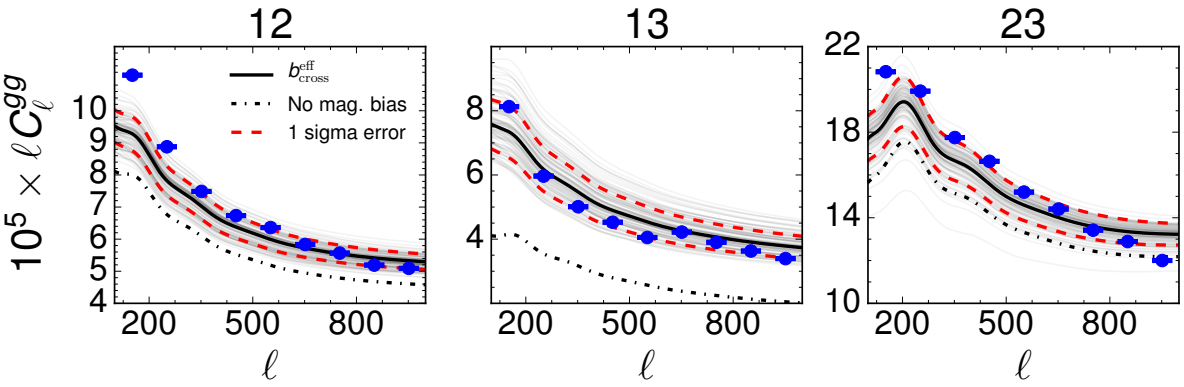

Figure 6.22: Galaxy-galaxy cross-spectra between the different samples. The solid black line gives the predicted theory curve using $b_{\rm cross}^{\rm eff}$, and the dot-dashed black line gives the predicted theory curve with no magnification bias included. Gray lines show C_ℓ^{gg} from 100 realizations of dN/dz (with bias modified from the best-fit $b_{\rm cross}^{\rm eff}$ in Table 6.4 to fit $C_\ell^{\kappa g}$ for a given dN/dz); and dashed red lines show 1 σ uncertainty in C_ℓ^{gg}, with contributions both from uncertain dN/dz and from statistical errors on $b_{\rm cross}^{\rm eff}$. Uncertainty on C_ℓ^{gg} for dN/dz from the two halves of the sky is comparable to the 1 σ uncertainty. In all cases, a cross shot-noise term is fit to the data and also included in the theory curves.

Chapter 7

The Integrated Sachs Wolfe Effect with Planck and unWISE galaxies

Abstract

On large scales, galaxies are correlated with CMB temperature due to the integrated Sachs-Wolfe effect. We present a detection of the galaxy-ISW cross-correlation in three bins at $z \sim 0.6$, 1.1 and 1.5, with signal-to-noise 1.5, 3.4, and 3.4. We show that this measurement is robust to methodological choices and systematics. This provides a direct measurement of dark energy throughout the epoch when dark energy makes a substantial contribution to the energy density of the universe.

7.1 Introduction

On super-horizon scales ($\ell < 200$) the cosmic microwave background (CMB) power spectrum is dominated by the Sachs-Wolfe effect (Sachs & Wolfe 1967, Rees & Sciama 1968). On these scales, fluctuations in the gravitational potential generate fluctuations in the CMB as photons are redshifted and blueshifted from exiting the potentials. For adiabatic fluctuations in a matter-dominated universe, the temperature fluctuations for the Sachs-Wolfe effect are

$$\frac{\Delta T}{T} = -\frac{1}{3}\Phi \tag{7.1}$$

where the factor of $-1/3$ comes both from gravitational redshifting as photons exit the potential (contributing $-\Phi$) and clocks running slow within the gravitational potential (contributing $2\Phi/3$) (Sachs & Wolfe 1967, White & Hu 1997). Since the dimensionless angular power spectrum of potential fluctuations is flat, this creates a characteristic "Sachs-Wolfe plateau" at low ℓ in the primary CMB.

The Integrated Sachs-Wolfe effect is an additional effect from gravitational redshifting as photons propagate across the universe. In matter domination, gravitational potentials

are constant in time, so photons redshift in and out of potentials with no effect. However, potentials decay during dark energy domination, and this leads to a net blueshift of photons as the potentials decay while they move through them. This effect is very small and is only detectable in cross-correlation with large-scale structure; in the CMB temperature auto-spectrum, it is much smaller than the noise from the Sachs-Wolfe effect in the primary CMB.

The integrated Sachs-Wolfe effect is powerful as a direct measurement of dark energy, which has been detected from its impact on the distance-redshift relation, matter clustering, and the primary CMB (Riess et al. 1998, Perlmutter et al. 1999, Riess et al. 2004). As a result, measurements of the ISW effect can test dark energy (Crittenden & Turok 1996) and probe extensions to ΛCDM such as modified gravity (Hu 2002, Renk et al. 2017) or spatial curvature (Kamionkowski 1996).

Since the first detection of the ISW cross-correlation by Boughn & Crittenden (2004), there have been many ISW detections with a variety of galaxy samples and CMB data from WMAP (Scranton et al. 2003, Fosalba et al. 2003, Nolta et al. 2004, Corasaniti et al. 2005, Padmanabhan et al. 2005, Vielva et al. 2006, Giannantonio et al. 2006, Cabré et al. 2006, Rassat et al. 2007, McEwen et al. 2007, Giannantonio et al. 2012, Goto et al. 2012, Hernández-Monteagudo et al. 2014, Ferraro et al. 2015, Moura-Santos et al. 2016, Shajib & Wright 2016) or Planck (Planck Collaboration et al. 2014a, 2016e, Stölzner et al. 2018, Ansarinejad et al. 2020). The highest significance detections range from 4 to 5σ (Giannantonio et al. 2008, Planck Collaboration et al. 2016e, Stölzner et al. 2018). These measurements have been used to constrain cosmological parameters and dark energy, including the curvature of the universe and the dark energy equation of state (Nolta et al. 2004, Pietrobon et al. 2006, McEwen et al. 2007, Vielva et al. 2006, Giannantonio et al. 2008, Ho et al. 2008, Xia et al. 2009, Zhao et al. 2010, Li & Xia 2010).

The unWISE catalog (Schlafly et al. 2019) is ideal for an ISW cross-correlation measurement. It contains $\sim$ 500 million galaxies across the entire sky out to $z \sim 2$, covering the entire dark-enegy dominated epoch. The sky and redshift coverage are ideal for overlap with the ISW kernel. Additionally, we split the sample into three redshift bins using the unWISE galaxies' infrared colors, allowing us to probe the ISW tomographically.

The outline of the paper is as follows. We review the integrated Sachs Wolfe effect in Sec. 7.2, describe the galaxy samples and CMB data in Sec. 7.3, and present the measurement in Sec. 7.4. We report a 3-4σ detection of the ISW effect in cross-correlation between Planck and unWISE. Finally in Sec. 7.6 we summarize our results and directions for future research. Where necessary we assume a fiducial ΛCDM cosmology with the Planck 2018 maximum likelihood parameters (the final column in Table 2 in Planck Collaboration et al. (2018e)). We quote magnitudes in the Vega system, noting that we can easily convert these to AB magnitudes with AB = Vega + 2.699, 3.339 in W1, W2, respectively.

7.2 Theory

The integrated Sachs-Wolfe effect comes from the blueshifting of CMB photons due to a changing gravitational potential

$$\left(\frac{\Delta T}{T}\right)_{\rm ISW} = -2\int d\chi \dot{\Phi} \tag{7.2}$$

where the factor of 2 comes from the fact that both the spatial and time components of the perturbed potential contribute to the ISW effect. In the linear regime, $\dot{\Phi}$ is only nonzero in dark energy domination.

Since the ISW is the only physical correlation between foreground galaxies and CMB temperature at low ℓ, the cross-power spectrum C_ℓ^{Tg} is given by

$$C_\ell^{Tg} = C_\ell^{\dot{\Phi}g} = \frac{2}{\pi}\int k^2\, dk\, P(k) K_\ell^{\dot{\Phi}}(k)\, K_\ell^g(k) \tag{7.3}$$

The kernel functions $K_\ell^{\dot{\Phi}}(k)$ and $K_\ell^g(k)$ are

$$K_\ell^g(k) = \int dz\, b(z) \frac{dN}{dz} D(z)\, j_\ell[k\chi(z)] \tag{7.4}$$

$$K_\ell^{\dot{\Phi}}(k) = \frac{3\Omega_m H_0^2}{k^2}\int dz\, \frac{d}{dz}\left[(1+z)D(z)\right]\, j_\ell[k\chi(z)] \tag{7.5}$$

where dN/dz is the galaxy redshift distribution, $b(z)$ is the bias evolution, $D(z)$ is the linear growth factor, and j_ℓ are spherical Bessel functions. We also consider the cross-correlation between the ISW and cosmic magnification, $C_\ell^{\dot{\Phi}\mu}$

$$C_\ell^{T\mu} = C_\ell^{\dot{\Phi}\mu} = \frac{2}{\pi}\int k^2\, dk\, P(k) K_\ell^{\dot{\Phi}}(k)\, K_\ell^\mu(k) \tag{7.6}$$

with kernel $K_\ell^\mu(k)$

$$K_\ell^\mu(k) = (5s-2)\,\frac{3}{2}\Omega_m H_0^2 \int dz\, (1+z) g_i(\chi(z)) D(z) j_\ell[k\chi(z)] \tag{7.7}$$

where s is the response of the number density to magnification, and

$$g_i(\chi) = \int_\chi^{\chi_\star} d\chi'\, \frac{\chi(\chi'-\chi)}{\chi'}\, H(z')\, \frac{dN_i}{dz'} \tag{7.8}$$

Note that these are only valid in the linear regime where the power spectrum $P(k,z)$ can be split into $P(k)$ and $D(z)$. In our full fits, we replace the linear $P(k)$ with the nonlinear $P(k)$ from HALOFIT (Mead et al. 2015), although we find this makes very little difference on the large scales we consider.

Label	$\mathrm{W1}-\mathrm{W2} > x$	$\mathrm{W1}-\mathrm{W2} < x$	$\mathrm{W2} < x$	$\bar{z}$	δz	$\bar{n}$	b	s
Blue		$(17-\mathrm{W2})/4+0.3$	16.7	0.6	0.3	3409	1.56	0.455
Green	$(17-\mathrm{W2})/4+0.3$	$(17-\mathrm{W2})/4+0.8$	16.7	1.1	0.4	1846	2.23	0.648
Red	$(17-\mathrm{W2})/4+0.8$		16.2	1.5	0.4	144	3.29	0.842

Table 7.1: Color and magnitude cuts for selecting galaxies of different redshifts, together with the mean redshift, $\bar{z}$, and the width of the redshift distribution, δz (as measured by matching to objects with photometric redshifts on the COSMOS field Laigle et al. (2016)), number density per deg^2 within the unWISE mask, $\bar{n}$, mean bias b, and response of the number density to magnification, $s \equiv d\log_{10} N/dm$. Galaxies are additionally required to have W2 > 15.5, to be undetected or not pointlike in Gaia (see §6.2.3), and to not be flagged as diffraction spikes, latents or ghosts. See Krolewski et al. (2019) for further details.

7.3 Data

7.3.1 unWISE galaxy samples

As in Krolewski et al. (2019) and Schlafly et al. (2019), we form three galaxy samples using the WISE W1 and W2 magnitudes; these are the same samples described in Krolewski et al. (2019), and we refer the reader to that paper for a more comprehensive discussion of the samples. Table 7.1 gives the adopted color selection for the three samples considered in this work, which we term the blue, green, and red samples Schlafly et al. (2019). Table 6.1 also summarizes important properties of each sample including the redshift distribution, the number density, galaxy bias, and response of number density to galaxy magnification $s \equiv d\log_{10} N/dm$. We measure s using galaxies with ecliptic latitude $|\lambda| > 60°$, where the WISE depth of coverage is greater and thus the measurement of s is less affected by incompleteness Krolewski et al. (see discussion in Appendix D in 2019).

We require that the blue and green samples have $15.5 < \mathrm{W2} < 16.7$, and the red sample has $15.5 < \mathrm{W2} < 16.2$; in Krolewski et al. (2019) we find that deeper red samples are potentially affected by systematics.

We remove potentially spurious sources (diffraction spikes, latents, ghosts) and Each of the samples is required to be either undetected or not pointlike in Gaia. Here a source is taken as "pointlike" if

$$\mathrm{pointlike}(G, A) = \begin{cases} \log_{10} A < 0.5 & \text{if } G < 19.25 \\ \log_{10} A < 0.5 + \frac{5}{16}(G - 19.25) & \text{otherwise}\,, \end{cases} \tag{7.9}$$

where G is the Gaia G band magnitude and A is `astrometric_excess_noise` from Gaia DR2 Gaia Collaboration et al. (2018). A source is considered "undetected" in Gaia if there is no Gaia DR2 source within 2.75″ of the location of the WISE source. High `astrometric_excess_noise` indicates that the Gaia astrometry of a source was more uncertain than typical for resolved sources; this cut essentially takes advantage of the 0.1″ angular

resolution of Gaia to morphologically separate point sources from galaxies. From COSMOS, we estimate that this reduces the stellar contamination in our samples to $< 1\%$.

We base the unWISE mask on the 2018 Planck lensing mask (Planck Collaboration et al. 2018f). We additionally mask a small portion of the sky at $|b| < 10°$, and mask bright infrared stars, diffraction spikes, nearby galaxies, planetary nebulae, and low latitude pixels with a substantial number of fainter stars which will reduce the effective area in a pixel by masking galaxies within 2.75" of each star. The full details of the mask construction are in section 2.3 of Krolewski et al. (2019); this mask yields $f_{\rm sky} = 0.586$.

7.3.2 Planck CMB data

We use the SMICA CMB temperature map as our fiducial temperature map in the ISW analysis.[1] We use the common confidence mask (combined confidence mask for the different temperature pipelines) as described in Section 4.2 of Planck Collaboration et al. (2018d). SMICA produces a temperature map from a linear combination of the Planck input channels (30 to 857 GHz) with multipole-dependent weights, up to $\ell \sim 4000$. We also test the COMMANDER, NILC, SEVEM, and SMICA-noSZ maps, to test the robustness of our result. Additionally, SEVEM provides single-frequency cleaned CMB maps at 70, 100, 143 and 217 GHz, and we check these maps as well (Planck Collaboration et al. 2018d). To measure the covariance of the signal, we use 300 noise-plus-systematics simulations released as part of the Planck 2018 data release (Planck Collaboration et al. 2018b,c,d), which were processed through each of the map-making pipelines.

7.4 Measurements

7.4.1 Methods

In order to estimate the binned cross and auto power spectra, we use a pseudo-C_ℓ estimator (Hivon et al. 2002) based on the harmonic coefficients of the galaxy and lensing fields. We follow the same procedure as in Krolewski et al. (2019). The measured pseudo-C_ℓ on the cut sky are calculated as

$$\tilde{C}_\ell^{XY} = \frac{1}{2\ell+1} \sum_m X_{\ell m} Y^\star_{\ell m} \tag{7.10}$$

where $X, Y \in \{g_1, g_2, g_3, \kappa\}$ are the observed fields on the cut sky. Because of the mask, these differ from the true C_ℓ that are calculated from theory, but their expectation value is related through a mode-coupling matrix, $M_{\ell\ell'}$, such that

$$\langle \tilde{C}_\ell \rangle = \sum_{\ell'} M_{\ell\ell'} C_{\ell'} \tag{7.11}$$

[1] Obtained from the Planck Legacy Archive, http:/pla.esac.esa.int

The matrix $M_{\ell\ell'}$ is purely geometric and can be computed from the power spectrum of the mask itself. While Eq. (7.11) is not directly invertible for all ℓ, the MASTER algorithm (Hivon et al. 2002) provides an efficient method to do so assuming that the power spectrum is piecewise constant in a number of discrete bins, b. Defining a "binned" mode-coupling matrix, $\mathcal{M}_{bb'}$ (Alonso et al. 2018), we can recover unbiased binned bandpowers

$$C_b = \sum_{b'} \mathcal{M}^{-1}_{bb'} \tilde{C}_{b'} \quad . \tag{7.12}$$

We use the implementation in the code `NaMaster`[2] (Alonso et al. 2018).

We mask the galaxy map with the unWISE mask including bright stars and galaxies, and the CMB map with the "common" mask for CMB temperature, apodized with a Gaussian smoothing kernel with FWHM 1 degree. We also correct the unWISE density map by an "area lost" mask to account for the reduction in available area in each pixel due to Gaia stars (since we mask any source within 2.75" of a star). We test our pipeline on Gaussian simulations to ensure that we recover the correct power spectrum. From a test on 100 Gaussian realizations, we find that the power spectrum must be corrected by the "mask deconvolution transfer function," which deviates from unity by a few percent. We apply this transfer function to the data.

Since the azimuthal modes of the map are most affected by Galactic latitude-dependent foregrounds, we remove the $m = 0$ mode from the sum in Eq. 7.10. This makes a very modest ($< 0.2\sigma$) impact on our results, and we validate this procedure by calculating the mask deconvolution transfer function for Gaussian mocks.

We use the 300 Planck simulations to determine the covariance of the ISW power spectra. We apply our pipeline to measure the cross-correlation between each simulation and the unWISE maps, and then measure the covariance of these 300 power spectra. We find that the error bars from the Planck mocks are generally quite similar to the Gaussian error bars, except in the lowest ℓ bin where the Gaussian approximation underestimates the true error by $\sim 30\%$. As a further check, we find that the error bars from the Planck mocks are generally similar to the scatter of the individual C_ℓ within each bin.

7.4.2 Linear bias and redshift distribution of unWISE galaxies

Theory predictions for the ISW cross-correlation require both the redshift distribution of the galaxy sample, dN/dz, and its bias evolution $b(z)$ (Section 7.2). Following Krolewski et al. (2019), we combine these quantities and report both the normalized bias-weighted redshift distribution,

$$f(z)\frac{dN}{dz} \equiv \frac{b_{\rm sml,p}(z)\frac{dN}{dz}}{\int dz\, b_{\rm sml,p}(z)\frac{dN}{dz}} \tag{7.13}$$

as measured from cross-correlations with spectroscopic galaxies and quasars, and the redshift distribution dN/dz as measured by matching unWISE sources to deep optical imaging with

[2] https://github.com/LSSTDESC/NaMaster

multiband photometric redshifts (Laigle et al. 2016) in the COSMOS field. We then fit for the average bias (scaling $f(z)dN/dz$) using the galaxy-CMB lensing cross-spectrum.

However, the cross-correlation redshifts are measured on fairly small scales (2.5 to 10 h^{-1} Mpc in configuration space) so the bias will not be identical to the linear bias on large scales appropriate for ISW. It is therefore possible that the quasi-linear bias that we measure in the cross-correlation redshifts evolves differently with redshift as the linear bias. We construct simple HODs for the WISE sample (Appendix B in Krolewski et al. 2019), and we can gain some understanding into the nonlinear bias evolution of the WISE sample using N-body sims populated with these HODs. We find that the systematic shift and error from nonlinear bias evolution is smaller than the uncertainty from the measurement error in dN/dz. We optionally apply the "nonlinear bias correction," derived from the HODs, as a correction to $f(z)\frac{dN}{dz}$ and find that it does not have a significant effect on the results.

Despite its limitations, we believe this approach is preferable to simply using the dN/dz from COSMOS. Solely using the COSMOS dN/dz would require a parameterized form for the bias evolution $b(z)$; however, there is no physical reason to expect the bias evolution to follow such a parameterized form. Moreover, this approach is sensitive to systematic errors in dN/dz, such as blending or variations in the unWISE samples on the sky.

Using the measured cross-correlation $f(z)dN/dz$, I fit for an "effective bias" $b^{\rm eff}$ from the lensing cross-correlations:

$$b^{\rm eff} = \int dz\, b_{\rm sml,p}(z)\frac{dN}{dz} \tag{7.14}$$

We measure the bias from $C_\ell^{\kappa g}$ at $100 < \ell < 1000$, using HALOFIT (Mead et al. 2015) for the small-scale nonlinear power.

In Table 7.2, I give the best-fit $b^{\rm eff}$ for each sample. The first set of errorbars are statistical error and the second set are error from uncertain dN/dz (computed as the standard deviation of the best-fit bias from the 100 sampled dN/dz as in Krolewski et al. (2019)). I also give $b^{\rm eff}$ using the nonlinear bias correction from the HOD in $f(z)dN/dz$.

Sample	Linear $b^{\rm eff}$	Linear $b^{\rm eff}$ with nonlinear bias correction
Blue	$1.56 \pm 0.0276 \pm 0.0355$	1.54
Green	$2.23 \pm 0.0352 \pm 0.0308$	2.17
Red	$3.29 \pm 0.09 \pm 0.1541$	3.10

Table 7.2: Linear bias from fit to $C_\ell^{\kappa g}$ for three samples (see Krolewski et al. 2019; for data and methods); these reproduce Table 4 in that paper. The error bars are statistical (first set) and systematic from uncertain dN/dz (second set), and the second column gives $b^{\rm eff}$ using the nonlinear bias correction from the HOD.

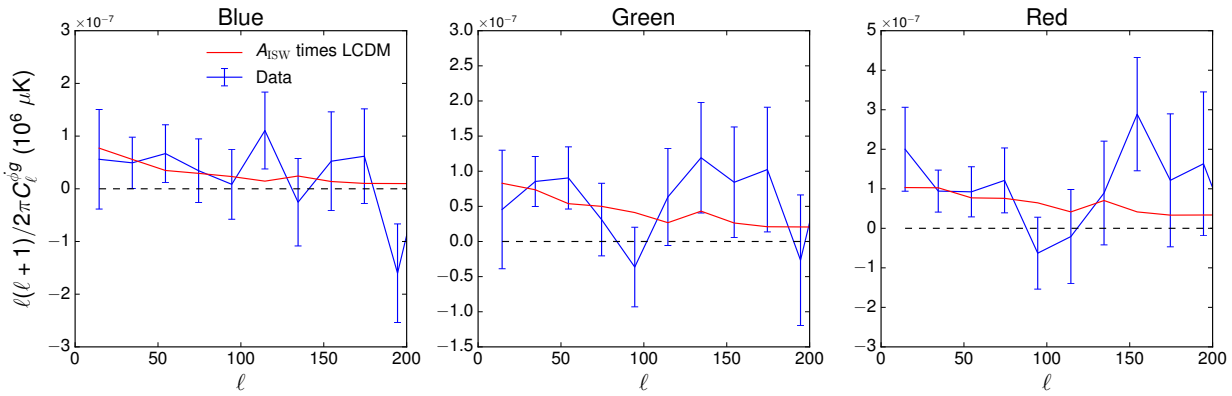

Figure 7.1: ISW data (blue) and prediction from ΛCDM, scaled by $A_{\rm ISW}$ (red) for the three unWISE samples. Error bars are estimated from 300 Planck temperature mocks cross-correlated with the unWISE samples.

7.5 ISW measurement

In Fig. 7.1, we show the measured ISW cross-correlation and the ΛCDM theory curve in the fiducial cosmology, multiplied by a scaling factor $A_{\rm ISW}$. The theory curve includes both the $\dot\Phi$ galaxy correlation and the $\dot\Phi$ magnification correlation. Following previous work, we measure the ISW signal at $5 < \ell < 105$, with $\Delta\ell = 20$ bins. We find $A_{\rm ISW} = 0.73 \pm 0.44$ for blue (1.5σ), 1.18 ± 0.41 for green (3.4σ), and 1.56 ± 0.53 for red (3.4σ), for a combined significance between 3 and 4 σ. To work with data that is roughly constant, we fit $A_{\rm ISW}$ to $\ell(\ell+1)C_\ell$ rather than C_ℓ.

We test the impact of changing $\ell_{\rm min}$ on our results. We find that using $\ell_{\rm min} = 2$ rather than $\ell_{\rm min} = 5$ leads to a large spike in the lowest ℓ bin, presumably due to correlations between CMB foregrounds and systematics in the unWISE map. As a result, we restrict the measurement to $\ell \geq 5$.

In Table 7.3, we perform a variety of systematics checks. We replace the default SMICA map with several other CMB temperature methods (Planck Collaboration et al. 2018d); also test a map with the thermal Sunyaev-Zel'dovich effect explicitly nulled (to remove this

Temperature map	Blue $A_{\rm ISW}$	Green $A_{\rm ISW}$	Red $A_{\rm ISW}$
Smica	0.73 ± 0.44	1.18 ± 0.41	1.56 ± 0.53
Commander	0.71 ± 0.44	1.18 ± 0.41	1.57 ± 0.53
Sevem	0.76 ± 0.44	1.22 ± 0.41	1.62 ± 0.53
Nilc	0.72 ± 0.44	1.21 ± 0.41	1.60 ± 0.53
NoSZ	0.86 ± 0.44	1.28 ± 0.41	1.64 ± 0.53
Sevem 70 GHz	0.61 ± 0.44	1.11 ± 0.41	1.54 ± 0.53
Sevem 100 GHz	0.77 ± 0.44	1.23 ± 0.41	1.64 ± 0.53
Sevem 143 GHz	0.75 ± 0.44	1.21 ± 0.41	1.61 ± 0.53
Sevem 217 GHz	0.95 ± 0.44	1.30 ± 0.41	1.66 ± 0.53
Smica, $\ell_{\rm min} = 15$	0.80 ± 0.49	1.24 ± 0.42	1.45 ± 0.55
Smica, $\ell_{\rm min} = 25$	0.79 ± 0.51	1.25 ± 0.44	1.37 ± 0.57

Table 7.3: $A_{\rm ISW}$ for the three unWISE samples for a variety of different systematics tests: changing the method used to construct the CMB temperature maps; using a map with the thermal Sunyaev-Zel'dovich effect nulled (to remove contributions from tSZ as a contaminant); single-frequency foreground subtracted maps (with residual contributions from foregrounds varying with frequency); and changing $\ell_{\rm min}$ for the default Smica map.

as a foreground); and test single-frequency foreground-subtracted maps using the SEVEM method (which again have different residual sensitivity to foregrounds). We do not find that using any of these maps lead to a significant shift in $A_{\rm ISW}$. Finally, we also try changing $\ell_{\rm min}$, to 15 or 25, and find that this also makes no significant difference to the results. Finally, we test the impact of uncertain dN/dz and errors in the bias from Table 7.2, and find that these generally have $\leq 5\%$ impact on $A_{\rm ISW}$, considerably smaller than the $\sim 30\%$ statistical errors on $A_{\rm ISW}$.

7.6 Conclusions

We measure ISW cross-correlations between Planck lensing and unWISE infrared galaxies at $z \sim 0.6$, 1.1, and 1.5. We detect the cross-correlation at 1.5 (3.4, 3.4) σ for $z \sim 0.6$ (1.1, 1.5), for a combined significance between 3 and 4 σ. This yields a direct tomographic measurement of dark energy and will enable interesting constraints on modifications to gravity.

Bibliography

Acker, A., Cuisinier, F., Stenholm, B., & Terzan, A. 1992, A&A, 264, 217
Adelberger, K. L., Shapley, A. E., Steidel, C. C., et al. 2005, ApJ, 629, 636
Affleck, I., & Dine, M. 1985, Nuclear Physics B, 2, 361
Aihara, H., Armstrong, R., Bickerton, S., et al. 2018, PASJ, 70, S8
Aird, J., Coil, A. L., Moustakas, J., et al. 2012, ApJ, 746, 90
Alam, S., Albareti, F. D., Allende Prieto, C., et al. 2015, ApJS, 219, 12
Alam, S., Ata, M., Bailey, S., et al. 2017, MNRAS, 470, 2617
Alcock, C., & Paczynski, B. 1979, Nature, 281, 358
Alexander, D. M., & Hickox, R. C. 2012, New A Rev., 56, 93
Allison, R., Caucal, P., Calabrese, E., Dunkley, J., & Louis, T. 2015a, PRD, 92, 123535
Allison, R., Lindsay, S. N., Sherwin, B. D., et al. 2015b, MNRAS, 451, 849
Almgren, A. S., Bell, J. B., Lijewski, M. J., Lukić, Z., & Van Andel, E. 2013, ApJ, 765, 39
Alonso, D., Sanchez, J., & Slosar, A. 2018, ArXiv e-prints, arXiv:1809.09603
Alpaslan, M., Driver, S., Robotham, A. S. G., et al. 2015, MNRAS, 451, 3249
Altay, G., Colberg, J. M., & Croft, R. A. C. 2006, MNRAS, 370, 1422
Andrae, R., & Jahnke, K. 2011, MNRAS, 418, 2014
Ansarinejad, B., Mackenzie, R., Shanks, T., & Metcalfe, N. 2020, MNRAS, 493, 4830
Aragón-Calvo, M. A., Jones, B. J. T., van de Weygaert, R., & van der Hulst, J. M. 2007, A&A, 474, 315
Aragón-Calvo, M. A., van de Weygaert, R., Jones, B. J. T., & van der Hulst, J. M. 2007, ApJl, 655, L5
Aragon-Calvo, M. A., & Yang, L. F. 2014, MNRAS, 440, L46
Arnaud, M., Pratt, G. W., Piffaretti, R., et al. 2010, A&A, 517, A92
Aryal, B., & Saurer, W. 2004, A&A, 425, 871
Ata, M., Baumgarten, F., Bautista, J., et al. 2018, MNRAS, 473, 4773
Bailin, J., & Steinmetz, M. 2005, ApJ, 627, 647
Baker, T., Ferreira, P. G., & Skordis, C. 2013, PRD, 87, 024015
Banerjee, A., & Dalal, N. 2016, JCAP, 11, 015
Bardeen, J. M., Bond, J. R., Kaiser, N., & Szalay, A. S. 1986, ApJ, 304, 15
Barnes, D. J., Kay, S. T., Henson, M. A., et al. 2017, MNRAS, 465, 213
Barreira, A., Cautun, M., Li, B., Baugh, C. M., & Pascoli, S. 2015, JCAP, 8, 028
Bates, D. J., Tojeiro, R., Newman, J. A., et al. 2019, MNRAS, 486, 3059

Battaglia, N., Bond, J. R., Pfrommer, C., & Sievers, J. L. 2012a, ApJ, 758, 74
—. 2012b, ApJ, 758, 75
—. 2013, ApJ, 777, 123
Battaglia, N., Ferraro, S., Schaan, E., & Spergel, D. N. 2017, JCAP, 11, 040
Battaglia, N., Hill, J. C., & Murray, N. 2015, ApJ, 812, 154
Baxter, E., Clampitt, J., Giannantonio, T., et al. 2016, MNRAS, 461, 4099
Behroozi, P., Wechsler, R., Hearin, A., & Conroy, C. 2018, ArXiv e-prints, arXiv:1806.07893
Behroozi, P. S., Wechsler, R. H., & Wu, H.-Y. 2013, ApJ, 762, 109
Bennett, C. L., Halpern, M., Hinshaw, G., et al. 2003, ApJS, 148, 1
Bentz, M. C., & Manne-Nicholas, E. 2018, ArXiv e-prints, arXiv:1808.01329
Bett, P. 2012, MNRAS, 420, 3303
Beygu, B., Kreckel, K., van der Hulst, J. M., et al. 2016, MNRAS, 458, 394
Beygu, B., Peletier, R. F., van der Hulst, J. M., et al. 2017, MNRAS, 464, 666
Bianchini, F., Bielewicz, P., Lapi, A., et al. 2015, ApJ, 802, 64
Bianchini, F., Wu, W. L. K., Ade, P. A. R., et al. 2020, ApJ, 888, 119
Blanton, M. R., Kazin, E., Muna, D., Weaver, B. A., & Price-Whelan, A. 2011, AJ, 142, 31
Blanton, M. R., & Roweis, S. 2007, AJ, 133, 734
Blanton, M. R., Brinkmann, J., Csabai, I., et al. 2003, AJ, 125, 2348
Blanton, M. R., Schlegel, D. J., Strauss, M. A., et al. 2005, AJ, 129, 2562
Blanton, M. R., Bershady, M. A., Abolfathi, B., et al. 2017, AJ, 154, 28
Blas, D., Lesgourgues, J., & Tram, T. 2011, Journal of Cosmology and Astro-Particle Physics, 2011, 034
Bleem, L. E., et al. 2012, Astrophys. J., 753, L9
Blumenthal, G. R., Faber, S. M., Flores, R., & Primack, J. R. 1986, ApJ, 301, 27
Blumenthal, G. R., Faber, S. M., Primack, J. R., & Rees, M. J. 1984, Nature, 311, 517
Böhringer, H., Dolag, K., & Chon, G. 2012, A&A, 539, A120
Bolton, J. S., Puchwein, E., Sijacki, D., et al. 2016, ArXiv e-prints
Bolton, J. S., Viel, M., Kim, T.-S., Haehnelt, M. G., & Carswell, R. F. 2008, MNRAS, 386, 1131
Bond, J. R., Kofman, L., & Pogosyan, D. 1996, Nature, 380, 603
Bongiorno, A., Merloni, A., Brusa, M., et al. 2012, MNRAS, 427, 3103
Booth, C. M., & Schaye, J. 2010, MNRAS, 405, L1
Bos, E. G. P., van de Weygaert, R., Dolag, K., & Pettorino, V. 2012, MNRAS, 426, 440
Boughn, S., & Crittenden, R. 2004, Nature, 427, 45
Bovy, J., Hennawi, J. F., Hogg, D. W., et al. 2011, ApJ, 729, 141
Bovy, J., Myers, A. D., Hennawi, J. F., et al. 2012, ApJ, 749, 41
Bridle, S., & King, L. 2007, New Journal of Physics, 9, 444
Brown, M. J. I., Zheng, Z., White, M., et al. 2008, ApJ, 682, 937
Brunino, R., Trujillo, I., Pearce, F. R., & Thomas, P. A. 2007, MNRAS, 375, 184
Bryant, J. J., Bland-Hawthorn, J., Lawrence, J., et al. 2016, in Proc. SPIE, Vol. 9908, Ground-based and Airborne Instrumentation for Astronomy VI, 99081F
Bullock, J. S., Dekel, A., Kolatt, T. S., et al. 2001, ApJ, 555, 240

Bundy, K., Bershady, M. A., Law, D. R., et al. 2015, ApJ, 798, 7
Burkert, A. 2009, in Astronomical Society of the Pacific Conference Series, Vol. 419, Galaxy Evolution: Emerging Insights and Future Challenges, ed. S. Jogee, I. Marinova, L. Hao, & G. A. Blanc, 3
Cabanela, J. E., & Aldering, G. 1998, AJ, 116, 1094
Cabré, A., Gaztañaga, E., Manera, M., Fosalba, P., & Castander, F. 2006, MNRAS, 372, L23
Cai, Y.-C., Neyrinck, M., Mao, Q., et al. 2017, MNRAS, 466, 3364
Cai, Y.-C., Padilla, N., & Li, B. 2015, MNRAS, 451, 1036
Cai, Y.-C., Taylor, A., Peacock, J. A., & Padilla, N. 2016a, MNRAS, 462, 2465
Cai, Z., Fan, X., Bian, F., et al. 2016b, ArXiv e-prints, arXiv:1609.02913
Cantalupo, S., Arrigoni-Battaia, F., Prochaska, J. X., Hennawi, J. F., & Madau, P. 2014, Nature, 506, 63
Cantalupo, S., Lilly, S. J., & Haehnelt, M. G. 2012, MNRAS, 425, 1992
Cappellari, M., & Emsellem, E. 2004, Publ. Astron. Soc. Pac. , 116, 138
Carlstrom, J. E., Holder, G. P., & Reese, E. D. 2002, Ann. Rev. Astron.& Astrophys. , 40, 643
Castorina, E., Carbone, C., Bel, J., Sefusatti, E., & Dolag, K. 2015, Journal of Cosmology and Astro-Particle Physics, 2015, 043
Castorina, E., Sefusatti, E., Sheth, R. K., Villaescusa-Navarro, F., & Viel, M. 2014, Journal of Cosmology and Astro-Particle Physics, 2014, 049
Catelan, P., Kamionkowski, M., & Blandford, R. D. 2001, MNRAS, 320, L7
Caucci, S., Colombi, S., Pichon, C., et al. 2008, MNRAS, 386, 211
Cautun, M., van de Weygaert, R., Jones, B. J. T., & Frenk, C. S. 2014, MNRAS, 441, 2923
Cawthon, R., Davis, C., Gatti, M., et al. 2018, MNRAS, 481, 2427
Ceccarelli, L., Padilla, N. D., Valotto, C., & Lambas, D. G. 2006, MNRAS, 373, 1440
Cen, R., & Ostriker, J. 1992, ApJ, 393, 22
Cen, R., & Safarzadeh, M. 2015, ApJL, 809, L32
Chabrier, G. 2003, Publ. Astron. Soc. Pac. , 115, 763
Chang, Y.-Y., van der Wel, A., Rix, H.-W., et al. 2013, ApJ, 762, 83
Chatterjee, S., Di Matteo, T., Kosowsky, A., & Pelupessy, I. 2008, MNRAS, 390, 535
Chatterjee, S., Ho, S., Newman, J. A., & Kosowsky, A. 2010, ApJ, 720, 299
Chatterjee, S., & Kosowsky, A. 2007, ApJL, 661, L113
Chen, Y.-C., Ho, S., Blazek, J., et al. 2019, MNRAS, 485, 2492
Chen, Y.-C., Ho, S., Brinkmann, J., et al. 2016, MNRAS, 461, 3896
Chen, Y.-C., Ho, S., Freeman, P. E., Genovese, C. R., & Wasserman, L. 2015, MNRAS, 454, 1140
Chen, Y.-C., Ho, S., Tenneti, A., et al. 2015, MNRAS, 454, 3341
Cherinka, B., Andrews, B. H., Sánchez-Gallego, J., et al. 2018, arXiv e-prints, arXiv:1812.03833 [astro-ph.IM]
Chiang, Y.-K., & Ménard, B. 2019, ApJ, 870, 120
Chisari, N., Laigle, C., Codis, S., et al. 2016, MNRAS, 461, 2702

Chuang, C.-H., Pellejero-Ibanez, M., Rodríguez-Torres, S., et al. 2017, MNRAS, 471, 2370
Ciotti, L., & Ostriker, J. P. 1997, ApJL, 487, L105
Clampitt, J., Cai, Y.-C., & Li, B. 2013, MNRAS, 431, 749
Clampitt, J., & Jain, B. 2015, MNRAS, 454, 3357
Codis, S., Pichon, C., Devriendt, J., et al. 2012, MNRAS, 427, 3320
Codis, S., Gavazzi, R., Dubois, Y., et al. 2015, MNRAS, 448, 3391
Colas, T., D'Amico, G., Senatore, L., Zhang, P., & Beutler, F. 2019, arXiv e-prints, arXiv:1909.07951
Comparat, J., Prada, F., Yepes, G., & Klypin, A. 2017, MNRAS, 469, 4157
Conroy, C. 2013, Ann. Rev. Astron.& Astrophys. , 51, 393
Conroy, C., Wechsler, R. H., & Kravtsov, A. V. 2006, ApJ, 647, 201
Conroy, C., & White, M. 2013, ApJ, 762, 70
Conroy, C., Coil, A. L., White, M., et al. 2005, ApJ, 635, 990
Conselice, C. J. 2014, Ann. Rev. Astron.& Astrophys. , 52, 291
Corasaniti, P.-S., Giannantonio, T., & Melchiorri, A. 2005, PRD, 71, 123521
Costanzi, M., Villaescusa-Navarro, F., Viel, M., et al. 2013, Journal of Cosmology and Astro-Particle Physics, 2013, 012
Courteau, S. 1997, AJ, 114, 2402
Craven, P., & Wahba, G. 1978, Numer. Math., 31, 377
Crichton, D., Gralla, M. B., Hall, K., et al. 2016, MNRAS, 458, 1478
Crittenden, R. G., & Turok, N. 1996, Phys. Rev. Lett., 76, 575
Croft, R. A. C., Weinberg, D. H., Katz, N., & Hernquist, L. 1997, ApJ, 488, 532
Croom, S. M., Boyle, B. J., Shanks, T., et al. 2005, MNRAS, 356, 415
Croom, S. M., Richards, G. T., Shanks, T., et al. 2009, MNRAS, 392, 19
Croton, D. J., Springel, V., White, S. D. M., et al. 2006, MNRAS, 365, 11
Cuesta, A. J., Betancort-Rijo, J. E., Gottlöber, S., et al. 2008, MNRAS, 385, 867
Cutri, R. M., Wright, E. L., Conrow, T., et al. 2013, Explanatory Supplement to the AllWISE Data Release Products, Tech. rep.
da Silva, A. C., Kay, S. T., Liddle, A. R., & Thomas, P. A. 2004, MNRAS, 348, 1401
da Silva, A. C., Kay, S. T., Liddle, A. R., et al. 2001, ApJL, 561, L15
D'Amico, G., Senatore, L., & Zhang, P. 2020, arXiv e-prints, arXiv:2003.07956
Danovich, M., Dekel, A., Hahn, O., Ceverino, D., & Primack, J. 2015, MNRAS, 449, 2087
Das, S., Sherwin, B. D., Aguirre, P., et al. 2011, Phys. Rev. Lett., 107, 021301
Davies, F. B., Hennawi, J. F., Bañados, E., et al. 2018, ArXiv e-prints, arXiv:1802.06066
Davis, C., Rozo, E., Roodman, A., et al. 2018, MNRAS, 477, 2196
Davis, M., Efstathiou, G., Frenk, C. S., & White, S. D. M. 1985, ApJ, 292, 371
Davis, M., & Peebles, P. J. E. 1983, ApJ, 267, 465
de Sainte Agathe, V., Balland, C., du Mas des Bourboux, H., et al. 2019, A&A, 629, A85
Degraf, C., Oborski, M., Di Matteo, T., et al. 2011, MNRAS, 416, 1591
Dekel, A. 1985, ApJ, 298, 461
DESI Collaboration, Aghamousa, A., Aguilar, J., et al. 2016, ArXiv e-prints, arXiv:1611.00036 [astro-ph.IM]

Dey, A., Schlegel, D. J., Lang, D., et al. 2019, AJ, 157, 168
Dicke, R. H., Peebles, P. J. E., Roll, P. G., & Wilkinson, D. T. 1965, ApJ, 142, 414
Diener, C., Lilly, S. J., Knobel, C., et al. 2013, ApJ, 765, 109
Diener, C., Lilly, S. J., Ledoux, C., et al. 2015, ApJ, 802, 31
Dodelson, S., Heitmann, K., Hirata, C., et al. 2016, ArXiv e-prints, arXiv:1604.07626
Doran, M., & Robbers, G. 2006, JCAP, 6, 026
Doroshkevich, A. G. 1970, Astrofizika, 6, 581
Drory, N., MacDonald, N., Bershady, M. A., et al. 2015, AJ, 149, 77
Dubois, Y., Pichon, C., Welker, C., et al. 2014, MNRAS, 444, 1453
Duffy, A. R., Schaye, J., Kay, S. T., & Dalla Vecchia, C. 2008, MNRAS, 390, L64
Dutta Chowdhury, D., & Chatterjee, S. 2017, ApJ, 839, 34
Eardley, E., Peacock, J. A., McNaught-Roberts, T., et al. 2015, MNRAS, 448, 3665
Efstathiou, G. 2004, Mon. Not. Roy. Astron. Soc., 349, 603
Efstathiou, G., Bond, J. R., & White, S. D. M. 1992, MNRAS, 258, 1P
Efstathiou, G., & Migliaccio, M. 2012, MNRAS, 423, 2492
Efstathiou, G., Sutherland, W. J., & Maddox, S. J. 1990, Nature, 348, 705
Eftekharzadeh, S., Myers, A. D., White, M., et al. 2015, MNRAS, 453, 2779
Eilers, A.-C., Davies, F. B., Hennawi, J. F., et al. 2017, ApJ, 840, 24
Einasto, J., Klypin, A. A., Saar, E., & Shandarin, S. F. 1984, MNRAS, 206, 529
Elmegreen, D. M., Elmegreen, B. G., Rubin, D. S., & Schaffer, M. A. 2005, ApJ, 631, 85
Fakhouri, O., & Ma, C.-P. 2009, MNRAS, 394, 1825
Fall, S. M. 1983, in IAU Symposium, Vol. 100, Internal Kinematics and Dynamics of Galaxies, ed. E. Athanassoula, 391
Fall, S. M., & Efstathiou, G. 1980, MNRAS, 193, 189
Fan, X., Strauss, M. A., Becker, R. H., et al. 2006, AJ, 132, 117
Faucher-Giguère, C.-A., Prochaska, J. X., Lidz, A., Hernquist, L., & Zaldarriaga, M. 2008, ApJ, 681, 831
Ferrarese, L. 2002, ApJ, 578, 90
Ferrarese, L., & Merritt, D. 2000, ApJL, 539, L9
Ferraro, S., & Hill, J. C. 2018, Phys. Rev., D97, 023512
Ferraro, S., Hill, J. C., Battaglia, N., Liu, J., & Spergel, D. N. 2016, Phys. Rev., D94, 123526
Ferraro, S., Sherwin, B. D., & Spergel, D. N. 2015, PRD, 91, 083533
Fixsen, D. J. 2009, ApJ, 707, 916
Flender, S., Nagai, D., & McDonald, M. 2017, ApJ, 837, 124
Forero-Romero, J. E., Contreras, S., & Padilla, N. 2014, MNRAS, 443, 1090
Forero-Romero, J. E., Hoffman, Y., Gottlöber, S., Klypin, A., & Yepes, G. 2009, MNRAS, 396, 1815
Fosalba, P., Gaztañaga, E., & Castand er, F. J. 2003, ApJL, 597, L89
Franx, M., Illingworth, G., & de Zeeuw, T. 1991, ApJ, 383, 112
Franzetti, P., Scodeggio, M., Garilli, B., et al. 2007, A&A, 465, 711
Fukugita, M., & Yanagida, T. 1986, Physics Letters B, 174, 45
Gaia Collaboration, Prusti, T., de Bruijne, J. H. J., et al. 2016, A&A, 595, A1

Gaia Collaboration, Brown, A. G. A., Vallenari, A., et al. 2018, A&A, 616, A1
Ganeshaiah Veena, P., Cautun, M., van de Weygaert, R., et al. 2018, MNRAS, 481, 414
García-García, C., Alonso, D., & Bellini, E. 2019, arXiv:1906.11765 [astro-ph.CO]
Gatti, M., Vielzeuf, P., Davis, C., et al. 2018, MNRAS, 477, 1664
Gebhardt, K., Bender, R., Bower, G., et al. 2000, ApJL, 539, L13
Geller, M. J., & Huchra, J. P. 1989, Science, 246, 897
Giannantonio, T., Crittenden, R., Nichol, R., & Ross, A. J. 2012, MNRAS, 426, 2581
Giannantonio, T., Scranton, R., Crittenden, R. G., et al. 2008, PRD, 77, 123520
Giannantonio, T., Crittenden, R. G., Nichol, R. C., et al. 2006, PRD, 74, 063520
Giannantonio, T., Fosalba, P., Cawthon, R., et al. 2016, MNRAS, 456, 3213
Giardino, G., de Oliveira, C. A., Arribas, S., et al. 2016, in Astronomical Society of the Pacific Conference Series, Vol. 507, Multi-Object Spectroscopy in the Next Decade: Big Questions, Large Surveys, and Wide Fields, ed. I. Skillen, M. Barcells, & S. Trager, 305
Giavalisco, M., Steidel, C. C., & Macchetto, F. D. 1996, ApJ, 470, 189
Glikman, E., Djorgovski, S. G., Stern, D., et al. 2011, ApJL, 728, L26
Goldberg, D. M., & Vogeley, M. S. 2004, ApJ, 605, 1
Górski, K. M., Hivon, E., Banday, A. J., et al. 2005, ApJ, 622, 759
Goto, T., Szapudi, I., & Granett, B. R. 2012, MNRAS, 422, L77
Graham, A. W., & Scott, N. 2015, ApJ, 798, 54
Gralla, M. B., Crichton, D., Marriage, T. A., et al. 2014, MNRAS, 445, 460
Granett, B. R., Neyrinck, M. C., & Szapudi, I. 2008, ApJL, 683, L99
Greco, J. P., Hill, J. C., Spergel, D. N., & Battaglia, N. 2015, ApJ, 808, 151
Gregory, S. A., Thompson, L. A., & Tifft, W. G. 1981, ApJ, 243, 411
Gruen, D., Friedrich, O., Amara, A., et al. 2016, MNRAS, 455, 3367
Gunn, J. E., & Gott, J. Richard, I. 1972, ApJ, 176, 1
Gunn, J. E., & Peterson, B. A. 1965, ApJ, 142, 1633
Gunn, J. E., Siegmund, W. A., Mannery, E. J., et al. 2006, AJ, 131, 2332
Gupta, N., Saro, A., Mohr, J. J., Dolag, K., & Liu, J. 2017, MNRAS, 469, 3069
Guth, A. H. 1981, PRD, 23, 347
Guzzo, L., Scodeggio, M., Garilli, B., et al. 2014, A&A, 566, A108
Haardt, F., & Madau, P. 1996, ApJ, 461, 20
—. 2012, ApJ, 746, 125
Hahn, O., Carollo, C. M., Porciani, C., & Dekel, A. 2007a, MNRAS, 381, 41
Hahn, O., Porciani, C., Carollo, C. M., & Dekel, A. 2007b, MNRAS, 375, 489
Hahn, O., Teyssier, R., & Carollo, C. M. 2010, MNRAS, 405, 274
Hall, K. R., Zakamska, N. L., Addison, G. E., et al. 2019, MNRAS, 490, 2315
Hamaus, N., Cousinou, M.-C., Pisani, A., et al. 2017, JCAP, 7, 014
Hamaus, N., Pisani, A., Sutter, P. M., et al. 2016, Physical Review Letters, 117, 091302
Hamaus, N., Sutter, P. M., & Wandelt, B. D. 2014, Physical Review Letters, 112, 251302
Hand, N., Appel, J. W., Battaglia, N., et al. 2011, ApJ, 736, 39
Hanson, D., Challinor, A., & Lewis, A. 2010, General Relativity and Gravitation, 42, 2197
Häring, N., & Rix, H.-W. 2004, ApJL, 604, L89

Hartlap, J., Simon, P., & Schneider, P. 2007, A&A, 464, 399
Haynes, M. P., & Giovanelli, R. 1984, AJ, 89, 758
Heitmann, K., Lukić, Z., Fasel, P., et al. 2008, Computational Science and Discovery, 1, 015003
Henden, N. A., Puchwein, E., Shen, S., & Sijacki, D. 2018, ArXiv e-prints, arXiv:1804.05064
Hennawi, J. F., Strauss, M. A., Oguri, M., et al. 2006, AJ, 131, 1
Hernández-Monteagudo, C., Ross, A. J., Cuesta, A., et al. 2014, MNRAS, 438, 1724
HI4PI Collaboration, Ben Bekhti, N., Flöer, L., et al. 2016, A&A, 594, A116
Hickox, R. C., Mullaney, J. R., Alexander, D. M., et al. 2014, ApJ, 782, 9
Higuchi, Y., Oguri, M., & Hamana, T. 2013, MNRAS, 432, 1021
Hikage, C., Oguri, M., Hamana, T., et al. 2019, PASJ, 71, 43
Hildebrandt, H., Köhlinger, F., van den Busch, J. L., et al. 2020, A&A, 633, A69
Hill, J. C., Baxter, E. J., Lidz, A., Greco, J. P., & Jain, B. 2018, PRD, 97, 083501
Hill, J. C., Ferraro, S., Battaglia, N., Liu, J., & Spergel, D. N. 2016, Phys. Rev. Lett., 117, 051301
Hill, J. C., & Spergel, D. N. 2014, Journal of Cosmology and Astro-Particle Physics, 2014, 030
Hinterbichler, K. 2012, Reviews of Modern Physics, 84, 671
Hirata, C. M., Ho, S., Padmanabhan, N., Seljak, U., & Bahcall, N. A. 2008, Phys. Rev., D78, 043520
Hirata, C. M., Mandelbaum, R., Ishak, M., et al. 2007, MNRAS, 381, 1197
Hirata, C. M., & Seljak, U. 2004, Phys. Rev. D, 70, 63526
Hivon, E., Górski, K. M., Netterfield, C. B., et al. 2002, ApJ, 567, 2
Ho, S., Hirata, C., Padmanabhan, N., Seljak, U., & Bahcall, N. 2008, PRD, 78, 043519
Hojjati, A., McCarthy, I. G., Harnois-Deraps, J., et al. 2015, JCAP, 2015, 047
Hojjati, A., Tröster, T., Harnois-Déraps, J., et al. 2017, MNRAS, 471, 1565
Hopkins, P. F., & Hernquist, L. 2009, ApJ, 698, 1550
Hopkins, P. F., Hernquist, L., Cox, T. J., et al. 2006a, ApJS, 163, 1
—. 2006b, ApJ, 639, 700
Horndeski, G. W. 1974, Int. J. Theor. Phys., 10, 363
Horowitz, B., & Seljak, U. 2017, MNRAS, 469, 394
Hoyle, F., & Fowler, W. A. 1963, Nature, 197, 533
Hoyle, F., Rojas, R. R., Vogeley, M. S., & Brinkmann, J. 2005, ApJ, 620, 618
Hu, W. 1999, Astrophys. J., 522, L21
Hu, W. 2001, PRD, 64, 083005
Hu, W. 2002, Phys. Rev., D66, 083515
Hu, W. 2002, PRD, 65, 023003
Hu, W., Eisenstein, D. J., & Tegmark, M. 1998, Phys. Rev. Lett., 80, 5255
Hu, W., & Okamoto, T. 2002, ApJ, 574, 566
Hui, L., & Gnedin, N. Y. 1997, MNRAS, 292, 27
Ivanov, M. M., Simonović, M., & Zaldarriaga, M. 2019, arXiv e-prints, arXiv:1909.05277
—. 2020, PRD, 101, 083504

Jahnke, K., Bongiorno, A., Brusa, M., et al. 2009, ApJL, 706, L215
Jain, B., & Khoury, J. 2010, Annals of Physics, 325, 1479
Jakobs, A., Viola, M., McCarthy, I., et al. 2017, ArXiv e-prints, arXiv:1712.05463
Jasche, J., Kitaura, F. S., Li, C., & Enßlin, T. A. 2010, MNRAS, 409, 355
Jennings, E., Li, Y., & Hu, W. 2013, MNRAS, 434, 2167
Jiang, L., McGreer, I. D., Fan, X., et al. 2016, ApJ, 833, 222
Joachimi, B., Semboloni, E., Bett, P. E., et al. 2013, MNRAS, 431, 477
Johnson, A., Blake, C., Amon, A., et al. 2017, MNRAS, 465, 4118
Jones, B. J. T., van de Weygaert, R., & Aragon-Calvo, M. A. 2010, MNRAS, 408, 897
Kaiser, N. 1986, MNRAS, 222, 323
—. 1987, MNRAS, 227, 1
Kamionkowski, M. 1996, PRD, 54, 4169
Kashikawa, N., Ishizaki, Y., Willott, C. J., et al. 2015, ApJ, 798, 28
Katz, N., Hernquist, L., & Weinberg, D. H. 1992, ApJL, 399, L109
Katz, N., Weinberg, D. H., & Hernquist, L. 1996, ApJs, 105, 19
Kauffmann, G., & Heckman, T. M. 2009, MNRAS, 397, 135
Kay, S. T., Peel, M. W., Short, C. J., et al. 2012, MNRAS, 422, 1999
Kelly, B. C., & Shen, Y. 2013, ApJ, 764, 45
Kesden, M., Cooray, A., & Kamionkowski, M. 2003, PRD, 67, 123507
Khandai, N., Di Matteo, T., Croft, R., et al. 2015, MNRAS, 450, 1349
Khochfar, S., Emsellem, E., Serra, P., et al. 2011, MNRAS, 417, 845
Kiessling, A., Cacciato, M., Joachimi, B., et al. 2015, Space Sci. Rev., 193, 67
King, A. R., Zubovas, K., & Power, C. 2011, MNRAS, 415, L6
Kirk, D., Rassat, A., Host, O., & Bridle, S. 2012, MNRAS, 424, 1647
Kirk, D., Brown, M. L., Hoekstra, H., et al. 2015, \ssr, 193, 139
Kitanidis, E., White, M., Feng, Y., et al. 2019, arXiv e-prints, arXiv:1911.05714
Klypin, A. A., & Shandarin, S. F. 1983, MNRAS, 204, 891
Knox, L., & Millea, M. 2020, PRD, 101, 043533
Knox, L., & Page, L. 2000, Phys. Rev. Lett., 85, 1366
Kollmeier, J. A., Onken, C. A., Kochanek, C. S., et al. 2006, ApJ, 648, 128
Komatsu, E., & Kitayama, T. 1999, ApJL, 526, L1
Komatsu, E., & Seljak, U. 2002, MNRAS, 336, 1256
Kormendy, J. 2016, Astrophysics and Space Science Library, Vol. 418, Elliptical Galaxies and Bulges of Disc Galaxies: Summary of Progress and Outstanding Issues, ed. E. Laurikainen, R. Peletier, & D. Gadotti, 431
Kormendy, J., & Bender, R. 2009, ApJL, 691, L142
Kormendy, J., & Gebhardt, K. 2001, in American Institute of Physics Conference Series, Vol. 586, 20th Texas Symposium on relativistic astrophysics, ed. J. C. Wheeler & H. Martel, 363
Kormendy, J., & Ho, L. C. 2013, Ann. Rev. Astron.& Astrophys. , 51, 511
Kormendy, J., & Richstone, D. 1995, Ann. Rev. Astron.& Astrophys. , 33, 581
Koukoufilippas, N., Alonso, D., Bilicki, M., & Peacock, J. A. 2020, MNRAS, 491, 5464

Kovács, A., Sánchez, C., García-Bellido, J., et al. 2017, MNRAS, 465, 4166
Krajnović, D., Cappellari, M., de Zeeuw, P. T., & Copin, Y. 2006, MNRAS, 366, 787
Krause, E., Chang, T.-C., Doré, O., & Umetsu, K. 2013, ApJL, 762, L20
Krauss, L. M., & Turner, M. S. 1995, General Relativity and Gravitation, 27, 1137
Kravtsov, A. V., & Borgani, S. 2012, Ann. Rev. Astron.& Astrophys. , 50, 353
Kravtsov, A. V., Nagai, D., & Vikhlinin, A. A. 2005, ApJ, 625, 588
Kreckel, K., Platen, E., Aragón-Calvo, M. A., et al. 2012, AJ, 144, 16
Kriek, M., Shapley, A. E., Reddy, N. A., et al. 2015, ApJs, 218, 15
Krolewski, A., Ferraro, S., Schlafly, E., & White, M. J. 2020
Krolewski, A., Ferraro, S., Schlafly, E. F., & White, M. 2019, arXiv e-prints, arXiv:1909.07412
Krolewski, A., Lee, K.-G., Lukić, Z., & White, M. 2017, ApJ, 837, 31
Krolewski, A. G., & Eisenstein, D. J. 2015, ApJ, 803, 4
Kron, R. G. 1980, ApJS, 43, 305
Kulkarni, G., Worseck, G., & Hennawi, J. F. 2018, ArXiv e-prints, arXiv:1807.09774
Lacy, M., Mason, B., Sarazin, C., et al. 2019, MNRAS, 483, L22
Laigle, C., McCracken, H. J., Ilbert, O., et al. 2016, ApJS, 224, 24
Lam, T. Y., Clampitt, J., Cai, Y.-C., & Li, B. 2015, MNRAS, 450, 3319
Laureijs, R., Amiaux, J., Arduini, S., et al. 2011, ArXiv e-prints, arXiv:1110.3193 [astro-ph.CO]
Laurent, P., Eftekharzadeh, S., Le Goff, J.-M., et al. 2017, JCAP, 7, 017
Lavaux, G., & Wandelt, B. D. 2012, ApJ, 754, 109
Law, D. R., Shapley, A. E., Steidel, C. C., et al. 2012, Nature, 487, 338
Law, D. R., Yan, R., Bershady, M. A., et al. 2015, AJ, 150, 19
Law, D. R., Cherinka, B., Yan, R., et al. 2016, AJ, 152, 83
Le Brun, A. M. C., McCarthy, I. G., & Melin, J.-B. 2015, MNRAS, 451, 3868
Le Brun, A. M. C., McCarthy, I. G., Schaye, J., & Ponman, T. J. 2017, MNRAS, 466, 4442
Le Fèvre, O., Cassata, P., Cucciati, O., et al. 2013, A&A, 559, A14
Le Fèvre, O., Tasca, L. A. M., Cassata, P., et al. 2015, A&A, 576, A79
Leauthaud, A., Massey, R., Kneib, J.-P., et al. 2007, ApJs, 172, 219
Leauthaud, A., Saito, S., Hilbert, S., et al. 2017, MNRAS, 467, 3024
Lee, J. 2011, ApJ, 732, 99
Lee, J., & Erdogdu, P. 2007, ApJ, 671, 1248
Lee, J., & Park, D. 2009, ApJL, 696, L10
Lee, J., & Pen, U.-L. 2000, ApJl, 532, L5
—. 2001, ApJ, 555, 106
Lee, J., & Pen, U.-L. 2002, ApJl, 567, L111
Lee, J., & Pen, U.-L. 2007, ApJl, 670, L1
Lee, K.-G. 2012, ApJ, 753, 136
Lee, K.-G., Hennawi, J. F., White, M., Croft, R. A. C., & Ozbek, M. 2014a, ApJ, 788, 49
Lee, K.-G., Suzuki, N., & Spergel, D. N. 2012, AJ, 143, 51
Lee, K.-G., & White, M. 2016, ArXiv e-prints

Lee, K.-G., Bailey, S., Bartsch, L. E., et al. 2013, AJ, 145, 69
Lee, K.-G., Hennawi, J. F., Stark, C., et al. 2014b, ApJl, 795, L12
Lee, K.-G., Hennawi, J. F., Spergel, D. N., et al. 2015, ApJ, 799, 196
Lee, K.-G., Hennawi, J. F., White, M., et al. 2016, ApJ, 817, 160
Lee, K.-G., Krolewski, A., White, M., et al. 2017, ArXiv e-prints, arXiv:1710.02894
Levi, M., Bebek, C., Beers, T., et al. 2013, arXiv e-prints, arXiv:1308.0847
Lewis, A., & Challinor, A. 2006, PhysRep, 429, 1
Lewis, A., Challinor, A., & Lasenby, A. 2000, ApJ, 538, 473
Li, B., Zhao, G.-B., & Koyama, K. 2012, MNRAS, 421, 3481
Li, H., & Xia, J.-Q. 2010, JCAP, 2010, 026
Libeskind, N. I., Hoffman, Y., Forero-Romero, J., et al. 2013, MNRAS, 428, 2489
Liddle, A. R., Lyth, D. H., Viana, P. T. P., & White, M. 1996, MNRAS, 282, 281
Lilly, S. J., Le Fèvre, O., Renzini, A., et al. 2007, ApJs, 172, 70
Limber, D. N. 1953, ApJ, 117, 134
Linder, E. V., & Cahn, R. N. 2007, Astroparticle Physics, 28, 481
Lintott, C., Schawinski, K., Bamford, S., et al. 2011, MNRAS, 410, 166
Loh, J. M. 2008, ApJ, 681, 726
Loh, J. M., & Stein, M. L. 2004, Statistica Sinica, 14, 69
Lonsdale, C. J., Smith, H. E., Rowan-Robinson, M., et al. 2003, Publ. Astron. Soc. Pac. , 115, 897
Lotz, J. M., Madau, P., Giavalisco, M., Primack, J., & Ferguson, H. C. 2006, ApJ, 636, 592
Loverde, M., & Afshordi, N. 2008, PRD, 78, 123506
LSST Science Collaboration, Abell, P. A., Allison, J., et al. 2009, ArXiv e-prints, arXiv:0912.0201 [astro-ph.IM]
Lukić, Z., Stark, C. W., Nugent, P., et al. 2015, MNRAS, 446, 3697
Lynden-Bell, D. 1969, Nature, 223, 690
Ma, C.-P., & Bertschinger, E. 1995, ApJ, 455, 7
Ma, Y.-Z., Van Waerbeke, L., Hinshaw, G., et al. 2015, JCAP, 2015, 046
Madau, P., & Dickinson, M. 2014, Ann. Rev. Astron.& Astrophys. , 52, 415
Madhavacheril, M. S., & Hill, J. C. 2018, Phys. Rev., D98, 023534
Magorrian, J., Tremaine, S., Richstone, D., et al. 1998, AJ, 115, 2285
Mainzer, A., Bauer, J., Grav, T., et al. 2011, ApJ, 731, 53
Mainzer, A., Bauer, J., Cutri, R. M., et al. 2014, ApJ, 792, 30
Makarov, D., Prugniel, P., Terekhova, N., Courtois, H., & Vauglin, I. 2014, A&A, 570, A13
Makiya, R., Ando, S., & Komatsu, E. 2018, MNRAS, 480, 3928
Malavasi, N., Arnouts, S., Vibert, D., et al. 2016, ArXiv e-prints, arXiv:1611.07045
Maller, A. H., & Dekel, A. 2002, MNRAS, 335, 487
Maller, A. H., Dekel, A., & Somerville, R. 2002, MNRAS, 329, 423
Mandelbaum, R., Hirata, C. M., Ishak, M., Seljak, U., & Brinkmann, J. 2006, MNRAS, 367, 611
Mandelbaum, R., Blake, C., Bridle, S., et al. 2011, MNRAS, 410, 844
Mao, Q., Berlind, A. A., Scherrer, R. J., et al. 2017a, ApJ, 835, 160

—. 2017b, ApJ, 835, 161
Marconi, A., & Hunt, L. K. 2003, ApJL, 589, L21
Marleau, F. R., Clancy, D., & Bianconi, M. 2013, MNRAS, 435, 3085
Marques, G. A., & Bernui, A. 2019, arXiv:1908.04854 [astro-ph.CO]
Martel, H., Shapiro, P. R., & Weinberg, S. 1998, ApJ, 492, 29
Martin, J. 2012, Comptes Rendus Physique, 13, 566
Martini, P. 2004, Coevolution of Black Holes and Galaxies, 169
Massara, E., Villaescusa-Navarro, F., Viel, M., & Sutter, P. M. 2015, JCAP, 11, 018
McCarthy, I. G., Le Brun, A. M. C., Schaye, J., & Holder, G. P. 2014, MNRAS, 440, 3645
McCarthy, I. G., Schaye, J., Bird, S., & Le Brun, A. M. C. 2017, MNRAS, 465, 2936
McCarthy, I. G., Schaye, J., Ponman, T. J., et al. 2010, MNRAS, 406, 822
McConnachie, A., Babusiaux, C., Balogh, M., et al. 2016, ArXiv e-prints, arXiv:1606.00043 [astro-ph.IM]
McConnell, N. J., & Ma, C.-P. 2013, ApJ, 764, 184
McDonald, P., Seljak, U., Burles, S., et al. 2006, ApJS, 163, 80
McEwen, J. D., Vielva, P., Hobson, M. P., Martínez-González, E., & Lasenby, A. N. 2007, MNRAS, 376, 1211
McGreer, I. D., Jiang, L., Fan, X., et al. 2013, ApJ, 768, 105
McLure, R. J., & Dunlop, J. S. 2002, MNRAS, 331, 795
McQuinn, M. 2015, ArXiv e-prints
McQuinn, M., & White, M. 2013, MNRAS, 433, 2857
Mead, A. J., Peacock, J. A., Heymans, C., Joudaki, S., & Heavens, A. F. 2015, MNRAS, 454, 1958
Meisner, A. M., Lang, D., & Schlegel, D. J. 2017a, AJ, 154, 161
—. 2017b, AJ, 153, 38
—. 2018, Research Notes of the American Astronomical Society, 2, 1
Melchior, P., Sutter, P. M., Sheldon, E. S., Krause, E., & Wandelt, B. D. 2014, MNRAS, 440, 2922
Ménard, B., Scranton, R., Schmidt, S., et al. 2013, arXiv e-prints, arXiv:1303.4722
Mendel, J. T., Simard, L., Palmer, M., Ellison, S. L., & Patton, D. R. 2014, ApJS, 210, 3
Merritt, D., & Ferrarese, L. 2001, MNRAS, 320, L30
Micheletti, D., Iovino, A., Hawken, A. J., et al. 2014, A&A, 570, A106
Miralda-Escudé, J., Cen, R., Ostriker, J. P., & Rauch, M. 1996, ApJ, 471, 582
Mo, H. J., Mao, S., & White, S. D. M. 1998, MNRAS, 295, 319
Modi, C., White, M., & Vlah, Z. 2017, JCAP, 8, 009
Momcheva, I. G., Brammer, G. B., van Dokkum, P. G., et al. 2016a, ApJs, 225, 27
—. 2016b, ApJS, 225, 27
Mortonson, M. J., Weinberg, D. H., & White, M. 2013, arXiv e-prints, arXiv:1401.0046
Moster, B. P., Somerville, R. S., Maulbetsch, C., et al. 2010, ApJ, 710, 903
Moura-Santos, E., Carvalho, F. C., Penna-Lima, M., Novaes, C. P., & Wuensche, C. A. 2016, ApJ, 826, 121
Mukhanov, V. F., & Chibisov, G. V. 1981, Soviet Journal of Experimental and Theoretical

Physics Letters, 33, 532
Mukhanov, V. F., Feldman, H. A., & Brandenberger, R. H. 1992, PhysRep, 215, 203
Myers, A. D., Outram, P. J., Shanks, T., et al. 2005, MNRAS, 359, 741
Myers, A. D., Palanque-Delabrouille, N., Prakash, A., et al. 2015, ApJS, 221, 27
Nadathur, S., & Hotchkiss, S. 2015, MNRAS, 454, 2228
Nadathur, S., & Percival, W. J. 2017, ArXiv e-prints, arXiv:1712.07575
Nagai, D. 2006, ApJ, 650, 538
Nagai, D., Kravtsov, A. V., & Vikhlinin, A. 2007, ApJ, 668, 1
Najita, J., Willman, B., Finkbeiner, D. P., et al. 2016, ArXiv e-prints, arXiv:1610.01661 [astro-ph.IM]
Nanayakkara, T., Glazebrook, K., Kacprzak, G. G., et al. 2016, ApJ, 828, 21
Navarro, J. F., Abadi, M. G., & Steinmetz, M. 2004, ApJ, 613, 41
Navarro, J. F., Frenk, C. S., & White, S. D. M. 1997, ApJ, 490, 493
Navarro, J. F., & Steinmetz, M. 2000, ApJ, 538, 477
Nelson, D., Pillepich, A., Genel, S., et al. 2015, Astronomy and Computing, 13, 12
Newman, J. A. 2008, ApJ, 684, 88
Neyrinck, M. C. 2008, MNRAS, 386, 2101
Nolta, M. R., Wright, E. L., Page, L., et al. 2004, ApJ, 608, 10
Norberg, P., Baugh, C. M., Gaztañaga, E., & Croton, D. J. 2009, MNRAS, 396, 19
Novak, G. S., Ostriker, J. P., & Ciotti, L. 2011, ApJ, 737, 26
Oke, J. B., Cohen, J. G., Carr, M., et al. 1995, Publ. Astron. Soc. Pac. , 107, 375
Okumura, T., Jing, Y. P., & Li, C. 2009, ApJ, 694, 214
Omori, Y., & Holder, G. 2015, arXiv e-prints, arXiv:1502.03405
Omori, Y., Giannantonio, T., Porredon, A., et al. 2018, arXiv e-prints, arXiv:1810.02342
Osato, K., Flender, S., Nagai, D., Shirasaki, M., & Yoshida, N. 2018, MNRAS, 475, 532
Osborne, S. J., Hanson, D., & Doré, O. 2014, JCAP, 1403, 024
Ostriker, J. P., & Peebles, P. J. E. 1973, ApJ, 186, 467
Ostriker, J. P., & Steinhardt, P. J. 1995, Nature, 377, 600
Padmanabhan, N., Hirata, C. M., Seljak, U., et al. 2005, PRD, 72, 043525
Pahwa, I., Libeskind, N. I., Tempel, E., et al. 2016, MNRAS, 457, 695
Palanque-Delabrouille, N., Magneville, C., Yèche, C., et al. 2016a, A&A, 587, A41
—. 2016b, A&A, 589, C2
Pan, D. C., Vogeley, M. S., Hoyle, F., Choi, Y.-Y., & Park, C. 2012, MNRAS, 421, 926
Pandey, S., Baxter, E. J., & Hill, J. C. 2020, PRD, 101, 043525
Pandey, S., Baxter, E. J., Xu, Z., et al. 2019, PRD, 100, 063519
Pâris, I., Petitjean, P., Ross, N. P., et al. 2017, A&A, 597, A79
Pâris, I., Petitjean, P., Aubourg, É., et al. 2018, A&A, 613, A51
Park, D., & Lee, J. 2007, Physical Review Letters, 98, 081301
Patiri, S. G., Cuesta, A. J., Prada, F., Betancort-Rijo, J., & Klypin, A. 2006, ApJl, 652, L75
Peacock, J. A., & Bilicki, M. 2018, MNRAS, 481, 1133
Peebles, P. J. E. 1968, ApJ, 153, 1
—. 1969, ApJ, 155, 393

—. 1982, ApJL, 263, L1
—. 1984, ApJ, 284, 439
—. 2001, ApJ, 557, 495
Peebles, P. J. E., & Yu, J. T. 1970, ApJ, 162, 815
Pen, U.-L., Lee, J., & Seljak, U. 2000, ApJL, 543, L107
Penny, S. J., Brown, M. J. I., Pimbblet, K. A., et al. 2015, MNRAS, 453, 3519
Penzias, A. A., & Wilson, R. W. 1965, ApJ, 142, 419
Perlmutter, S., Aldering, G., Goldhaber, G., et al. 1999, ApJ, 517, 565
Philcox, O. H. E., Ivanov, M. M., Simonović, M., & Zaldarriaga, M. 2020, arXiv e-prints, arXiv:2002.04035
Pichon, C., Pogosyan, D., Kimm, T., et al. 2011, MNRAS, 418, 2493
Pichon, C., Vergely, J. L., Rollinde, E., Colombi, S., & Petitjean, P. 2001, MNRAS, 326, 597
Pierpaoli, E., Scott, D., & White, M. 2000, Science, 287, 2171
Pietrobon, D., Balbi, A., & Marinucci, D. 2006, PRD, 74, 043524
Pineda, J. C. B., Hayward, C. C., Springel, V., & Mendes de Oliveira, C. 2017, MNRAS, 466, 63
Pisani, A., Sutter, P. M., Hamaus, N., et al. 2015, PRD, 92, 083531
Planck Collaboration, Ade, P. A. R., Aghanim, N., et al. 2013a, A&A, 550, A131
—. 2013b, A&A, 557, A52
—. 2014a, A&A, 571, A19
—. 2014b, A&A, 571, A16
—. 2014c, A&A, 571, A17
—. 2014d, A&A, 571, A20
—. 2014e, A&A, 571, A21
—. 2014f, A&A, 571, A23
Planck Collaboration, Adam, R., Ade, P. A. R., et al. 2016a, A&A, 594, A1
Planck Collaboration, Ade, P. A. R., Aghanim, N., et al. 2016b, A&A, 594, A15
—. 2016c, A&A, 594, A16
—. 2016d, A&A, 594, A21
—. 2016e, A&A, 594, A21
—. 2016f, A&A, 594, A23
Planck Collaboration, Akrami, Y., Arroja, F., et al. 2018a, ArXiv e-prints, arXiv:1807.06205
Planck Collaboration, Akrami, Y., Argüeso, F., et al. 2018b, arXiv e-prints, arXiv:1807.06206
Planck Collaboration, Aghanim, N., Akrami, Y., et al. 2018c, arXiv e-prints, arXiv:1807.06207
Planck Collaboration, Akrami, Y., Ashdown, M., et al. 2018d, arXiv e-prints, arXiv:1807.06208
Planck Collaboration, Aghanim, N., Akrami, Y., et al. 2018e, arXiv e-prints, arXiv:1807.06209
—. 2018f, ArXiv e-prints, arXiv:1807.06210
Planelles, S., Fabjan, D., Borgani, S., et al. 2017, MNRAS, 467, 3827
Pollina, G., Baldi, M., Marulli, F., & Moscardini, L. 2016, MNRAS, 455, 3075

Porciani, C., Dekel, A., & Hoffman, Y. 2002, MNRAS, 332, 325
Porciani, C., Magliocchetti, M., & Norberg, P. 2004, MNRAS, 355, 1010
Pritchard, J. R., & Loeb, A. 2012, Reports on Progress in Physics, 75, 086901
Pullen, A. R., Alam, S., He, S., & Ho, S. 2016, MNRAS, 460, 4098
Rahman, M., Ménard, B., & Scranton, R. 2016a, MNRAS, 457, 3912
Rahman, M., Ménard, B., Scranton, R., Schmidt, S. J., & Morrison, C. B. 2015, MNRAS, 447, 3500
Rahman, M., Mendez, A. J., Ménard, B., et al. 2016b, MNRAS, 460, 163
Rakic, O., Schaye, J., Steidel, C. C., & Rudie, G. C. 2012, ApJ, 751, 94
Ramos-Ceja, M. E., Basu, K., Pacaud, F., & Bertoldi, F. 2015, A&A, 583, A111
Rassat, A., Land, K., Lahav, O., & Abdalla, F. B. 2007, MNRAS, 377, 1085
Rees, M. J., & Sciama, D. W. 1968, Nature, 217, 511
Reid, B., Ho, S., Padmanabhan, N., et al. 2016, MNRAS, 455, 1553
Reid, B. A., & Spergel, D. N. 2006, ApJ, 651, 643
Reines, A. E., & Volonteri, M. 2015, ApJ, 813, 82
Renk, J., Zumalacárregui, M., Montanari, F., & Barreira, A. 2017, JCAP, 2017, 020
Richards, G. T., Strauss, M. A., Fan, X., et al. 2006, AJ, 131, 2766
Richardson, J., Zheng, Z., Chatterjee, S., Nagai, D., & Shen, Y. 2012, ApJ, 755, 30
Riess, A. G., Casertano, S., Yuan, W., Macri, L. M., & Scolnic, D. 2019, ApJ, 876, 85
Riess, A. G., Filippenko, A. V., Challis, P., et al. 1998, AJ, 116, 1009
Riess, A. G., Strolger, L.-G., Tonry, J., et al. 2004, ApJ, 607, 665
Rodríguez-Torres, S. A., Comparat, J., Prada, F., et al. 2017, MNRAS, 468, 728
Rollinde, E., Petitjean, P., Pichon, C., et al. 2003, MNRAS, 341, 1279
Rorai, A., Hennawi, J. F., & White, M. 2013, ApJ, 775, 81
Rorai, A., Becker, G. D., Haehnelt, M. G., et al. 2017, MNRAS, 466, 2690
Ross, A. J., Percival, W. J., Sánchez, A. G., et al. 2012a, MNRAS, 424, 564
Ross, A. J., Samushia, L., Burden, A., et al. 2014, MNRAS, 437, 1109
Ross, A. J., Beutler, F., Chuang, C.-H., et al. 2017, MNRAS, 464, 1168
Ross, N. P., Shen, Y., Strauss, M. A., et al. 2009, ApJ, 697, 1634
Ross, N. P., Myers, A. D., Sheldon, E. S., et al. 2012b, ApJS, 199, 3
Ross, N. P., McGreer, I. D., White, M., et al. 2013, ApJ, 773, 14
Rowe, B., & Silk, J. 2011, MNRAS, 412, 905
Ruan, J. J., McQuinn, M., & Anderson, S. F. 2015, ApJ, 802, 135
Rubin, V. C., Ford, W. K., J., & Thonnard, N. 1980, ApJ, 238, 471
Rubin, V. C., & Ford, W. Kent, J. 1970, ApJ, 159, 379
Ryden, B. S. 1995, ApJ, 452, 25
Sachs, R. K., & Wolfe, A. M. 1967, ApJ, 147, 73
Sakharov, A. 1991, Sov. Phys. Usp., 34, 392
Salpeter, E. E. 1964, ApJ, 140, 796
Sánchez, C., Clampitt, J., Kovacs, A., et al. 2017, MNRAS, 465, 746
Sánchez-Blázquez, P., Peletier, R. F., Jiménez-Vicente, J., et al. 2006, MNRAS, 371, 703
Sanders, D. B., Soifer, B. T., Elias, J. H., Neugebauer, G., & Matthews, K. 1988, ApJL,

328, L35
Savorgnan, G. A. D., Graham, A. W., Marconi, A., & Sani, E. 2016, ApJ, 817, 21
Scannapieco, E., & Oh, S. P. 2004, ApJ, 608, 62
Scannapieco, E., Thacker, R. J., & Couchman, H. M. P. 2008, ApJ, 678, 674
Schaan, E., & Ferraro, S. 2019, Phys. Rev. Lett., 122, 181301
Schaye, J., Aguirre, A., Kim, T.-S., et al. 2003, ApJ, 596, 768
Schlafly, E. F., Meisner, A. M., & Green, G. M. 2019, The Astrophysical Journal Supplement Series, 240, 30
Schlafly, E. F., Green, G. M., Lang, D., et al. 2018, The Astrophysical Journal Supplement Series, 234, 39
Schmidt, M. 1963, Nature, 197, 1040
Schmidt, S. J., Ménard, B., Scranton, R., Morrison, C., & McBride, C. K. 2013, MNRAS, 431, 3307
Schmidt, S. J., Ménard, B., Scranton, R., et al. 2015, MNRAS, 446, 2696
Schmidt, T. M., Hennawi, J. F., Worseck, G., et al. 2017, ArXiv e-prints, arXiv:1710.04527
Schmittfull, M., & White, M. 2016, MNRAS, 463, 332
Schneider, D. P., Richards, G. T., Hall, P. B., et al. 2010, AJ, 139, 2360
Scottez, V., Benoit-Lévy, A., Coupon, J., Ilbert, O., & Mellier, Y. 2018, MNRAS, 474, 3921
Scottez, V., Mellier, Y., Granett, B. R., et al. 2016, MNRAS, 462, 1683
Scoville, N., Aussel, H., Brusa, M., et al. 2007, ApJs, 172, 1
Scranton, R., Connolly, A. J., Nichol, R. C., et al. 2003, arXiv e-prints, astro
Seljak, U. 2000, MNRAS, 318, 203
Seljak, U., Makarov, A., McDonald, P., & Trac, H. 2006, Phys. Rev. Lett., 97, 191303
Seljak, U., & Zaldarriaga, M. 1996, ApJ, 469, 437
Seljak, U., Makarov, A., McDonald, P., et al. 2005, PRD, 71, 103515
Shajib, A. J., & Wright, E. L. 2016, Astrophys. J., 827, 116
Shajib, A. J., & Wright, E. L. 2016, ApJ, 827, 116
Shankar, F., Lapi, A., Salucci, P., De Zotti, G., & Danese, L. 2006, ApJ, 643, 14
Shankar, F., Weinberg, D. H., & Shen, Y. 2010, MNRAS, 406, 1959
Shankar, F., Bernardi, M., Sheth, R. K., et al. 2016, MNRAS, 460, 3119
Shaw, L. D., Nagai, D., Bhattacharya, S., & Lau, E. T. 2010, ApJ, 725, 1452
Shen, Y., Greene, J. E., Strauss, M. A., Richards, G. T., & Schneider, D. P. 2008, ApJ, 680, 169
Shen, Y., Strauss, M. A., Ross, N. P., et al. 2009, ApJ, 697, 1656
Shen, Y., McBride, C. K., White, M., et al. 2013, ApJ, 778, 98
Sherwin, B. D., et al. 2012, Phys. Rev., D86, 083006
Sherwin, B. D., van Engelen, A., Sehgal, N., et al. 2017, PRD, 95, 123529
Sheth, R. K., Mo, H. J., & Tormen, G. 2001, MNRAS, 323, 1
Sheth, R. K., & Tormen, G. 1999, MNRAS, 308, 119
Sheth, R. K., & van de Weygaert, R. 2004, MNRAS, 350, 517
Singh, P., Majumdar, S., Nath, B. B., Refregier, A., & Silk, J. 2016, MNRAS, 456, 1495
Skillman, S. W., Warren, M. S., Turk, M. J., et al. 2014, ArXiv e-prints, arXiv:1407.2600

Slosar, A., & White, M. 2009, JCAP, 6, 9
Slosar, A., Land, K., Bamford, S., et al. 2009, MNRAS, 392, 1225
Slosar, A., Font-Ribera, A., Pieri, M. M., et al. 2011, JCAP, 2011, 001
Smee, S. A., Gunn, J. E., Uomoto, A., et al. 2013, AJ, 146, 32
Smith, K. M., Zahn, O., & Dore, O. 2007, Phys. Rev., D76, 043510
Soergel, B., Giannantonio, T., Efstathiou, G., Puchwein, E., & Sijacki, D. 2017, MNRAS, 468, 577
Sousbie, T., Pichon, C., Colombi, S., Novikov, D., & Pogosyan, D. 2008, MNRAS, 383, 1655
Spacek, A., Richardson, M., & Scannapieco, E. 2017a, ArXiv e-prints, arXiv:1711.05304
Spacek, A., Scannapieco, E., Cohen, S., Joshi, B., & Mauskopf, P. 2016, ApJ, 819, 128
—. 2017b, ApJ, 834, 102
Spergel, D., Gehrels, N., Baltay, C., et al. 2015, ArXiv e-prints, arXiv:1503.03757 [astro-ph.IM]
Spergel, D. N., Verde, L., Peiris, H. V., et al. 2003, ApJS, 148, 175
Spitler, L. R., Labbé, I., Glazebrook, K., et al. 2012, ApJL, 748, L21
Springel, V., Di Matteo, T., & Hernquist, L. 2005, MNRAS, 361, 776
Springel, V., & Hernquist, L. 2003, MNRAS, 339, 289
Stanek, R., Rasia, E., Evrard, A. E., Pearce, F., & Gazzola, L. 2010, ApJ, 715, 1508
Stark, C. W., Font-Ribera, A., White, M., & Lee, K.-G. 2015, MNRAS, 453, 4311
Stark, C. W., White, M., Lee, K.-G., & Hennawi, J. F. 2015, MNRAS, 453, 311
Starobinsky, A. A. 1980, Physics Letters B, 91, 99
Steidel, C. C., Erb, D. K., Shapley, A. E., et al. 2010, ApJ, 717, 289
Steidel, C. C., Shapley, A. E., Pettini, M., et al. 2004, ApJ, 604, 534
Steigman, G., & Turner, M. S. 1985, Nuclear Physics B, 253, 375
Steinmetz, M., & Navarro, J. F. 1999, ApJ, 513, 555
Stölzner, B., Cuoco, A., Lesgourgues, J., & Bilicki, M. 2018, PRD, 97, 063506
Strauss, M. A., Weinberg, D. H., Lupton, R. H., et al. 2002, AJ, 124, 1810
Sunyaev, R. A., & Zeldovich, Y. B. 1970, Ap&SS, 7, 3
—. 1972, Comments on Astrophysics and Space Physics, 4, 173
Sutter, P. M., Lavaux, G., Hamaus, N., et al. 2014a, MNRAS, 442, 462
Sutter, P. M., Lavaux, G., Wandelt, B. D., & Weinberg, D. H. 2012, ApJ, 761, 44
Sutter, P. M., Lavaux, G., Wandelt, B. D., et al. 2014b, MNRAS, 442, 3127
Sutter, P. M., Pisani, A., Wandelt, B. D., & Weinberg, D. H. 2014c, MNRAS, 443, 2983
Takada, M., Ellis, R. S., Chiba, M., et al. 2014, PASJ, 66, R1
Takahashi, R., Sato, M., Nishimichi, T., Taruya, A., & Oguri, M. 2012, ApJ, 761, 152
Tanabashi, M., Hagiwara, K., Hikasa, K., et al. 2018, Phys. Rev. D, 98, 030001
Tanaka, M., Coupon, J., Hsieh, B.-C., et al. 2018, PASJ, 70, S9
Tanimura, H., Hinshaw, G., McCarthy, I. G., et al. 2020, MNRAS, 491, 2318
Tejos, N., Morris, S. L., Crighton, N. H. M., et al. 2012, MNRAS, 425, 245
Tempel, E., & Libeskind, N. I. 2013, ApJl, 775, L42
Tempel, E., Stoica, R. S., Martínez, V. J., et al. 2014, MNRAS, 438, 3465
Tempel, E., Stoica, R. S., & Saar, E. 2013, MNRAS, 428, 1827

Tenneti, A., Mandelbaum, R., & Di Matteo, T. 2015, ArXiv e-prints
The Simons Observatory Collaboration, Ade, P., Aguirre, J., et al. 2018, ArXiv e-prints, arXiv:1808.07445
Theuns, T., Viel, M., Kay, S., et al. 2002, ApJL, 578, L5
Timmons, N., Cooray, A., Feng, C., & Keating, B. 2017, ApJ, 849, L6
Tinker, J., Kravtsov, A. V., Klypin, A., et al. 2008, ApJ, 688, 709
Tinker, J. L., & Conroy, C. 2009, ApJ, 691, 633
Tinker, J. L., Robertson, B. E., Kravtsov, A. V., et al. 2010, ApJ, 724, 878
Tinker, J. L., Brownstein, J. R., Guo, H., et al. 2017, ApJ, 839, 121
Tojeiro, R., Percival, W. J., Brinkmann, J., et al. 2012, MNRAS, 424, 2339
Treister, E., Natarajan, P., Sand ers, D. B., et al. 2010, Science, 328, 600
Trowland, H. E., Lewis, G. F., & Bland-Hawthorn, J. 2013, ApJ, 762, 72
Trujillo, I., Carretero, C., & Patiri, S. G. 2006, ApJl, 640, L111
Vagnozzi, S., Brinckmann, T., Archidiacono, M., et al. 2018, Journal of Cosmology and Astro-Particle Physics, 2018, 001
Vale, A., & Ostriker, J. P. 2004, MNRAS, 353, 189
van de Voort, F., Quataert, E., Hopkins, P. F., et al. 2016, MNRAS, 463, 4533
van de Weygaert, R., & Platen, E. 2011, in International Journal of Modern Physics Conference Series, Vol. 1, International Journal of Modern Physics Conference Series, 41
van den Bosch, F. C., Abel, T., Croft, R. A. C., Hernquist, L., & White, S. D. M. 2002, ApJ, 576, 21
Van Der Wel, A., Bell, E. F., Häussler, B., et al. 2012, ApJs, 203, 24
Van Der Wel, A., Franx, M., Van Dokkum, P. G., et al. 2014, ApJ, 788, 28
van Engelen, A., Bhattacharya, S., Sehgal, N., et al. 2014, Astrophys. J., 786, 13
Van Waerbeke, L., Hinshaw, G., & Murray, N. 2014, PRD, 89, 023508
Varela, J., Betancort-Rijo, J., Trujillo, I., & Ricciardelli, E. 2012, ApJ, 744, 82
Veale, M., White, M., & Conroy, C. 2014, MNRAS, 445, 1144
Verdier, L., Melin, J.-B., Bartlett, J. G., et al. 2016, A&A, 588, A61
Viel, M., Becker, G. D., Bolton, J. S., et al. 2008a, Phys. Rev. Lett., 100, 041304
Viel, M., Colberg, J. M., & Kim, T.-S. 2008b, MNRAS, 386, 1285
Viel, M., & Haehnelt, M. G. 2006, MNRAS, 365, 231
Viel, M., Haehnelt, M. G., & Springel, V. 2010, JCAP, 2010, 015
Viel, M., Schaye, J., & Booth, C. M. 2013, MNRAS, 429, 1734
Vielva, P., Martínez-González, E., & Tucci, M. 2006, MNRAS, 365, 891
Vikram, V., Lidz, A., & Jain, B. 2017, MNRAS, 467, 2315
Villaescusa-Navarro, F., Marulli, F., Viel, M., et al. 2014, Journal of Cosmology and Astro-Particle Physics, 2014, 011
Villaescusa-Navarro, F., Vogelsberger, M., Viel, M., & Loeb, A. 2013, MNRAS, 431, 3670
Vittorio, N., & Silk, J. 1985, ApJL, 297, L1
Vogelsberger, M., Genel, S., Sijacki, D., et al. 2013, MNRAS, 436, 3031
Vogelsberger, M., Genel, S., Springel, V., et al. 2014, Nature, 509, 177
Wake, D. A., Bundy, K., Diamond-Stanic, A. M., et al. 2017, AJ, 154, 86

Wang, P., Guo, Q., Kang, X., & Libeskind, N. I. 2018, ApJ, 866, 138
Wang, P., & Kang, X. 2018, MNRAS, 473, 1562
Warren, M. S. 2013, ArXiv e-prints, arXiv:1310.4502 [astro-ph.IM]
Weinberg, D. H., Davé, R., Katz, N., & Kollmeier, J. A. 2003, in American Institute of Physics Conference Series, Vol. 666, The Emergence of Cosmic Structure, ed. S. H. Holt & C. S. Reynolds, 157
Weinberg, D. H., Hernsquit, L., Katz, N., Croft, R., & Miralda-Escudé, J. 1997, in Structure and Evolution of the Intergalactic Medium from QSO Absorption Line System, ed. P. Petitjean & S. Charlot, 133
Weinberg, D. H., Mortonson, M. J., Eisenstein, D. J., et al. 2013, PhysRep, 530, 87
Weinberg, S. 1989, Reviews of Modern Physics, 61, 1
White, M. 2002, ApJS, 143, 241
White, M., Hernquist, L., & Springel, V. 2002, ApJ, 579, 16
White, M., & Hu, W. 1997, A&A, 321, 8
White, M., Martini, P., & Cohn, J. D. 2008, MNRAS, 390, 1179
White, M., & Padmanabhan, N. 2017, MNRAS, 471, 1167
White, M., Pope, A., Carlson, J., et al. 2010, ApJ, 713, 383
White, M., Myers, A. D., Ross, N. P., et al. 2012, MNRAS, 424, 933
White, S. D. M. 1984, ApJ, 286, 38
Willott, C. J., Delorme, P., Reylé, C., et al. 2010, AJ, 139, 906
Wilson, M. J., Peacock, J. A., Taylor, A. N., & de la Torre, S. 2015, ArXiv e-prints, arXiv:1511.07799
Wisnioski, E., Förster Schreiber, N. M., Wuyts, S., et al. 2015, ApJ, 799, 209
Wright, A. H., Hildebrandt, H., van den Busch, J. L., & Heymans, C. 2019, arXiv e-prints, arXiv:1909.09632
Wright, E. L., Eisenhardt, P. R. M., Mainzer, A. K., et al. 2010, AJ, 140, 1868
Xia, J.-Q., Viel, M., Baccigalupi, C., & Matarrese, S. 2009, JCAP, 2009, 003
Yan, R., Bundy, K., Law, D. R., et al. 2016a, AJ, 152, 197
Yan, R., Tremonti, C., Bershady, M. A., et al. 2016b, AJ, 151, 8
Yang, J., Wang, F., Wu, X.-B., et al. 2016, ApJ, 829, 33
Yu, Q., & Tremaine, S. 2002, MNRAS, 335, 965
Zaldarriaga, M., & Seljak, U. 1999, PRD, 59, 123507
Zeldovich, I. B., Einasto, J., & Shandarin, S. F. 1982, Nature, 300, 407
Zel'dovich, Y. B. 1970, A&A, 5, 84
Zel'dovich, Y. B., & Novikov, I. D. 1965, Soviet Physics Doklady, 9, 834
Zhai, Z., Tinker, J. L., Hahn, C., et al. 2017, ApJ, 848, 76
Zhang, S., Wang, T., Wang, H., & Zhou, H. 2013, ApJ, 773, 175
Zhang, Y., Yang, X., Faltenbacher, A., et al. 2009, ApJ, 706, 747
Zhang, Y., Yang, X., Wang, H., et al. 2015, ApJ, 798, 17
—. 2013, ApJ, 779, 160
Zhao, G.-B., Giannantonio, T., Pogosian, L., et al. 2010, PRD, 81, 103510
Zheng, Z., Berlind, A. A., Weinberg, D. H., et al. 2005, ApJ, 633, 791

Zivick, P., Sutter, P. M., Wandelt, B. D., Li, B., & Lam, T. Y. 2015, MNRAS, 451, 4215
Zjupa, J., & Springel, V. 2017, MNRAS, 466, 1625